The Molecular Control of Cell Movements

during Early Vertebrate Development

Thesis by

Andrew Josef Ewald

In Partial Fulfillment of the Requirements

for the Degree of

Doctor of Philosophy

California Institute of Technology

Pasadena, California

2003

(Defended March 14, 2003)

ii

Acknowledgments

I would like first of all to thank Scott Fraser, for his support and guidance through this work. I can truly say that without his advice and enthusiasm this thesis would not have been possible. I would also like to thank the members of my thesis committee, Marianne Bronner-Fraser, Richard Roberts, and Pamela Bjorkman, for their invaluable advice and comments through the years. I would also like to thank Richard Harland for very useful discussion of frog development. I also thank John Wallingford for his advice and guidance in experimental design and for great discussions on how to understand vertebrate morphogenesis.

I would like to thank everyone in the Fraser Lab, and, in particular, I would like to thank Rusty Lansford, Helen McBride, David Crotty, Mike Tyszka, David Koos, Paul Kulesa, and Carole Lu, for stimulating discussions and assistance. I would also like to thank Gary Belford, Mary Flowers, Sonia Collazo, Aura Keeter, and Tatayana Demyanenko, for technical assistance and for keeping the entire lab running smoothly.

I would like to thank Russ Kerschmann, Mark Reddington, Michael Bolles, Mike Haugh, Lynn Garrett, Benn Herrera, and Paul Gutherie, for their assistance and contributions to those aspects of the thesis that involved surface imaging microscopy. I also thank Resolution Sciences Corporation for having donated imaging time to this project.

I would also like to thank David Chan and Hsiuchen Chen for being stimulating collaborators on the mitochondrial fusion project. I would like to thank Kevin Thigpen for technical assistance in the early stages of the optical tweezers project, the Molecular Materials Resource Center for access to the optical tweezers facility, and the Beckman Institute Executive Committee for financial support to upgrade the optical tweezers facility for these experiments. I would like to thank Chris Chen, Sri Rhagavan, and Linda Griffith for useful conversations on patterning proteins on solid supports.

Finally, I would like to thank my parents Irene and Michael Ewald, my brothers, Carl and Jonathan, my friends, and Shannon Marshall, for their support and encouragement throughout the long process of graduate school.

Abstract

The early development of vertebrate embryos is characterized by massive, coordinated cell movements. These movements shape the embryo, distribute different cell types, shape complex tissues, and bring tissues into their correct spatial relationships. We have examined two early cell movements: the dorsal mesoderm of the frog embryo during gastrulation as a model for the coordinated movement of connected sheets of cells and the neural crest in the chicken embryo, as a model for cell migration.

The dorsal mesoderm in the frog embryo moves as a sheet of cells, due to strong connections among the cells. Cell intercalation within this sheet drives the elongation of the embryo during the process of gastrulation, whereby the round, morphologically symmetric early embryo is converted into a tadpole. We have demonstrated the existence of propagating intercellular waves of calcium within the dorsal mesoderm during gastrulation. These waves appear to be specific to the dorsal mesoderm and directly required for the cell movements of gastrulation. To build an integrated picture of how different signaling pathways interact to control gastrulation, we have developed a novel means of quantitatively imaging whole embryos with subcellular resolution. We have used this digital atlas to carefully examine the major events of gastrulation in normal embryos and embryos overexpressing a mutant form of the Disheveled protein.

The neural crest is a transient population of cells in the vertebrate embryo that arises in the neural tube and migrates to give rise to neurons, glia, bone and other cell types. During migration individual neural crest cells make extensive temporary connections with other cells, but migrate as individuals, rather than as a connected sheet. We have used patterned substrates and optical tweezers to present them with carefully controlled molecular stimuli. We have characterized their normal cellular behaviors and their response to ephrin-B ligands in a spatially and temporally defined manner.

Table of Contents

List of Illustrations

Introduction

Primary Goal of Thesis

The goal of my PhD thesis was to gain a greater understanding of the cell movements that shape the early development of the vertebrate body plan and to work out the molecular regulation of these cell movements. I was particularly interested in determining the structure of information flow in biological systems. I did not simply want to discover how one gene or signal controlled one particular cell movement, but rather to gain insight into how information is encoded and executed during early morphogenesis. Towards this end, I focused my efforts on studying two classical systems for studying early cell movements: the avian neural crest and the frog axial mesoderm during gastrulation. The avian neural crest provides a model for the migration of individual cells through a developing tissue and the axial mesoderm provides a model for the coordinated movement of a tightly connected epithelial sheet of cells.

Structure of Thesis

The opening chapter of the thesis will discuss the goals of my research, the reasons for selecting each model system, the methodology employed, the major techniques developed, and the major biological conclusions resulting from each aspect of my work. It will continue with a more philosophical reflection on why certain types of experiments provided more biological insights than others and conclude with an outline of my future plans for related research.

Cell Movements

I choose to work on the molecular control of cell movements for several reasons; first among them being a simple fascination with the degree of autonomy and information processing power that even these seemingly simple systems possess. It is simply fascinating to watch a cell explore its environment, interact with its neighbors, and shape an embryo. On a more practical level, cell movements are an important thing to study as they are the primary means by which the body plan of early vertebrate embryos is established. A very early embryo does not look like a miniature adult, it looks like a ball of cells. That ball of cells needs to quickly and precisely execute a dramatic series of cell movements to build the basic shape of the organism. Recent large-scale efforts (e.g., the Human Genome Project) have been tremendously successful in enumerating the components of biological systems: the challenge is now to understand how the components interact within dynamic systems. Finally, now is an opportune time to study the nature and molecular control of cell movements because the confluence of fluorescent labeling techniques (e.g., green fluorescent protein, GFP) and commercial laser scanning microscopes makes it possible to begin to follow these events, as they happen, in cells, tissues, and embryos [1].

Choice of Model Systems

The avian neural crest was selected as a model system for cell migration because of the rich embryological literature on its origins, induction, and

migration pathways (reviewed in [2-5]). It is also an experimentally tractable system as the premigratory neural crest is readily accessible and easily labeled via dye injection, electroporation [6, 7], and viral infection [8]. Additionally, as I was interested in studying cell migration in a vertebrate model system, the neural crest was a good choice as it is a shared derived characteristic of vertebrate embryos, and is believed to be evolutionarily critical to the diversification and success of the vertebrates [4, 9]. Finally, there was a strong history at Caltech and in the Fraser Lab of studying the neural crest, and significant progress had recently been made in understanding the control of neural crest cell migration [10-12].

The frog axial mesoderm was selected as a model for epithelial sheet movements for the rich literature describing its cell movements, recently reviewed in [13-15]. Additionally, the frog *Xenopus laevis* is experimentally convenient as it is routine to produce large numbers of embryos, the embryos develop approximately synchronously, and the tissues of the frog are readily amenable to explant culture. Critically for the success of our experiments, the explanted dorsal marginal zone of a gastrulating frog appears to execute its normal convergent extension cell movements autonomously, even when isolated from the rest of the embryo [16].

Methodology

The basic approach that I took was to develop imaging techniques to visualize cellular movements, document the normal biology of the system, then perturb

some potentially important molecular signal and observe the consequences. One aspect of developmental biology that I find intellectually satisfying and experimentally demanding is the necessity to consider dynamics and information flow across many length and timescales. Molecular recognition and signaling can take place on any timescale from nanoseconds through minutes. Cell behavior has observable dynamics from milliseconds through days. The development of the organism can take days, but the body plan, at least in amphibians, is established in the first few hours. It is very difficult *a priori* to determine on which timescales a given process is occurring. Even if a given range of cell behavior persists for only a few minutes, such as the formation of bottle cells in early gastrulation in the frog, it is quite difficult to determine when the crucial information exchange occurred and committed the organism to that decision.

The manner that I chose to address this challenge was to attempt to build cell behavioral assays capable of analyzing cell movements across several length and timescales. Rather than choose to study cell migration over hours and read out a single cellular decision at a handful of fixed time points, I attempted to experimentally observe and manipulate neural crest cell migration and frog gastrulation through a linked series of assays ranging from very short-term cell behavior through consequences of cell behavior read out over hours, through the long-term effects of molecular perturbations on avian and amphibian development over many hours through days.

I had originally hoped to study the role of Eph/ephrin signaling on neural crest migration in a mechanistic manner from its immediate early effects on cytoskeletal and membrane dynamics *in vitro* through a characterization of the intermediate cell migration decisions made by trunk neural crest cells aberrantly misexpressing ephrin ligands as they migrated through the somite, through the visualization of the entire migratory neural crest population and its derivatives in whole embryos over time as a function of ephrin disruptions.

Similarly, with the frog axial mesoderm, we understood that the coordination of motility within the axial mesoderm would require long-range, fast communication and hypothesized that calcium signaling would be ideally suited to these requirements. We therefore examined short timescale calcium fluctuations with fluorescent techniques, examined the consequences of disrupted calcium signaling in explanted tissues and whole embryos, and systematically analyzed the normal events of gastrulation in whole embryos using novel microscopic techniques developed for the purpose.

Technical Accomplishments

Overview

My thesis work concentrated on the development and application of fluorescent microscopic techniques for the purpose of visualizing cell movements *in vitro* and *in vivo* and the consequences in whole embryos of disrupting these cell

movements. During the course of my thesis work, I developed new methodology in three areas: microscopy and optics, culture and imaging of cell and embryos, and assay development. The first half of each experimental paradigm within this thesis was to visualize the normal behavior of the system, using some type of microscopic imaging technique. This description provided the means to understand what to expect as the normal state(s) of the system. To make progress in understanding the regulation of the cell movements, it is necessary to interfere with the normal molecular signaling processes that might govern the cell movements. The most technically advanced, and risky, aspects of my thesis dealt with developing systematic ways to challenge cell behavior. I present the major technical highlights from each of these sections below, and the details are presented in the relevant body chapters of the thesis.

Microscopy

Each of the chapters in this thesis focuses on visualizing some aspect of embryonic development with a light microscope. Over the course of my thesis, I visualized membrane and cytoskeletal dynamics with green fluorescent protein (GFP) fusions for the neural crest cultures (Chapter 2), visualized nuclear and mitochondrial organelle dynamics with neural crest and mouse fibroblast cultures (Chapter 2 and Appendix 1, respectively), visualized intercellular calcium dynamics within explants of gastrulating frog tissue (Chapter 4), and visualized whole embryos at subcellular resolution to study the relationship between cell polarity and tissue and embryo structure (Chapters 5 and 6). Most of this work

involved learning and applying fairly standard high performance microscopic techniques. Two of these projects required developing more original methods.

As described in detail in Chapter 2, we needed to visualize cytoskeletal dynamics within neural crest cells with relatively high temporal resolution (i.e., several scans per minute) over relatively long periods (i.e., several to many hours). The essential difficulty is that fluorescent labels are readily destroyed in the process of imaging. We made two changes that made successful imaging possible. First, we tested a broad range of Zeiss objective lenses to determine which gave the best light throughput for confocal imaging. Beyond the obvious increase in imaging performance from high numerical aperture objectives, we observed a significant benefit to using relatively simple, less optically corrected lenses, such as the Zeiss Fluar 20x lens. The more significant change was to design a custom set of filters and dichroics from Chroma Corporation. We designed and Chroma fabricated several competing types of primary dichroics and emission filters. After careful testing we selected the best components and integrated them into our Zeiss 310, 410, and Pascal confocal microscopes. For my neural crest cytoskeletal imaging experiments I observed a tenfold increase in sensitivity on the Zeiss 410 confocal. I was able to use this increased sensitivity to image at lower laser intensities and thereby dramatically reduce photobleaching. For many experiments, we were able to observe such a dramatic reduction in photobleaching that it became essentially undetectable. We interpreted this to mean that there is an experimentally achievable threshold within cells below

which there is effectively no photobleaching and above which damage is constantly and cumulatively being done.

The other main microscopic innovation in this thesis is the application of surface imaging microscopy (SIM) to early embryonic samples. Early in graduate school it became clear that there was a level of anatomy and three dimensional context that was critically necessary to understand neural crest cell migration and frog gastrulation that was inaccessible by traditional confocal microscopic means. In collaboration with Resolution Sciences Corporation, we adapted an existing microscopic techniques, surface imaging microscopy, to enable high resolution high contrast imaging of large thick biological specimens. The results of this collaboration are reported in Chapters 5 and 6. We had originally hoped to use SIM to visualize the entire population of migratory neural crest cells in normal chick embryos and embryos with different disruptions in Eph signaling, using fluorescent antibodies or GFP. We were unable to reliably detect these specific probes with SIM though and so our focus shifted to visualizing the frog gastrula.

Culture and Labeling of Cells

A perquisite of any imaging-based assay is the ability to successfully reproduce some aspect of the sample's normal physiology or development on the microscope stage. This effort typically takes two parts: introducing contrast to enable visualization of the structure or process of interest, then culturing that sample on the microscope stage. As I will discuss at further length in Chapter 2, I refined culture methods for quail neural tube explants to reliably produce

disperse cultures of healthy cells in serum free media. I then tested a variety of GFP fusion proteins for their ability to label structures within primary neural crest cells, specifically the actin cytoskeleton, the nucleus, and the plasma membrane and identified good labels for each. Finally, it was necessary to build imaging chambers for culturing neural crest cells on custom fabricated glass substrates both in conventional incubators and on the microscope stage. Examples of the most useful fusion proteins and culture chambers will be presented in Chapter 2.

This knowledge of labeling and culture techniques laid the technical foundation for the imaging of calcium waves in frog explants (Chapter 4) and mitochondrial structure and dynamics (Appendix 1). Though we were studying very different underlying biological processes the technical aspects of the experiments were quite similar.

Assay Development

The core of my efforts to understand the molecular regulation of cell movements was to observe cell behavior, challenge that cell behavior with a molecular perturbation, then observe the resulting effects of the perturbation. This represents a very standard experimental design. We were somewhat more innovative in the choice of molecular perturbations. For the neural crest cell migration experiments I developed two fundamentally different assays for challenging migrating neural crest cells in vitro. The first involved the creation of patterns of proteins on glass substrates. By observing neural crest cells

interacting with fixed spatial patterns of proteins on glass substrates we wanted to document the kinetics of the cell behavioral response to a repulsive boundary, in a way that was similar to the repulsive boundary these cells encountered within the caudal half of the somite during normal migration. The second assay was more specifically focused on the timing of the normal response of a neural crest cell to ephrin-B ligand. It involved coating glass beads with ephrin ligand and then presenting those beads to migrating neural crest cells using optical tweezers. We bound the proteins tightly to the beads so that the stimulus would not begin until the cell was in contact with the bead; the bead was not a diffusing source of protein. Using this assay, we documented the timing of the response of the beads, compared the effect of single beads to clusters of beads, compared the effect of presentation to different regions of the cell, and compared the effects of presenting the beads to isolated cells or to cells in contact with other neural crest cells.

For the frog gastrulation project, I developed labeling approaches to visualize calcium dynamics in living frog dorsal marginal zone explants, then we imaged the calcium dynamics and associated cell movements in the presence and absence of pharmaceutical inhibitors of calcium release. Once it was clear that there was a requirement for calcium signaling in gastrulation, I began applying surface imaging microscopy to systematically documenting the events of frog gastrulation and to visualizing the polarity of cells within different tissues as a function of developmental stage and Disheveled signaling activity.

Biological Conclusions

Neural Crest Cell Migration

The dynamics of neural crest cells migrating alone on patterned glass substrates was simply too variable to enable strong conclusions about the effect of ephrin signaling upon them. Some cells were repulsed by contact with ephrin-B regions and some seemed to prefer it; many did not appear to notice the difference. A more detailed discussion of the reasons for this are presented in Chapter 2.

More insight into neural crest cell migration was gained by focal application of ephrin coated beads (Chapter 3). Since the protein was bound strongly to the beads, I was able to very tightly control the timing of neural crest exposure to ephrin stimulus. The typical response to ephrin coated bead is a local collapse of lamellapodia, not filopodia, and an associated global increase in protrusive activity. This response is fast (1-5 minutes), implying that it can occur without recourse to transcription or translation. This response is also in sharp contrast to that observed in previous studies [10, 12], as previous authors reported a 20-40 minute delay in response, followed by a global collapse of all cellular projections. The nature of the reaction I observe is a reorganization of the polarity of the cell, accomplished by local collapse of lamellapodia, but leaving retraction fibers, and a globally increased protrusive activity. Interestingly, cells remain sensitive to multiple stimulations over a short (i.e., 1 minute) timescale. We observed

reductions in the strength of the cellular reaction to an ephrin stimulation when the cell in question was in contact with neighboring cells, as well as weaker reactions when the bead was presented to the lateral surface of the cell rather than its leading edge. Finally contact with multiple beads elicited a more severe reaction from cells than did a single bead. All of the noted differences were significant when compared to beads coated in Protein-G instead.   The background level of protrusive cellular activity was high though, complicating the analysis, as detailed further in Chapter 3.

Frog Gastrulation

In Chapter 5, I present the results of our efforts to understand the mechanisms by which large numbers of cells coordinate their motility during gastrulation. We hypothesized that calcium waves could provide a means for cells in the dorsal mesoderm to coordinate their cell movements during gastrulation. We looked for and observed long-distance, intercellular propagating waves of calcium within the dorsal mesoderm.   These waves were typical in the dorsal mesoderm, and specific to it. We did not observe waves in explants of animal cap ectoderm or ventral mesoderm. Inhibition of calcium release, using the drug thapsigargin, prevented elongation of dorsal marginal zone explants, and blocked the elongation of the prospective notochord domain within whole embryos. This effect appeared to be a direct effect on morphogenesis, as the fate specification of dorsal marginal zone explants treated with thapsigargin remained normal, as assayed by molecular marker analysis.

Based on this increased knowledge of the molecular control of gastrulation cell movements, as well as parallel work done on the role of Wnt signaling in the dorsal mesoderm [17], I decided to take a more systematic approach to the evaluation of phenotypes within frog embryos. Since the frog embryo is more than a millimeter thick and highly opaque at gastrula stages, confocal and two photon microscopy are unable to observe deep events within the living embryo. To gain a deeper understanding of the structure of the *Xenopus* gastrula, and the relative phenotypic consequences of different disruptions of gastrulation, we used a novel form of fluorescence microscopy, surface imaging microscopy (SIM), as discussed in Chapter 6. We imaged a full developmental time series of *Xenopus* development, from blastula through early neurula stages. To take best advantage of these digital datasets, we have developed computational methods to normalize each of these embryos to a common set of coordinates, based on the blastocoel, blastopore, and the dorsal midline. We then extracted surfaces from these volumes and documented the characteristic events of gastrulation: tissue separation, archenteron elongation, and mesendoderm migration, and blastopore closure. We have also begun to compare and contrast these processes in normal embryos and those in which the dorsal mesoderm overexpresses a mutant form of the Disheveled protein, Xdd1 [17, 18].

Conclusions and Way Forward

Relative O/I Merits of Different Approaches

As I have reflected on the relative information content of different categories of experiments, several ideas have emerged. The underlying theme to all my biologically informative experiments is that the (sub)cellular behavior that I was interested in understanding was autonomously present in the explanted sample on which I performed my experiments. My job as an experimentalist was simply to keep the cell or tissue alive and healthy and it would then perform its characteristic behavior, whether this was a calcium wave propagating through a dorsal marginal zone explant, or mitochondrial fusion and transport in a fibroblast, or large scale morphogenetic movements in the frog gastrula. The key to these experiments is that I could reproducibly prepare samples that would exhibit similar behaviors, and differences could be inferred to be chiefly due to natural variation.

Once the natural variability was understood, I could then perturb some aspect of the molecular machinery, and attribute any observed differences in cell behavior to effects of the perturbation. The more biophysical approaches sought to create the conditions under which the neural crest cells would respond uniformly to inherently artificial stimuli, such as photolithographed patterns of ephrin protein. I failed to appreciate at the time that there were very few truly autonomous cell behaviors of a neural crest cell in culture, and as such it is difficult to know *a priori* what to expect a neural crest cell to do in response to an artificial stimulus.

The only autonomous, repeatable cell behaviors that I observed in my neural crest cultures were delamination from the neural tube and outgrowth from the neural tube. Even these proved highly variable once I looked carefully at the details. I was seeking to build an assay with single cell predictability, where there would be, at least statistically, a consistent observable cellular response to my imposed ephrin stimulation. As a consequence, all of my neural crest cell migration guidance experiments had a high threshold to surpass before they could begin to produce biologically relevant information. First I needed to successfully engineer the physical and chemical conditions for presentation of the molecular guidance cue. In each case I succeeded in doing this, with several different substrate pattern generation techniques (described in detail in Chapter 2), as well as focal presentation of beads using optical tweezers (Chapter 3). The problem is that in each case this was merely the prelude to the experiment. I couldn't begin to do developmental biology in any of these paradigms, until I established that the neural crest cells had a highly reproducible reaction to our artificial stimulus. They didn't.

A reproducible reaction implies two separate things. First, it implies that the background level of cell behavior in the absence of intentionally imposed stimulus is low. This is not the case. Neural crest cells, left to their own devices, are incredibly dynamic and are in a constant state of extension and retraction, sampling their environment and making contact with other cells.

Second it implies that the cells will behave similarly to each other, from dish to dish, and day to day. Again with neural crest cells this is not the case. There is considerable variation in cell size, cell shape, and degree of activity. This makes it very difficult to interpret whether a given difference in cell reaction is due to a constant reaction to a varying stimulus or to varying reactions to the same stimulus. Once the cell being studied is in contact with another neural crest cell it is nearly impossible to parse apart what part of its action is due to the cell and what due to the substrate or bead. In my substrate experiments, I observed a strong community effect, where cells in extensive contact with each other rarely observed the imposed boundaries, but isolated cells could respond more readily. In the optical tweezers experiments the bead similarly evoked a less dramatic reaction in cells with extensive cell-cell contact.

Normal Neural Crest Cells

The cells that were most interpretable in both substrate and tweezers experiments were isolated highly polarized cells. They are also highly unusual and highly unstable cells. Neural crest cells seem to have a strong affinity for each other even in culture. Pioneer cells far from the main outgrowth are quite uncommon. Recent *in vivo* time-lapse data [19-21] implies strongly that the functional migration unit for a neural crest cell is not a single neural crest cell, but rather that they typically migrate in chains or small groups of cells.

Simplest Functional Unit

I am still a strong believer in reductionist science. I don't believe that all genes or proteins or cells are equivalently important to a given process. I still believe that the most direct way to test if a given component is necessary is to pharmaceutically break that component or genetically remove it and then see if the process proceeds normally.   I would now place more emphasis on the functional part of the phrase 'simplest functional unit' than I did at the onset of graduate school. It is experimentally convenient to have a simpler system. It is necessary that the system still retains the essential features of its *in vivo* behavior.

By focusing so completely on experimentally imposed migration guidance choices, I was, in effect, using neural crest cells as expensive, hard to manipulate, and short lived fibroblasts. To take best advantage of their properties as a migratory system I would have needed to carry more of the system into culture, as has recently been done [22, 23] to study neural crest cell migration and muscle cell precursor migration. A better starting point for studying neural crest cell migration would be the trunk explant [24] or the intact embryo. The imaging and culture approaches that I developed for examining neural crest cell migration *in vitro* would be best applied to the analysis of a phenotype that has already been observed *in vivo*, rather than an assay for critical migration components, that all then need to be tested for *in vivo* relevance.

Therein lies the strength of the frog experiments that I have finished. By starting with the dorsal marginal zone explant, we were able to observe cellular calcium release events and correlate those with cellular movements, link those movements and their regulation to the behavior of the tissue as a whole and then demonstrate the necessity of calcium signaling for the successful completion of gastrulation. Similarly, by employing high resolution imaging techniques such as SIM to study the effects of Disheveled disruptions that we already know are important to the development of the organism [17, 25], we gain deeper insights into the details of a process that we already know is important.

Future Directions

I plan to continue the work described in Chapter 6 to explore the coupling of different morphogenetic processes during frog gastrulation. Inhibition of Dsh signaling in the dorsal mesoderm blocks convergent extension cell movements, but our preliminary data using SIM analysis suggests that the elongation of the developing gut, the archenteron, is fairly normal. I will be measuring the degree of coupling of blastopore closure to archenteron elongation, and dorsal mesodermal convergent extension, as a function of disruptions in calcium release and Wnt signaling.

My Role in Collaborative Projects

Much of my thesis work was done in close collaboration with a group of very talented and generous scientists. I owe them my deepest gratitude for assisting in my thinking and guiding different aspects of my experiments. For simplicity, I will acknowledge each project independently.

Confocal Optimization:

I worked with Michael Stanley of Chroma Corporation and Scott Fraser on the design of the components and Fritz Rohweder of Carl Zeiss Corporation in testing these dichroic mirrors and interference filters for the purpose of optimizing our Zeiss 410 laser scanning confocal microscope for imaging green fluorescent protein.

Substrate Patterning:

This project originated from previous work of Rusty Lansford in the Fraser Lab, and began under his mentorship. I had useful conversations with Grant Walkup regarding silane monolayers. I consulted with Michael Roukes, and was trained by members of his lab in the use of equipment for substrate fabrication. I am also indebted to Linda Griffith, of MIT, and Chris Chen and Srivatsan Raghavan, of Johns Hopkins, for valuable discussions of alternate patterning methodologies and for donating reagents.

Surface Imaging Microscopy:

The idea of applying surface imaging microscopy to imaging early embryos arose from discussions between myself and Russell Kerschmann, of Resolution Sciences Corporation and he donated instrument time at the company to the project. Helen McBride assisted in developing histological techniques for preserving early embryos through the processing steps. Mark Reddington, of Resolution Sciences Corporation, carried out the imaging at the company, on samples that I prepared and analyzed.

Frog Calcium:

This project emerged from discussions between myself, John Wallingford, Scott Fraser, and Richard Harland. The origins of the project predated my involvement, but I was involved in planning and carrying out the experiments from the first. I was chiefly responsible for developing labeling and imaging techniques to visualize the calcium dynamics. John did all of the microsurgical manipulations and in situ hybridizations. I was involved in the design and analysis of all of the experiments.

Digital Analysis of Frog Gastrulation

I originally developed the surface imaging microscopy approaches to visualize the avian neural crest in intact embryos. After many trials it became clear that SIM was extremely good at imaging bright small molecule dyes, and inefficient at imaging dim specific labels such as antibodies or green fluorescent protein. This

dichotomy emerged shortly after finishing the frog calcium project and I realized that the technique would be very well suited to imaging intact frog embryos and comparing normal embryos to experimentally altered embryos. I prepared the normal embryos and Mark Reddington imaged them at Resolution Sciences Corporation. To take best advantage of the full range of information present in these digital embryos I collaborated with J. Michael Tyszka to develop MatLab programs to digitally segment the embryos, and with John Wallingford to prepare embryos expressing mutant forms of the Disheveled protein. John Wallingford has also played a key advisory role in the project.

Mitochondrial Fusion:

One unexpected consequence of the confocal microscopy optimizations was that we had developed a strong capacity to visualize many fluorescent protein fusion proteins with little or no photobleaching. One of the tests that established this was done on a mitochondrial targeted yellow fluorescent protein. Through a stroke of serendipity a new professor, David Chan, arrived at Caltech shortly thereafter who was very actively studying the genetics of mitochondrial fusion, but lacked a means to visualize it. The culture, labeling, and imaging techniques that I had developed to examine neural crest cells proved ideally suited to visualizing mitochondrial fusion and so I collaborated with David and members of his lab to characterize the morphology and dynamics of mouse embryo fibroblasts from a variety of genetic backgrounds. This project is outside of the main theme of my thesis and is reported in Appendix 1.

1. Lichtman JW, Fraser SE: **The neuronal naturalist: watching neurons in their native habitat**. *Nat Neurosci* 2001, **4 Suppl**:1215-1220.
2. Baker CV, Bronner-Fraser M: **The origins of the neural crest. Part I: embryonic induction**. *Mech Dev* 1997, **69**:3-11.
3. Bronner-Fraser M: **Origins and developmental potential of the neural crest**. *Exp Cell Res* 1995, **218**:405-417.
4. Hall B: *The Neural Crest in Development and Evolution*, 1st edn. New York: Springer; 1999.
5. Le Douarin N, Kalcheim C: *The Neural Crest*, 2nd edn. Cambridge: Cambridge University Press; 1999.
6. Itasaki N, Bel-Vialar S, Krumlauf R: **'Shocking' developments in chick embryology: electroporation and in ovo gene expression**. *Nat Cell Biol* 1999, **1**:E203-207.
7. Swartz M, Eberhart J, Mastick GS, Krull CE: **Sparking new frontiers: using in vivo electroporation for genetic manipulations**. *Dev Biol* 2001, **233**:13-21.
8. Okada A, Lansford R, Weimann JM, Fraser SE, McConnell SK: **Imaging cells in the developing nervous system with retrovirus expressing modified green fluorescent protein**. *Exp Neurol* 1999, **156**:394-406.
9. Baker CV, Bronner-Fraser M: **The origins of the neural crest. Part II: an evolutionary perspective**. *Mech Dev* 1997, **69**:13-29.
10. Krull CE, Lansford R, Gale NW, Collazo A, Marcelle C, Yancopoulos GD, Fraser SE, Bronner-Fraser M: **Interactions of Eph-related receptors and ligands confer rostrocaudal pattern to trunk neural crest migration**. *Curr Biol* 1997, **7**:571-580.
11. Smith A, Robinson V, Patel K, Wilkinson DG: **The EphA4 and EphB1 receptor tyrosine kinases and ephrin-B2 ligand regulate targeted migration of branchial neural crest cells**. *Curr Biol* 1997, **7**:561-570.
12. Wang HU, Anderson DJ: **Eph family transmembrane ligands can mediate repulsive guidance of trunk neural crest migration and motor axon outgrowth**. *Neuron* 1997, **18**:383-396.
13. Keller R: **Shaping the vertebrate body plan by polarized embryonic cell movements**. *Science* 2002, **298**:1950-1954.
14. Keller R, Davidson L, Edlund A, Elul T, Ezin M, Shook D, Skoglund P: **Mechanisms of convergence and extension by cell intercalation**. *Philos Trans R Soc Lond B Biol Sci* 2000, **355**:897-922.
15. Wallingford JB, Fraser SE, Harland RM: **Convergent extension: the molecular control of polarized cell movement during embryonic development**. *Dev Cell* 2002, **2**:695-706.
16. Schechtman A: **The mechanics of amphibian gastrulation**. *Univ. Cal. Pub. Zool.* 1942, **51**:1-39.
17. Wallingford JB, Rowning BA, Vogeli KM, Rothbacher U, Fraser SE, Harland RM: **Dishevelled controls cell polarity during Xenopus gastrulation**. *Nature* 2000, **405**:81-85.

18. Rothbacher U, Laurent MN, Deardorff MA, Klein PS, Cho KW, Fraser SE: **Dishevelled phosphorylation, subcellular localization and multimerization regulate its role in early embryogenesis**. *Embo J* 2000, **19**:1010-1022.

19. Kulesa P, Bronner-Fraser M, Fraser S: **In ovo time-lapse analysis after dorsal neural tube ablation shows rerouting of chick hindbrain neural crest**. *Development* 2000, **127**:2843-2852.

20. Kulesa PM, Fraser SE: **Neural crest cell dynamics revealed by time-lapse video microscopy of whole embryo chick explant cultures**. *Dev Biol* 1998, **204**:327-344.

21. Kulesa PM, Fraser SE: **In ovo time-lapse analysis of chick hindbrain neural crest cell migration shows cell interactions during migration to the branchial arches**. *Development* 2000, **127**:1161-1172.

22. Santiago A, Erickson CA: **Ephrin-B ligands play a dual role in the control of neural crest cell migration**. *Development* 2002, **129**:3621-3632.

23. Knight B, Laukaitis C, Akhtar N, Hotchin NA, Edlund M, Horwitz AR: **Visualizing muscle cell migration in situ**. *Curr Biol* 2000, **10**:576-585.

24. Krull CE, Kulesa PM: **Embryonic explant and slice preparations for studies of cell migration and axon guidance**. *Curr Top Dev Biol* 1998, **36**:145-159.

25. Wallingford JB, Harland RM: **Xenopus Dishevelled signaling regulates both neural and mesodermal convergent extension: parallel forces elongating the body axis**. *Development* 2001, **128**:2581-2592.

Towards an Understanding of the Interactions Between Migrating Neural Crest Cells and Substrate Bound Guidance Molecules

Neural crest cell migration serves as a model system to study how the interactions of individual cells with their neighbors and their environment contributes to the guidance of migrating cell populations in the vertebrate embryo. In order to study how cells respond to cues from their environment, we cultured neural crest cells on patterned *in vitro* substrates to present the cells with a choice between migration on two different substrates, while simultaneously imaging the cell behavioral responses to these substrates.

In the course of developing this assay system, we developed improved methods for long-term imaging of fluorescent proteins with a confocal laser scanning microscope. We also tested a range of culture chambers for keeping neural crest cells healthy and developing normally on a microscope stage, and simplified the neural tube explant culture protocols.

To test the interactions of migrating neural crest cells with ephrin-B ligands, we generated patterns of ephrin-B protein on substrates coated in fibronectin and imaged the resulting cellular response to these patterns. We developed a novel photolithographic patterning method for building patterns of proteins on glass, and compared that to more established adsorption based methods. We found that our patterns were sharper and more robust, and that neural crest cells are generally repelled by ephrin-B ligands, in accordance with previous studies [1, 2]. However, the variation between individual neural crest cells and between cultures was too great to permit strong conclusions to be drawn. Since we greatly increased reduced the variation in implementation of the migration assay, but the variability in the cell behavior persisted, we conclude based on these experiments that the variability in the cellular response is due to differences inherent in the neural crest cells themselves and how different neural crest cells interpret the same guidance cue. We finish by discussing the basis for this variability and by discussing possible future directions for this type of experimental paradigm.

Andrew J. Ewald and Scott E. Fraser

Biological Imaging Center

California Institute of Technology

Background and Significance

The neural crest is a transitory, embryonic population of cells that emerges from the dorsal neural tube of vertebrate embryos in an anterior to posterior wave of migration that gives rise to a diverse range of derivatives, including neurons, glia, bone, cartilage, smooth muscle cells, melanocytes, among others [3-7]. Neural crest cells migrate over hundreds of microns in stereotypic patterns according to their level of origin in the anterior-posterior (A-P) axis, and each A-P level has a different mix of characteristic derivatives. As they migrate, at least some neural crest cells are individually multipotent, capable of giving rise to descendants in multiple locations and of multiple cell types, including both neurons and glia [8, 9]. It is a matter of controversy within the field whether a subpopulation of neural crest cells are more restricted in their developmental potential. Excellent reviews cover both sides of this discussion [4, 5].

We are interested in determining the factors that guide crest cells to their eventual destinations. Classical studies have shown that neural crest cells follow stereotyped migration patterns based on the location of origin of the crest within the neural tube, reviewed in [7]. An interesting example of these patterns occurs in the trunk of the developing avian spinal cord. Crest cells in this region migrate in a segmental fashion, always migrating through the anterior and not the posterior half of the adjacent somite pairs. This segmental pattern is conferred by the mesodermal tissue through which the cell migrates, not by the location of origin of the crest cells themselves, as surgical rotation of the mesoderm results

in a corresponding rotation in the segmental pattern [10]. We wanted to connect this observed migration pattern with the molecular factors and cellular rules which generate it.

Many candidate mechanisms have been proposed to guide neural crest cells. Cells could be following guidance cues that are diffusible, in the extracellular matrix, or bound to the plasma membranes of other cells. Crest cell migration might be driven by population pressure inside the neural tube, or cells may be actively following a gradient of chemoattractant originating outside of the neural tube. It is comparatively easy to propose a possible mechanism for crest cell guidance; the difficulty lies in developing an experimental approach that will distinguish between different candidate mechanisms within the full complexity of the developing embryo. Rather than try to solve the whole problem at once, several groups have attempted to develop *in vitro* migration assay systems to allow candidate molecules and tissues to be individually evaluated for their effects on crest cell migration.

Intense research has focused on the molecular or physical origin of the segmental migration of trunk neural crest cells. Work prior to 1997 chiefly focused on the role of extracellular matrix differences in guiding the neural crest, reviewed in [11, 12]. Many molecular differences were discovered between the rostral and caudal half somite. Molecules that have been observed in the correct time and place to be involved in trunk neural crest guidance include chondroitin

sulfate proteoglycans such as versican [13], N-Cadherin, Cad7, Cad6b [14], RhoB [15], F-spondin [16], Collapsin-1 (a semaphorin) [17], MMP2 [18], and peanut agglutinin binding molecules [19]. Following the report of the repulsive effect of Eph/ephrin signaling on migrating trunk neural crest cells [1, 2], much of the attention of the field turned in this direction.

It has been shown that neural crest cells avoid regions of a culture dish which contain ephrin-B1, and that disruption of ephrin-B1 signaling results in crest cells migrating through the posterior half of the somite [1,2]. It has also been shown that neural crest cells migrate through regions that are low in F-Spondin expression and avoid areas that highly express F-Spondin [16]. Furthermore, disruption of F-Spondin function with neutralizing antibodies is sufficient to allow neural crest cells to migrate into regions they would normally avoid [16]. It is not easy to reconcile these results. They appear to show that two unrelated molecules are each independently sufficient to establish permissive and repulsive neural crest migration zones within the embryo, while at the same time implying that disruption of either one will convert the repulsive zones into permissive zones.

It is difficult to reconcile these experiments because the assays used were designed to classify molecules as either repressive or permissive. It is clear from these papers alone that neural crest cell migration is influenced by many, different factors. If we want to understand migration guidance, we need to move

beyond a binary classification of molecules as permissive or inhibitory and instead try to compare the ways in which different signals affect neural crest cells, alone and in combination, in the hope that we will then be better able to understand how these signals will interact *in vivo*. I sought to build *in vitro* assays general enough to be capable of eventually distinguishing between the influences of each of these molecules, but focused experimentally on the effects of Eph/ephrin signaling on the neural crest. Once we characterized the response of neural crest cells to ephrin ligands, we planned a quantitative, combinatorial evaluation of the effects of other guidance molecules, both alone and in combinations.

Eph/ephrin Background

The Eph proteins are a family of receptor tyrosine kinases, with a cognate family of ligands, whose actions are implicated in the control of a variety of embryonic processes [20-23].   One of the first *in vivo* roles discovered for the Eph/ephrin family was in the topographic projection of retinal axons to the tectum [24]. This role was first identified through a series of choice assays developed by Friedrich Bonhoeffer and colleagues, which involved allowing axons from different regions of the retina to choice between crude membrane fragments [25].   They then modified the assay to present axons with a choice between ever purer membrane fractions until they were able to demonstrate that the repulsive activity was replicated purified ephrin proteins [24].   Similar assays were used to demonstrate a role for Eph/ephrin signaling in mouse [1] and chick [1, 2, 26]

neural crest cell migration. Different assays established the role of Eph/ephrin signaling in frog neural crest cell migration as well [27, 28].

Initially Eph/ephrin signaling was believed to be an intrinsically repulsive guidance mechanism, but this simple story was soon complicated by the discovery [29] that Eph/ephrin differences uniquely mark arteries and veins, prior to morphological differentiation, and that the function of ephrin proteins is required for formation of the cardiovascular system. Mice lacking these genes suffer profound defects in angiogenesis and cardiovascular development [30-32]. Additional complications emerged as it became clear that ephrin signaling is not obligately repulsive, but instead can mediate adhesive interactions as well [33], possibly through the use of different splice variants of the Eph receptor [34]. Recent efforts demonstrated that the cytoplasmic domains of ephrin-B2 as critical for arterial development, but dispensable for cranial neural crest migration [35]. Finally, progress has also been made in working out various aspects of signal transduction downstream of both Eph and ephrin [36] [[37].

Cell Migration Assays

Central Logic of Our Experiments

There were two guiding principles in our design of a cell migration assay. We wanted to evaluate cellular responses to a choice between two substrates, not control cell behavior. The second was that we sought to improve the technical underpinnings of the stripe assay in order to remove extraneous sources of non-

biological variability (e.g., systematic patterning artifacts) so that we could quantitatively measure both the normal response of neural crest cells to ephrin-B ligands and the normal degree of variability in that response. By carefully controlling the presentation of ephrin-B guidance cues to neural crest cells, we sought to standardize the experimental design sufficiently that different neural crest cells would be presented with the same migration choice. By visualizing and measuring those responses using time-lapse microscopy, we expected that we could catalog the range of possible responses and that we would eventually be able to predict what a given cell should do in response to a given experimental setup, Once we knew what that reaction was, so long as it was predictable, we then planned to study the signal transduction requirements for that response via pharmaceutical inhibition of various cellular pathways, starting with transcription and translation.

We based our approach loosely on an assay known as the "stripe assay," which has been used to test the involvement of specific molecules on axon guidance and neural crest migration behavior [1, 24, 27]. In this assay, candidate molecules are physically adsorbed in patterns onto nitrocellulose-coated tissue culture plastic. Cells are then cultured on these patterned surfaces, and candidate molecules are scored based on the degree to which cells have accumulated on the stripes at some later time (Figure 2-1). If more cells avoid the stripes than occupy them, the candidate molecule is classified as a repulsive agent. If there is no obvious pattern, then the molecule is judged to be

permissive. Some efforts have been made to extend this analysis by filming the cells, using time-lapse microscopy, as they are migrating [2]. However, these efforts are greatly hindered by the intrinsic unsuitability of the classic stripe assay for high-resolution microscopy.

The problems are not intrinsic in the conceptual design of the assay, but rather in the experimental implementation. The first problem is that patterns are defined by a physical grid of flow channels, which is pressed into nitrocellulose coated plastic. This approach severely limits pattern design to those which are amenable to flow channels. Additionally, cells are sensitive to very small differences in surface topology [38, 39]; consistent with this concern, a recent research article utilizing the stripe assay reported a tendency of cells to non-specifically avoid the stripe that is laid down first, independent of protein content [40]. Furthermore, since the deposition relies on non-specific adsorption, it is difficult to produce highly uniform regions; inevitably there are regions of high and low protein adsorption even in identically treated areas. Finally, both the plastic tissue culture dish and the nitrocellulose used to coat the dish directly hinder high-resolution imaging. Plastic is autofluorescent and scatters light, while the nitrocellulose leaves cell sized artifacts throughout the field of view. We sought to address both of these deficiencies by developing a more robust patterning chemistry on thin glass coverslips.

Materials and Methods/Experimental Techniques

Time-Lapse Imaging

Time-lapse movies were collected on a Zeiss 410 confocal laser scanning microscope (CLSM) or a Zeiss Pascal CLSM. For imaging neural crest cultures, the CLSM were outfitted with a temperature controlled chamber which maintains a constant 37° C.

Neural crest cells display extensive protrusive activity in culture. In order to temporally resolved the membrane and cytoskeletal dynamics of neural crest cell migration, it proved necessary to acquire images every 1-20 seconds. Conversely we needed to follow these cells for minutes to hours in order to determine their reaction to the substrate patterns. This balance of frequent imaging over long time periods required that we be very careful not to damage the cells with excessive light exposure. When we began this project we could image actin-GFP in neural crest cells at very high resolution, but the signal would fade very rapidly. To successfully image such dim fluorescent labels, three elements were critical: careful choice of objective lenses, custom designed filters and dichroics, and careful management of light exposure.

The brightness of an image on a standard confocal microscope scales with the fourth power of the numerical aperture (NA) of the objective lens. The numerical aperture captures both the geometry of the lens and the optical properties of the immersion media between the lens and the sample. Due to this steep

dependence of brightness on NA, small changes in the NA have very large effects on the collected image, as demonstrated in Figure 2-1. We tested the full range of Zeiss objective lenses for imaging and found the 20x Fluar, 40x C-Apochromat, and 63x Plan-Apochromat to provide superior performance for our applications.

The second change that we made to the Zeiss 410 was to upgrade all of the emission filters and dichroic mirrors with custom optics from Chroma Corporation (Brattleboro, VT). In collaboration with Michael Stanley of Chroma Corporation we optimized the internal optics of the 410 for imaging green fluorescent protein. We conducted tests on the efficiency of the system before and after the upgrade and observed a tenfold increase in sensitivity on the green channel, as illustrated in Figure 2-2.

The single most important factor for successful imaging of dim fluorescent labels in living samples is the careful management of the excitation light power levels. It is typically possible to generate equivalent quality images of the same sample over incident power levels that vary by at least tenfold. There is no obvious signal from the microscope or the image that one could get equivalent results with less light. To accommodate this fact, we generally started imaging with very significant (100-300 fold) attenuation of the incident laser intensity, and only slowly increased the laser power until a reasonable image was achieved. This approach was critical to our fluorescent imaging, as we empirically noted a

threshold effect in our samples, whereby the cells could tolerate a certain amount of light without photobleaching or obvious photodamage. However once that threshold was exceeded the damage could be swift and irreparable. The effect of incident light power on image quality and photobleaching is demonstrated in Figure 2-3.

Imaging Chambers

Prior *in vitro* culture of neural tube explants in the Fraser Lab had been performed in standard 35 mm plastic tissue culture dishes [2]. These chambers were inexpensive and convenient, but the thick plastic bottom was incompatible with differential interference contrast microscopy and was too thick to allow access for high NA objective lenses. To overcome these difficulties we tested several alternative imaging chambers, illustrated in Figure 2-4. There were three basic variants, the porthole chamber, the o-ring chamber, and the chambered coverslip. Porthole chambers were convenient and inexpensive to prepare in large numbers. Four well multidishes (Nunc Nunclon Delta 176740) or 35 mm tissue culture dishes (Falcon 35-3001) were modified in the Chemistry Machine Shop at Caltech, by removing a 15-17 mm circle from the bottom surface of each of the wells. We then attach a patterned glass substrate to the bottom surface of the culture well using silicon grease. By replacing portions of the lids of these chambers with glass, we are able to create an all glass optical path, thereby allowing differential interference contrast (DIC) microscopy methods. These chambers have worked well for imaging and can be reused by cleaning and sterilizing with 70% ethanol and hard UV between uses. The four well chambers

allowed us to use smaller amounts of media and protein reagents. When combined with a programmable moveable microscope stage, these multiwell imaging chambers allow us to simultaneously image several neural crest cultures.

Alternate designs included an o-ring chamber (pictured in Figure 2-4B) that was made by Herb Adams at Caltech's Central Plant. This chamber is very similar to the Attofluor cell chamber (Molecular Probes, A-7816), except that the top of the chamber is made of Delrin instead of stainless steel. We substituted Delrin for stainless steel for all surfaces in contact with cells, because an all stainless steel cell culture chamber was tested and found to be acutely toxic to neurons and neural crest cells (though not to NIH/Swiss 3T3 fibroblasts). This highlights the importance of careful selection of materials for cell culture, and the importance of testing a chamber with the actual cells of interest. With the Delrin top it was compatible with neural crest cell cultures and was convenient to load, but it was difficult to maintain sterile cultures in the chamber and so it was not used frequently. Another convenient commercially available option was the Nalge/Nunc Lab-Tek chamber (Figure 2-4C), which consisted of plastic culture chambers bonded to either coverslips or slides. Though more fragile, the coverglass chambers were more useful as the slide chambers were too thick for the working distance of high performance microscope objectives. These were the chambers of choice when working with cells, such as fibroblasts, that readily

adhere to bare glass (as in the mouse embryo fibroblasts used in the paper described in Appendix 1), but were not as useful with neural crest cells.

Labeling Neural Crest Cells In Vitro and In Vivo

In order to specifically highlight different subcellular components of migrating neural crest cells, I tested a range of different green fluorescent protein (GFP) fusion proteins. In a separate, but synergistic research effort within the Fraser Lab, Rusty Lansford has been developing a set of retroviruses to deliver proteins to avian cells. He generated replication-defective VSV-G pseudotyped retroviral viruses that express GFP or LacZ marker to infect avian embryos [41]. Pseudotyping alters the host range of a virus by exchanging the surface antigens among both DNA and RNA viruses [42]. The resulting VSV-G pseudotyped retroviruses possess a broad host range and can be concentrated 1000-fold with minimal loss of biological activity These viruses are capable of infecting nearly any cell in the avian embryo, including neural crest cells, and do not appear to negatively affect cellular development. I tested a large number of these viral constructs in avian embryos. The most useful were viruses that delivered a nuclear GFP (Clontech Histone2B EGFP), mitochondrial YFP (Clontech EYFP-Mito 632347), membrane GFP (Clontech Gap43-EGFP), or actin GFP (Clontech EGFP-Actin 632348). The GFP fusion proteins express well in avian cells and I have successfully imaged each of them for extended durations in living cells using confocal microscopy.

The major advantage of these labels was that they are readily applied to cultured neural crest cells or injected into neural tubes *in situ*, they are cell permanent, and they integrate stably into the target cell's genome, providing a faithful lineage label. The drawback is that there is a typical delay of 18-24 hours between infection and expression.

Neural Crest Explant Cultures

To enable us to study neural crest cell migration in the simplest possible context, we cultured isolated neural tubes *in vitro*. Neural tube explants can be maintained in culture for days, and each neural tube can produce hundreds of neural crest cells. Trunk neural crest explants were performed in general accordance with standard methods [43], with several variations. When I first joined the lab it was common to allow neural tubes to adhere to the substrate in a minimal volume of media for 45 minutes prior to adding the full amount of media to the culture dish. This protocol gave unpredictable results and I tested simply adding the neural tubes to the bottom of a dish full of media and found that it worked well with all substrates.

Additionally, when I joined the lab the standard neural crest culture medium was Dulbecco's Modified Eagle's Medium (DMEM) with 10% chick embryo extract, 15% horse serum, 1% penicillin/streptomycin, 1% non-essential amino acids, and 1% L-glutamine. This is a very rich medium containing an unknown number of stimulatory proteins. After consulting with Martin Garcia-Castro, I tested a serum-free media and a chemically defined media and had good results with

both. The serum free media produced equally robust cultures as the serum containing media. The chemically defined media was only suitable for short term culture. Full details of the media formulations, suppliers, and a detailed protocol for neural tube explant cultures are presented in Appendix 2.

One final improvement on the neural tube explant protocol was that I noticed that cultures changed dramatically after 24 hours if the neural tube was allowed to remain with the neural crest cells. The cells grew into a dense monolayer and did not interact much with substrate patterns. When the neural tube was removed at 6 hours after explanting the neural crest cells maintained a disperse arrangement, and removal after 15.5 hours produced an intermediate arrangement. For details see Figure 2-7. Recombinant ephrin-B1 for migration experiments was initially acquired through a generous gift from Regeneron Corporation to Rusty Lansford. Subsequent stocks were commercially acquired from R&D Systems (473-EB-200). In both cases ephrin-B1 was fused to the FC domain.

Traditional Adsorption Based Stripe Assays

Patterns of proteins were prepared on plastic and glass substrates via non-specific adsorption of protein through flow channels in silicone molds (acquired from Juergen Jung, MPI f. Entwicklungsbiologie). These were done in accordance with published protocols. Appendix 2 presents a detailed protocol for this method.

As an alternative I tried generating patterns of proteins by adsorbing proteins to vacuum deposited chlorosilane monolayers on glass, after consultations with Chris Chen and Sri Rhagavan of Johns Hopkins University. The protocol I used is in Appendix 2 and representative good and bad patterns are presented in Figure 2-15. Eventually, I concluded that it was not possible to push the analysis of neural crest response to ephrin-B signaling further with adsorbed stripe patterns and focused exclusively on photolithographically produced patterned substrates.

A New Method to Produce Patterned Substrates

We wanted to design an experimentally convenient, cost effective, additive patterning technique capable of patterning proteins on glass surfaces with 2-10 micron resolution. It was also critical that the final product be compatible with culturing primary neural crest cells. We believe our current assay system satisfies all of these criteria.

A schematic overview of our approach is presented in Figure 2. We begin with glass coverslips, acid wash them, then coat them in a self assembled layer of aminopropyltriethoxy-silane (APTES). Self assembled layers of this type have several advantages. First, the reagents are cheap and the layers are experimentally easy to prepare. Second, their lateral organization is largely independent of the terminal group (in this case a primary amine), so that we can subsequently derivatize the surface with crosslinkers and proteins without unduly

disrupting the structure of the silane layer [44]. We designed the system to covalently link the proteins to the surface, as previous studies had demonstrated that antibody activity on a surface was preserved for longer if the antibody was covalently immobilized, rather than adsorbed [45]. For these studies, we have used a commercially available photoactivatible cross-linker, 4-benzoylbenzoic acid succinimidyl ester (Molecular Probes B-1577).

At the time we began these studies, there was intense interest binding proteins to surfaces to generate biosensors of various kinds. Many of these approaches relied on photopatterning, as conventional microchip patterning technology is already based on photolithography (reviewed in [46]). Several papers were of particular use as we developed our own protocols [47-49].

Two different protocols that we developed for generating photolithographic patterns of proteins on glass are presented in Appendix 2. The main protocol was optimized to make use of only ethanol and dimethylsulfoxide as organic solvents. This optimization proved critical for maintaining viable primary cultures on the coverslips. An older protocol is also presented in Appendix 2 for comparison.

Many of the published methods of generating patterned protein surfaces used a destructive patterning technique (i.e., hard X-ray irradiation) to render some portion of the surface incompatible with protein binding. We were concerned that

patterns of this type would also make those regions less compatible with cellular migration, thereby biasing our assay. For this reason, we make uniform layers of a photoactivatible molecule, then use light to add our test protein in a pattern, and a migration permissive molecule (i.e., fibronectin) uniformly on the surface. Our method yields patterned substrates which structurally differ only in the amount and type of protein immobilized, the surface structure of the layer does not change.

Selection of Photoactivatible Group

We chose to work with a benzophenone based cross-linker, because benzophenone functional groups can be repeatedly excited at their excitation maximum. Many of the other commonly available photoreactive groups will bind to a solvent molecule if no protein is around. Under those circumstances all work would be done under a red safe light [50]. The bifunctional crosslinker reacts chemically with the primary amine of the APTES layer in neat DMSO, forming a uniform layer of photoreactive molecules, as assayed by the distribution of bound fluorescent molecules. The photoreactive benzophenone functionality of the crosslinker was chosen chiefly because it has an activation peak at about 350 nm, which should not damage proteins [50, 51]. This particular cross-linker was well suited to our current needs.

Photolithography

The photolithography is carried out in Michael Roukes' physics lab on a standard mask aligner. The mask aligner provides us with a convenient way of positioning our sample coverslip in close proximity to the lithographic mask. The derivatized coverslip is coated in a small volume (30-100 microliters over ~5 square centimeters) of concentrated protein solution (generally ~1 mg/mL) and positioned using the mask aligner's stage. The stage has micrometer controls that allow translation in all three dimensions, as well as rotation in the plane, to allow the coverslip to be brought into close proximity to the patterned mask.

Once the coverslip is positioned, the sample is exposed to fluorescent light from a highly uniform mercury arc lamp (<10% intensity variation over the width of the 3 inch sample stage). We have found empirically that exposures at a luminescence of 10 mW/cm^2, for between 2 and 10 minutes give steadily increasing concentrations of bound protein, as assayed by the fluorescence of immobilized fluorescein tagged proteins. After exposure, the coverslips are rinsed in phosphate buffered saline (PBS) several times and are then ready for use. To get patterns of multiple proteins, you can use several exposures, though in practice we never achieved more than two.

A major technical challenge for getting the patterned substrates to work as a migration assay is how to provide a uniformly permissive surface, with no differences in levels of adhesiveness. Neural crest cells require extracellular

matrix proteins to migrate and we used fibronectin to support migration. Initially we added fibronectin to the photolithography solution and attached it to the surface at the same time as the ephrin, then followed up with solution adsorption of fibronectin everywhere. We became concerned that this could be convoluting an adhesive difference in with the ephrin difference though, so in most of our experiments ephrin was immobilized with a fluorescent bovine serum albumin (to visualize the pattern), then the whole coverslip was soaked in 10 ug/mL human fibronectin (BD Labware).

Results

Improved Vital Labels

We developed labeling and imaging protocols to specifically label the nucleus, mitochondria, actin cytoskeleton, and plasma membrane of migrating primary neural crest cells. Figure 2-6 contains representative images of the four best GFP fusion proteins we test. These GFP fusions fall into two of major classes based on their role in our experiments: cellular markers and cytoskeletal labels.

The nuclear, mitochondrial, and plasma membrane fusions are excellent markers for tracking the positions of migrating cells. The nuclear localized GFP is a fusion of histone 2B with EGFP (H2B-EGFP) and provides a very bright concentrated signal that was extremely useful for following the trajectories of many cells which are closely spaced. It serves as a direct substitute in our

experiments for more traditional dyes such as DiI or rhodamine dextran, since H2B-EGFP is brighter, bleaches less quickly, doesn't dilute with cell divisions, and provides a more easily tracked geometry. The plasma membrane fusion is a short membrane localization sequence (~30 amino acids) from the GAP-43 protein fused to EGFP. It is an excellent marker for membrane movements, filopodia, and membrane ruffles in relatively disperse cell populations, such as neural crest cells migrating on coverslips at low density. The mitochondrial label is a fusion of a mitochondrial targeting sequence with EYFP. It is a very interesting marker for double labeling experiments as its distinct localization allows its presence to be verified, even when coexpressed with other EYFP fusion proteins. Coincidentally, test movies of neural crest cells labeled with mito-EYFP led directly to the collaboration described in Appendix 1.

Three other GFP fusions allowed us to image the cytoskeleton in living neural crest cells. We tested fusions of EGFP, EYFP, and ECFP to human beta-actin, human alpha-tubulin, and tau (a microtubule binding protein). We have infected neural crest cells with retroviruses containing each of these three proteins. Morphologically the neural crest cells appear to be normal. Of the three, the actin GFP proved most useful as it gave us the most specific cytoskeletal staining with the least cytoplasmic background.

Photolithography of Biological Macromolecules

Our photolithographic method of producing patterned substrates reliably produced patterned substrates. Improvements over the old style "stripe assay" include improved optical clarity, covalent protein tethering, and much greater uniformity and fidelity in our patterns. Since the pattern was imposed by light, rather than fluid flow, we were able to design the pattern to match the experiment, rather than the reverse. Sample patterns, visualized by immobilizing fluorescently tagged proteins, are presented below to give an idea of the current resolution and uniformity of our system (Figure 2-10B). We have immobilized streptavidin, bovine serum albumin, various antibodies, ephrin-B1, and fibronectin. For contrast, we also show a representative image of fluorescently tagged protein prepared using the standard adsorption approach (Figure 2-10A).

Furthermore, we have tested these substrates for toxicity and all current data shows that they are highly supportive of neural crest cell outgrowth, migration, proliferation, and differentiation. Patterned substrates were not initially compatible with primary neural crest cell cultures and Appendix 2 presents a solvent optimized protocol (A2-2) and an earlier protocol (A2-4) that gave good patterns but left some type of residue that was toxic to neural crest cells. Cultures explanted on substrates prepared with protocol A2-2 were indistinguishable in health and morphology from cultures prepared on plastic. Thus, we believe that we have generated a suitable substrate for testing the effects of candidate guidance cues on neural crest cell migration.

Traditional "Stripe Assays"

To provide a baseline for comparison with previous work, I repeated the stripe assays with ephrin-B1 stripes on a background of fibronectin according to published protocols [2]. My findings generally confirmed the results of that paper, in that cells seemed to generally avoid the ephrin-B1 areas, but the response was somewhat variable. The full range of responses are presented in Figure 2-11. A close examination of one of those time-lapse movies (Figure 2-12) reveals that though several of the neural crest cells appear confined by the adsorbed stripes of ephrin-B1 (notably the cell indicated with the small white arrow), other cells (large white arrow), do not respect the stripe boundaries and migrate over them.

One confounding variable that was addressed was that cultures became less reactive to the substrates over time, possibly due to cell differentiation within the cultures, and so I focused my imaging efforts on the first 12-24 hours after explanting, while the cells were first encountering the patterns. This precluded labeling the neural crest cells with viruses, unless the virus was injected into very early embryos first, and so I began imaging with differential interference contrast microscopy.

Photolithographic Stripe Assays

We used our new photolithographed substrates to evaluate the effects of ephrin-B1 on neural crest migration. Figure 2-13 presents representative still images from time-lapse movies of neural crest cultures on substrates where ephrin-B1 was laid down in stripes against a uniform background of fibronectin. For clarity of presentation, the bright field image was overlaid with traces of where the stripes were. In each case presented here there were fewer cells in the ephrin-B1 regions, but this was not universally true in all dishes or all experiments.

Our observations agreed generally with results obtained from the previous patterning method [2]; neural crest cells could migrate onto regions containing ephrin-B1, but they would subsequently undergo an ephrin mediated collapse, pull off the ephrin-B1 region and undergo extensive membrane ruffling. The montage in Figure 2-14 captures a retraction event: we can see that the neural crest cell has migrated into an ephrin-B1 domain, and that it actively explores its environment with multiple lamellapodia. We can also see that the cell retracts its entire cell body onto a permissive region and blebs for several minutes.

In the montage series on glass, we can see clearly that the retraction is not a single event, but rather three sequential retractions. It is very interesting to note that in the final frame, even though the neural crest cell is nearly completely collapsed, the cell maintains very fine connections to the ephrin-B1 containing region it just left, indicating that the cell collapses its lamellapodia, but leaves

retraction fibers. The fact that the crest cell maintains connections to the ephrin-B1 surface, even during the collapse, strongly implies that the ephrin-B1 region is adequate for neural crest adhesion, and that the collapse is due to a signaling event, not a lack of mechanical traction and is consistent with growth cone behavior in response to other guidance cues [52]. Another interesting detail that emerges from the new series is that the lamellapodia do not simply pull back: the uppermost lamillapod clearly sends a "pulse" of membrane up towards its distal end. Only after this pulse does the lamellapod collapse.

Though this frame by frame analysis is compelling, it would not be accurate to characterize it as typical. It was typical of one category of cellular response to ephrin-B1 patterns, but other categories existed. Some cells seemed more mildly repulsed by ephrin-B1 regions, many more seemed to ignore them entirely, and in a rare experiment or two neural crest cells accumulated preferentially on regions that should have contained more ephrin-B1. We successfully achieved greater experimental control over the patterning, culture, and imaging methods, but this increased experimental control did not effectively reduce the variability in the observed cellular response.

Discussion

Previously, repulsive cues for neural crest cell migration were defined by the relative abundance of cells on patterned substrates [1, 2]. We designed an improved migration assay to standardize the experimental conditions in the expectation that this improved experimental control would result in more

consistent cellular responses. We then planned to use this consistent cellular response (whatever it turned out to be), as the normal cell behavior and attempt to work out the subcellular processes required to generate this behavior. The key requirement of our assay was cellular predictability; the cell's response to our imposed migration choice needed to be reasonably consistent from cell to cell and day to day.

I was very consciously modeling my efforts on the growth cone turning assay, in which small amounts of soluble molecules were introduced into a culture dish near a pathfinding growth cone. Certain molecules (e.g., netrin) cause growth cones to reliably turn towards or away from the stimulus. By interfering with cellular signaling pathways and then observing the resulting effect on the expected turning response, great progress has recently been made in determining downstream molecular players in these signal transduction cascades [53-57].

In our case there was a long list of desired improvements to the assay: optically better culture chambers, improved specific contrast, cell culture in serum free media, improved patterning methods, cell culture compatibility with the improved substrates, and cellular interaction with the imposed patterns. All of these individual features were achieved and several were dramatic successes. What I failed to sufficiently appreciate early in graduate school was that all of these were contingent successes, contingent on the nature of the final cellular response to

these patterns. If the cells reacted consistently to the patterns, then we could do, as planned, signal transduction experiments and work out the cellular requirements for ephrin-B1 signaling. Unfortunately improved experimental control did not bring appreciably improved cellular predictability. We could only conclude, as was already known, that neural crest cells appear repulsed by ephrin-B1.

When we began these experiments, ephrin-B ligands were known to be a repulsive guidance molecule for neural crest cells *in vitro*, but there was significant variability in the response of individual cells to patterns of ephrin-B. By improving the technical implementation of the assay we sought to test whether we were observing a constant response to a variable signal (e.g., variations in the substrate pattern) or a variable response to a constant signal. Since we made the cell culture and the patterning significantly more consistent and observed no reduction in the variability we concluded that the variation was inherent in the neural crest cells themselves.

Connection to Chapter 3

One interpretation that we did take away from these experiments was that the stripe assay was intrinsically unsuited to determining the timing and events of the early cell behavioral response to ephrin-B1 signaling in neural crest cells, as it was difficult to reliably image a cell's first contact with the ephrin-B1 substrate. The one aspect of the stripe assay that I became dissatisfied with was that each

cell experienced the pattern differently. Some migrated out onto the stripe pattern directly and others likely never saw it. The control over the time course of the assay was left up to the cell and to chance. I wanted a greater ability to control the presentation of the ligand exposure directly. To address this lingering variability, and create a greater uniformity of cellular experience within the assay, I designed another migration assay, described in Chapter 3, to specifically address test the timing and typical response of migrating primary neural crest cells to focal ephrin-B stimulus.

1. Wang HU, Anderson DJ: **Eph family transmembrane ligands can mediate repulsive guidance of trunk neural crest migration and motor axon outgrowth**. *Neuron* 1997, **18**:383-396.
2. Krull CE, Lansford R, Gale NW, Collazo A, Marcelle C, Yancopoulos GD, Fraser SE, Bronner-Fraser M: **Interactions of Eph-related receptors and ligands confer rostrocaudal pattern to trunk neural crest migration**. *Curr Biol* 1997, **7**:571-580.
3. Baker CV, Bronner-Fraser M: **The origins of the neural crest. Part I: embryonic induction**. *Mech Dev* 1997, **69**:3-11.
4. Bronner-Fraser M: **Origins and developmental potential of the neural crest**. *Exp Cell Res* 1995, **218**:405-417.
5. Anderson DJ: **Genes, lineages and the neural crest: a speculative review**. *Philos Trans R Soc Lond B Biol Sci* 2000, **355**:953-964.
6. Hall B: *The Neural Crest in Development and Evolution*, 1st edn. New York: Springer; 1999.
7. Le Douarin N, Kalcheim C: *The Neural Crest*, 2nd edn. Cambridge: Cambridge University Press; 1999.
8. Bronner-Fraser M, Fraser S: **Developmental potential of avian trunk neural crest cells in situ**. *Neuron* 1989, **3**:755-766.
9. Fraser SE, Bronner-Fraser M: **Migrating neural crest cells in the trunk of the avian embryo are multipotent**. *Development* 1991, **112**:913-920.
10. Bronner-Fraser M, Stern C: **Effects of mesodermal tissues on avian neural crest cell migration**. *Dev Biol* 1991, **143**:213-217.
11. Perris R: **The extracellular matrix in neural crest-cell migration**. *Trends Neurosci* 1997, **20**:23-31.
12. Henderson DJ, Copp AJ: **Role of the extracellular matrix in neural crest cell migration**. *J Anat* 1997, **191 (Pt 4)**:507-515.
13. Landolt RM, Vaughan L, Winterhalter KH, Zimmermann DR: **Versican is selectively expressed in embryonic tissues that act as barriers to neural crest cell migration and axon outgrowth**. *Development* 1995, **121**:2303-2312.
14. Nakagawa S, Takeichi M: **Neural crest emigration from the neural tube depends on regulated cadherin expression**. *Development* 1998, **125**:2963-2971.
15. Liu JP, Jessell TM: **A role for rhoB in the delamination of neural crest cells from the dorsal neural tube**. *Development* 1998, **125**:5055-5067.
16. Debby-Brafman A, Burstyn-Cohen T, Klar A, Kalcheim C: **F-Spondin, expressed in somite regions avoided by neural crest cells, mediates inhibition of distinct somite domains to neural crest migration**. *Neuron* 1999, **22**:475-488.
17. Eickholt BJ, Mackenzie SL, Graham A, Walsh FS, Doherty P: **Evidence for collapsin-1 functioning in the control of neural crest migration in both trunk and hindbrain regions**. *Development* 1999, **126**:2181-2189.

18. Cai DH, Brauer PR: **Synthetic matrix metalloproteinase inhibitor decreases early cardiac neural crest migration in chicken embryos**. *Dev Dyn* 2002, **224**:441-449.

19. Krull CE, Collazo A, Fraser SE, Bronner-Fraser M: **Segmental migration of trunk neural crest: time-lapse analysis reveals a role for PNA-binding molecules**. *Development* 1995, **121**:3733-3743.

20. Drescher U, Bonhoeffer F, Muller BK: **The Eph family in retinal axon guidance**. *Curr Opin Neurobiol* 1997, **7**:75-80.

21. Mellitzer G, Xu Q, Wilkinson DG: **Control of cell behaviour by signalling through Eph receptors and ephrins**. *Curr Opin Neurobiol* 2000, **10**:400-408.

22. Orioli D, Klein R: **The Eph receptor family: axonal guidance by contact repulsion**. *Trends Genet* 1997, **13**:354-359.

23. Xu Q, Mellitzer G, Wilkinson DG: **Roles of Eph receptors and ephrins in segmental patterning**. *Philos Trans R Soc Lond B Biol Sci* 2000, **355**:993-1002.

24. Drescher U, Kremoser C, Handwerker C, Loschinger J, Noda M, Bonhoeffer F: **In vitro guidance of retinal ganglion cell axons by RAGS, a 25 kDa tectal protein related to ligands for Eph receptor tyrosine kinases**. *Cell* 1995, **82**:359-370.

25. Walter J, Kern-Veits B, Huf J, Stolze B, Bonhoeffer F: **Recognition of position-specific properties of tectal cell membranes by retinal axons in vitro**. *Development* 1987, **101**:685-696.

26. Santiago A, Erickson CA: **Ephrin-B ligands play a dual role in the control of neural crest cell migration**. *Development* 2002, **129**:3621-3632.

27. Smith A, Robinson V, Patel K, Wilkinson DG: **The EphA4 and EphB1 receptor tyrosine kinases and ephrin-B2 ligand regulate targeted migration of branchial neural crest cells**. *Curr Biol* 1997, **7**:561-570.

28. Helbling PM, Tran CT, Brandli AW: **Requirement for EphA receptor signaling in the segregation of Xenopus third and fourth arch neural crest cells**. *Mech Dev* 1998, **78**:63-79.

29. Wang HU, Chen ZF, Anderson DJ: **Molecular distinction and angiogenic interaction between embryonic arteries and veins revealed by ephrin-B2 and its receptor Eph-B4**. *Cell* 1998, **93**:741-753.

30. Adams RH, Wilkinson GA, Weiss C, Diella F, Gale NW, Deutsch U, Risau W, Klein R: **Roles of ephrinB ligands and EphB receptors in cardiovascular development: demarcation of arterial/venous domains, vascular morphogenesis, and sprouting angiogenesis**. *Genes Dev* 1999, **13**:295-306.

31. Gerety SS, Anderson DJ: **Cardiovascular ephrinB2 function is essential for embryonic angiogenesis**. *Development* 2002, **129**:1397-1410.

32. Gerety SS, Wang HU, Chen ZF, Anderson DJ: **Symmetrical mutant phenotypes of the receptor EphB4 and its specific transmembrane**

ligand ephrin-B2 in cardiovascular development. *Mol Cell* 1999, **4**:403-414.

33. Huynh-Do U, Vindis C, Liu H, Cerretti DP, McGrew JT, Enriquez M, Chen J, Daniel TO: **Ephrin-B1 transduces signals to activate integrin-mediated migration, attachment and angiogenesis**. *J Cell Sci* 2002, **115**:3073-3081.

34. Holmberg J, Clarke DL, Frisen J: **Regulation of repulsion versus adhesion by different splice forms of an Eph receptor**. *Nature* 2000, **408**:203-206.

35. Adams RH, Diella F, Hennig S, Helmbacher F, Deutsch U, Klein R: **The cytoplasmic domain of the ligand ephrinB2 is required for vascular morphogenesis but not cranial neural crest migration**. *Cell* 2001, **104**:57-69.

36. Cowan CA, Henkemeyer M: **The SH2/SH3 adaptor Grb4 transduces B-ephrin reverse signals**. *Nature* 2001, **413**:174-179.

37. Wahl S, Barth H, Ciossek T, Aktories K, Mueller BK: **Ephrin-A5 induces collapse of growth cones by activating Rho and Rho kinase**. *J Cell Biol* 2000, **149**:263-270.

38. Brunette DM: **Effects of Surface Topography of Implant Materials on Cell Behavior in vitro and in vivo**. In: *Nanofabrication and Biosystems* Edited by Hoch HC, Jelinski LW, Craighead HG. pp. 423. Cambridge: Cambridge University Press; 1996: 423.

39. Clark P: **Cell and Neuron Growth Cone Behavior on Micropatterned Surfaces**. In: *Nanofabrication and Biosystems* Edited by Hoch HC, Jelinski LW, Craighead HG. pp. 423. Cambridge: Cambridge University Press; 1996: 423.

40. Hornberger MR, Dutting D, Ciossek T, Yamada T, Handwerker C, Lang S, Weth F, Huf J, Wessel R, Logan C, Tanaka H, Drescher U: **Modulation of EphA receptor function by coexpressed ephrinA ligands on retinal ganglion cell axons**. *Neuron* 1999, **22**:731-742.

41. Okada A, Lansford R, Weimann JM, Fraser SE, McConnell SK: **Imaging cells in the developing nervous system with retrovirus expressing modified green fluorescent protein**. *Exp Neurol* 1999, **156**:394-406.

42. Zavada J: **The Psuedotypic Paradox**. *J Gen Virol* 1982, **63**:15-24.

43. Bronner-Fraser M: **Manipulations of Neural Crest Cells or Their Migratory Pathways**. In: *Methods in Avian Embryology* Edited by Bronner-Fraser M, vol. 51. pp. 61-79. New York: Academic Press; 1996: 61-79.

44. Arkles B: **Silane Coupling Agent Chemistry**. In: *Silicon Compounds: Register and Review* Edited by Technologies UC, 5th ed. pp. 301. Bristol: United Chemical Technologies; 1996: 301.

45. OrtegaVinuesa JL, BastosGonzalez D, HidalgoAlvarez R: **Effect of storage time on the immunoreactivity of IgG physically adsorbed or chemically bound to latex beads**. *Journal of Colloid and Interface Science* 1996, **184**:331-334.

46. Sigrist H, Collioud A, Clemence JF, Gao H, Luginbuhl R, Sanger M, Sundarababu G: **Surface Immobilization of Biomolecules by Light**. *Optical Engineering* 1995, **34**:2339-2348.
47. Sigrist H, Gao H, Wegmuller B: **Light-Dependent, Covalent Immobilization of Biomolecules on Inert Surfaces**. *Bio-Technology* 1992, **10**:1026-1028.
48. Sanger M, Sigrist H: **Light-dependent immobilization of biomolecules on material and lipid bilayer membrane surfaces**. *Sensors and Actuators a-Physical* 1995, **51**:83-88.
49. Rozsnyai LF, Benson DR, Fodor SPA, Schultz PG: **Photolithographic Immobilization of Biopolymers on Solid Supports**. *Angewandte Chemie-International Edition in English* 1992, **31**:759-761.
50. Dorman G, Prestwich G: **Benzophenone Photophores in Biochemistry**. *Biochemistry* 1994, **33**:5661-5673.
51. Prestwich G, Dorman G, Elliot J, Marecak D, Chaudhary A: **Benzophenone Photoprobes for Phosphoinositides, Peptides, and Drugs**. *Photochemistry and Photobiology* 1997, **65**:222-234.
52. Raper JA, Grunewald EB: **Temporal retinal growth cones collapse on contact with nasal retinal axons**. *Exp Neurol* 1990, **109**:70-74.
53. Timothy M. Gomez ER, Mu-ming Poo, Nicholas C. Spitzer: **Filopodial Calcium Transients Promote Substrate-Dependent Growth Cone Turning**. *Science* 2001, **291**:1983-1987.
54. Hopker VH, Shewan D, Tessier-Lavigne M, Poo M, Holt C: **Growth-cone attraction to netrin-1 is converted to repulsion by laminin-1**. *Nature* 1999, **401**:69-73.
55. Song H, Ming G, He Z, Lehmann M, McKerracher L, Tessier-Lavigne M, Poo M: **Conversion of neuronal growth cone responses from repulsion to attraction by cyclic nucleotides**. *Science* 1998, **281**:1515-1518.
56. Ming GL, Song HJ, Berninger B, Holt CE, Tessier-Lavigne M, Poo MM: **cAMP-dependent growth cone guidance by netrin-1**. *Neuron* 1997, **19**:1225-1235.
57. Ming GL, Wong ST, Henley J, Yuan XB, Song HJ, Spitzer NC, Poo MM: **Adaptation in the chemotactic guidance of nerve growth cones**. *Nature* 2002, **417**:411-418.

Figure 2-1: A schematic view of the conceptual design of the stripe assay. Alternating stripes of a potential guidance molecule (gray) are overlaid on a uniformly permissive background (white). The neural tube (blue) is then explanted onto the surface. If the cells accumulate uniformly the test molecule is classified as permissive. If the accumulate preferentially on the white areas, the test molecule is classified as repulsive.

Figure 2-2: A comparison of the relative brightness of images collected by different objective lenses. All images are collected on a Zeiss Pascal confocal laser scanning microscope, of Bodipy Fl phallacidin stained bovine pulmonary artery endothelial cells (Molecular Probes, FluoCells #1, F-14780). Each pair of images (A-B and C-D) were collected with the same imaging parameters; the only difference between the two images is in the objective lens. It is worth noting that the higher numerical aperture (NA) lens will generate a brighter image both because it delivers light more efficiently and because it collects the light more efficiently.

Figure 2-3: Panel A depicts the portion of the emission spectrum of GFP which is accessible to a typical filter and dichroic combination. As much as half of the emission spectra does not even arrive at the detector, as it is not efficiently transmitted through the intermediate optics. Panel B shows that the redesigned filters that we generated (Chroma Corporation, primary dichroic q497lp and emission filter HQ500lp) transmit a greater fraction of the emission spectra of

GFP, resulting in increased collection efficiency. These savings can be used to generate a higher quality image with the same amount of light, or to generate an equivalent quality image with less intense light or in a shorter period of time. Panel C shows the quality of images of actin-GFP labeled fibroblasts that we were able to generate with a Zeiss NT 488/568 primary dichroic and a LP515 emission filter. Panel D shows the quality of images that we collected, of a different region of the same sample, with the Chroma q497lp primary dichroic and Chroma HQ 500lp emission filter.

Figure 2-4: The effects of incident laser power on image quality are dramatic, and careful management of laser power is critical to successful imaging of fluorescent probes in living samples. Panels A-C represent images collected from the same field of view within a Bodipy-Fl phallacidin sample (Molecular Probes Fluocell #1). As the power is increased, the image gets brighter, when imaging parameters are kept constant. When the imaging parameters are varied, Panels D-F, a similar quality image is generated by each power level. The consequences of using too much laser power are illustrated in Panel G: three separate regions were exposed to differing amounts of light for 2 minutes each. The 5% power region is essentially undetectable, whereas significant photobleaching has occurred in each of the other regions. Panel G was collected at 0.7 x magnification, with respect to Panels A-F, illustrating the damage done to the sample by collecting images A-F.

Figure 2-5: Several different types of imaging chambers were tested for use with primary neural crest cell cultures. Panel A shows porthole chambers of different configurations, as well as wafer handling forceps (Gelman 30033-042). Standard tissue culture chambers were modified by the Chemistry Machine Shop by boring 15-17 mm holes through the bottom surface. The most common chamber used was the Falcon 35 mm tissue culture chamber (35-3001). When it was desirable to have multiple wells, the Nunc Nunclon 4 well chamber (176-740) was used. Coverslips were secured into these chambers with silicon grease. For ease of coverslip loading, a custom chamber (Herb Adams, Caltech Central Plant) was occasionally used, as in Panel B. For routine imaging of strongly adherent cells, i.e., mouse embryo fibroblasts, LAB-TEK 2 well chambers (Nalge Nunc 155380) were used, as in Panel C.

Figure 2-6: A wide range of GFP fusion proteins were tested in primary neural crest cells. The most useful were actin GFP (Panel A), membrane GFP (Panel B), nuclear GFP (Panel C), and mitochondrial EYFP (Panel D). A-C are images of primary neural crest cells. D is an image of a mouse embryo fibroblast.

Figure 2-7: The timing of neural tube removal from neural tube explant cultures was an important factor in determining the final density of the neural crest cell culture. Each of these images is a representative sample from the same batch of neural tube explant cultures, photographed 46 hours after explanting. The neural tube was mechanically removed with forceps at 6 hours (Panel A), 15.5 hours

(Panel B), or 24 hours (Panel C) after explanting. The observed difference in culture density persisted for days after neural tube removal.

Figure 2-8: A schematic view of the chemistry underlying our photolithographic patterning. Coverslips were first cleaned in a strong acid peroxide solution, then coated in a self-assembled monolayer of aminopropyltriethoxsilane, which served to functionalize the glass surface with a layer of primary amines. This silane layer was then further derivatized with a bifunctional crosslinker 4-benzoylbenzoic aicd, succinimidyl ester (Molecular Probes B-1577). The succinimidyl ester binds to the primary amine within the silane layer, producing a surface of benzophenone groups. Upon irradiation with soft ultraviolet light these benzophenone groups are photoactivated and can insert into C-H bonds in any nearby molecules. Thereby patterned exposure to UV light results in patterned immobilization of proteins on the glass coverslip. Full details of the experimental protocols are available in Appendix 2.

Figure 2-9: Schematic view of the coverslip irradiation procedure. The benzophenone functionalized coverslip was loaded onto a patterned chrome on glass photomask, with a small volume of protein solution in between. The whole glass sandwich was then loaded into a mask aligner in the Roukes Lab at Caltech. The photomask allowed UV light through to the sample in a defined pattern and proteins were preferentially immobilized where the light hit, resulting in a positive patterning process.

Figure 2-10: A comparison of protein patterns generated via two different patterning approaches. Panels A and B present views at two different magnifications of patterns of rhodamine labeled bovine serum albumin on plastic, generated via protein adsorption. There are regions within the sample that are well patterned, but the quality is highly variable. Panels C-E present views at three different magnification of three different patterns of the same fluorescent protein generated by photolithography. These examples are typical of coverslips from a successful patterning batch. Details of the experimental protocols used to generate each batch are presented in Appendix 2.

Figure 2-11: Representative frames from time-lapse movies recording neural crest cell behavior on substrates of ephrin-B1 (red stripes) patterned in stripes against a background of fibronectin. In each case nine frames of the resulting time-lapse movie are presented. Some cells in each field of view appear confined between the stripes and most appear to ignore the pattern. In Panel D, several distinct lines of cells accumulate preferentially on the stripe pattern. The variability in the cellular response was attributed to variations in the patterning and to the heterogeneous nature of neural crest cultures.

Figure 2-12: Details of cell behavior in a ephrin-B1 versus fibronectin neural crest choice assay. Figure 2-12 presents an expanded view of the movie from

Figure 2-11 B. Membrane GFP labeled neural crest cells are cultured on a plastic substrate with adsorbed ephrin-B1 (red stripes) versus fibronectin everywhere. One cell (large arrow) migrates freely across the stripes, without seeming restricted. Another cell within the same field of view (small arrow) appears trapped by the ephrin-B1 stripes and is unable to exit its current lane until a thin projection crosses over into the adjacent lane (Frame 500), whereupon it is able to freely migrate over a domain it had previously found repulsive. Such differences in cellular response made interpreting experimental results very difficult.

Figure 2-13: Stripe assays presented neural crest cells with the choice between migrating in regions of photoimmobilized ephrin-B1 versus fibronectin everywhere. Consistently there were fewer cells in regions of ephrin-B1, but only slightly fewer, and the morphology of cells on stripes was often little different than cells in permissive regions.

Figure 2-14: High-resolution description of cell behavior as a neural crest cell encountered a pattern of ephrin-B1 vs. fibronectin. This individual neural crest appears repelled by contact with ephrin-B1, and extends and retracts pseudopodial projections on the ephrin-B1 surface, only to finally collapse and retract off the stripe. This reaction is very similar in extent and timing to that reported in previous studies with adsorbed stripes of ephrin-B1 [1, 2]. It was very difficult to determine what the typical response of a neural crest cell was; this

2-39

reaction was consistently observable, but was not the only observable reaction; many cells seemed different to the imposed photolithographic pattern, particularly if they were in contact with other cells.

Figure 2-16: Vacuum deposition of silane layers onto glass coverslips, followed by adsorption of protein in patterns defined by flow channels, was capable of generating high quality patterns (Panel B). However, variability was still quite high (Panel A). These patterning techniques were adapted from Chris Chen's lab at Johns Hopkins. Details of the experimental technique are given in Appendix 2.
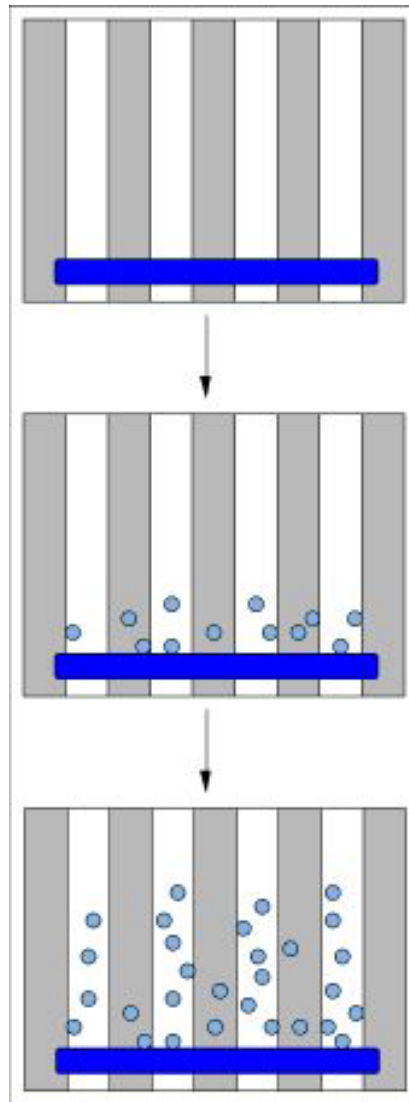
20x Plan Neofluar, 0.5 NA

20x Fluar NA 0.75

A
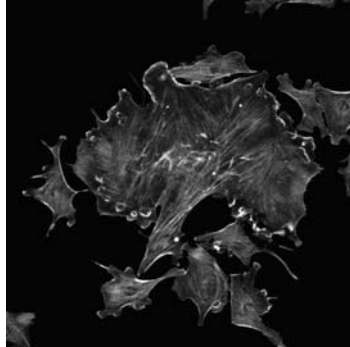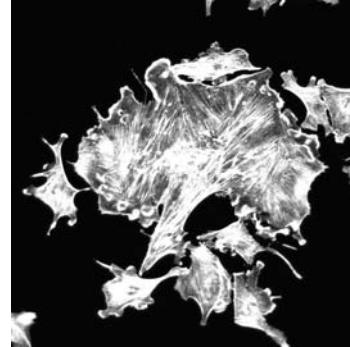
B

40x Plan Neofluar, 0.75 NA
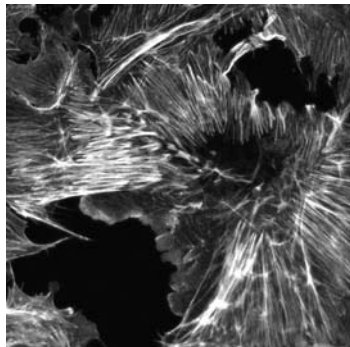
40x C-Apochromat, 1.2 NA

C
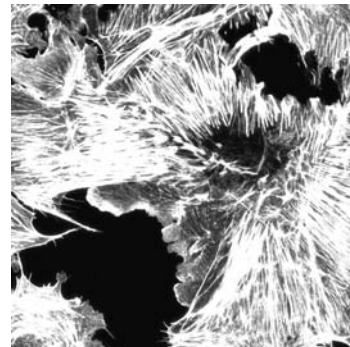
D

Standard Filter Design

Chroma q497lp Dichroic and HQ500lp Filter

% Transmittance

% Transmittance

A

500
515

B

500

Wavelength (nm)

Wavelength (nm)
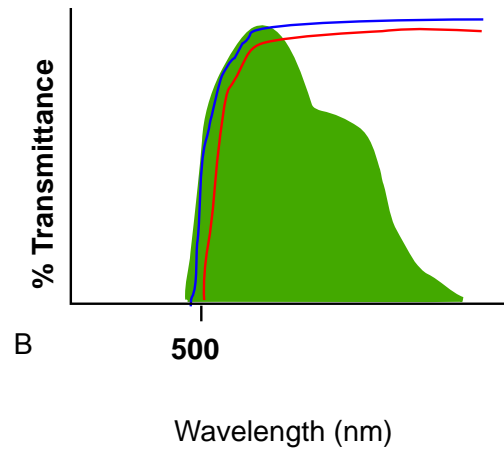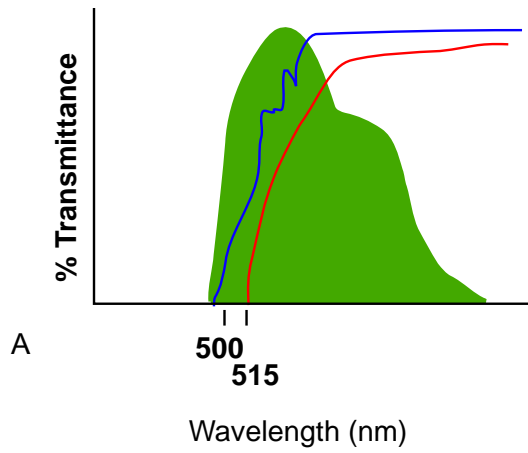
■ = Emission spectrum of GFP

▬ = Transmission spectrum of emission filter

▬ = Transmission spectrum of dichroic mirror

30% Laser Power

10% Laser Power

3% Laser Power

Standard
Filters

C

30% Laser Power

10% Laser Power

3% Laser Power

SEF
Filters

D
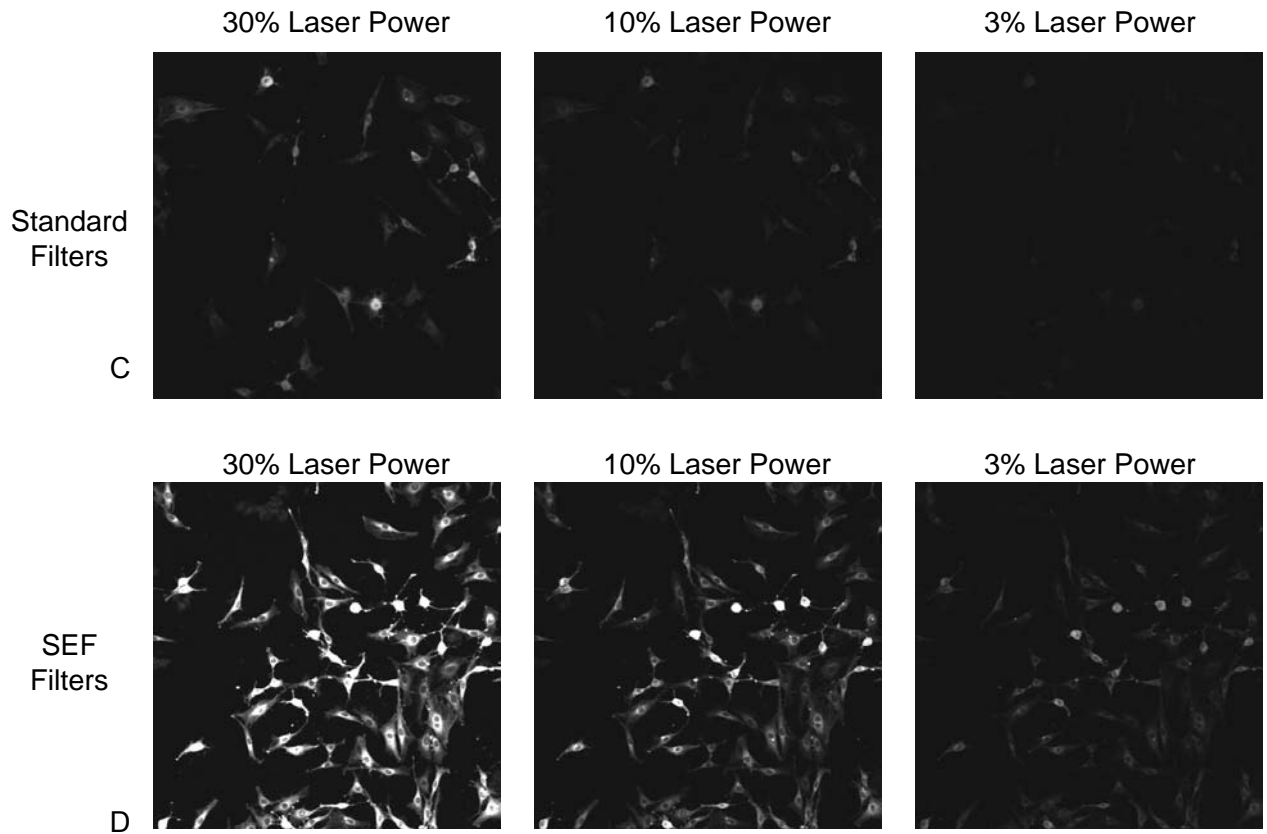
2-43

Effect of Power on Image Quality

5%   15%   45%

Identical Imaging
Parameters

Different Gains
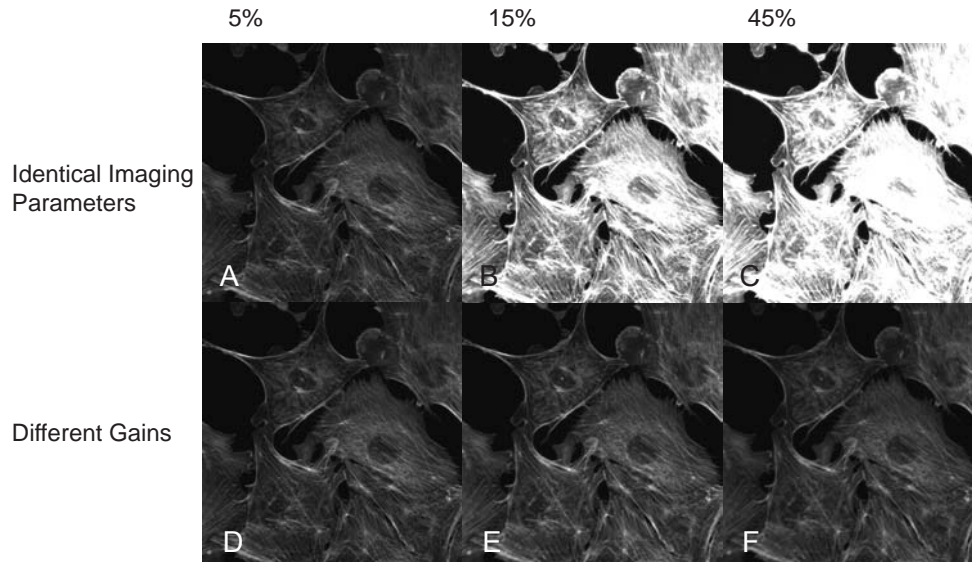
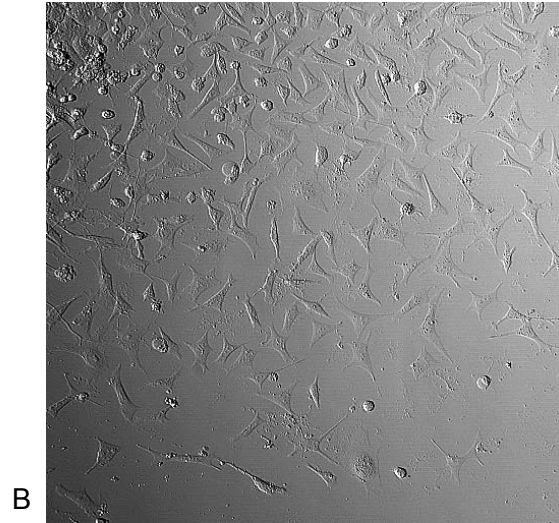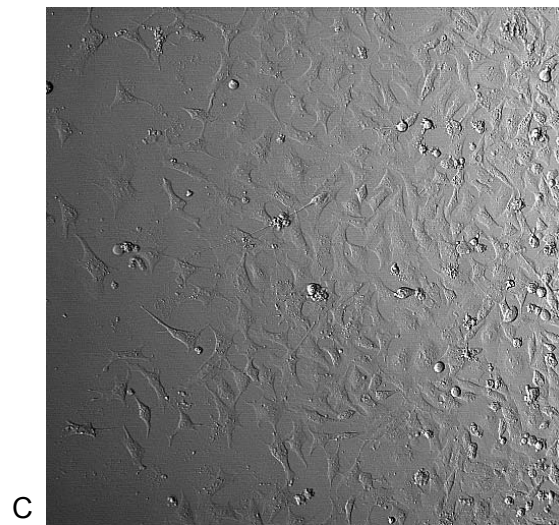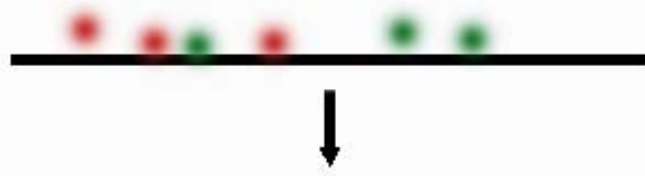Photobleaching After 2 Minutes of Scanning at Different Power Levels

A

B

C

Disperse

A

Intermediate

B

Dense

C
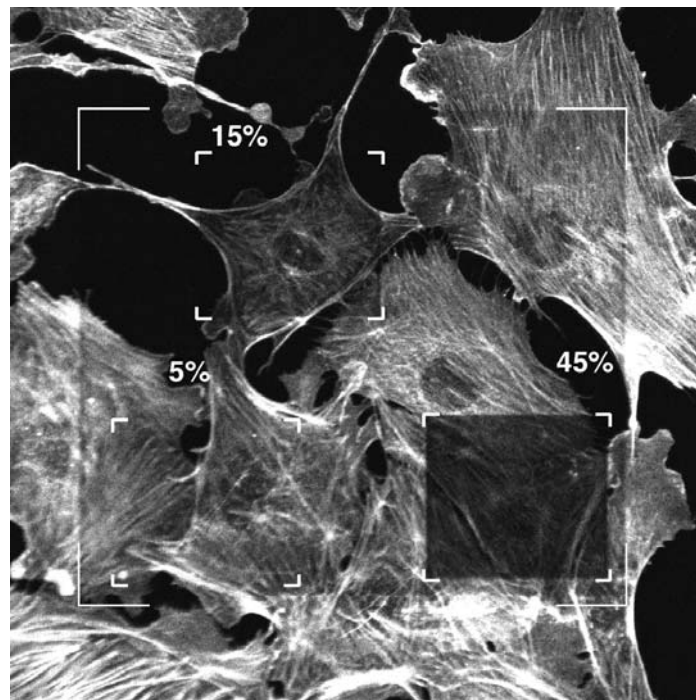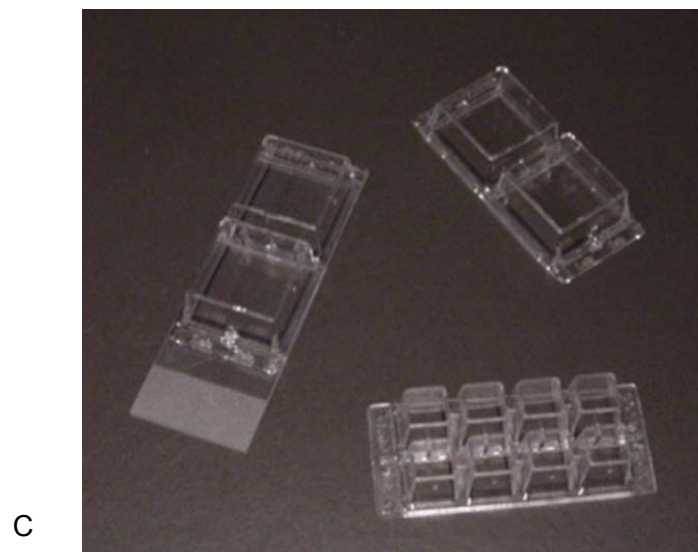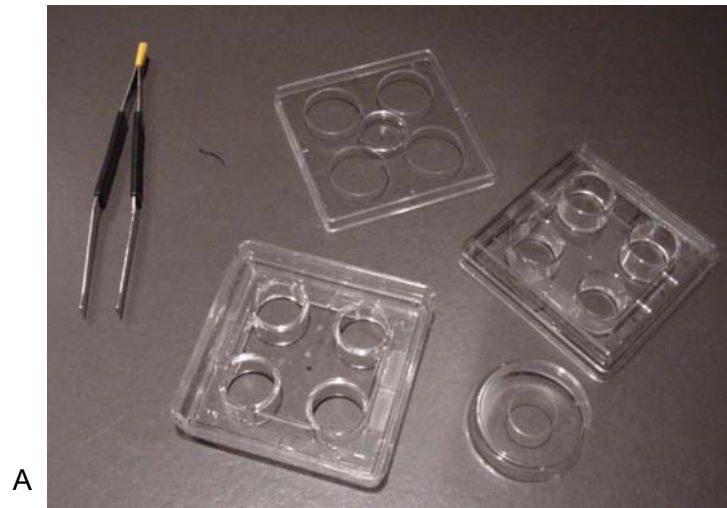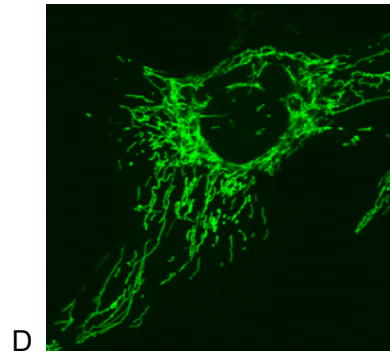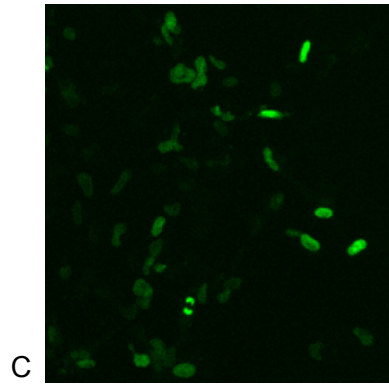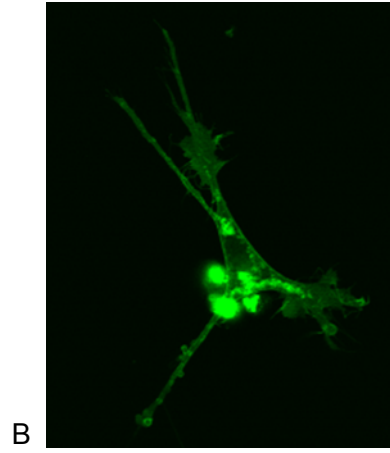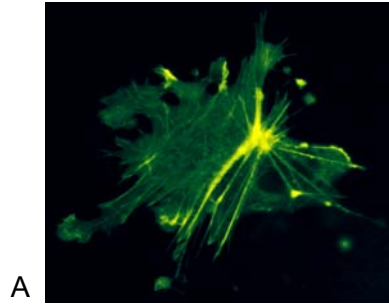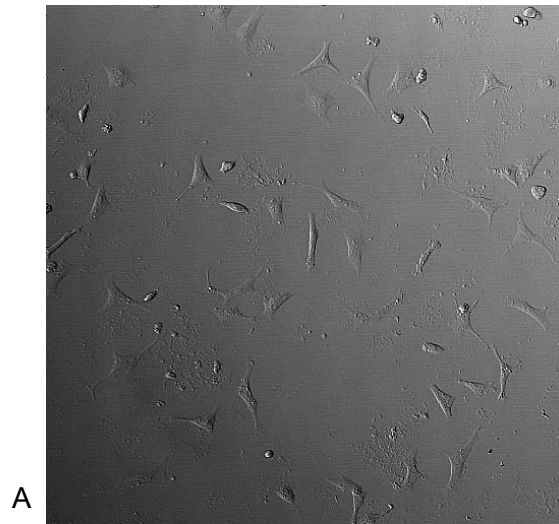
Acid Cleaning

Silanization
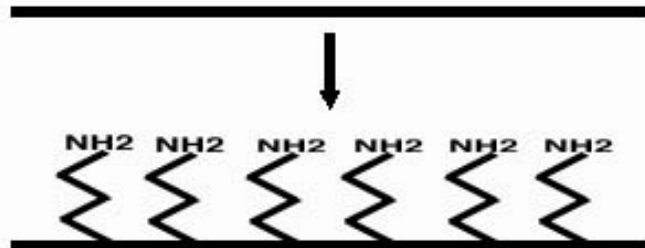
Derivatization
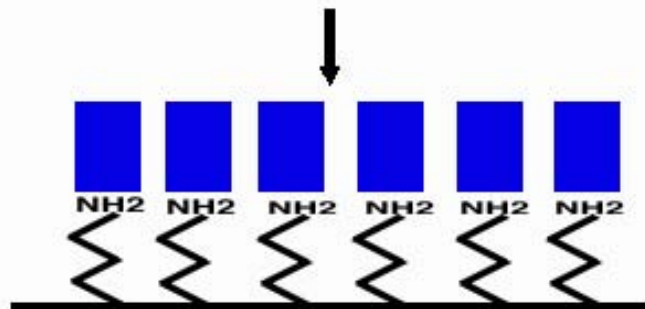
UV Exposure

Patterned Glass Substrate

UV Light

Chrome

Protein Solution

Coverslip

Immobilized Protein
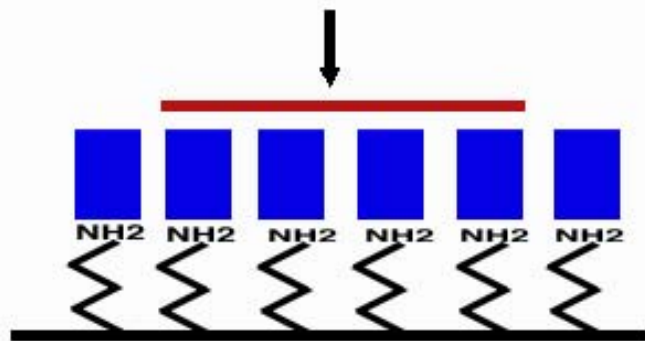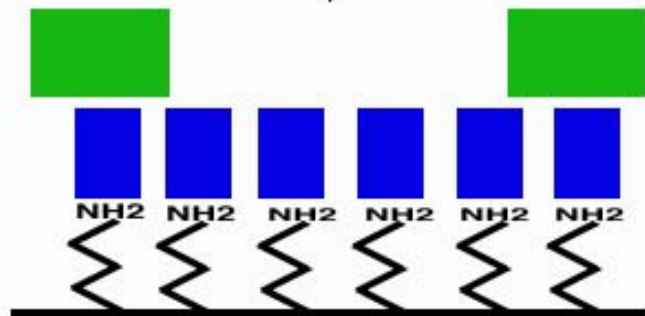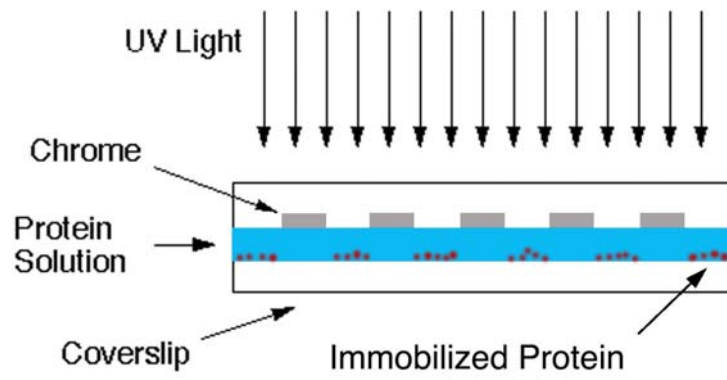
Fluorescent Proteins on Plastic, Generated with Flow Channels

A   250 microns   B   125 microns
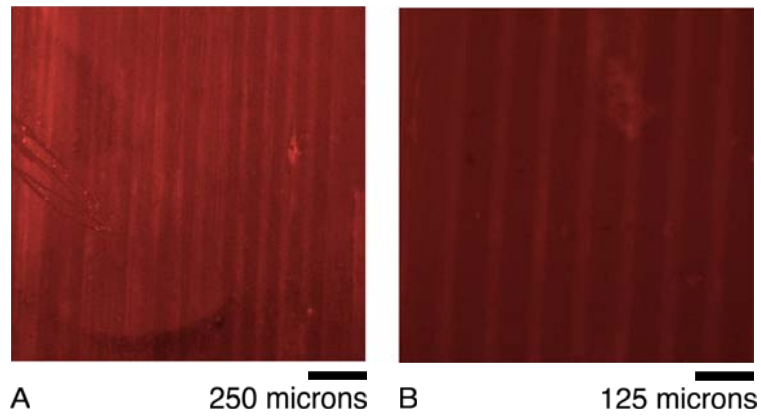
Photolithographed Fluorescent Protein Patterns

C   10x

D   20x

E   40x
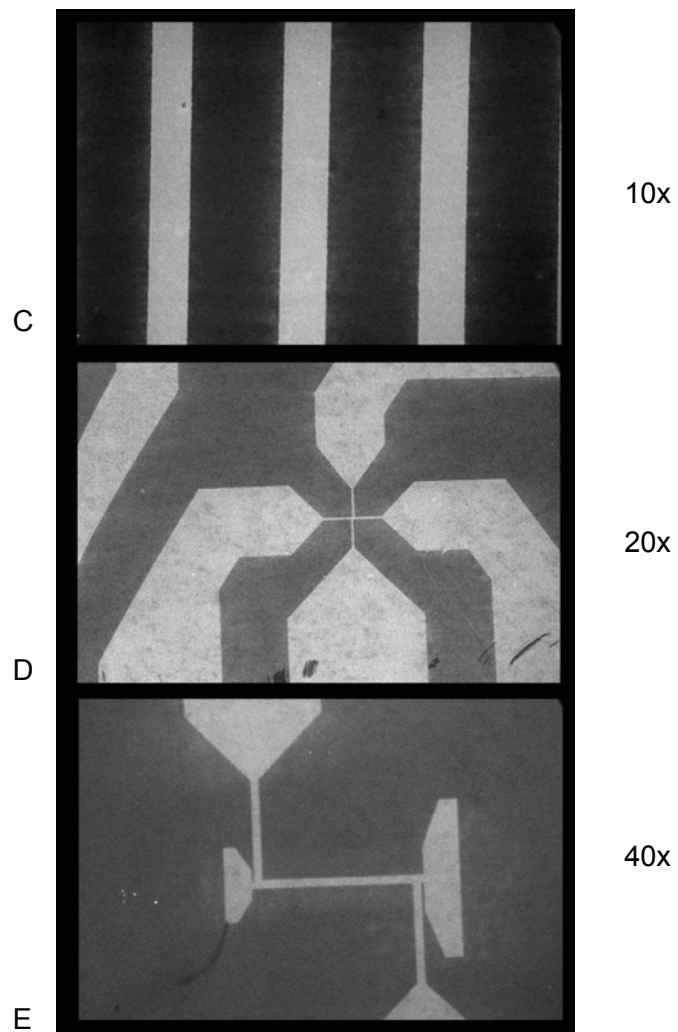
Bonhoeffer style stripe assays: ephrin-B1 vs FN on plastic.

12/12/98-12/14/98
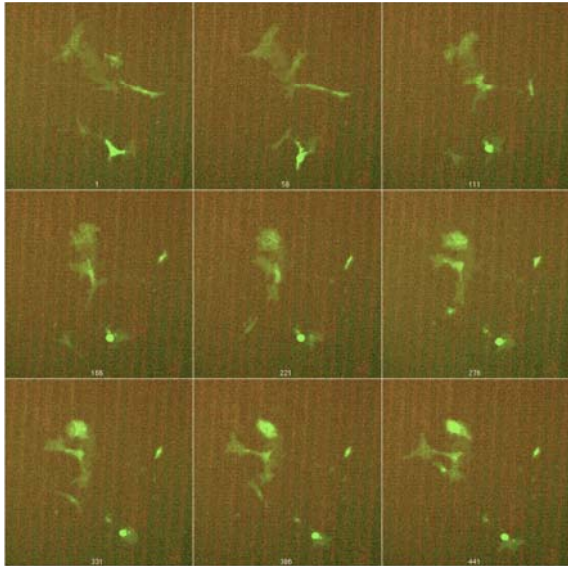
Series 5: 20x, z=1
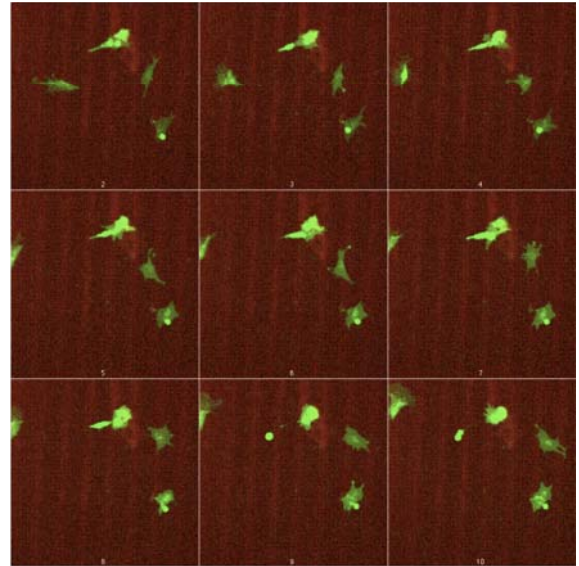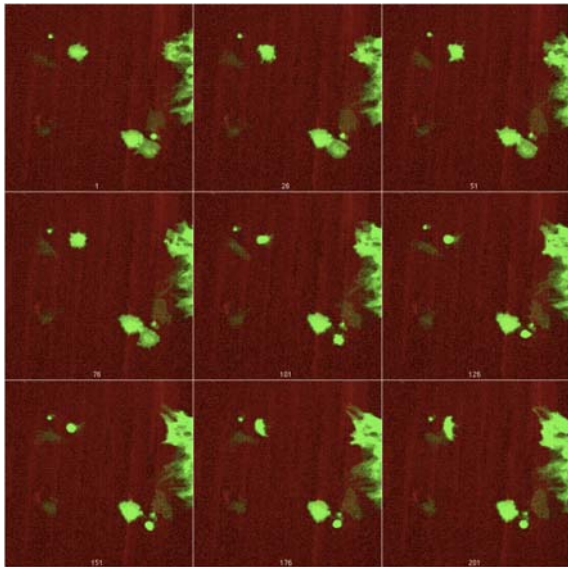
Series 6: 20x, z=1

Series 7: 20x, z=1
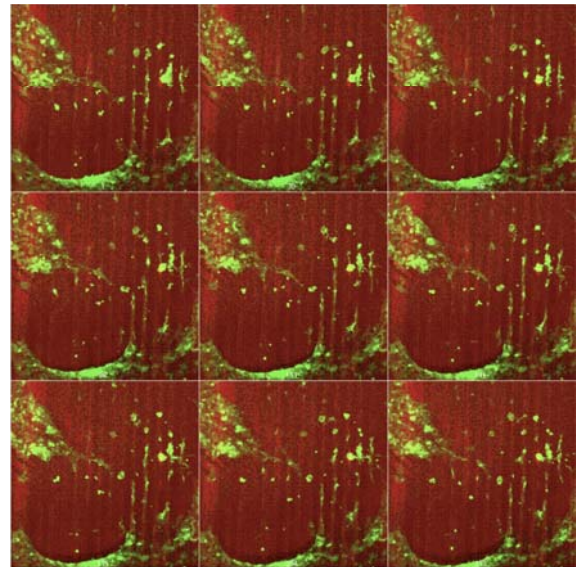
Series 8: 10x, z=1

Membrane GFP Time Lapse of Neural Crest Cells on a Pattern of ephrin-B1 vs. Fibronectin
Series 6, Gap43-GFP, 20x, 900 images, taken every 30s   12/13/98
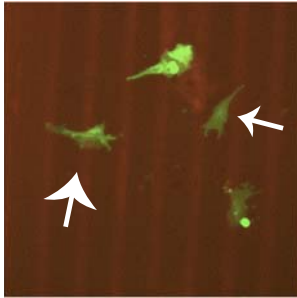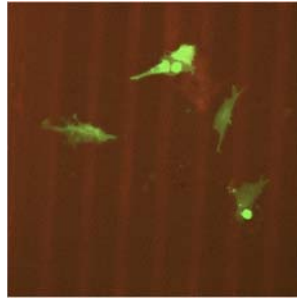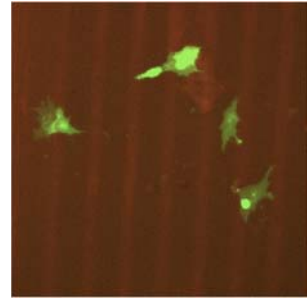
Frame 100   Frame 150   Frame 300
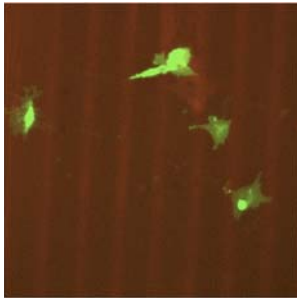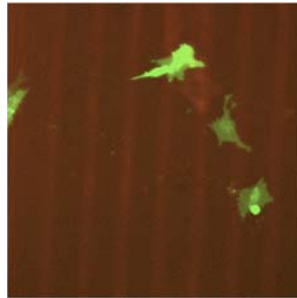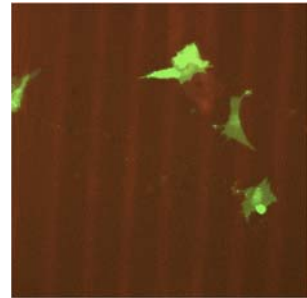
Frame 360   Frame 500   Frame 550
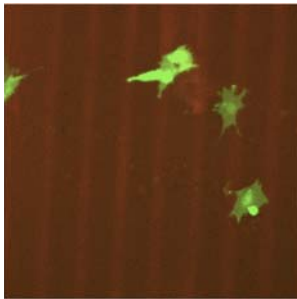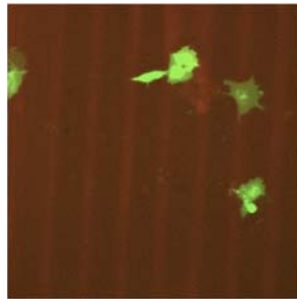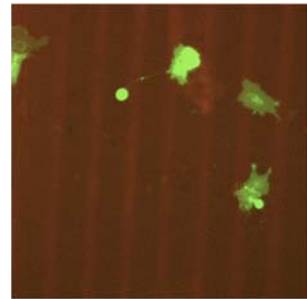
Frame 613   Frame 680   Frame 800
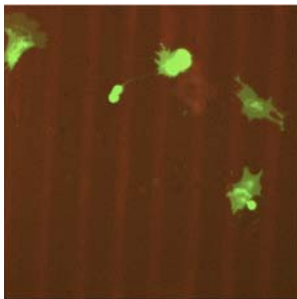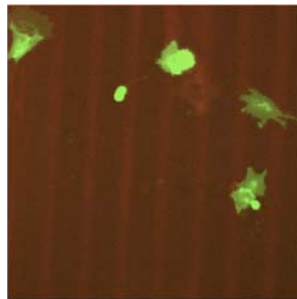
Frame 867   Frame 900

Neural Crest Cells on Photolithographed ephrin-B1 Striped Substrates
Red Shading Indicates ephrin-B1 Containing Area   2/21/00

A

B

C
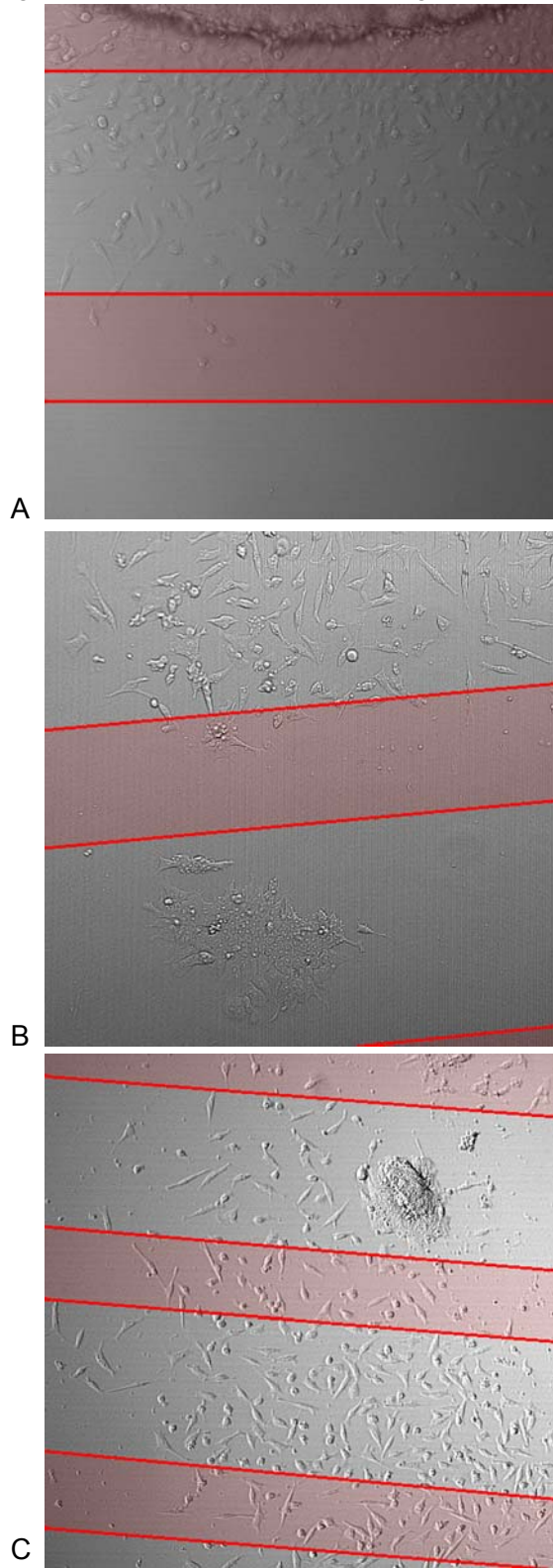
Membrane GFP Time Lapse of a Single Neural Crest Cell Encountering a Stripe of ephrin-B1
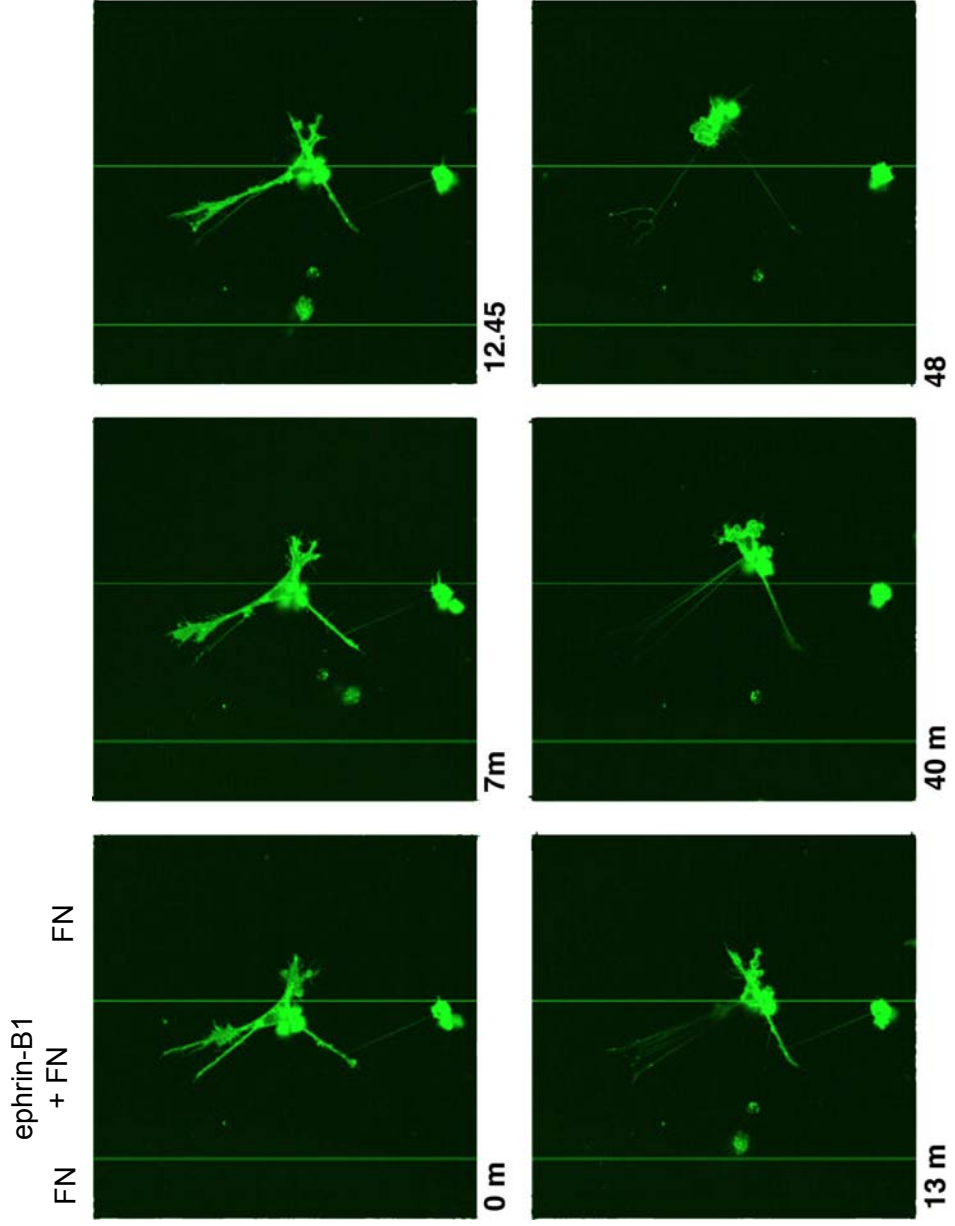
Patterns of Fluorescent Proteins on Vacuum Deposited Silane Surfaces

A

B
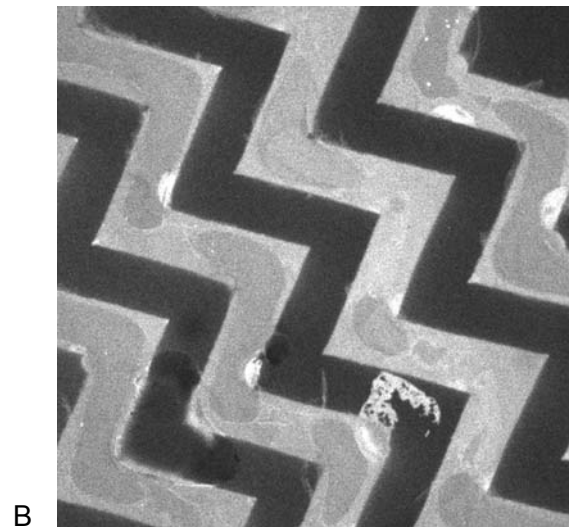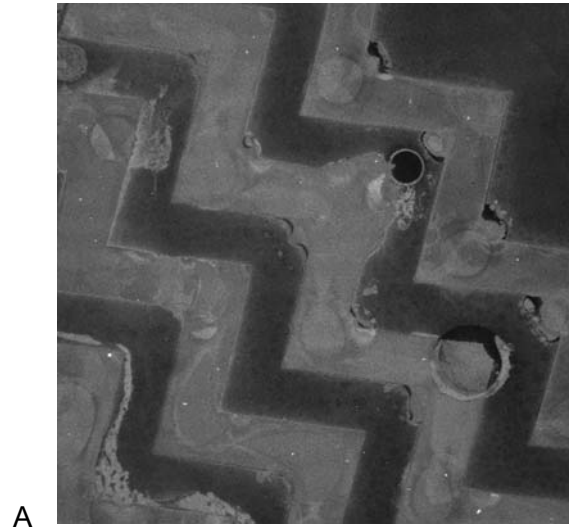
Cell Behavioral Responses to Eph/ephrin Signaling in

Primary Migrating Neural Crest Cells

Eph/ephrin signaling is known to be important during many embryonic processes, and is of particular importance to the migration of neural crest cells. To better understand the exact role of Eph/ephrin signaling in neural crest cell migration, we developed a novel cell migration assay to study the early cell behavioral responses of migrating primary avian neural crest cells to focal stimulation with ephrin-B ligands. We developed protocols for derivatizing small glass beads with ephrin-B proteins and for presenting these beads to migrating neural crest cells in culture, in a spatially and temporally defined manner, using optical tweezers. We continuously imaged the cells before, during, and following contact with ephrin-B beads and observed increased severity and frequency of lamellapodial collapse and cellular polarity change in response to ephrin-B1 beads when compared to beads coated in Protein-G.

We concluded from these experiments that the primary reaction of neural crest cells to ephrin stimulus is to change the directionality/polarity of the cell, rather than a global collapse of all projections, as has been previously reported [1, 2]. This polarity change occurs quickly (1-4 minutes) and as such is unlikely to involve transcription or translation, though these mechanisms were not explicitly ruled out. Additionally cells reacted more strongly to beads presented on their leading edges than their lateral surfaces and a cluster of beads presented simultaneously elicited a stronger effect than a single bead. Cells also proved capable of responding to multiple sequential stimuli, even when presented only minutes apart. We close by discussing the strengths and weaknesses of this assay.

Andrew J. Ewald and Scott E. Fraser

Biological Imaging Center

California Institute of Technology

Introduction

Migrating neural crest cells have been shown in published reports [1, 2] and in research for this thesis (Chapter 2) to be repelled by ephrin-B1. The published reports showed that, at the population level, migrating neural crest cells avoid regions of a *in vitro* substrate that contain more ephrin-B1. However, their assay was unable to address the mechanism or kinetics of this repulsion in detail. Furthermore there was significant observed variability in the response of individual neural crest cells within their assay. In Chapter 2 we attempted to address whether this heterogeneity in response was due to some inherent heterogeneity in the neural crest cells themselves or an artifactual variability caused by unintended systematic variations in the substrate pattern of ephrin-B1. To address that question I improved the neural crest cultures to more reliably produce similar cells, identified serum free culture conditions, improved the imaging conditions to better resolve cellular responses to the patterns, and significantly improved the substrate patterning techniques to produce more reliable patterns of ephrin-B1. The variability persisted and was so great as to prevent a meaningful analysis of single cell behavior.

We then focused on one remaining source of experimental variation inherent to the stripe assay: since we could not control when or how often the neural crest cells encountered the ephrin-B1 regions of the substrate each neural crest cell experienced the experiment differently. Some crest cells likely never encountered the ephrin regions at all, some migrated out onto the stripes directly and may have adapted to their presence, and only an unpredictable and small subset encountered the stimulus for the

first time while we were watching. For these reasons I came to believe that the stripe assay, whether implemented via adsorbed or photolithographed proteins, was intrinsically an assay for measuring the average response of a population of cells to a guidance cue and was not suited to detailed single cell analysis of the kinetics and nature of ephrin-B induced changes in cell behavior.

I instead devised a new, complementary assay for focusing on these questions. By derivatizing glass beads with ephrin-B1 and then using optical tweezers to manipulate the beads into contact with the cell, I sought to strip away most of the variability in the cell's experiences within each experiment. Optical tweezers are a particularly good tool for presenting beads to cells as their maximum force output is significantly less than the maximum force a cell can exert [3]. The forces exerted by an optical trap on a cell are small from a cellular perspective, while alternate modes of bead presentation, such as mechanical presentation with a glass micropipette, are capable of imparting much larger forces. Each neural crest cell migrated unrestricted on a fibronectin coated glass coverslip until the moment that it was introduced to an ephrin coated bead. By controlling the exact timing of first onset of the stimulus we sought to measure the early cell behavioral response of primary migrating neural crest cells to ephrin-B signaling.

Conceptually analogous experiments have been done through solution addition of EphB receptors to retinal axons [4] in a modified growth cone collapse assay, and the effect of solution addition of EphB receptors on the cytoskeleton of NG108 cells was monitored at 1 hour after stimulation in another report [5]. In the first report growth cones were

observed to collapse in response to EphB receptors and in the second the actin cytoskeleton was reorganized in response to soluble EphB receptors. Our experiments are complementary to these as ours were conducted in primary neural crest cells, with addition of surface bound ephrins, rather than Eph receptors. Both the Eph "receptors" and the ephrin "ligands" are capable of transducing signals into the cell upon which they are expressed, so it is interesting to study both directions of stimulus. There is some recent evidence that the stimulation of Eph expressing cells with ephrin ligand is the relevant signaling pathway for neural crest migration (as opposed to stimulation of ephrin expressing cells with Eph receptor), as the cytoplasmic domain of ephrin-B2 was shown to be dispensable for cranial neural crest migration in a mouse knockout [6].

We chose to focus our efforts on the *in vitro* study of neural crest cells in order to maximize our control over the cell's microenvironment. We feel that it is of particular relevance that we are using primary neural crest cells, within hours of explanting from the embryo, as these cells normally see and respond to ephrin-B ligands and should maintain fairly normal gene expression over this time period. Such studies are particularly useful for examining the role of ephrin signaling in guiding the neural crest, because ephrin-B knockouts in mouse are difficult to assay for neural crest migration defects, due to a pronounced cardiovascular defect [6-10]. It is also worth highlighting the results of a recent paper [11] that demonstrated a repulsive role ephrin-B signaling for early migrating trunk neural crest cells and a migration promoting role for ephrin-B signaling with late migrating neural crest cells. This dual role for ephrin signaling, which depends on cellular context, is consistent with published studies in other systems that

note that ephrin signaling can switch between mediating repulsive and adhesive interactions [12, 13].

We chose to focus our efforts with this new optical tweezers based migration assay on two specific areas: the nature and timing of the early cell behavioral response to ephrin-B stimulus, and the differential sensitivity of different regions of the neural crest cell to stimulation. These two questions take best advantage of the optical tweezers ability to precisely control the spatial and temporal presentation of ephrin protein. This specific control is missing in solution addition experiments where proteins are applied to the bath. It is also worth noting that the tight binding of protein to the glass beads makes the ephrin stimulus intrinsically directional (one part of the cell sees the bead and the rest doesn't) in a way that is difficult to mimic with a solution addition of protein. The key aspect of the timing that we sought to address was the delay between observing a cell migrating onto a stripe and observing it collapsing in response to a stripe [1]. This delay was reported to be between 20-40 minutes and we originally sought to determine the nature of the delay by comparing the effect of transitory contact between the bead and cell and persistent contact. This proved unnecessary for two reasons: first the cells tended to irreversibly pull the beads out of the trap and second the cells reacted much quicker than previously reported, typically 1-5 minutes after first contact.

Materials and Methods:

A. Laser Tweezers

Optical tweezers work by tightly focusing a beam of light and then using the focus of that beam to apply force to small objects. When the gradient force directed towards the focus of the laser is greater than the scattering force of the laser beam in the direction of the beam, then it becomes possible to stably hold a small particle in the center of the trap [14]. The gradient force is associated with changes in the momentum of light as it reflects and refracts off the dielectric interface of the glass bead and water [15]. For our experiments we used the optical tweezers facility of the Molecular Materials Research Center of the Beckmann Institute at Caltech. Figure 1 shows an image of the optical tweezers set-up and identifies the major components. Briefly, as depicted in Figure 1, the light from a B&W TEK BWR-1500 Nd:YVO4 infrared laser passes through a telescope (optics which expand then focus the beam), through a beam expander, and into a prism which splits the light into two separate beams, each of which is directed onto the surface of an adjustable mirror. The beams then recombine at a second prism, pass through a focusing lens and are directed into the Keller port of a Zeiss Axiovert S100 TV microscope with a 40x Plan Neofluar Phase 3 oil immersion objective. As a result of the prism splitting the beam to two independently adjustable mirrors, there are two independently adjustable optical traps built into the system. Both the mirrors and the stage are manually controlled, which required careful manipulation to avoid jerking the bead out of the trap. With practice, the system provided good trapping power and good control of the beads. The one caveat to the system is that it does not provide full

automatic laser safety protection. A supplemental infrared blocking filter was installed internally within the Axiovert microscope, but it should not be counted on to provide complete protection from focused IR light.

Microscopy

We continuously imaged the cells using Phase 3 contrast on a Zeiss Axiovert S100 TV microscope with a 40x Plan Neofluar Phase 3 oil objective lens. Images were collected by a Hamamatsu C5985 CCD camera and digitized by a Flashbus frame grabber card and acquired in the Metavue software program (Universal Imaging Corporation). The system provided good contrast on the details of lamellapodial and filopodial dynamics, without the need for any exogenous contrast. We were capable of acquiring 640 x 480 pixel tiff files at video rate, but this produced too many large files (1800 per minute). Instead we collected at 1 frame per second. This proved sufficient, and for many analysis steps we only examined every 10th frame, as a 30 minute movie at 1 frame per second yielded 1800 frames. Image processing was done in Adobe Photoshop 7.0 and Image J.

Functionalization of Glass Microspheres

For these experiments, we used recombinant mouse ephrin-B1 (R&D Systems), expressed as a fusion with the FC domain. We tethered this to glass beads via a biotinylated Protein-G (Calbiochem), that was linked to the bead via streptavidin coupled to a biotinylated alkyl silane self assembled monolayer. We decided on this somewhat indirect coupling approach based on previous reports that the function of

ephrin-B ligands within *in vitro* assays was dependent on the oligomeric state of the ligand, with clustered ligands being more active [16]. Our method should provide a series of strong attachments that, combined with washing after ephrin-B1 treatment, couple the proteins strongly to the beads. Thus we would expect that the bead is not a source of diffusing ephrin-B1, but rather only a contact mediated source. This is consistent with our experimental observations that cells do not appear affected by beads that they are not in contact with. Our detailed protocol for derivatizing glass beads is presented in A2-11, with full details of suppliers and part numbers for all components. That protocol is based on a protocol originally developed by Kevin Thigpen for other purposes.

Neural Crest Cell Preparations

Trunk neural crest explants were performed in general accordance with standard methods [17]. Our neural tube explant protocol was optimized as described in Chapter 2 and is presented in detail with suppliers and part numbers for all components in A2-6. Briefly 44-52 hour quail embryos were surgically extracted, the trunk segments were mechanically isolated, and the neural tube were enzymatically separated from the surrounding tissues with dispase II. The neural tubes were isolated from the attached notochord and rinsed through serum containing media to quench the dispase. They were then explanted onto glass substrates treated with human fibronectin. The typical culture media was F12 basal media supplemented with N2 protein supplement, penicillin and streptomycin. For imaging, the media was supplemented with 20 mM Hepes buffer.

Fibronectin Substrates

The glass substrates for these experiments were 40 mm coverslips (BiopTechs), which were coated with an alkyl silane layer and then treated with fibronectin, as described in A2-13. They should have been very uniform from batch to batch and region to region.

Culture Chambers

We used a Bioptechs closed FCS2 chamber, with integral heating and perfusion. The temperature was maintained at 37° C and fresh media was perfused at a slow rate into the chamber. Beads were added using a one milliliter syringe connected via a T-junction in the tubing just before the entry point the chamber. Beads were added to a flowing stream of media. This approach yielded reasonable, but not complete, control over the timing and amount of bead addition. It was typically necessary to clamp the exit hosing whenever adjusting the connection on the syringe, to prevent air bubbles being sucked through the chamber. Likewise, it was typically necessary to mix up the beads in the syringe prior to injection. Sometimes the beads would clump up into small clusters of 2-10 beads, for unknown reasons.

Basic Protocol

The timing of a typical optical tweezers experiment on neural crest cells is presented in A2-9. The details of the actual migration assay were as follows. At the end of day 3, I explanted neural tubes onto fibronectin substrates. First thing the next morning I verified that neural crest cells had emigrated out and mechanically removed the neural

tubes with forceps. I then loaded a coverslip with cells into the FCS2 chamber, took it to the tweezers room and loaded it into the set-up. I then typically allowed 30 minutes for the cells to equilibrate to their new surroundings. Once the culture had adapted I selected an isolated cell and begin a 30 minute time-lapse, collecting a frame every second. Once I had a couple minutes of images of that cell I pulsed the beads into the chamber. It often took a few seconds to a minute or two for the beads to work their way into the field of view. I then captured a bead and presented it to the cell, typically on the leading edge. Since the cell could pull the bead out of the trap, and to prevent heating up the cell, I then turned off the trap and simply watched the cell's behavior from that point for a total of 30 minutes. Occasionally a second bead would be trapped and introduced to the cell following the first stimulation.

Data Analysis

Each of the 30 minute movies (1800 frames) was reduced to a 180 frames by selecting every 10th frame using Image J. I then applied a Sharpen More filter and a Northeast Shadows filter to the stacks in Image J and saved the stacks out as .avi files for ease of use across computers. Initial scoring was to attempt to blindly identify control movies (Protein-G beads), from experimental movies (ephrin-B1). I scored them and was unable to reliably, blindly classify all of the movies as either control or experimental. Katy McCabe also agreed to blindly score all of the movies to determine which ones were control and which ones were experimental. She was also unable to do so accurately and similarly made errors of all types: incorrect classification of control as experimental and experimental as control as well as correct identifications. I concluded

from our inability to reliably distinguish control from experimental movies that all categories of cell behaviors were present in both conditions. To address whether there was a difference in frequency or severity of response I scored each movie for the number of major collapses per movie (30 minutes), the number of polarity changes per 30 minutes, and a score of 0-2 for overall reaction. If the cell appeared indifferent to the bead I assigned it a score of 0. Mildly repulsed was 1 and strongly repulsed was 2. David Koos also scored them blind. He systematically assigned lower scores than I did, but my low scores received low scores from him and his high scores received high scores from me. There were observed differences between control and experimental in the scoring of both David Koos and I.

Results

Optical Tweezers Migration Assay Works

All of the necessary components for the migration assay: primary cell culture, bead derivatization, bead perfusion, temperature control, bead capture, bead presentation to cells, and image collection and analysis all worked well as a synchronized assay. It was routinely possible to perform 8-10 separate bead experiments in a day, with 2 days of preparation. Some of this preparation would be suitable for more than one day of experiments, so in a long week 20-30 movies experiments could, in principle, be collected. Since these are intrinsically single-cell experiments accumulating significant numbers still takes some time. However, the key is that enough experiments can be run in a day to test multiple conditions (e.g., Protein-G and ephrin-B1) and reliably get

multiple examples of each one, even allowing for some experiments not going as planned.

Interpretability

One unanticipated limitation in the assay, that only emerged during data analysis, was that it was very difficult to interpret the behavior of cells that were already contracted, were not highly polarized, or were in contact with other cells. The cell that we were forced to look for was a highly polarized, highly flattened, migratory cell that was isolated from its neighbors. These cells were not typical of most in the dish. The underlying reason for this bias is that it was very difficult to interpret if a cell with no obvious polarity, or with most of its projections already retracted, had been repulsed by the bead or was simply maintaining a pre-existing semi-collapsed state. Since we were scoring for changes in cell behavior or cell polarity, it was necessary for the cell to have an obvious polarity or baseline level of protrusive activity at the beginning of the assay. Cells in contact with their neighbors will be addressed later in this analysis.

Types of Experiments Run

There were three major types of experiments run on neural crest cells. The first and most generally informative were leading edge stimulations, where a polarized cell was hit on its currently most active lamellapodia with one or more beads. To test whether there were regional differences in cellular response, some neural crest cells were instead contacted on a lateral surface distant from the leading edge. Finally to query

the ability of neural crest cells to process multiple stimulations some neural crest cells were serially or simultaneously contacted with several beads.

Reaction of Cells Was Intrinsic to Beads, Not to Laser Trap

We interpret the cells' reactions in these experiments to be primarily due to some direct influence of the bead, rather than the laser trap for two reasons, both unplanned. For both it is important to remember that beads are added by perfusing a pulse of them into the culture chamber. As such we had only partial control over where the beads went and some beads would land near cells through no conscious choice of our own. Since there were sometimes surplus beads in the cellular environment, cells could encounter beads on the surface that had never been manipulated with the laser. In multiple independent experiments cells acquired beads in this manner and reacted indistinguishably from cells that encountered beads from the laser trap. As further evidence occasionally cells would lose contact with a bead that they were repulsively reacting to. Their repulsive reaction would quickly cease after losing contact with the bead and they would assume a neutral polarity.

Difference in Degree and Frequency, Not in Category of Cell Behaviors

Our primary control for the specificity of the interaction between the cell and the bead was to contrast the cellular response to a bead coated in ephrin-B1 via Protein-G and a bead that was prepared identically but simply never exposed to Protein-G. There were no categorical differences in cell behavior between the two conditions, in that blind

scoring did not identify cell behaviors that were present in the ephrin-B1 experiments, but not in the Protein-G experiments (as independently and blindly scored by Andrew Ewald an Katy McCabe). Categorical differences would obviously have been desirable. Instead we developed three metrics and tested for differences in degree or frequency of reaction. We counted for number of polarity/directionality changes per 30 minutes, number of major retractions/collapses per 30 minutes (Figure 3-2), and degree of reaction (Figure 3-3): 0 for neutral, 1 for mildly repulsed by bead, and 2 for strongly repulsed by bead. Differences existed in all three categories. The detailed scoring for all analyzed movies is reported in Appendix 2. Cells contacting ephrin-B1 beads collapse more often, changed their cellular polarity more often, and responded more severely to ephrin-B1 beads (Figure 3-3). It is worth noting that cells in both conditions demonstrated a high degree of protrusive activity, making all of these judgments somewhat difficult. It is also worth noting that cells responded more dramatically to a cluster of ephrin-B beads than to a single bead.

As a more objective test of the noted differences, a second blind evaluation was made of all of the movies by David Koos. These scores were systematically lower than those of Andrew Ewald, but the high Koos scores were high Ewald scores and the low Ewald scores were low Koos scores. The details of the two sets of scores are presented in Appendix 2 and the conclusions are summarized in Figure 3-4. Both sets of scores reveal a marked difference between Protein-G and ephrin-B1 experiments.

Typical Interaction of Cell with Beads

In the majority of cases, with both ephrin-B1 and Protein-G beads, the cell would take the bead out of trap and retain it with sufficient force that the trap could not take it back. Most beads that were captured in this manner were retrogradely transported and they were rarely released. Due to this unexpected phenomenon we were unable to directly test the differences in cellular response to transient vs. sustained contact with ephrin-B1 beads. Most neural crest cells that were going to exhibit a response to ephrin-B beads had done so within 1-4 minutes from first contact. A good example of a rapid reorganization is Figure 3-5. Within 1 minute of contact with an ephrin-B1 bead on its leading edge the experimental cell has begun to reverse its polarity and by four minutes it has retracted its previously dominant lamellapodia and extended a new one in the opposite direction. This reversal of polarity is the prototypical strong reaction of a polarized neural crest cell to ephrin-B1 beads. Figure 3-6 presents a similar case: the cell in question is migrating towards the bottom of the frame until it is contacted with a cluster of ephrin-B beads. It takes the cluster of beads, transports them towards the nucleus, collapses its proximal lamellapodia, and extends a new leading edge on the opposite side of the cell.

Contact with the lateral edge of a neural crest cell with ephrin-B1 beads was sufficient in some cases to dramatically reorganize the cells polarity, as seen in Figure 3-7, but this was not typical. In general the cellular reaction to lateral edge ephrin-B1 presentation was less dramatic. Figure 3-8 presents the relative proportion of repulsion scores for lateral versus leading edge presentation. We conclude from these limited data that

neural crest cells are more responsive to ephrin-B signaling on the leading edge of the cell. This graph also serves to highlight the differential response that only subtly different modes of ephrin-B presentation can evoke. It also highlights that our pooled averages for the experiments are averaging across different experimental designs which evoked different responses of differing severity.

Figure 3-9 highlights a highly polarized cell that has received two sequential ephrin-B stimuli on its leading edge. It responds by to the first by bifurcating its broad lamellapodia and briefly assuming a bipodal shape, before collapsing the lamellapodia near the site of the second contact and migrating away. This experiment demonstrates the ability of a neural crest cell to sequentially respond to two stimuli over a span of less than a minute. Interestingly, the response is also sequential, not additive, implying that the cell either remained sensitive or quickly regained sensitivity to ephrin-B stimuli very shortly after the first contact. These sorts of details are only accessible via time-lapse microscopy.

The examples cited in figures so far were all strong (score=2) reactions to ephrin-B1. To give a fuller sense of the range of response, Figure 3-10 presents a neural crest cell that reacts mildly to ephrin-B1 stimulus (score=1 AJE, 0 DK). This movie also highlights the difficulty in scoring the response of cells without obvious directional polarity or large leading edge lamellapodia. The fractional loss of adherent surface area in this case may well be more than in Figure 3-9, but it is more difficult to determine the nature of its response. Figure 3-11 presents a polarized neural crest cell that was presented with a

Protein-G bead on its most active lamellapodia. This lamellapodia collapses nearly completely and there are also several small retraction events coincident with transient contact between the cell and beads on the surface (Score=2 AJE, DK). Finally Figure 3-12 shows a mild reaction to a Protein-G bead. The global shift from the first to second frame is due to a shift in the position of the stage, not cell movement. The cell is already somewhat retracted so it is a bit difficult to score, but the lamellapodia in contact with the bead retracts noticeably (Score=1 AJE, 0 DK).

Discussion

Conclusions

We conclude from these experiments that the normal response of a neural crest cell to ephrin-B ligand is to quickly (1-4 minutes) retract local lamellapodia coincident with a global increase in protrusive activity elsewhere. In cases where the cell maintains contact with the bead that region of the cell tends to remain collapsed, and the cell typically migrates in the opposite direction. This response is different than the 20-40 minute delay then global collapse that was previously reported [1]. We attribute the differences in timing to the fact that our assay enables more accurate determination of the time of first contact, and possibly to the fact that a bead coated in ephrin protein may be a more intense signal to the cell, due to its very high local concentration. The leading edge of the cell was more sensitive to ephrin-B stimulus than the lateral edge, and clusters of beads elicited a stronger response than individual beads. These conclusions are consistent with recent reports of migrating neural crest cells in the

hindbrain of chick embryos: neural crest cells migrate in a directional manner, with few undergoing prolonged global collapses in normal embryos [18-20].

Level of Confidence in Conclusions

We are not unambiguously certain of the above conclusions. The differences between the Protein-G and ephrin-B1 conditions, while present, are not overwhelming. The movies of neural crest cells strongly reacting to ephrin-B1, taken on their own, while highly suggestive about the kinetics and mechanism of the cell behavioral changes in neural crest migration induced by ephrin-B signaling, can not be considered compelling without further experimental support. There are two basic problems. The first is that there is a considerable variability in the response within a given condition. The second is that the Protein-G beads evoke a strong reaction, in a subset of experiments.

Variability

Our most likely explanation for the variability in the response of neural crest cells to ephrin-B beads is intrinsic biological differences between cells, as we have controlled nearly every other aspect of the experiments. A recent paper supports this idea, as they noticed that early migrating neural crest cells are repelled by ephrin-B1 and late migrating cells perceive ephrin-B signal as migration promoting [11]. One way to address this concern is to more rigorously restrict the types of neural crest cells in the culture, by experimentally isolating only early or late neural migrating neural crest cells and then contrasting their response to ephrin-B1 beads. Another possibility is that

there is a threshold effect, whereby a certain amount of ephrin-B stimulus is required to elicit a reaction. This might vary from cell to cell based on receptor expression level. There is some support for this idea in our observation that clusters of beads elicited stronger reactions than single beads.

More troubling is the variability in the response of cells to Protein-G beads. I can think of two likely explanations. The first is that the background level of protrusive activity, in isolated neural crest cells *in vitro*, is so high that our interpretations of cause and effect are suspect. Visual inspection of cultures and long-term time-lapse data on neural crest cell cultures provides some support for this idea. I have noted that the "quietest" cells in a culture are those in extensive contact with their neighbors; isolated highly polarized cells tend to collapse and extend dramatically even in the absence of obvious guidance information. Another possibility, of greater concern, is that the cellular reaction has nothing to do with ephrin signaling and instead is a response to the Protein-G, streptavidin, or bead chemistry. The coupling proteins should be innocuous to neural crest cells, but this possibility can not be excluded. Alternately the cell could be reacting through some more basal cell adhesion mechanism. Arguing against this idea are studies of cellular reactions to fibronectin coated beads, presented with optical tweezers, in which highly local responses (8-12 um2) to the bead were observed [3]. In contrast we are definitely observing global responses throughout the cell.

Possibilities for Improvement

The next direction for this project, to identify the best future assays modifications, would be to simply conduct more leading edge neural crest experiments. We expected that we would gain significantly more control over a cell's experience in this assay, as contrasted with the stripe assay (Chapter 2), and we did. However, Figure 8 demonstrates that cells contacted with ephrin-B beads on different parts of their circumference react differently This is an interesting observation, but it means that tighter control needs to be exercised on the type of experiment being conducted (leading or lateral edge, etc.) and that serendipitous experimental variation (i.e. cell contact with other cells or additional beads) needs to be excluded from the core analysis. In practice this means performing significantly more migration experiments. Another avenue worth considering is to alter the coupling chemistry used to attach the protein to the bead. The possibility still exists that some variation of experimental technique will cause a subset of the neural crest behavior to become more prominent or disappear, and thereby increase our confidence that the dynamics we observe are specific.

We could achieve a qualitative improvement in interpretability if we could visualize the activation of Eph signaling in the neural crest cell, while monitoring its morphology. The problem with monitoring cell morphology alone is that it is very difficult to be certain when, and in which cells, Eph signaling has been activated. This variability alone could explain all the differences within each condition; the cells that responded strongly to ephrin-B1 beads may be the only cells in which Eph signaling was activated. It could

also let us directly assay for the necessary threshold of ephrin contact required for Eph signaling. At present we are not aware of any dynamic means of monitoring Eph signaling in living cells.

Posthoc Evaluation of Experimental Design

Having completed this project, I have had time to consider the quality of the experimental design and the return of biological conclusions for time invested. I developed and pursued this assay consciously aware that it was a high-risk high-reward undertaking. If neural crest cells responded in a more consistently different way to ephrin-B1 beads than Protein-G, and if their background level of cell behavior in isolation was lower, I still believe that this experimental paradigm would be a powerful way to evaluate the immediate early response of neural crest cells to Eph/ephrin signaling. Once those clear behavioral responses emerged, there are many experimental possibilities, including testing the effect of different mutations on the ability of the resulting protein to evoke the characteristic response. The problem is that unless a clear, repeatable characteristic response exists (which is unknowable until tested), the assay produces no firm conclusions. A related problem with this type of experiment is that is was very labor intensive, taking a full year to experimentally implement, and months to acquire and interpret the data. Simpler, faster assays have answered many of the questions we sought to address [4, 5, 11]. I still think the optical tweezers migration assay was a well-designed experiment, but in the future I will make a faster determination whether a high-risk assay seems like it will be productive or not. I will

also pay more attention to whether the same questions can be answered via technically simpler means.

One element that I feel was missing from this experimental design that I will seek to correct in the future is autonomous cellular behavior. The central problem with the interpretation of the time-lapse movies in this project was that there was no biologically known cell behavior that was preserved in our neural crest cultures. By way of contrast explants of the dorsal marginal zone of a frog gastrula are known to autonomously execute their normal convergent extension cell movements even when surgically isolated and cultured [21]. Because there was no normal cell behavior preserved in our assay, the only regularity in cellular response would have to come from a regular response to our applied stimulus. A simple experimental variation would be to assay for delamination of neural crest cells from the neural tube in culture and test for the role of different signaling pathways in that decision.

1. Krull CE, Lansford R, Gale NW, Collazo A, Marcelle C, Yancopoulos GD, Fraser SE, Bronner-Fraser M: **Interactions of Eph-related receptors and ligands confer rostrocaudal pattern to trunk neural crest migration**. *Curr Biol* 1997, **7**:571-580.

2. Wang HU, Anderson DJ: **Eph family transmembrane ligands can mediate repulsive guidance of trunk neural crest migration and motor axon outgrowth**. *Neuron* 1997, **18**:383-396.

3. Choquet D, Felsenfeld DP, Sheetz MP: **Extracellular matrix rigidity causes strengthening of integrin-cytoskeleton linkages**. *Cell* 1997, **88**:39-48.

4. Birgbauer E, Oster SF, Severin CG, Sretavan DW: **Retinal axon growth cones respond to EphB extracellular domains as inhibitory axon guidance cues**. *Development* 2001, **128**:3041-3048.

5. Cowan CA, Henkemeyer M: **The SH2/SH3 adaptor Grb4 transduces B-ephrin reverse signals**. *Nature* 2001, **413**:174-179.

6. Adams RH, Diella F, Hennig S, Helmbacher F, Deutsch U, Klein R: **The cytoplasmic domain of the ligand ephrinB2 is required for vascular morphogenesis but not cranial neural crest migration**. *Cell* 2001, **104**:57-69.

7. Wang HU, Chen ZF, Anderson DJ: **Molecular distinction and angiogenic interaction between embryonic arteries and veins revealed by ephrin-B2 and its receptor Eph-B4**. *Cell* 1998, **93**:741-753.

8. Adams RH, Wilkinson GA, Weiss C, Diella F, Gale NW, Deutsch U, Risau W, Klein R: **Roles of ephrinB ligands and EphB receptors in cardiovascular development: demarcation of arterial/venous domains, vascular morphogenesis, and sprouting angiogenesis**. *Genes Dev* 1999, **13**:295-306.

9. Gerety SS, Wang HU, Chen ZF, Anderson DJ: **Symmetrical mutant phenotypes of the receptor EphB4 and its specific transmembrane ligand ephrin-B2 in cardiovascular development**. *Mol Cell* 1999, **4**:403-414.

10. Gerety SS, Anderson DJ: **Cardiovascular ephrinB2 function is essential for embryonic angiogenesis**. *Development* 2002, **129**:1397-1410.

11. Santiago A, Erickson CA: **Ephrin-B ligands play a dual role in the control of neural crest cell migration**. *Development* 2002, **129**:3621-3632.

12. Holmberg J, Clarke DL, Frisen J: **Regulation of repulsion versus adhesion by different splice forms of an Eph receptor**. *Nature* 2000, **408**:203-206.

13. Huynh-Do U, Vindis C, Liu H, Cerretti DP, McGrew JT, Enriquez M, Chen J, Daniel TO: **Ephrin-B1 transduces signals to activate integrin-mediated migration, attachment and angiogenesis**. *J Cell Sci* 2002, **115**:3073-3081.

14. Ashkin A: **Forces of a Single-Beam Gradient Laser Trap on a Dielectric Sphere in the Ray Optics Regime**. In: *Laser Tweezers in Cell Biology* Edited by Sheetz MP, vol. 55. pp. 228. San Diego: Academic Press; 1998: 228.

15. Smith S, Bhalotra SR, Brody AL, Brown BL, Boyda EK, Prentiss M: **Inexpensive Optical Tweezers for Undergraduate Laboratories**. *American Journal of Physics* 1999, **67**:26-34.

16. Stein E, Lane AA, Cerretti DP, Schoecklmann HO, Schroff AD, Van Etten RL, Daniel TO: **Eph receptors discriminate specific ligand oligomers to**

determine alternative signaling complexes, attachment, and assembly responses. *Genes Dev* 1998, **12**:667-678.

17. Bronner-Fraser M: **Manipulations of Neural Crest Cells or Their Migratory Pathways**. In: *Methods in Avian Embryology* Edited by Bronner-Fraser M, vol. 51. pp. 61-79. New York: Academic Press; 1996: 61-79.

18. Kulesa P, Bronner-Fraser M, Fraser S: **In ovo time-lapse analysis after dorsal neural tube ablation shows rerouting of chick hindbrain neural crest**. *Development* 2000, **127**:2843-2852.

19. Kulesa PM, Fraser SE: **Neural crest cell dynamics revealed by time-lapse video microscopy of whole embryo chick explant cultures**. *Dev Biol* 1998, **204**:327-344.

20. Kulesa PM, Fraser SE: **In ovo time-lapse analysis of chick hindbrain neural crest cell migration shows cell interactions during migration to the branchial arches**. *Development* 2000, **127**:1161-1172.

21. Keller R, Davidson L, Edlund A, Elul T, Ezin M, Shook D, Skoglund P: **Mechanisms of convergence and extension by cell intercalation**. *Philos Trans R Soc Lond B Biol Sci* 2000, **355**:897-922.

Figure 1: Panel A shows the optical tweezers apparatus in the Molecular Materials Research Center. As there are a number of extraneous components on the optical table, Panel B shows the core optics of an optical tweezers set-up. For simplicity several components in the optical path that are not critical to its performance are neglected in the schematic. The light from an infrared laser is steered into a telescope that expands and condenses the beam onto a second mirror which directs the light through an aperture to a prism. The first prism splits the light into two independent paths, which are directed to two independently controlled steering mirrors. A second prism then recombines these two beams and directs them through a focusing lens, and onto a final mirror that directs the light into the Keller port on the bottom of the microscope.

Figure 2: Three different experimental conditions were compared for the number of polarity changes and number of major collapse/retractions per 30 minutes (the time of a typical experiment). The control condition was neural crest cells cultured on the same microscope with no laser trap and no beads. This baseline condition was compared to cells exposed to beads coated in either Protein-G or ephrin-B1. The plot is expressed as a percentage representation of each score within each condition. Protein-G was less responsive than ephrin-B1 according to both metrics, but both were more different from control than from each other.

Figure 3: The overall reaction of the cell to the bead was characterized as a single score, with 0 being neutral, 1 being mildly repulsive, and 2 being strongly repulsive.

Cells exposed to ephrin-B1 beads reacted more strongly overall. When cells that made contact with other cells through the course of the experiment were excluded, this difference became greater.

Figure 4: Two different independent scientists scored the overall responsiveness of the cells to the beads, with 0 being neutral, 1 being mildly repulsive, and 2 being strongly repulsive. One scorer (Koos) consistently scored lower than the other (Ewald), but both observed a difference between ephrin-B1 and Protein-G beads, with ephrin-B1 eliciting a stronger reaction in both cases.

Figure 5: Two cells were filmed for 30 minutes. The cell on the right was contacted with a bead on its leading edge at t=0, while strongly polarized towards the top of the frame. This polarity is reversed substantially within 1 minute and completely by four minutes. The cell loses contact with the bead and then assumes a neutral polarity. This is an example of a strong reaction to the bead and was scored a 2 by AJE.

Figure 6: One cell was migrating towards the bottom of the field and was contacted with a cluster of ephrin-B1 beads on its leading edge. Within eight minutes it completely reorganized its orientation and began migrating towards the top of the field. This is an example of a strong reaction to the bead and was scored a 2 by AJE.

Figure 7: An example of lateral edge presentation of ephrin-B1 beads to a neural crest cell. Within 4 minutes of contact the cell had withdrawn its most active lamellapodia and

by eight minutes it had reorganized to migrate in the opposite direction from its original orientation. This was considered a strong reaction to lateral presentation and was scored a 2 by AJE and DK.

Figure 8: The repulsion scores for leading edge and lateral edge experiments were separated from the totals and expressed as a percentage of the scores representation in the dataset. The differences between ephrin-B1 and Protein-G are not as dramatic in either case, but it is clear that the cell responds more strongly to contact on its leading edge than its lateral surfaces.

Figure 9: This cell was actively migrating towards the bottom of the frame and was organized with one broad downward pointing lamellapodia. The cell was contacted twice in rapid succession (less than 1 minute gap) on its leading edge with ephrin-B1 beads. The reaction was similarly sequential. First the broad lamellapodia collapsed in the vicinity of the first contact and the cell appeared bipodal. Then the area around the second contact collapsed and the cell began migrating away at right angles to its previous direction. This was considered a strong reaction and was scored a 2 by AJE.

Figure 10: This cell was not actively migrating and did not have an obvious directional polarity. It was contacted with an ephrin-B1 bead on one of its three projections. The cell contracted that projection modestly within four minutes and later withdrew a separate projection. Since it did not have an obvious polarity, it was difficult to score.

However, since it did appear to retract its projections this was characterized as a mild response to the bead and was scored a 1 by AJE and a 0 by DK.

Figure 11: This cell was contacted with a Protein-G bead on its leading edge and then it independently contacted several beads on the surface. The leading edge was completely withdrawn by 8 minutes and there were several smaller retraction events associated with contact between the cell and beads on the surface. This was characterized as a strong reaction to a Protein-G bead and was scored a 2 by AJE and DK.

Figure 12: This cell was contacted with a Protein-G bead on its leading edge. The shift from frame 1 to 2 is a shift in the position of the stage, not a cell movement. In response to the contact this cell retracted its modest leading edge and extended in several different directions. This was scored a 1 by AJE and a 0 by DK.

A

B

Laser

Mirror

Telescope

Mirror

Prism

Steering Mirror

Steering Mirror

Prism

Lens

Microscope

Average Number of Polarity Changes Per 30 Minutes

Average Number of Collapses per 30 Minutes
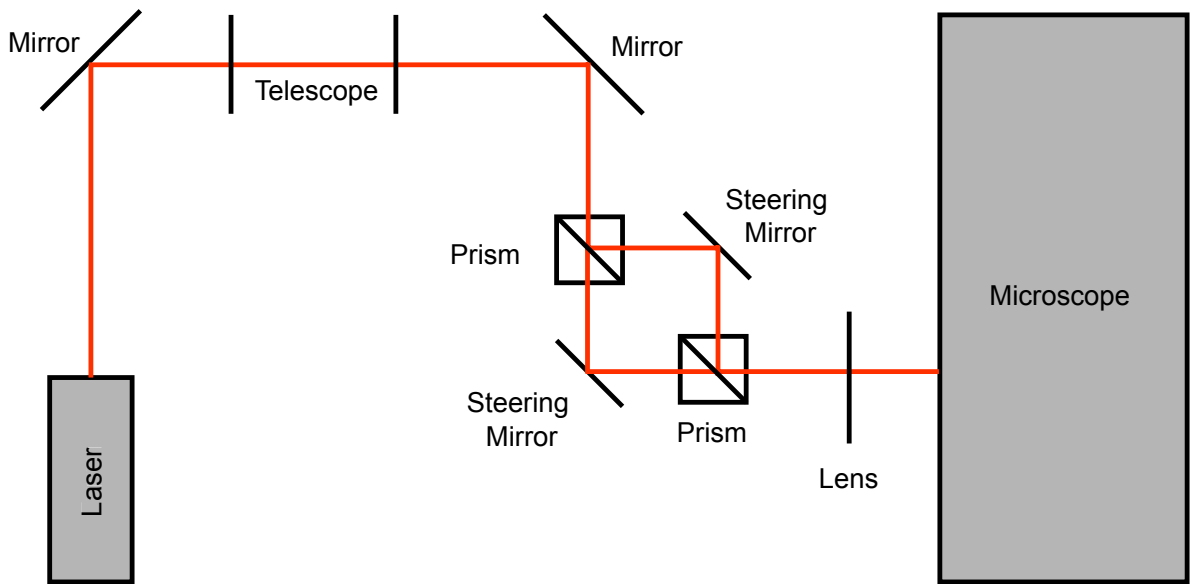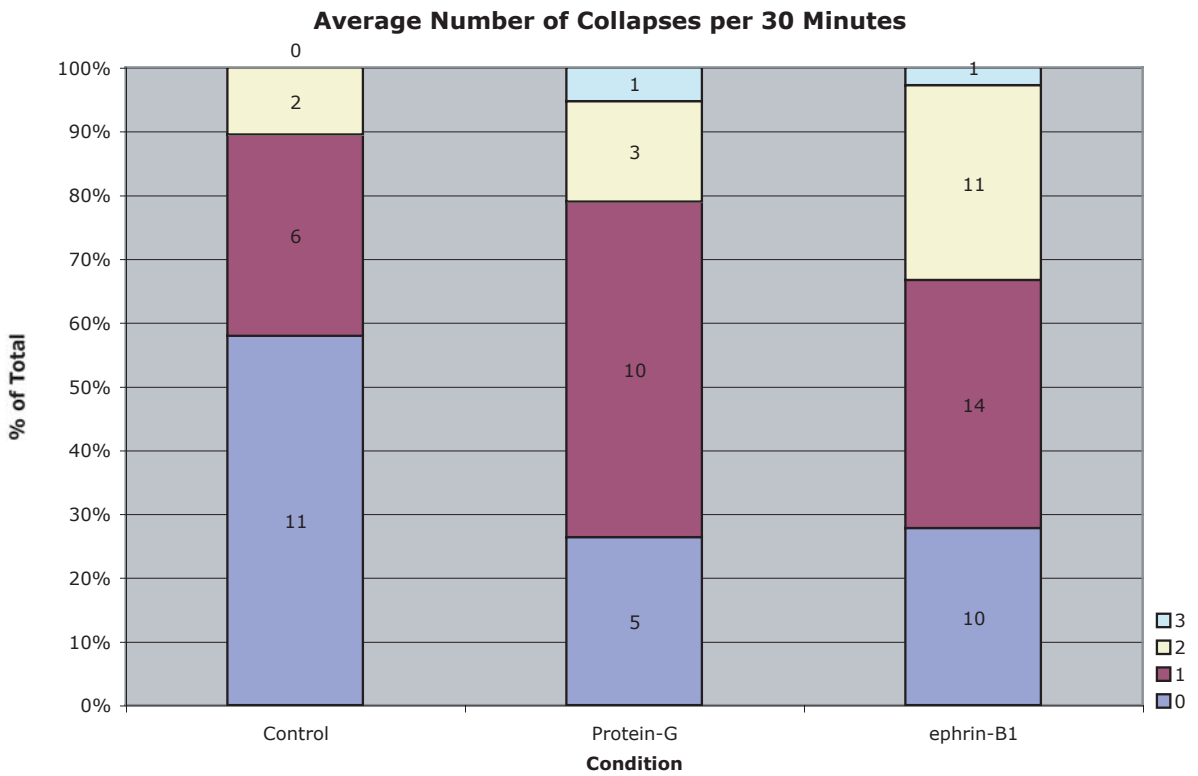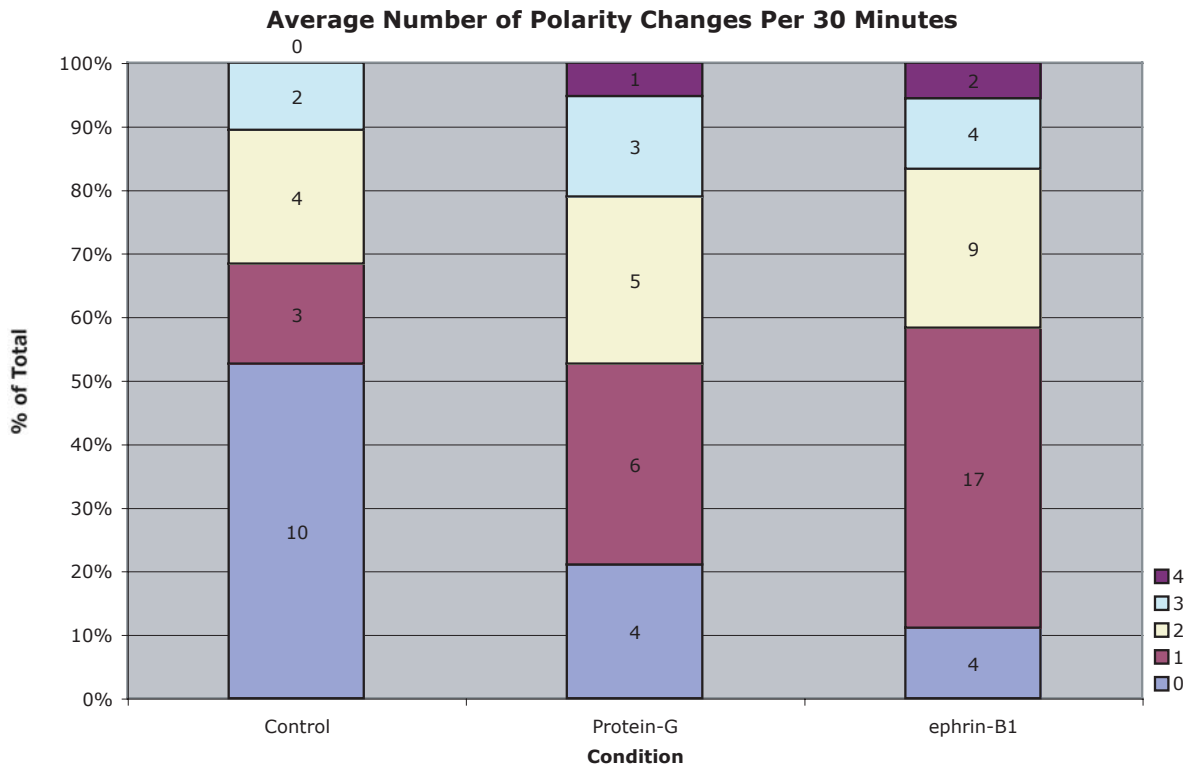
Degree of Repulsion:
0 = Neutral, 1 = Mildly Repulsive, 2 = Strongly Repulsive
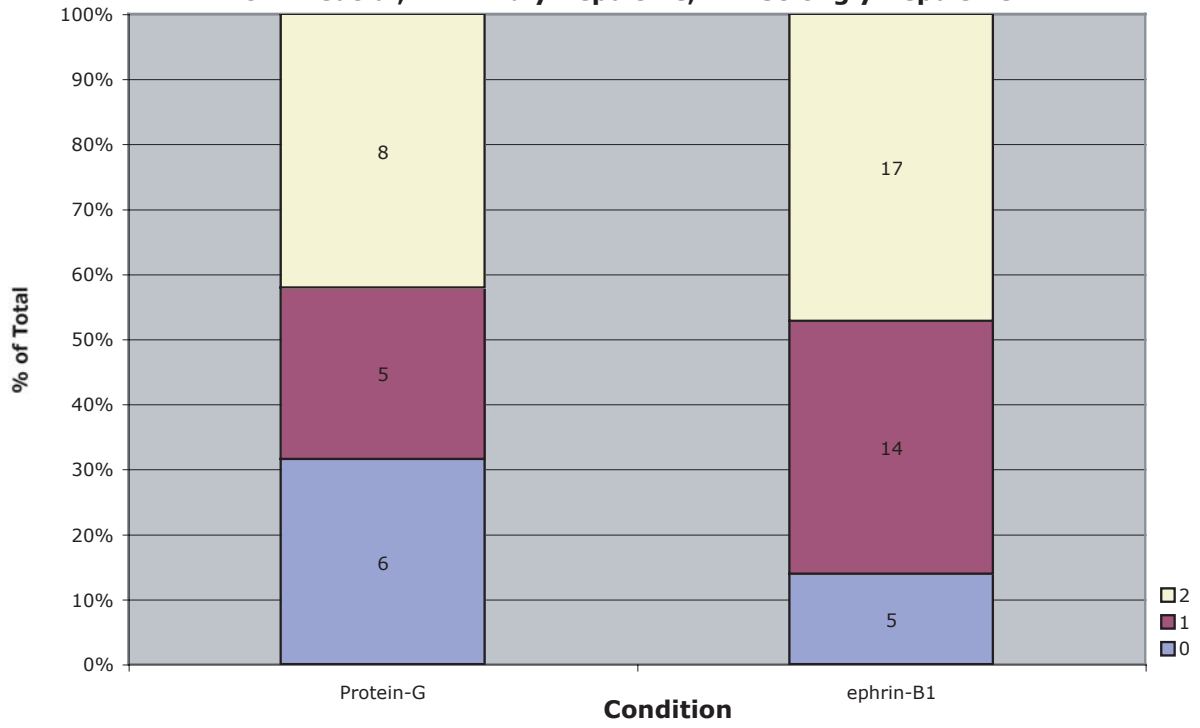
Repulsion Score in Isolated Cells:
0 = Neutral, 1 = Mildly Repulsive, 2 = Strongly Repulsive
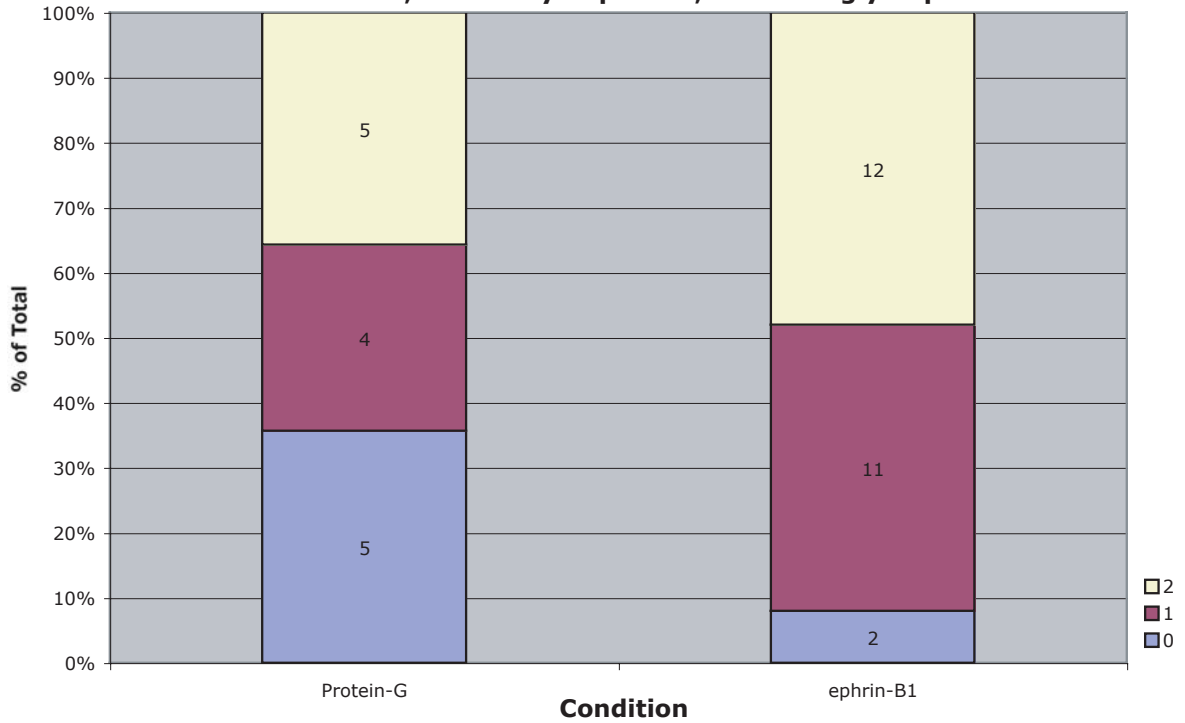
Comparison of Two Different Blind Evaluations of Cells with No Cell-Cell Contact

Movie 13

3-33

Movie 34

3-34

t=0

t=1 minute

t=2 minutes

t=4 minutes

t=8 minutes

t=12 minutes

t=16 minutes

t=20 minutes

Movie 22

3-35

t=0

t=1 minute

t=2 minutes

t=4 minutes

t=8 minutes

t=12 minutes

t=16 minutes

t=20 minutes
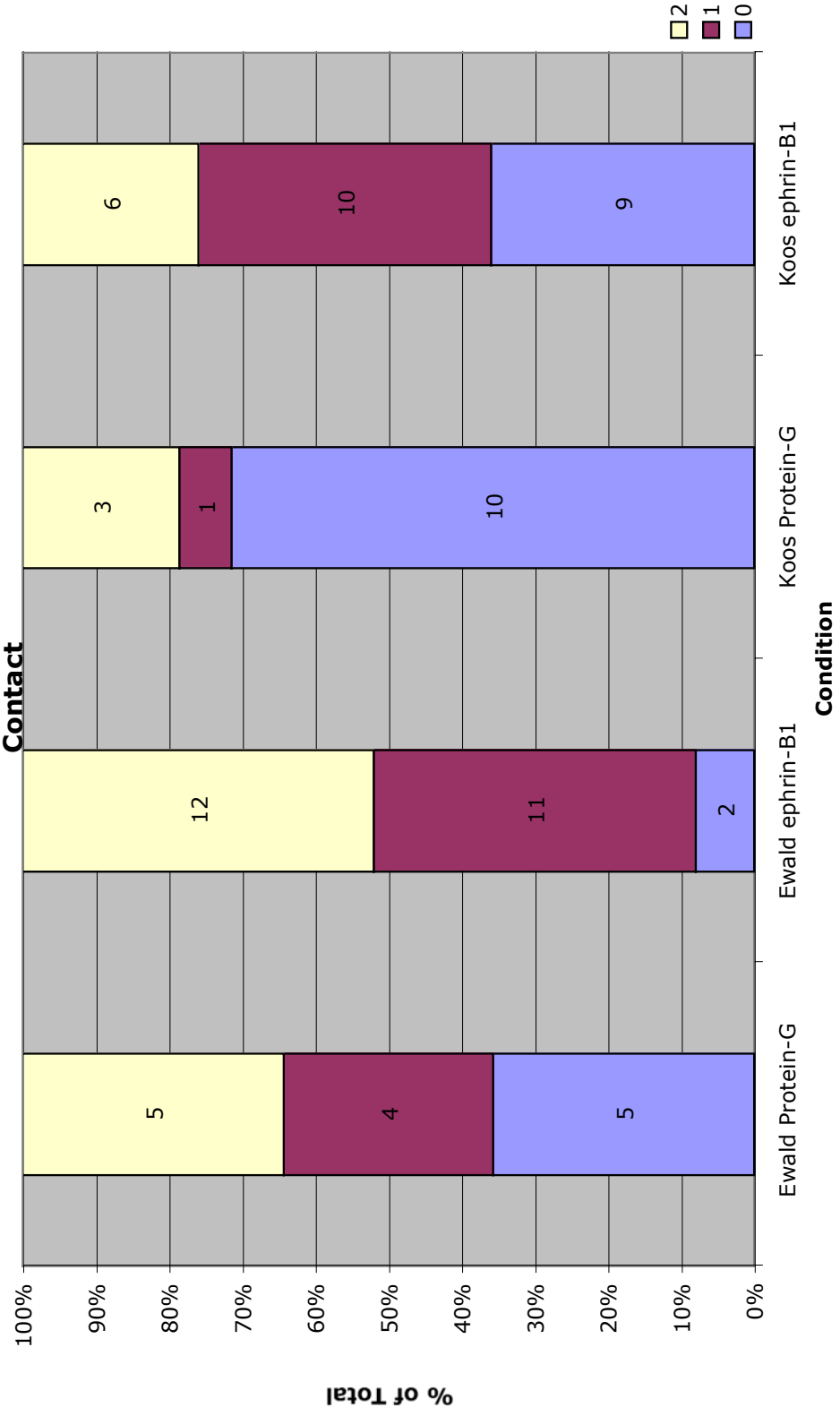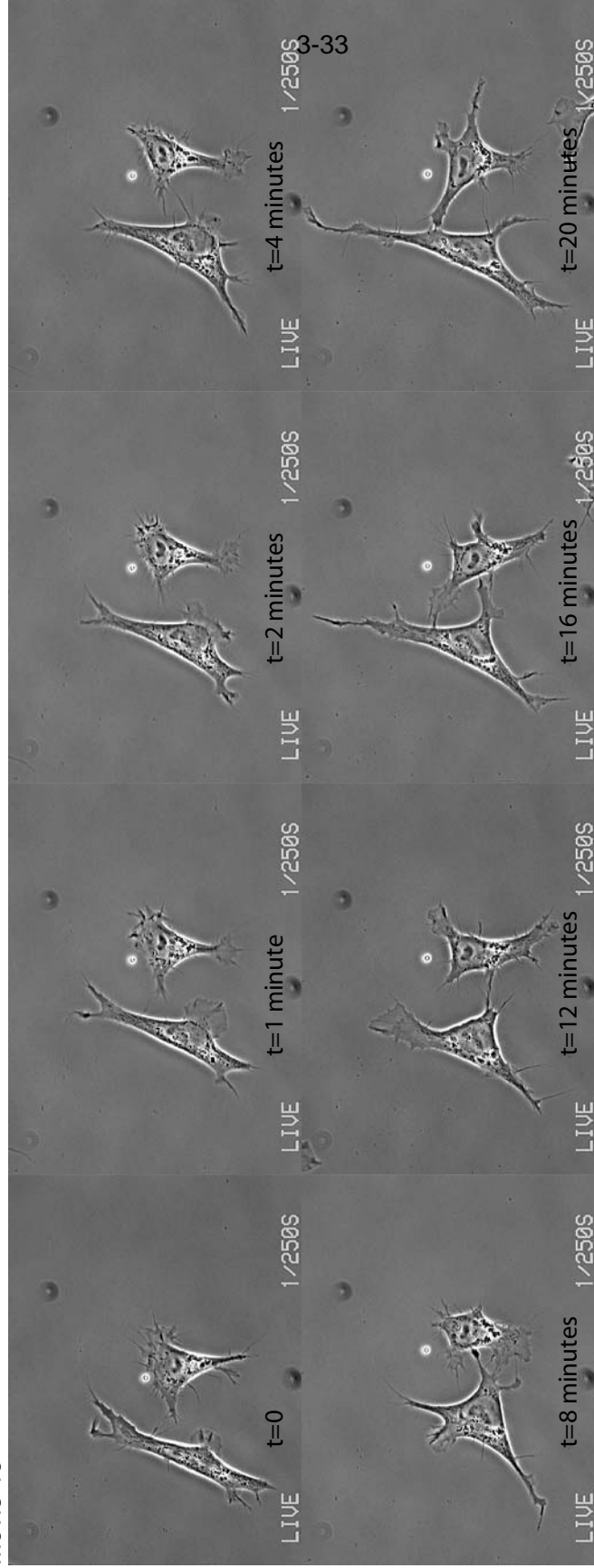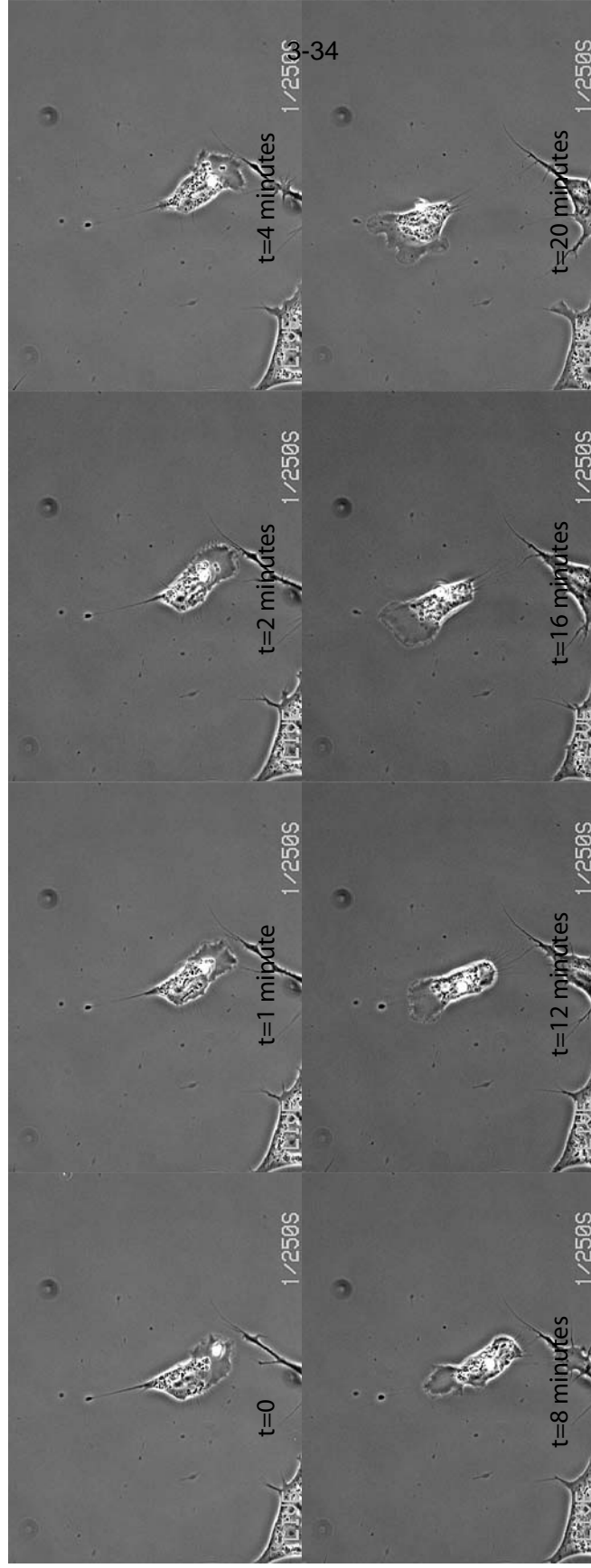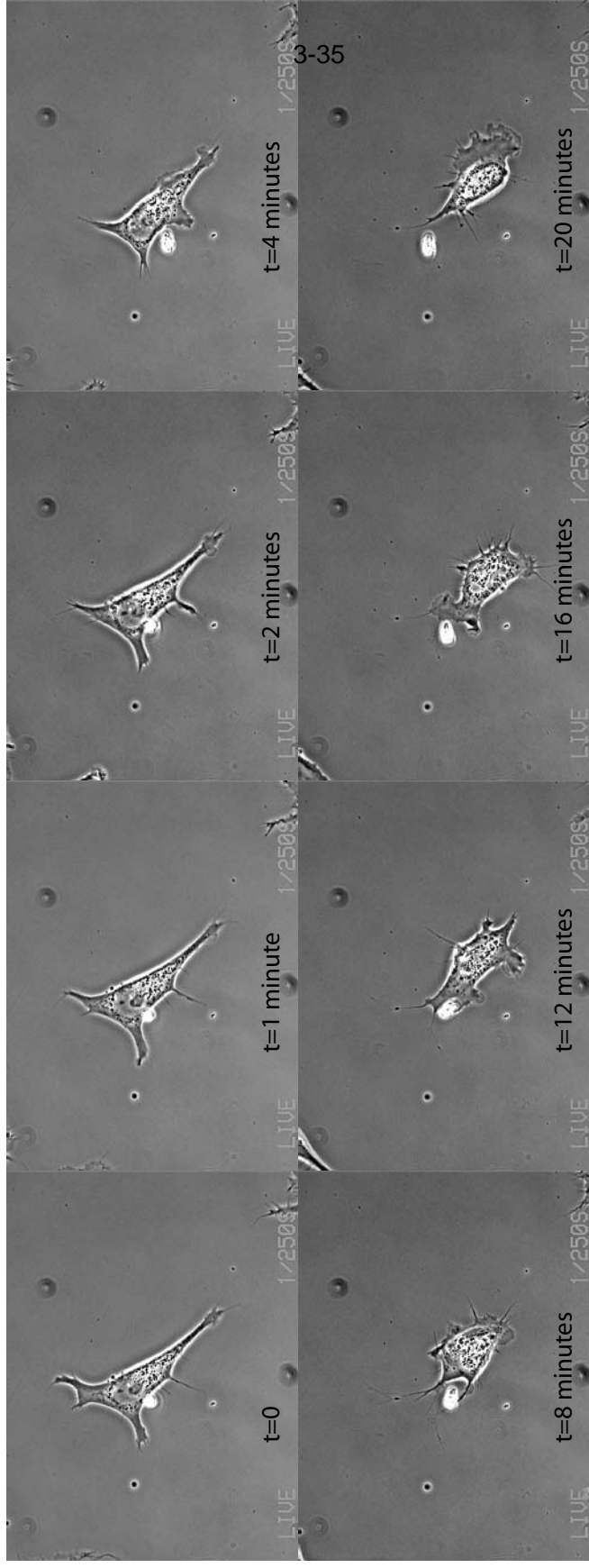
Comparison of Leading and Lateral Edge Bead Presentation

Movie 35

3-37

t=4 minutes

t=2 minutes

t=1 minute

t=0

t=20 minutes

t=16 minutes

t=12 minutes

t=8 minutes

Movie 5

3-38

t=0
t=1 minute
t=2 minutes
t=4 minutes

t=8 minutes
t=12 minutes
t=16 minutes
t=20 minutes

Movie 16

3-39

LIVE   t=4 minutes   1/250S

LIVE   t=20 minutes   1/250S

LIVE   t=2 minutes   1/250S

LIVE   t=16 minutes   1/250S

LIVE   t=1 minute   1/250S

LIVE   t=12 minutes   1/250S

LIVE   t=0   1/250S

LIVE   t=8 minutes   1/250S

Movie 8

3-40

LIVE t=0 1/250S
LIVE t=1 minute 1/250S
LIVE t=2 minutes 1/250S
LIVE t=4 minutes 1/250S

LIVE t=8 minutes 1/250S
LIVE t=12 minutes 1/250S
LIVE t=16 minutes 1/250S
LIVE t=20 minutes 1/250S

Calcium Signaling during
Convergent Extension in *Xenopus*

John B. Wallingford*, Andrew J. Ewald,
Richard M. Harland*, and Scott E. Fraser†,

Division of Biology and Beckman Institute (139-74)
California Institute of Technology
Pasadena, CA, 91125

*Department of Molecular and Cell Biology
401 Barker Hall,
University of California
Berkeley, CA 94720-3204

Abstract

Background: During *Xenopus* gastrulation, cell intercalation drives convergent extension of dorsal tissues. This process requires the coordination of motility throughout a large population of cells. The signaling mechanisms that regulate these movements in space and time remain poorly understood.

Results: To investigate the potential contribution of calcium signaling to the control of morphogenetic movements, we visualized calcium dynamics during convergent extension using a calcium-sensitive fluorescent dye and a novel confocal microscopy system. We find that dramatic intercellular waves of calcium mobilization occur in cells undergoing convergent extension in explants of gastrulating *Xenopus* embryos. These waves arose stochastically with respect to timing and position within the dorsal tissues. Waves propagated quickly and were often accompanied by a wave of contraction within the tissue. Calcium waves were not observed in explants of the ventral marginal zone or prospective epidermis. Pharmacological depletion of intracellular calcium stores abolished the calcium dynamics and also inhibited convergent extension without a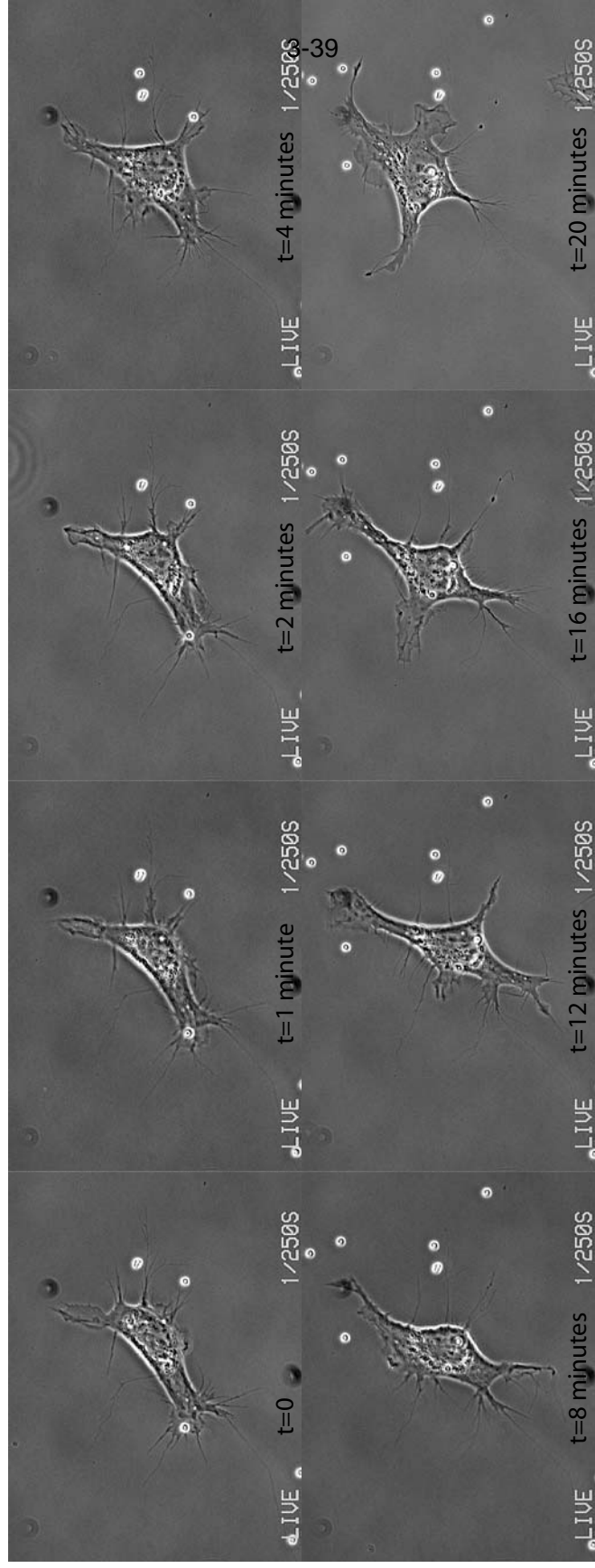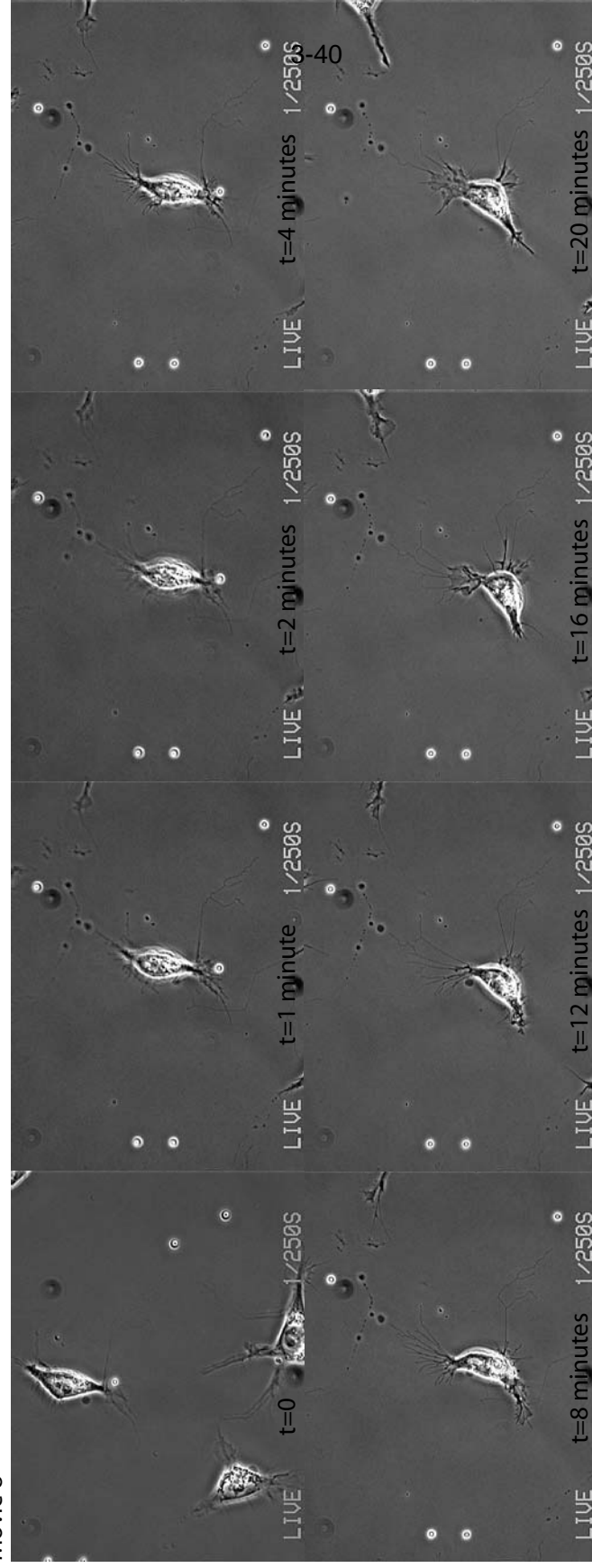ffecting cell fate. These data indicate a direct role for calcium signaling in the coordination of convergent extension cell movements.

Conclusions: The data presented here indicate that intercellular calcium signaling plays an important role in vertebrate convergent extension. We suggest that calcium waves may represent a widely used mechanism by which large groups of cells can coordinate complex cell movements.

Introduction

A wide variety of morphogenetic cell movements are required for normal development of vertebrate embryos. These include not only migrations of small populations of cells, such as germ cells, but also massive, coordinated rearrangements of entire tissues, such as folding of the neural plate to form a tube. Another example of such large-scale, coordinated cell movement is the process of convergent extension, in which cell intercalation elongates embryonic axes in both invertebrate and vertebrate embryos [1-7]. In some animals, this process is relatively simple; only about 40 cells intercalate in the ascidian notochord [4]. In contrast, convergent extension of the presumptive notochord of *Xenopus* embryos involves the intercalation of many hundreds of cells [8].

The process by which convergent extension occurs in the amphibian dorsal mesoderm has been very well described [8-15]. Intercalation is accomplished by a complicated suite of cellular behaviors, as individual cells polarize in the mediolateral axis, orient and stabilize lamellipodia, and exert traction on neighboring cells [10-12]. These behaviors propagate through the tissue from anterior to posterior as gastrulation proceeds [8, 11]. The need for reliable coordination of these cell behaviors suggests that several mechanisms must work in concert to control this process. For example, molecules which specify cell fates in the mesoderm, such as the transcription

factor brachyury, influence convergent extension [16]. In addition, convergent extension is also modulated by adhesion factors such as cadherins and protocadherins [17, 18]. Finally, signaling via Wnt pathways is also critical, as inhibition of Wnt, Frizzled, or Dishevelled activity suppresses convergent extension and cell intercalation [15, 19-24]

Since certain Wnt ligands and Frizzled receptors have been shown to signal through protein kinase C and elicit calcium release [25], it is possible that calcium signals may provide an additional level of regulation for convergent extension. Interestingly, intercellular calcium waves have been reported to occur in the marginal zone of gastrulating zebrafish embryos [26, 27]. Though the function of these waves remains to be elucidated, intercellular calcium waves allow rapid communication across large cell populations and have been shown to be involved in a wide variety of biological processes [28]. In this report, we describe intercellular waves of calcium mobilization which occur during the initiation of convergent extension in the dorsal marginal zone of *Xenopus*. Furthermore, using depletion of calcium from the endoplasmic reticulum, we show that calcium signaling is critical to the process of convergent extension, but is dispensable for dorsoventral cell fate specification in the mesoderm during gastrulation. These data indicate a direct role for calcium signaling in the control of convergent extension. We suggest that intercellular calcium waves represent a novel mechanism by which large groups of cells can coordinate complex morphogenetic movements during vertebrate development.

Results

Imaging of calcium dynamics in open-face explants of the dorsal mesoderm

To assess the role of calcium signaling in convergent extension we first examined calcium dynamics in the dorsal marginal zone of *Xenopus* embryos. We have previously used time-lapse confocal microscopy to examine cell behavior during *Xenopus* gastrulation over short periods of time (~15 minutes) [15]. However, photobleaching of fluorescent reagents and phototoxicity both limit prolonged imaging of living cells. To overcome these difficulties, we have developed a new confocal system where improved light harvesting allows long-term live imaging of cell behaviors.

To increase the efficiency of light collection from green emitting fluorophores, we used specially designed, high-Q dichroic mirrors and emission filters (Chroma Technology) which allow a very large fraction of the emission spectrum of calcium green to be collected (Fig. 4-1, A). We gained further benefit from the use of a high numerical aperture (0.75) Zeiss 20x Fluar objective. These improvements allow high-resolution images to be captured in a short time using very low excitation intensities, which is significant because photobleaching and phototoxicity increase disproportionately with excitation intensity.

Xenopus mesodermal cells involute into the embryo during gastrulation. Imaging of these internalized cells during convergent extension in intact

Figure 4-1: Imaging of calcium dynamics. **A.** Emission filters and dichroic mirrors used here were designed to reflect laser light efficiently at 488 nm, but transmit 90% of light at 505 nm, collecting a large fraction of the emission spectrum of calcium green. **B.** Experimental design for observation of calcium dynamics in the *Xenopus* DMZ. Embryos were injected with calcium green dextran at the 4-cell stage (1), and cultured to early gastrula stages. Open-face DMZ explants were then prepared (2) with deep cells apposed to coverglass (3). **C.** The confocal system used allows effective, long-term confocal time-lapse of living cells. Left panel shows a field of cells from a calcium green dextran-labeled DMZ explant after one 8-second scan; right panel shows the same field of cells after 254 additional 8-second scans over 85 minutes; mean fluorescent intensity was reduced by only 6%.

A

% Transmittance

100

50

500

Wavelength (nm)

— = Emission spectrum
     of calcium green

— = Transmission spectrum
     of emission filter

— = Transmission spectrum
     of dichroic mirror

B

1. Inject Calcium Green Dextran

2. Prepare "Keller" Explant

3. Observe Calcium Dynamics

Microscope

C

1 scan   255 scans
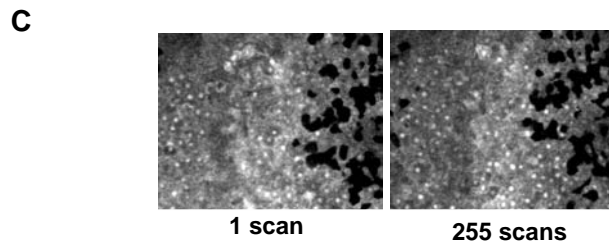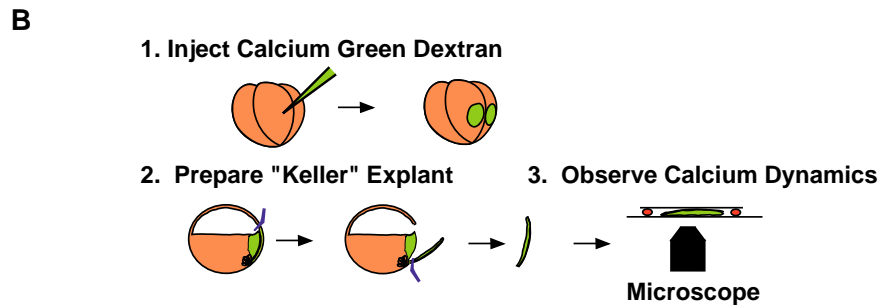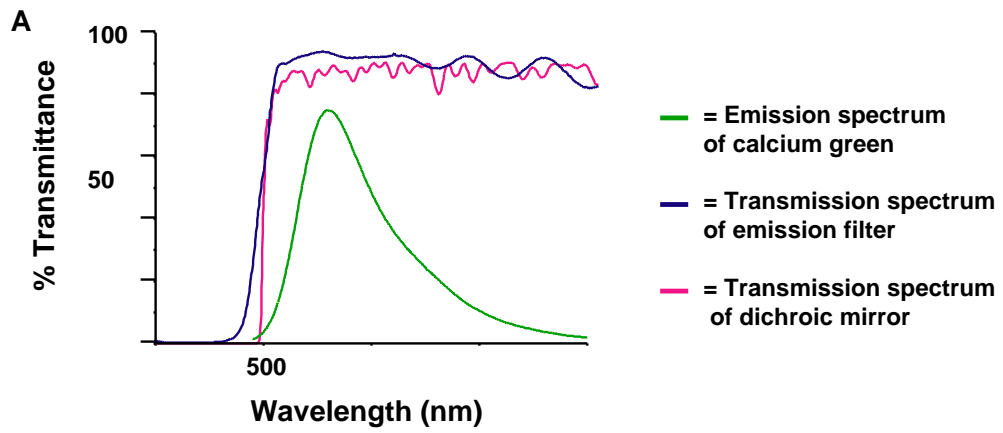
Xenopus gastrulae is not possible due to the opacity of the yolk contained in each cell. However, open-face "Keller" explants of the dorsal marginal zone (DMZ) of *Xenopus* gastrulae provide a well-defined system in which to examine the cell behaviors involved in convergent extension [8, 10-12, 15]   Briefly, the dorsal marginal zone of a *Xenopus* embryo is manually removed and cultured between coverslips separated by clay feet such that the deep cells which undergo convergent extension are directly apposed to the coverglass (Fig. 4-1, B). To examine calcium dynamics in the DMZ, presumptive dorsal cells of *Xenopus* embryos were loaded with calcium green dextran by microinjection at the 4-cell stage. At gastrula stages, open-face explants were prepared (Fig. 4-1, B) and time-lapse confocal microscopy produced high-resolution images with no significant attenuation of signal even after hundreds of scans (Fig. 4-1, C).

Intercellular calcium waves during convergent extension

Time-lapse microscopy of calcium green dextran-labeled deep cells during early gastrula stages revealed dramatic intercellular waves of calcium mobilization in the DMZ. Most striking was the occurrence of long-range waves (Fig. 4-2; MOVIES 1 & 2; available at http://bicsnap1.caltech.edu/jwetal/ jwetal.html) These large waves initiated in 2-4 adjacent cells and propagated 15-20 cell diameters from the initiation point at a rate of about 5 microns sec^{-1}. More common were smaller waves that also initiated in about 2-4 cells and

propagated radially 5-10 cell-diameters at a slower rate of approximately 2-3 micron sec^{-1} (MOVIES 3 & 4; Fig. 4-3). Waves appeared to arise stochastically

FIGURE 4-2 and Movies 1 & 2:

Long-range intercellular calcium waves in the dorsal marginal zone. **A)** Individual frames from confocal time-lapse of the large propagating calcium wave in MOVIE 1. Time points are indicated in white. Cell mixing produces a mosaic pattern of labeled (bright) and unlabeled (black) cells. A large calcium wave initiates (t= :00), travels approximately 20 cell diameters (t= 1:00), and subsides over approximately eight minutes (t= 8:00). Scale bar = 50 microns in this and all subsequent figures. **a')** Plot of DF/F$_0$ for each of the areas shown in the colored boxes in the last panel of A. Plot shows the propagatory nature of the rise in calcium levels and the more even recovery. **MOVIE 1)** This movie shows the patterns of calcium release in a DMZ explant labeled on the left side with calcium green dextran; the right side is unlabeled and is black, though cells are present in the field of view. In this and all DMZ movies, the dorsal lip of blastopore is at the bottom of the screen and the dorsal midline runs vertically through the middle of the screen; the mediolateral axis is horizontal. As the movie begins, several small flashes of calcium release can be observed throughout the explant (described below in Fig. 4-4, B). About halfway through the movie, a small intercellular calcium wave arises near the midline of the explant, followed closely by another, much larger calcium wave. Still frames depicting the large wave in this movie are presented above in Fig. 4-1, A. **MOVIE 2)** This movie shows a DMZ explant in which all the cells are labeled

with calcium green dextran. This explant undergoes a small wave, then a larger wave, then another small wave. These waves are less dramatic than those in MOVIE 1, possibly due to less effective calcium green dextran loading.

FIGURE 4-3 and MOVIES 3 & 4:

Short-range intercellular calcium waves in the DMZ. **A)** A small wave arises (t= :00) propagates approximately 10 cell diameters (t= 1:00), then dissipates over the following two minutes (t= 3:20). Scale bar = 50 microns   **a')** Plot of DF/F_0 for each of the areas shown in the colored boxes in the last panel of A. **MOVIE 3)** This movie shows the wave from Fig. 4-3, A. **B)** A small wave arises (t= :00), propagates approximately 10 cell diameters (t= 1:00), then dissipates over the following four minutes (t= 5:00). **MOVIE 4)** This movie shows the wave from Fig. 4-3, B. **b')** Plot of DF/F_0 for each of the areas shown in the colored boxes in the last panel of B. As with the larger waves, the plot shows a propagatory increase in calcium levels and a more even recovery.
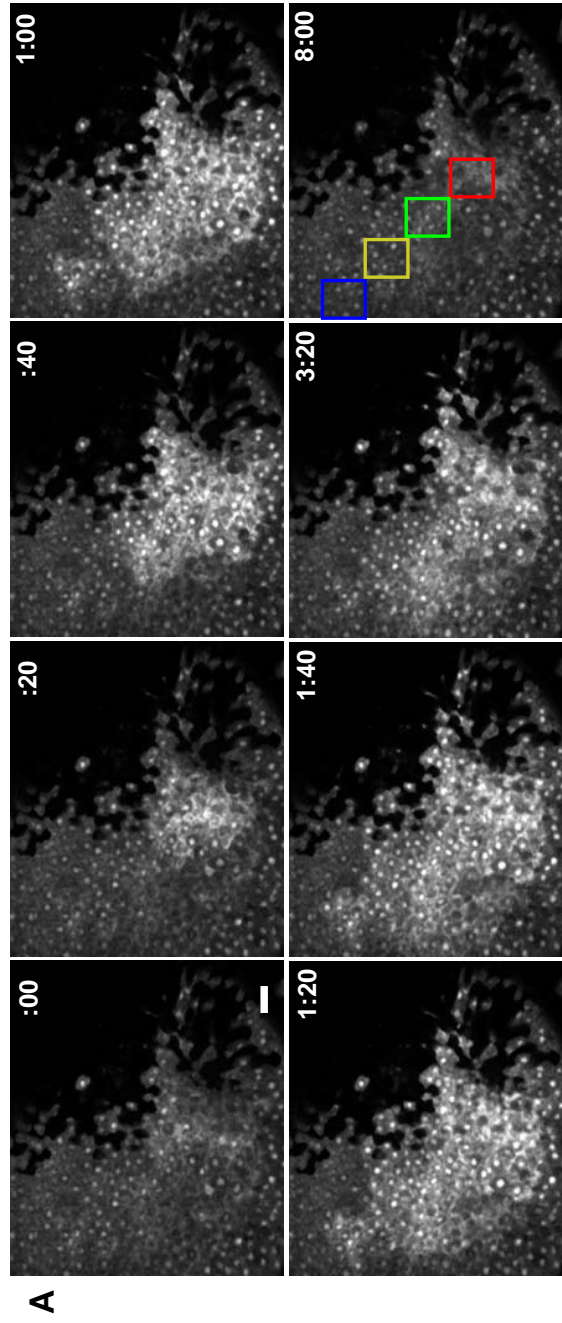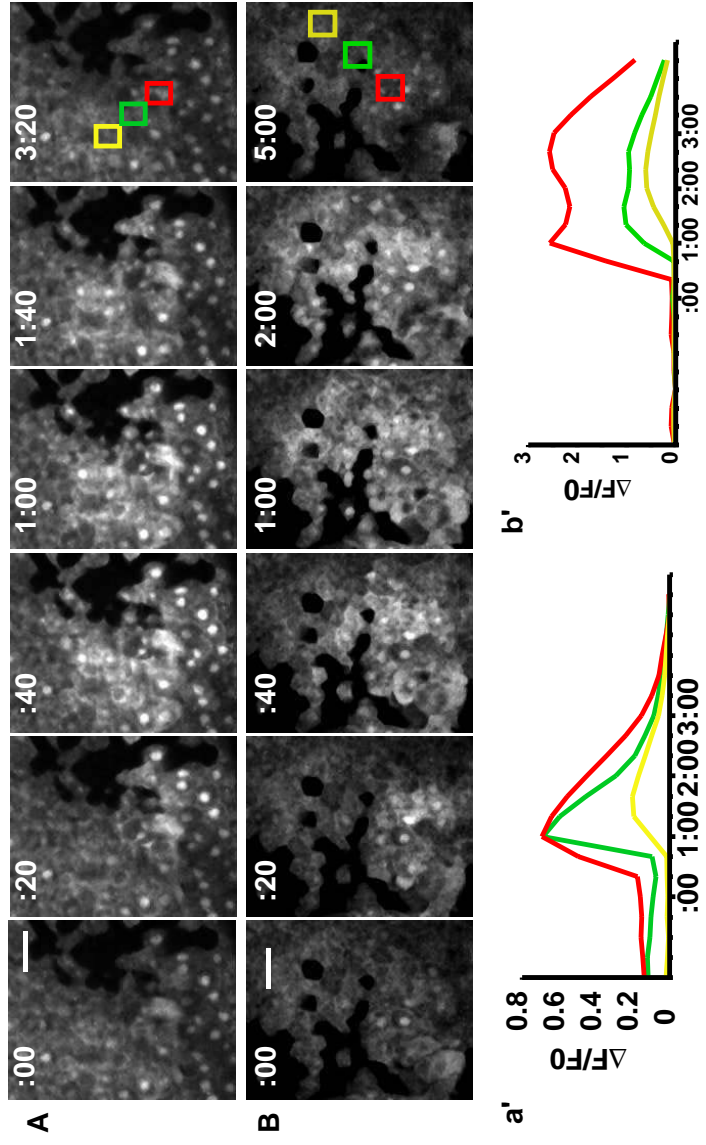
with respect to timing and location within the filmed DMZ explants. Most waves dissipated uniformly and simultaneously in all involved cells. Following wave propagation, calcium levels returned to baseline within a few minutes; in smaller waves, recovery was somewhat faster. Most calcium waves were accompanied by a wave of contraction within the tissue (Fig. 4-4, A; MOVIE 5).

The DMZ explant contains both dorsal mesoderm and posterior neural ectoderm, and both tissues undergo convergent extension [8, 10]. Most of the observed waves clearly arose in the mesoderm, near the dorsal lip of the blastopore; however, we also observed calcium waves in the neural ectoderm of DMZ explants (not shown), consistent with results obtained by imaging the externally visible neural plates of intact *Xenopus* embryos [29].

In addition to the intercellular waves, we also observed small flashes of calcium mobilization occurring simultaneously in a handful of adjacent cells in the DMZ (Fig. 4-4, B; MOVIE 6). These flashes initiated in 2-4 adjacent cells and occasionally spread to one or two additional adjacent cells, but no further. Such flashes were not accompanied by contraction. Flashes initiated stochastically in time and position, and were very short-lived, with calcium levels routinely increasing and recovering in less than 90 seconds (Fig. 4-4, B).

Calcium dynamics in DMZ explants were variable; 15 of 21 explants filmed displayed one or more waves, and 20 of 21 displayed calcium flashes. On average, calcium waves occurred in the dorsal marginal zone at a rate of 0.71/hour (Fig. 4-5; n=21). Calcium waves also varied in amplitude with some waves reaching DF/F_0 values of over 3 (Fig. 4-2, B and Fig 4-3, b'), while others

FIGURE 4-4 AND MOVIES 5 & 6:

Calcium waves and calcium flashes. **A)** High-magnification view of cells involved in the wave described in Fig. 4-2. During the four minutes preceding the wave, very little movement is observed (t= :00 - 4:00). The yellow outline at t= 4:40 indicates the position of two cells just prior to the calcium wave. The calcium wave propagates from left to right across the field of cells between t= 5:00 and t= 5:40. As the wave moves across and begins to dissipate, cells move dramatically (compare initial position to cells at t= 7:20). As the calcium levels recover, the cells move dramatically in the opposite direction beyond their original position (t= 8:00 - 12:00). Scale bar = 50 microns. **a')** Plot of DF/F_0 for each of the areas shown in the colored boxes in the last panel of A shows that local changes in calcium levels reflects the pattern of calcium release and recovery in the overall wave (compare with Fig 4-2, a'). **MOVIE 5)** This movie shows the cells in Fig. 4-4, A. **B)** High power view of cells involved in a calcium flash. Three cells dramatically increase calcium levels between t= :00 and t= :20. By t= 1:00 calcium levels are decreasing and return to baseline by t= 1:20. **b')** The plot of DF/F_0 for each of the areas shown in the colored boxes in the last panel show that the rise in calcium levels does not propagate to other cells in the frame. **MOVIE 6)** This movie shows the calcium flash in Fig. 4-4, B.
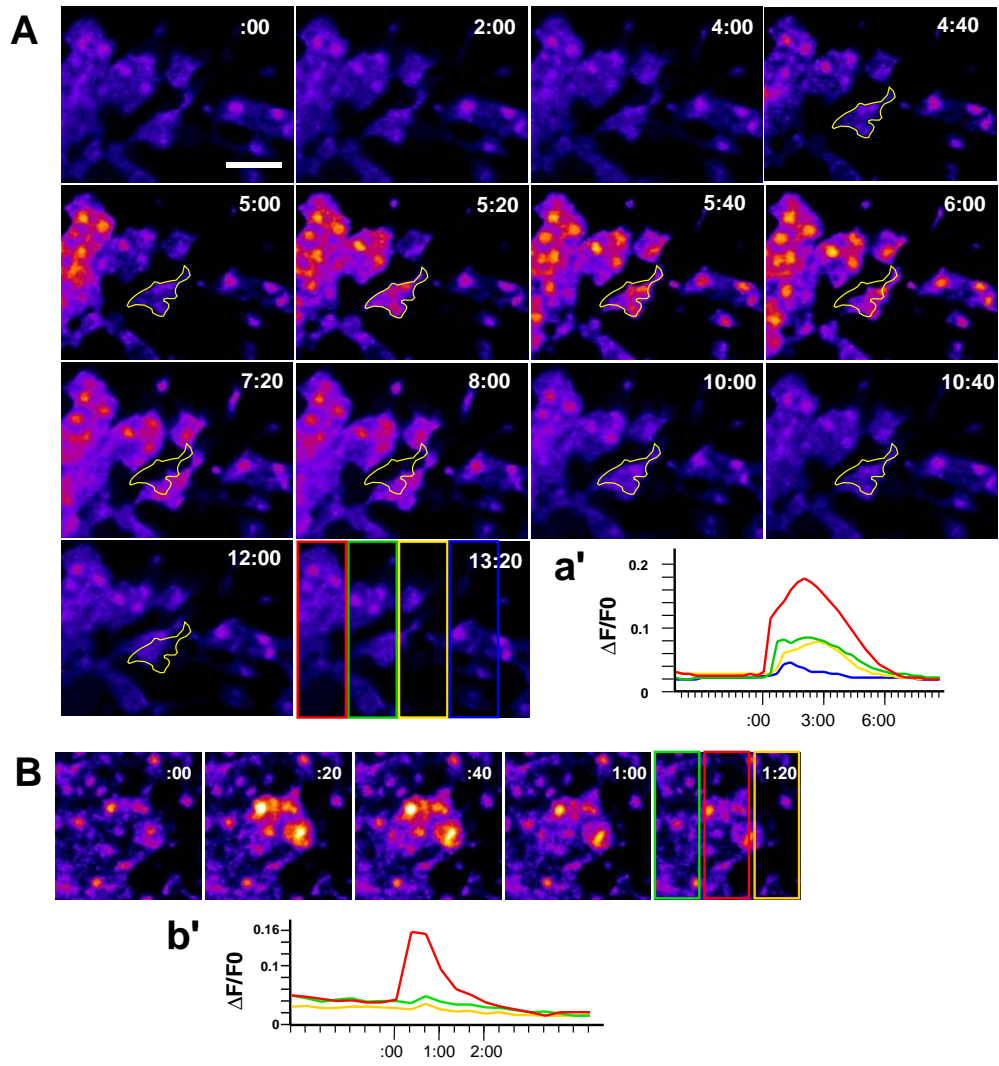
reach values of only about 1 (Fig 4-3, a'). Though also variable, local changes in calcium levels were of similar amplitude in both waves and flashes (Fig. 4-4, a', b'). It is important to note that variation in the intracellular concentration of calcium green may account for some variation in wave amplitude, due to leakage of the reagent from the injection wound.

We also performed time-lapse observations on explanted ventral marginal zone and explanted animal cap ectoderm. The ventral marginal zone undergoes only very weak convergent extension [13] and the animal cap undergoes epiboly, a very different morphogenetic process [30]. No intercellular calcium waves were observed in either tissue (Fig. 4-5; MOVIE 7). These data correlate propagating calcium waves with the robust convergent extension cell movements of the dorsal marginal zone.

In many systems, intercellular calcium waves arise in response to mechanical stimulation or wounding [28]. In contrast, calcium waves in the *Xenopus* DMZ arose spontaneously, and several lines of evidence demonstrate that the observed waves in the *Xenopus* DMZ did not arise as a result of the surgical manipulation of the tissue. Most importantly, no calcium waves were observed in explanted ventral marginal zones or animal caps (Fig. 4-5). Likewise, some DMZ explants displayed no calcium waves (Fig. 4-5). Furthermore, waves observed in DMZ explants did not initiate preferentially at the cut edges of the explant, but more frequently arose in the middle of the tissue (MOVIES 1 & 2). Finally, the occurrence of similar calcium waves in the marginal zone of intact, gastrulating zebrafish embryos [26] and in the neural

FIGURE 4-5 AND MOVIES 7 & 8:

Frequency of calcium waves. The graph plots waves/hour for different groups of explants; each point represents a single filmed explant. Calcium waves arise in DMZs at an average rate of 0.71/hour (see MOVIES 1-4). No calcium waves were observed in explanted animal caps (see MOVIE 7, described below) or in ventral marginal zones (VMZ). Calcium waves were not inhibited by expression of Nxfz-8, though the frequency was reduced. Treatment with thapsigargin abolished calcium wave activity (see MOVIE 8, described below). ** Indicates difference from wild-type is statistically significant to $p<0.05$ by the Mann-Whitney U test. **MOVIE 7)** This movie shows a representative time-lapse of an animal cap explant labeled with calcium green dextran. Small calcium flashes can be seen, but no calcium waves arise. **MOVIE 8)** This movie shows a representative DMZ treated with thapsigargin, no calcium waves are observed.
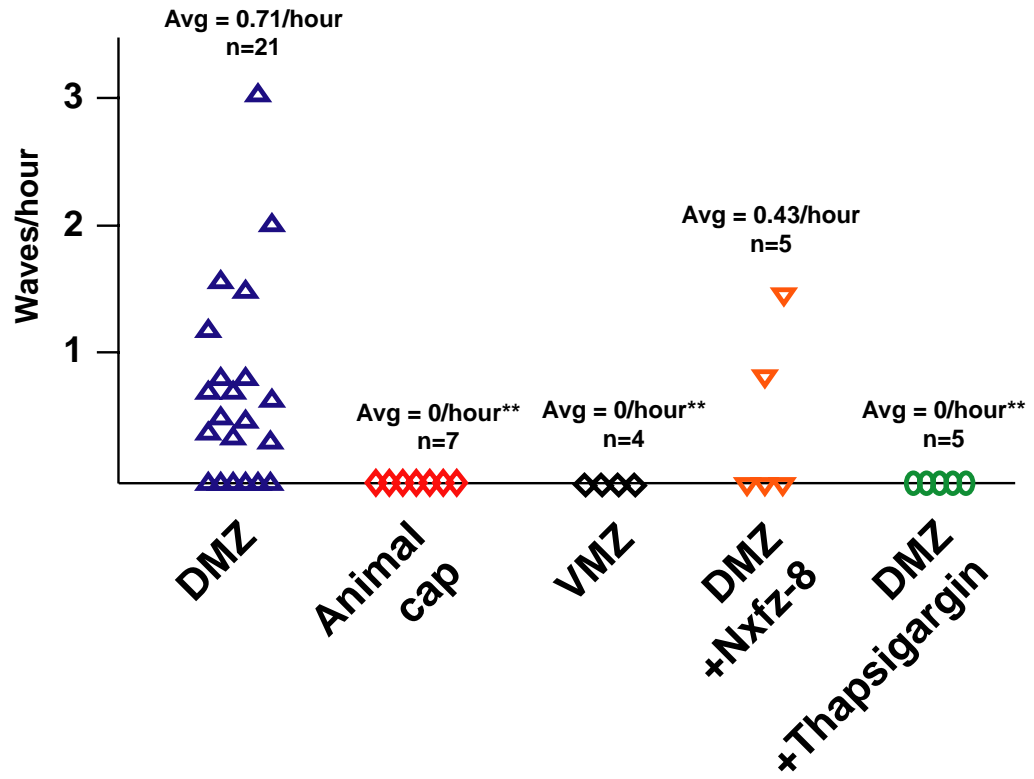
plates of intact *Xenopus* embryos [29] argues that these waves are part of normal development.

Calcium waves in the DMZ do not require Frizzled signaling

Non-canonical Wnt signals play a critical role in coordinating convergent extension. One non-canonical pathway signals via PKC to elicit calcium release [25, 31], raising the possibility that the observed calcium waves may require Wnt signals. To examine this possibility, we observed calcium dynamics in explants where Wnt signaling was compromised by expression of mutant Frizzled-8. An N-terminal fragment of *Xenopus* Frizzled-8 (Nxfz-8) inhibits both canonical and non-canonical Wnt signals and strongly suppresses convergent extension [20, 24]. Co-injection of 1 ng of Nxfz-8 mRNA did not inhibit calcium wave initiation or propagation, though the frequency was slightly diminished (Fig. 4-5).

Calcium waves in the DMZ require calcium from intracellular stores

Intercellular calcium waves in other systems often mobilize calcium from intracellular stores [28]. To determine the source of the released calcium in intercellular waves in the *Xenopus* DMZ, we treated DMZ explants with thapsigargin. Thapsigargin is a cell-permeable inhibitor of the calcium ATPase of the endoplasmic reticulum (ER) and effectively prevents regulated calcium release from internal stores [32-34]. Treatment of DMZ explants with 2 micromolar thapsigargin completely abolished the intercellular calcium waves

(Fig. 4-5, MOVIE 8) and dramatically suppressed calcium flashes (MOVIE 8), indicating that internal stores of calcium are required for these events.

Calcium release from intracellular stores is required during gastrulation for convergent extension, but not for cell-fate specification in the dorsal mesoderm

In the time-lapse observations of explants treated with thapsigargin (MOVIE 8), individual cells can be seen moving, demonstrating that thapsigargin did not completely suppress cell motility. Because thapsigargin effectively inhibited intercellular calcium dynamics (Fig. 4-5, MOVIE 8), it provides an effective tool with which to examine the possibility that calcium signaling plays a role in the coordination of convergent extension.

Convergent extension is a driving force in the closure of the blastopore during gastrulation [8, 11], and embryos exposed to thapsigargin during gastrulation fail to close their blastopores by stage 12 (Fig. 4-6). By this stage, control embryos displayed long, narrow notochords visible by *in situ* hybridization to the notochord-specific probe Xnot [35, 36] (Fig. 4-6, A, C). In embryos treated with thapsigargin, convergent extension was severely suppressed, and notochords remained short and broad (Fig. 4-6, B, G). In a few embryos, weaker suppression was observed (Fig. 4-6, B, far right). Treatment with thapsigargin did not change the total area of the Xnot expression domain (<3% difference), indicating that cell fate specification in the notochord was not inhibited.

FIGURE 4-6:

Thapsigargin treatment inhibits convergent extension but does not affect mesodermal cell fate. **A)** Control embryos at stage 12 have almost finished blastopore closure (dorsal view is shown, anterior at top). Xnot staining reveals long, narrow notochords. **B)** Embryos treated with thapsigargin fail to close their blastopores by stage 12. Xnot staining indicates that notochords have failed to converge and extend. In a few cases (far right embryo), some convergent extension occurs and the anterior notochord elongates, though the posterior notochord remains broad. **C)** Control embryos stained for Xnot. **D)** Embryos treated with BHQ fail to close their blastopores and notochords do not converge and extend, though Xnot is expressed strongly. **E)** Control embryos hybridized to MyoD; somites are elongated along each side of the notochord. **F)** Thapsigargin treated embryos express MyoD at normal levels, though somites fail to converge and elongate; MyoD expression domains remain short and broad. **G)** Quantitation of convergent extension by measurement of the length-to-width ratio (mean +/- standard error) of Xnot expression domains in control and thapsigargin-treated embryos. Total area of the Xnot expression domains differed by less than 3% between control and experimental embryos **H)** Length-to-width ratios of Xnot expression domains in control and BHQ-treated embryos. Slight differences in stages account for differences in control LWRs in THAP and BHQ experiments (see panels A and C, above)
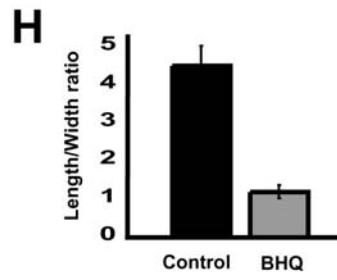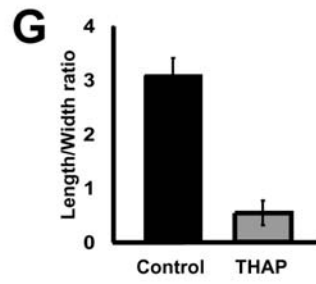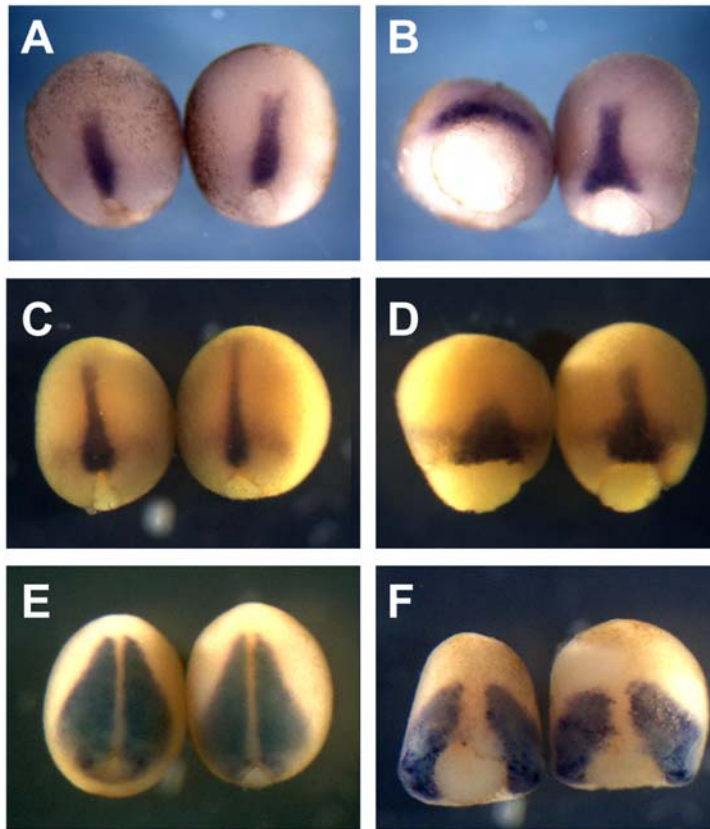
A different pharmacological inhibitor of the ER calcium ATPase, 2,5-di-(t-butyl)-1,4-benzohydroquinione (BHQ) [34], also suppressed convergent extension of the presumptive notochord without inhibiting expression of Xnot (Fig. 4-6, D, H). This result demonstrates that inhibition of convergent extension was not specific to thapsigargin, but is a common effect of depletion of calcium stores.

Convergent extension is most pronounced in the notochord, but also occurs in ventrolateral mesoderm such as somites [13], and identical cell behaviors are associated with convergent extension in both tissues [12]. At late gastrula stages, *in situ* hybridization to the muscle-specific marker MyoD confirmed that elongated arrays of somites flanked the notochord (Fig. 4-6, E). In thapsigargin-treated embryos, the somites remained short and broad, due to failure of convergent extension, though MyoD was expressed normally (Fig. 4-6, F).

We next examined the effects of thapsigargin on DMZ explants, which elongate *in vitro* as a result of convergent extension, accurately mimicking their morphogenetic behavior in intact embryos. These explants allow convergent extension to be assessed independently of other morphogenetic movements occurring in the embryo [8, 15]. In contrast to the dramatic elongation of control explants (Fig. 4-7 A, D), thapsigargin treated explants were strongly inhibited in elongation (Fig. 4-7, B, D). The shape of thapsigargin treated explants was variable, with some extending subtly; however, the difference in the mean

Figure 4-7:

Thapsigargin inhibits convergent extension of DMZ explants without affecting gene expression. **A)** Untreated control DMZ explants (n= 31) elongate significantly and change shape as a result of convergent extension, forming a rounded head and an elongate tail. **B)** DMZ explants treated with thapsigargin (2 mM) fail to elongate, though subtle narrowing of the mesoderm is sometimes observed (n= 33). This variability is consistent with that of treated whole embryos. **C)** BHQ treatment (10 mM) suppresses convergent extension (n=18). **D)** Quantitation of convergent extension of DMZ explants (mean LWR +/- standard error). **E)** RT-PCR demonstrates that thapsigargin treatment does not affect dorsovental patterning of the mesoderm in DMZ explants cultured to stage 22. **F)** Thapsigargin does not affect dorsal cell fate specification in DMZ explants cultured to stage 12. (THAP = 10 thapsigargin-treated DMZs; CTL= 10 untreated DMZ explants; -RT = no reverse transcriptase control).   EF1a and actin serve as loading controls.

A

B

C

D

Length/width ratio of
DMZ explants at st .22

5
4
3
2
1
0

Control   THAP   BHQ

E

THAP   CTL   -RT

Xnot

MyoD

Xwnt-8

Xvex

Edd

NCAM

EF1α

Actin

F

THAP   CTL   -RT

Xnot

Chordin

EF1α
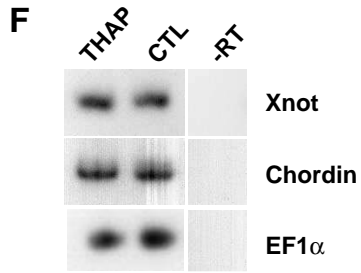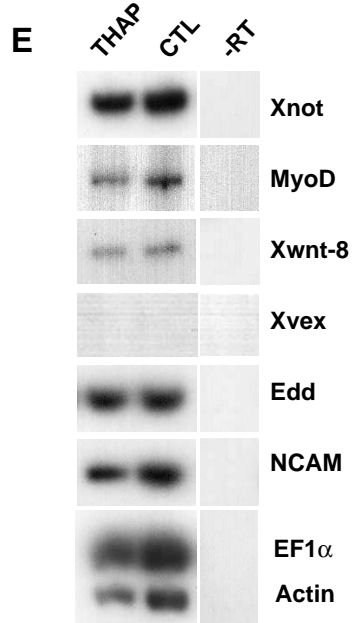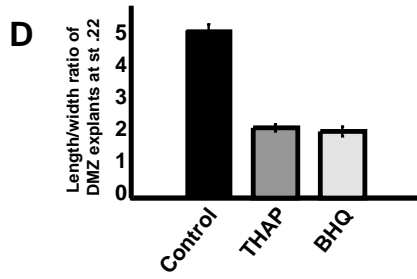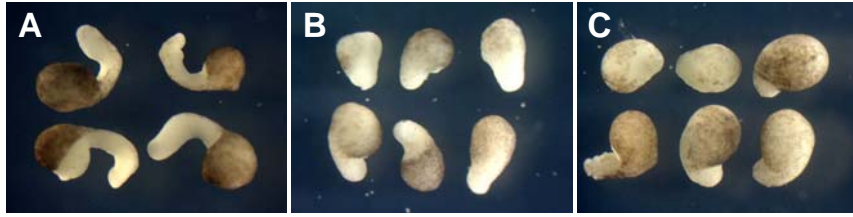
elongation of the two groups was highly significant (Fig. 4-7 D). BHQ also suppressed convergent extension in DMZ explants (Fig. 7, C, D).

Dorsoventral patterning of the mesoderm influences convergent extension [13], and calcium signaling has been implicated in the specification of cell fates in the *Xenopus* mesoderm prior to the onset of gastrulation [37-39]. As such, it is possible that thapsigargin treatment during gastrulation affected convergent extension indirectly by modulating cell fates in the DMZ. The strong expression of both Xnot and MyoD in thapsigargin- and BHQ-treated embryos (Fig. 4-6) argues against this possibility. RT-PCR analysis also demonstrated that thapsigargin treatment during gastrula stages did not alter cell fates in DMZ explants.

Treated DMZs cultured to tailbud stages expressed normal levels of the dorsal mesoderm marker Xnot, as well as the ventrolateral mesoderm markers, MyoD and Xwnt-8 (Fig. 4-7, E). Likewise, neither treated nor untreated explants expressed the ventral mesoderm marker Xvex (Fig. 4-7, E). Thapsigargin-treated DMZ explants cultured only to the late gastrula stages expressed normal levels of both Xnot and the dorsal mesoderm marker chordin (Fig. 4-7, F), demonstrating that thapsigargin did not transiently ventralize DMZs. Finally, the failure of convergent extension did not result from conversion of mesoderm to endoderm or neural ectoderm, as no increase in expression of NCAM or endodermin (Edd) was observed following thapsigargin treatment (Fig. 4-7, E). Together, these data strongly indicate that suppression of convergent extension following depletion of ER calcium stores is not

secondary to changes in mesodermal cell fate but is instead due to a direct effect on coordinated morphogenetic cell movements.

Discussion

Using an improved confocal system (Fig. 4-1), we have described intercellular calcium waves which occur during convergent extension in explants of the *Xenopus* dorsal marginal zone (Figs. 4-2, 4-3, 4-4). Calcium waves are correlated with convergent extension movements, and waves were not observed in explanted animal cap ectoderm or ventral marginal zone mesoderm (Fig. 4-5). These waves did not strictly require Frizzled signaling, indicating that they may function in parallel to Wnt signals in the control of morphogenesis.

Previous studies have implicated calcium signaling in the specification of ventral cell fates prior to gastrulation [37-39]. In this study we have used cell-permeable inhibitors of calcium release from the ER to examine the role of calcium signaling during gastrula stages. Inhibition of calcium dynamics with either thapsigargin (Fig. 4-5) or BHQ inhibited convergent extension but did not affect cell fate (Fig. 4-6, 4-7). Together, these data indicate an important role for calcium signaling in the control of convergent extension.

Variability of calcium events

The variability in frequency, extent, and amplitude of calcium dynamics in the *Xenopus* DMZ (Figs. 4-2, 4-3, 4-5) is notable, especially in light of the

variable effects of thapsigargin and BHQ on convergent extension (Figs. 4-6, 4-7). It is possible that this variability was due to a failure to capture episodic calcium events consistently or was a result of experimental manipulation. On the other hand, as calcium is but one of several potential regulators of convergent extension, the variability may indicate that this mechanism is not used to the same degree in each embryo. Intercellular calcium signaling may represent a tuning mechanism to ensure that convergent extension is reliably carried out in every embryo.

Mechanism of calcium wave propagation

The calcium waves in the DMZ use calcium from intracellular stores (Fig. 4-5), but the mechanism by which these waves propagate remains unclear. In other systems, the stimulus for calcium release from intracellular stores is propagated from cell to cell by a variety of mechanisms [28]. Some calcium waves propagate by release of ATP into the extracellular space, thereby activating purinergic receptors on neighboring cells, resulting in calcium release [40]. Other waves propagate by movement of IP_3 through gap junctions, which in turn stimulates calcium release in adjacent cells [41]. Interestingly, extracellularly-transduced calcium waves can propagate at rates comparable to those which propagate through gap junctions [42]. Previous examinations of the effects of gap-junction blocking agents on *Xenopus* development have not revealed specific defects in convergent extension [43, 44], which may suggest an extracellular route of propagation for the waves

observed in *Xenopus* embryos. On the other hand, many reagents commonly used to antagonize gap-junctional communication fail to eliminate gap-junction dependent intercellular calcium waves [45]. Finally, the observation of calcium waves in explants expressing Nxfz-8 argues that the initiation and propagation of these waves does not strictly require Frizzled signaling. It is important to note, however, that this does not preclude the possibility that the Wnt/Ca^{++} pathway functions to regulate convergent extension. Examinations of cell behaviors in embryos disrupted for Wnt/Ca^{++} function and in embryos treated with thapsigargin should shed light on this issue.

Calcium waves are a common feature of vertebrate convergent extension

Intercellular calcium waves have now been observed in the marginal zone of the zebrafish embryo [26], in the *Xenopus* neural plate [29], and in the *Xenopus* dorsal marginal zone (this report). All three of these tissues undergo convergent extension movements [6, 13] which involve grossly similar cell behaviors [12, 46, 47], and the velocity of calcium waves seen in each of these tissues is also roughly similar. Together, these findings suggest that calcium waves are a common characteristic of vertebrate convergent extension. Likewise, similar molecular mechanisms are involved in the control of convergent extension cell movements in all three of these tissues. For example, non-canonical Wnt signaling has been shown to be required for convergent extension of each of these tissues [14, 15, 23, 48, 49]. We have recently shown that non-canonical Wnt signals control the stability and polarity

of lamellipodia which drive convergent extension in *Xenopus* mesoderm [15]. It is tempting to speculate that calcium signaling may serve as an additional input into the machinery which coordinates cell polarity during convergent extension. In light of the role which intracellular calcium signals play in guiding migrations of single cells [50-52], we suggest that intercellular calcium waves may likewise provide a mechanism by which large groups of cells can coordinate complex morphogenetic movements during embryogenesis.

Materials and Methods

Embryos and microinjection: Female adult *Xenopus laevis* were ovulated by injection of human chorionic gonadotropin; eggs were fertilized *in vitro*, dejellied in 3% cysteine (pH 7.9) and subsequently reared in 1/3x MMR [53]. For microinjections, embryos were placed in a solution of 2.5% ficoll in 1/3x MMR, injected as described, and reared in ficoll + 1/3xMMR [53]. Calcium green dextran (10kD; Molecular Probes) was resuspended to 10mg/ml in sterile water and 5-10 nl was injected.

Imaging of calcium dynamics: For DMZ imaging, embryos were injected dorsally at the 4-cell stage and reared to gastrula stages as described above. At stage 10.25, 60-80° dorsal marginal zone explants were cut, centered on the midline of the dorsal blastopore lip. Eyebrow knives and forceps were used for dissections. Care was taken to remove involuted mesoderm, head

mesoderm, and endoderm. Explants were then placed with deep cells facing down in a culture chamber with a bottom made of coverglass for imaging with the inverted Zeiss 410 confocal modified as described in the text. A small fragment of coverglass supported by silicon grease or clay was used to hold the explant in place and prevent curling. For animal cap imaging, embryos were injected into the animal pole of 1-cell embryos and cultured until stage 9 in 1/3x MMR. Animal caps were removed using forceps at stage 9 and imaged as above. For VMZ imaging, embryos were injected ventrally at the 4-cell stage and reared to gastrula stage as described above. At stage 10.5, 60-80° ventral marginal zone explants were removed and imaged as DMZs, above. All explants were cut and reared in 1x Steinberg's solution [53]. All explants were imaged using eight-second scans every 20 seconds. Images were processed and DF/F_0 measured using NIH Image 1.62/fat.

Nxfz-8 expression: mRNA was prepared *in vitro* as described [53], mixed with calcium green dextran, and injected as above. Embryos from each injected batch were reared to tailbud stages to assess phenotypes and confirm that Nxfz-8 mRNA was functional.

Thapsigargin and BHQ treatments: Thapsigargin (Sigma) and BHQ (CalBiochem) were resuspended as 1000X stocks (2mM and 10mM, respectively) in ethanol and stored at -20° C. These doses were chosen

because both have been used effectively to inhibit calcium-regulated guidance of axons in culture [52].

For DMZ imaging, explants were cut as above and then transferred to a culture chamber containing 2 micromolar thapsigargin in 1x Steinberg's. Explants were cultured for approximately ten minutes before coverslipping to allow penetration of the thapsigargin, during which time explants were manually prevented from curling. Explants were then coverslipped in the same culture chamber allowing chronic exposure to thapsigargin under the coverslip during imaging.

For embryo treatments, vitelline envelopes were removed at stage 10+ and embryos were cultured in agarose wells in 2 micromolar thapsigargin or 10 micromolar BHQ in 1/3x MMR until stage 12, fixed in MEMFA, and processed for *in situ* hybridization [53]. Convergent extension of the Xnot expression domain was quantitated by measuring the length along the dorsal midline and the width along the blastopore lip.

For assessment of convergent extension, DMZ explants were prepared as above, but without coverslips. They were cultured in agarose wells in 1x Steinberg's plus 2mM thapsigargin until stage 12, then rinsed and cultured in 1x Steinberg's alone or cultured continuously in 10 micromolar BHQ until scoring. At control stage 22, convergent extension was quantitated in DMZ explants by measuring the length of the longest aspect and width at the collar point where the mesoderm extends from the neural ectoderm. Measurements

were performed using NIH Image 1.62/fat. RT-PCR was performed as described [53].

References:

1.   Vogt W: **Gestaltungsanalyse am amphibienkeim mit örtlicher vitalfärbung. II. Teil. Gastrulation und mesodermbildung bei urodelen und anuran.** *Wilhelm Roux Arch. EntwMech. Org.* 1929, **120**:384-706.
2.   Irvine KD, Wieschaus E: **Cell intercalation during Drosophila germband extension and its regulation by pair-rule segmentation genes**. *Development* 1994, **120**:827-841.
3.   Hardin J: **The cellular basis of sea urchin gastrulation**. *Curr Top Dev Biol* 1996, **33**:159-262.
4.   Miyamoto DM, Crowther RJ: **Formation of the notocord in the living ascidian**. *J. Embryol. Exp. Morph.* 1985, **86**:1-17.
5.   Trinkaus JP, Trinkaus M, Fink RD: **On the convergent cell movements of gastrulation in Fundulus**. *J Exp Zool* 1992, **261**:40-61.
6.   Warga RM, Kimmel CB: **Cell movements during epiboly and gastrulation in zebrafish**. *Development* 1990, **108**:569-580.
7.   Keller RE: **Vital dye mapping of the gastrula and neurula of Xenopus laevis. II. Prospective areas and morphogenetic movements of the deep layer**. *Dev Biol* 1976, **51**:118-137.
8.   Keller R, Shih J, Domingo C: **The patterning and functioning of protrusive activity during convergence and extension of the Xenopus organiser**. *Dev Suppl* 1992:81-91.
9.   Holtfreter J: **A study of the mechanics of gastrulation, Part II**. *J. Exp. Zool.* 1944, **95**:171-212.
10.   Keller R, Davidson L, Edlund A, Elul T, Ezin M, Shook D, Skoglund P: **Mechanisms of convergence and extension by cell intercalation**. *Philos Trans R Soc Lond B Biol Sci* 2000, **355**:897-922.

11.   Shih J, Keller R: **Patterns of cell motility in the organizer and dorsal mesoderm of Xenopus laevis**. *Development* 1992, **116**:915-930.

12.   Shih J, Keller R: **Cell motility driving mediolateral intercalation in explants of Xenopus laevis**. *Development* 1992, **116**:901-914.

13.   Keller R, Danilchik M: **Regional expression, pattern and timing of convergence and extension during gastrulation of Xenopus laevis**. *Development* 1988, **103**:193-209.

14.   McEwen DG, Peifer M: **Wnt signaling: Moving in a new direction**. *Curr Biol* 2000, **10**:R562-564.

15.   Wallingford JB, Rowning BA, Vogeli KM, Rothbächer U, Fraser SE, Harland RM: **Dishevelled controls cell polarity during *Xenopus* gastrulation**. *Nature* 2000, **405**:81-85.

16.   Conlon FL, Smith JC: **Interference with Brachyury Function Inhibits Convergent Extension, Causes Apoptosis, and Reveals Separate Requirements in the FGF and Activin Signalling Pathways**. *Dev Biol* 1999, **213**:85-100.

17.   Lee CH, Gumbiner BM: **Disruption of gastrulation movements in Xenopus by a dominant-negative mutant for C-cadherin**. *Dev Biol* 1995, **171**:363-373.

18.   Kim SH, Yamamoto A, Bouwmeester T, Agius E, Robertis EM: **The role of paraxial protocadherin in selective adhesion and cell movements of the mesoderm during Xenopus gastrulation**. *Development* 1998, **125**:4681-4690.

19.   Djiane A, Riou J, Umbhauer M, Boucaut J, Shi D: **Role of frizzled 7 in the regulation of convergent extension movements during gastrulation in Xenopus laevis**. *Development* 2000, **127**:3091-3100.

20.   Deardorff MA, Tan C, Conrad LJ, Klein PS: **Frizzled-8 is expressed in the Spemann organizer and plays a role in early morphogenesis**. *Development* 1998, **125**:2687-2700.

21.   Sokol SY: **Analysis of Dishevelled signalling pathways during Xenopus development**. *Curr Biol* 1996, **6**:1456-1467.

22.   Moon RT, Campbell RM, Christian JL, McGrew LL, Shih J, Fraser S: **Xwnt-5A: a maternal Wnt that affects morphogenetic movements after overexpression in embryos of Xenopus laevis**. *Development* 1993, **119**:97-111.

23.   Tada M, Smith JC: **Xwnt11 is a target of Xenopus Brachyury: regulation of gastrulation movements via dishevelled, but not through the canonical Wnt pathway**. *Development* 2000, **127**:2227-2238.

24.   Wallingford JB, Vogeli KM, Harland RM: **Regulation of convergent extension in Xenopus by Wnt5a and Frizzled-8 is independent of the canonical Wnt pathway**. *Int. J. Dev. Biol.* 2001, **45**:225-227.

25.   Kuhl M, Sheldahl LC, Park M, Miller JR, Moon RT: **The Wnt/Ca2+ pathway: a new vertebrate Wnt signaling pathway takes shape**. *Trends Genet* 2000, **16**:279-283.

26.   Gilland E, Miller AL, Karplus E, Baker R, Webb SE: **Imaging of multicellular large-scale rhythmic calcium waves during zebrafish gastrulation**. *Proc Natl Acad Sci U S A* 1999, **96**:157-161.

27.   Creton R, Speksnijder JE, Jaffe LF: **Patterns of free calcium in zebrafish embryos**. *J Cell Sci* 1998, **111**:1613-1622.

28.   Sanderson MJ, Charles AC, Boitano S, Dirksen ER: **Mechanisms and function of intercellular calcium signaling**. *Mol Cell Endocrinol* 1994, **98**:173-187.

29.   Leclerc C, Webb SE, Daguzan C, Moreau M, Miller AL: **Imaging patterns of calcium transients during neural induction in Xenopus laevis embryos**. *J Cell Sci* 2000, **113**:3519-3529.

30.   Keller RE: **The cellular basis of epiboly: an SEM study of deep-cell rearrangement during gastrulation in Xenopus laevis**. *J Embryol Exp Morphol* 1980, **60**:201-234.

31.   Slusarski DC, Corces VG, Moon RT: **Interaction of Wnt and a Frizzled homologue triggers G-protein-linked phosphatidylinositol signalling**. *Nature* 1997, **390**:410-413.

32.   Treiman M, Caspersen C, Christensen SB: **A tool coming of age: thapsigargin as an inhibitor of sarco-endoplasmic reticulum Ca(2+)-ATPases**. *Trends Pharmacol Sci* 1998, **19**:131-135.

33.   Thastrup O, Cullen PJ, Drobak BK, Hanley MR, Dawson AP: **Thapsigargin, a tumor promoter, discharges intracellular Ca2+ stores by specific inhibition of the endoplasmic reticulum Ca2(+)-ATPase**. *Proc Natl Acad Sci U S A* 1990, **87**:2466-2470.

34.   Wictome M, Michelangeli F, Lee AG, East JM: **The inhibitors thapsigargin and 2,5-di(tert-butyl)-1,4-benzohydroquinone favour the E2 form of the Ca2+,Mg(2+)-ATPase**. *FEBS Lett* 1992, **304**:109-113.

35.   von Dassow G, Schmidt JE, Kimelman D: **Induction of the Xenopus organizer: expression and regulation of Xnot, a novel FGF and activin-regulated homeo box gene**. *Genes Dev* 1993, **7**:355-366.

36.   Gont LK, Fainsod A, Kim SH, De Robertis EM: **Overexpression of the homeobox gene Xnot-2 leads to notochord formation in Xenopus**. *Dev Biol* 1996, **174**:174-178.

37.   Kume S, Muto A, Inoue T, Suga K, Okano H, Mikoshiba K: **Role of inositol 1,4,5-trisphosphate receptor in ventral signaling in Xenopus embryos**. *Science* 1997, **278**:1940-1943.

38.   Kuhl M, Sheldahl LC, Malbon CC, Moon RT: **Ca(2+)/calmodulin-dependent protein kinase II is stimulated by Wnt and Frizzled homologs and promotes ventral cell fates in Xenopus**. *J Biol Chem* 2000, **275**:12701-12711.

39.   Kume S, Inoue T, Mikoshiba K: **G-alpha-s family G proteins activate IP(3)-Ca(2+) signaling via g-beta-gamma and transduce ventralizing signals in Xenopus**. *Dev Biol* 2000, **226**:88-103.

40.   Osipchuk Y, Cahalan M: **Cell-to-cell spread of calcium signals mediated by ATP receptors in mast cells**. *Nature* 1992, **359**:241-244.

41.   Boitano S, Dirksen ER, Sanderson MJ: **Intercellular propagation of calcium waves mediated by inositol trisphosphate**. *Science* 1992, **258**:292-295.

42.   Jorgensen NR, Geist ST, Civitelli R, Steinberg TH: **ATP- and gap junction-dependent intercellular calcium signaling in osteoblastic cells**. *J Cell Biol* 1997, **139**:497-506.

43.   Paul DL, Yu K, Bruzzone R, Gimlich RL, Goodenough DA: **Expression of a dominant negative inhibitor of intercellular communication in the early Xenopus embryo causes delamination and extrusion of cells**. *Development* 1995, **121**:371-381.

44.   Levin M, Mercola M: **Gap junctions are involved in the early generation of left-right asymmetry**. *Dev Biol* 1998, **203**:90-105.

45.   Boitano S, Evans WH: **Connexin mimetic peptides reversibly inhibit Ca(2+) signaling through gap junctions in airway cells**. *Am J Physiol Lung Cell Mol Physiol* 2000, **279**:L623-630.

46.   Keller R, Shih J, Sater A: **The cellular basis of the convergence and extension of the Xenopus neural plate**. *Dev Dyn* 1992, **193**:199-217.

47.   Concha ML, Adams RJ: **Oriented cell divisions and cellular morphogenesis in the zebrafish gastrula and neurula: a time-lapse analysis**. *Development* 1998, **125**:983-994.

48.   Heisenberg C-P, Tada M, Rauch G-J, Saude L, Concha ML, Geisler R, Stemple DL, Smith JC, Wilson SW: **Silberblick/Wnt11 activity mediates convergent extension movements during zebrafish gastrulation**. *Nature* 2000, **405**:76-81.

49.   Wallingford JB, Harland RM: **Xenopus dishevelled signaling regulates both neural and mesodermal convergent extension: balanced forces elongating the body axis**. Submitted.

50.   Brundage RA, Fogarty KE, Tuft RA, Fay FS: **Calcium gradients underlying polarization and chemotaxis of eosinophils**. *Science* 1991, **254**:703-706.

51.   Zheng JQ: **Turning of nerve growth cones induced by localized increases in intracellular calcium ions**. *Nature* 2000, **403**:89-93.

52.   Hong K, Nishiyama M, Henley J, Tessier-Lavigne M, Poo M: **Calcium signalling in the guidance of nerve growth by netrin-1**. *Nature* 2000, **403**:93-98.

53.   Sive HL, Grainger RM, Harland RM: *Early Development of Xenopus laevis: A Laboratory Manual*. Cold Spring Harbor, N.Y.: Cold Spring Harbor Press; 2000.

Surface Imaging Microscopy, An Automated Method for Visualizing Whole Embryo Samples in Three Dimensions at High Resolution

Andrew Ewald*, Helen McBride*, Mark Reddington#^, Scott E. Fraser* and Russell Kerschmann#

* Biological Imaging Center and Division of Biology,
Caltech, Mail Code 139-74, Pasadena, CA, 91125
\# Resolution Sciences Corporation,
505 Tamal Plaza, Corte Madera, CA 94925
^ Present address: Biosearch Technologies, Inc.
81 Digital Drive, Novato, CA 94949

Summary

Modern biology is faced with the challenge of understanding the specification, generation, and maintenance of structures ranging from cells and tissues to organs and organisms. By acquiring images directly from the block face of an embedded sample, surface imaging microscopy (SIM) generates high resolution volumetric images of biological specimens across all of these scales.

Surface imaging microscopy expands our range of imaging tools by generating three-dimensional reconstructions of embryo samples at high resolution and high contrast. SIM image quality is not limited by depth or the optical properties of overlying tissue, and intrinsic or extrinsic alignment markers are not required for volume reconstruction. These volumes are highly isotropic, enabling them to be virtually sectioned in any direction without loss of image quality. Surface imaging microscopy provided a more accurate three-dimensional representation of a chick embryo than confocal microscopy of the same sample. SIM offers excellent imaging of embryos from three major vertebrate systems in developmental biology: mouse, chicken, and frog. Immediate applications of this technology are in visualizing and understanding complex morphogenetic events and in making detailed comparisons between normal and genetically modified embryos.

Introduction

Motivation

We are interested in understanding the way in which cellular function and behavior generates structures of high complexity, such as tissues and organs. The most logical structure around which to organize and synthesize these different categories of information is the three dimensional anatomy of the specimen. In short, we must know both where and when an event occurs before we can understand how. Such an effort will require imaging techniques spanning several orders of magnitude in spatial and temporal resolution. Current imaging techniques provide tools for high resolution imaging of small volumes or low resolution imaging of large volumes. A technique is needed to bridge this gap. Surface imaging microscopy meets this need.

Properties of the Basic Technique

Surface imaging microscopy (SIM) is an automated imaging technique that captures fluorescence images from the freshly cut surface of an opaque polymer block. The microscope is comprised of an integrated microtome and widefield fluorescence microscope, with a computer controlled translation stage that holds the embedded sample, draws it over a diamond knife, and returns the sample to the field of view of the objective lens. Images can be collected into one, two, or three independent fluorescent channels, and the signal can be either the inherent autofluorescence of the tissue or extrinsic contrast supplied by a fluorescent dye.

The depth of field in a SIM image is set by the amount of opacifier added to the embedding polymer. This amount can be empirically tuned to closely match the in-plane resolution of the image through the range of magnification of 2x-40x microscope objectives, corresponding to 8.8–0.4 micron resolution and sample sizes from 8–0.5 millimeters. The resulting SIM dataset is nearly isotropic, as the in-plane resolution of the microscope objective lens is matched to the thickness of the sections removed and to the depth of field of the image as determined by the penetration depth of light into the sample. The field of view of the microscope objective determines the in-plane sample size, but there is no inherent limit to the total depth of the specimen that can be sampled. The immediate output of SIM is a registered series of two-dimensional images, which are then computationally reconstructed into a three-dimensional volume. The realignment accuracy of the stage is sufficient that the misregistration between subsequent images is sub-resolution and no post-hoc realignment is necessary. Figure 5-1 schematically depicts a surface imaging microscope.

Results and Discussion

Quality of 2D Images
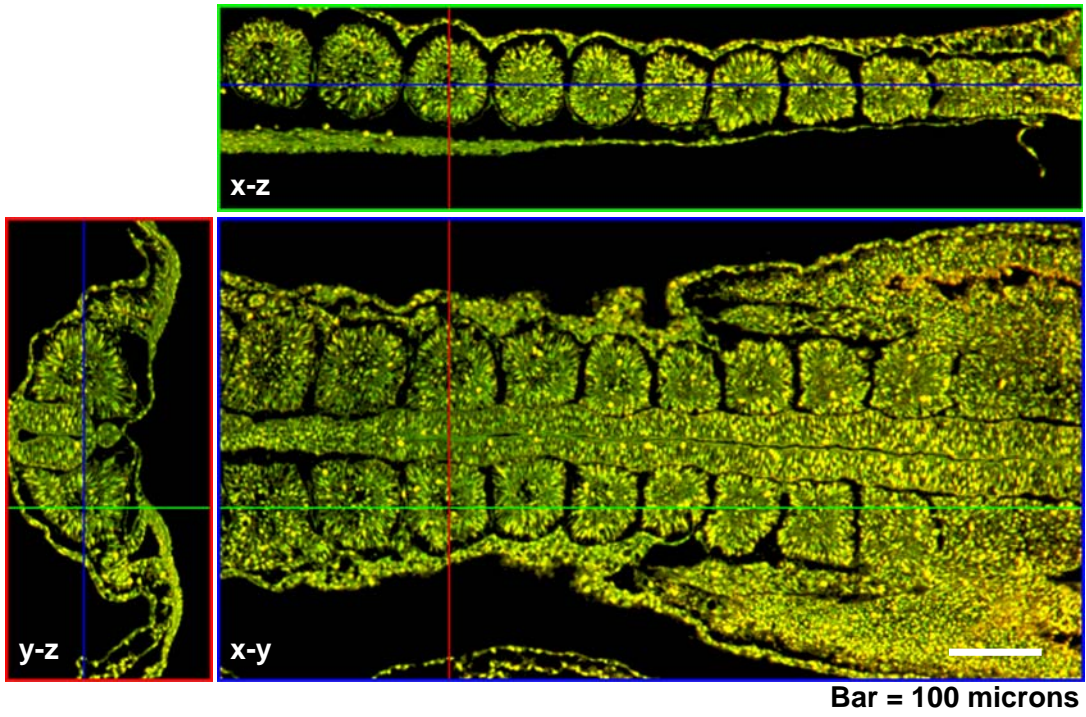
Figure 5-2 depicts three orthogonal views through a typical SIM dataset of a chick embryo (stained with Resolution Standard Stain). The main panel is the raw x-y image collected from the block surface. The x-y view demonstrates that the raw images of a SIM dataset have high contrast, high resolution, and excellent tissue preservation. Additionally the embryo is clearly distinct from the

Figure 5-1, Description of the Basic Technique: Schematic depiction of surface imaging microscopy (SIM). A fluorescently labeled specimen is fixed, labeled, dehydrated, infiltrated, and embedded in a black polymer, then loaded onto a motorized translation stage (TS). A computer (CPU) controls synchronizes the movement of the sample over a diamond knife, removing a thin section of material and returning the sample to the field of view of an objective lens. An image of the surface of the block is collected by a charge-coupled device (CCD) camera and the process repeats. This aligned series of two-dimensional images can then be computationally reassembled into a three-dimensional volume in standard image processing applications.

Figure 5-2, Evaluation of Image and Dataset: Two-dimensional data resulting from a SIM dataset of a fluorescently labeled chick trunk, stained with Resolution Standard Stain (Resolution Sciences Corporation, Corte Madera, CA). Anterior is to the left. Note in particular the similarity in contrast, resolution, and level of detail in the three views. The raw x-y image collected by the CCD camera corresponds closely to a frontal section through the embryo. This image is a representative single section from the dataset. The red and green lines mark the axial levels at which the orthogonal views were extracted. The x-z view is a computationally reconstructed sagittal view of the dataset, highlighting the developmental progression of somites as a function of distance along the anterior-posterior axis. The y-z view is a computationally reconstructed transverse view through the dataset, highlighting the neural tube, notochord, and paired somites. Scale bar = 100 microns.

Emission Filters

Dichroic Beam Splitter

Objective Lens

Sample

CCD

TS

CPU

Excitation Filters

Arc Lamp

Diamond knife

2D Raw Images

**3D Reconstruction**

Bar = 100 microns
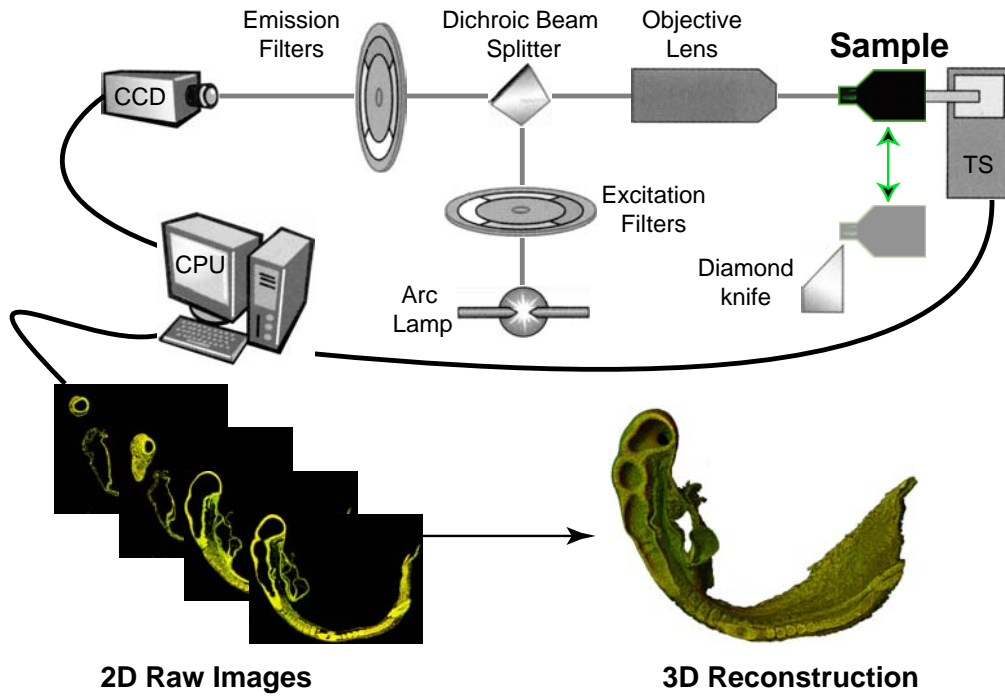
surrounding block, greatly facilitating three-dimensional reconstructions. It is also evident from the x-y view that there is minimal knife chatter in the image, and that SIM captures a wide field of view at cellular resolution. We have collected images of similar quality using tissue autofluorescence, DAPI, propidium iodide, Syto 62, and Topro-3 (Molecular Probes, Eugene, Oregon); Figure 5-3 shows 2D images acquired with each of these dyes. These dyes range in emission wavelength from the near UV through the near-IR and demonstrate that the embedding polymer and the imaging system are sensitive to the entire visible spectrum.

Quality of Datasets

Orthogonal sections through the dataset are necessary to critically assess many aspects of the quality of SIM datasets; these sections reveal time and depth dependent variations in image quality. Figure 5-2 presents x-z and y-z sections through the same dataset, at the levels indicated by the colored lines. Changes in fluorescence excitation intensity or camera efficiency over the course of the imaging would show up in the x-z or y-z sections as lines that were aberrantly brighter or darker than adjacent sections. This artifact is not typically present in SIM datasets. Misregistration of the blockface during imaging would cause smooth curves within features of the dataset to appear jagged, as structures that were adjacent in the sample are mistakenly separated in the resulting dataset. The contiguous outlines of individual cells and the smooth outlines defining tissue blocks and cavities argues that any registration errors are sub-resolution. No

Figure 5-3: SIM Images of Various Nuclear Dyes: A: Transverse section through the trunk of a chick embryo, labeled with DAPI and imaged using SIM. B: Frontal section through the trunk of a chick embryo, labeled with Syto 62, and imaged using SIM. C: Transverse section through a chick trunk, labeled with propidium iodide, and imaged using SIM. D: Transverse section through rhombomere four of a chick hindbrain, labeled with Topro-3, and imaged using SIM.

DAPI

(a)

Syto 62

(b)

Propidium Iodide

(c)

Topro-3

(d)
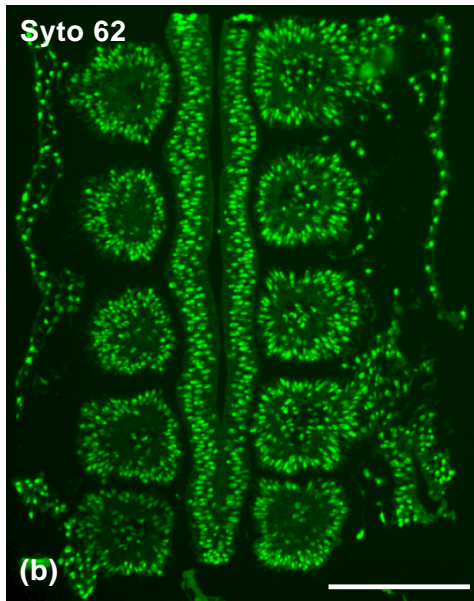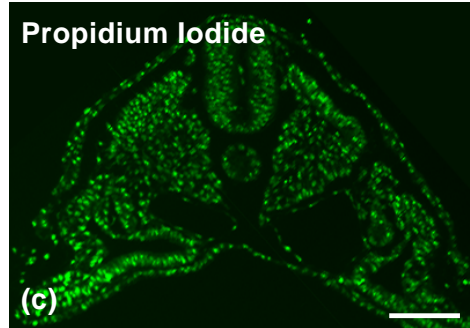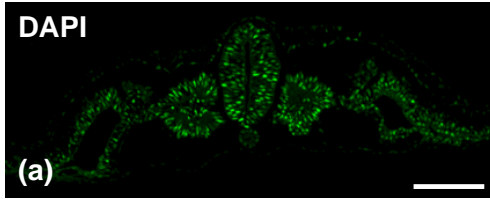
Bar = 50 microns

alignment algorithms have been used to process this dataset; the registration evident in Figure 5-2 is indicative of the alignment of the raw data.

SIM relies on staining samples in whole mount, then imaging thin optical sections of the surface of the sample. As a result the dye needs to penetrate adequately in the whole sample and then be sufficiently bright in the thin optical section. Inconsistencies in dye penetration would show in the x-z and y-z images as changes in color or intensity through structures of similar cellular composition, such as epithelial somites. Figure 5-2 is clear evidence that our labeling techniques yield uniformly stained samples and that SIM has the sensitivity to detect the fluorescent signal from thin optical sections.

A major technical advantage of SIM over previous blockface imaging efforts [1-4] is the isotropicity of the resulting 3D datasets. The axial resolution of any three dimensional imaging technique is best judged by evaluating x-z and y-z orthogonal sections through the dataset. We find the level of resolution, contrast, and detail preserved to be indistinguishable in the three dimensions. Therein lies the major strength of SIM: the in-plane tissue and cavity architecture preservation in SIM is comparable to that achieved in thin paraffin sections or confocal optical sections and its through plane resolution is currently unrivaled.

Comparison with Other Imaging Techniques

Current imaging techniques are not well suited to imaging millimeter scale samples at micron scale resolutions. Traditional histology has an extensive history of specific stains, both fluorescent and colorimetric, but is quite laborious and requires the viewing and/or photographing of hundreds to thousands of physical sections to gain an appreciation of complex three-dimensional structures. Methods that capture images of these sections and computationally warp them into three-dimensional volumes are of considerable use, but have not reported resolution or isotropicity similar to SIM [5, 6]. Previous efforts have also imaged the blockface of samples after physical sectioning, to build three-dimensional reconstructions of samples [1-4, 7]. SIM is distinguished from other block face approaches in the resolution, the contrast, and the tissue detail preserved through imaging. SIM resolves cells, subcellular structures, and can be used to label specific subpopulations of cells within an embryo, in contrast to lower resolution alternative methods relying on the inherent contrast in the tissue [3, 4]. Finally, the range of possible sample applications for SIM is broader; we have successfully imaged samples as delicate as early gastrulae chick embryos and samples as rigid as non-decalcified trabecular bone.

Several techniques exist which intrinsically collect three-dimensional volumes, rather than two-dimensional sections. Among them are optical coherence tomography (OCT), magnetic resonance imaging (MRI), and optical projection

tomography (OPT). OCT images backscattered light coming off a sample and has the potential to image 3 mm into a living specimen, but does so with 12-15 micron resolution and few options for specific contrast [8]. High-field MRI is excellent for imaging large specimens at 50-100 micron resolution. In fixed specimens, 35-50 micron resolution is achievable with long scan times and large magnetic fields [9]. OPT is an exciting new technique related to computed tomography that images fixed large samples that have been made optically transparent. It is unsuited to embryos containing very dense tissues such as cartilage or bone though, and has not been reported at cellular resolution [10]. It is currently a very exciting period in biological imaging, with rapid improvements being made across all imaging modes. SIM aids this progress by filling an unserved niche of cellular resolution on large samples, and should prove a highly complementary alternative to existing approaches.

Comparison of SIM with CLSM

To directly compare the performance of confocal laser scanning microscopy (CLSM) [11] with surface imaging microscopy, we imaged the same propidium iodide stained chick embryo with both techniques. The in-plane 2D images in Figure 5-4 (marked x-y) allow assessment of the image quality of the

Figure 5-4, Comparison of SIM with Confocal Microscopy: Comparative imaging of a chick trunk segment, stained with propidium iodide and imaged with both surface imaging microscopy and confocal laser scanning microscopy. Each technique is presented with three orthogonal views, starting with the original (x-y) plane of optical section, and following with computationally reconstructed views extracted from the resulting volume. Both datasets were collected with 1.7 micron optical resolution and sections were collected at 1.7 micron intervals. Note in particular the equivalence of the resolution, contrast, and level of detail in the x-y, x-z, and y-z views from the SIM dataset and the steep decline in image intensity as a function of depth into the dataset in the confocal dataset. Scale bar = 100 microns.

Surface Imaging Microscopy **Confocal Microscopy**

x-y

x-y

x-z

x-z

y-z

y-z
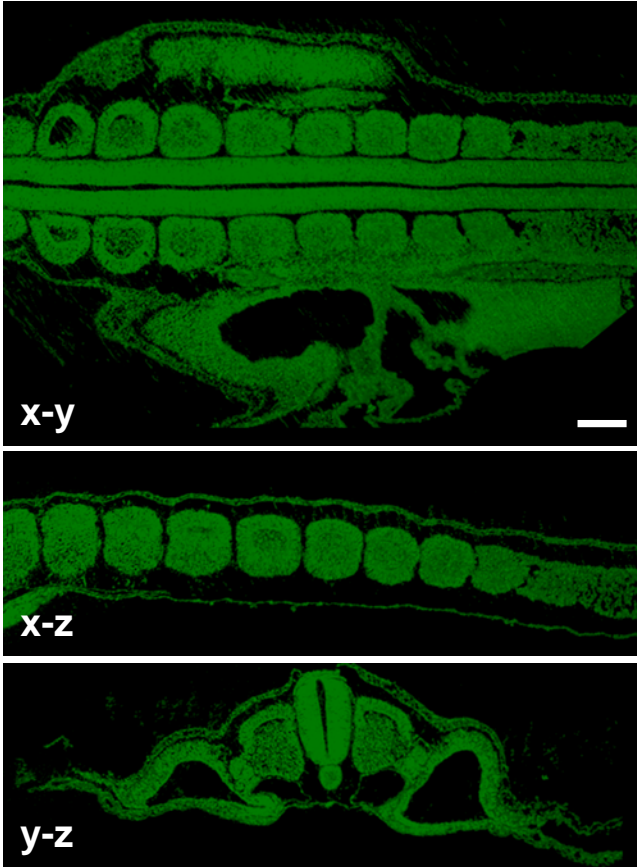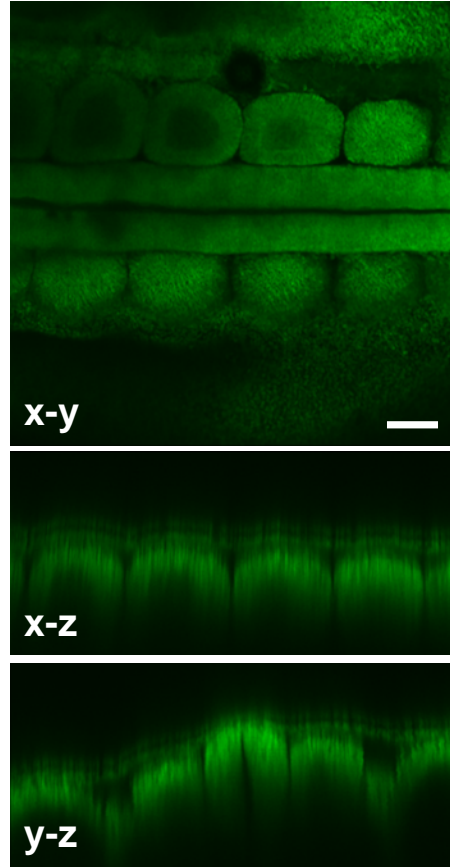
Bar = 100 microns

raw data in each imaging mode and show comparable image quality. The most striking differences are the shrinkage of structures in the SIM images, due to dehydration, and the larger overall field of view of the SIM images, which is due to the larger field of view of the surface imaging microscope compared to the Zeiss 410 CLSM. The shrinkage of tissue in alcohol is unavoidable and the shrinkage we observe is consistent with published norms [12].

The more informative views of the sample are the orthogonal x-z and y-z views through the resulting three-dimensional volume. The quality of the confocal images clearly falls off very quickly as a function of depth within the sample, even with the use of a water immersion C-Apochromat 10x objective lens. Even in regions of the volume where the quality is adequate, the through plane resolution is worse than the in-plane resolution. SIM, by contrast, has uniform image quality throughout the volume and has indistinguishable resolution and level of detail in the three directions. SIM in-plane image quality is not a function of depth or of the scattering, density, or degree of labeling of the tissue above or below the current plane of optical section. This has a trivial basis, in that there is no overlying tissue, but has profound consequences for image and dataset quality.

### Practical Resolution of SIM Datasets

SIM can be performed on a variety of sample sizes and magnifications. These magnifications provide a useful resolution and field of view range that brackets

whole embryos at tissue resolution through small tissue segments at subcellular resolution. Low (2-4x) magnification allows ready identification of tissues and organs within small organisms and enables the study of their morphological development and relative orientation with respect to each other. Intermediate (10x) magnification enables the study or tissues at cellular or subcellular resolution. High (20-40x) magnification enables the study of small blocks of tissue at cellular or subcellular resolution.

Range of Systems Tested

Figure 5-5 depicts 2D raw sections and 3D reconstructions of an intact mouse and frog embryo and a segment of a chick embryo at 10x magnification. SIM routinely provides high-resolution, high-contrast images throughout embryos from each of these species at a wide range of stages. The cells of the mouse embryo in Figure 5-5a are clearly visible, and mesenchymal tissue is quite distinct from epithelial cell layers. This level of resolution provides a clear view of the relationship between developing tissues and organs in the context of an intact embryo. The gastrula stage frog embryo in Figure 5-5b is composed of relatively large cells, whose shapes and polarities are quite evident in three-dimensional reconstruction, especially those of the cells lining the blastocoel and archenteron. Additionally the germ layer organization of the frog is quite evident, in the

Figure 5-5, Volumetric Images of Embryos from 3 Model Systems: A broad range of sample types are readily imaged using surface imaging microscopy, including chick, mouse and frog embryos. All three embryos were stained with Resolution Standard Stain. **(a)** A two-dimensional raw image collected from a 9.5 days post coitum (dpc) mouse embryo and three orthogonal three-dimensional reconstructions of the resulting dataset, corresponding to sagittal, transverse, and frontal perspectives. Note the excellent preservation of lumenal structures in the midbrain (MB), the somites (S), the heart (HR), the optic vesicle (OP), and the otic vesicle (OT). **(b)** A two-dimensional raw image collected from a Stage 12 frog embryo and three-dimensional reconstructions of this late gastrula frog embryo, highlighting the blastocoel (BC) and the archenteron (AR). Note the reconstruction of the cell shapes on the floor of the blastocoel and in the lining of the archenteron. **(c)** A two-dimensional raw image and three orthogonal three-dimensional reconstructions of a trunk segment from a 16 somite stage chick embryo described in Figure 5-2. Note the clear developmental progression of somites (S), extending from the segmental plate (SP), adjacent to the neural tube (NT). Scale bar = 250 microns.
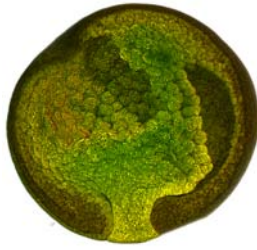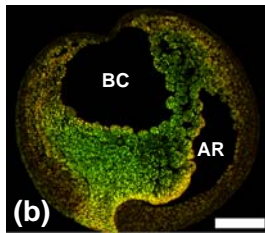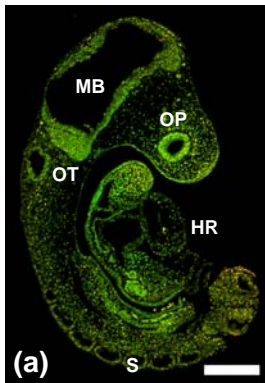
Bar = 250 microns

concentric epithelial shells surrounding the vegetal yolk mass. We have imaged

chick embryos from Hamburger and Hamilton Stage 4-16, frogs from Stage 9-22,

and mouse embryos from embryonic day 8.5-15.

Conclusions

We have demonstrated a new imaging technique based on the automated serial

collection of thin optical sections from the freshly cut surface of a fluorescently

labeled sample embedded in a highly opaque polymer. The realignment

accuracy is sub-resolution and there is little or no detectable variation in image

quality throughout the volume. The voxels of the dataset are highly isotropic,

allowing digital resampling of the dataset from arbitrary virtual planes of section.

This technique works across an order of magnitude in sample size and

resolution, with improvements on track to significantly extend this range. SIM

provides a unique combination of large sample size with high resolution and

specific contrast.

We have demonstrated, in three different vertebrate model systems, that the

practical resolution of a surface imaging microscope is sufficient to image small

blocks of tissue with subcellular detail, large blocks of tissue with cellular

resolution, and whole embryos with cellular to tissue resolution. We have also

established that SIM produces high-contrast, high-resolution, high signal-to-noise

ratio images with five different fluorescent dyes. Finally, direct comparisons, on

the same block of tissue, demonstrate the advantages of SIM vs. confocal

microscopy, particularly in terms of depth of penetration and maximal sample size.

We expect that the combined ease of review of the primary data and ease of transfer of data should allow SIM to provide novel opportunities for collaborations in which phenotypes can be rapidly evaluated and extensively analyzed by experts at different institutions. The digital 3D models that result from SIM datasets can also be used as a structural scaffold to integrate other categories of information [13].

Future technical challenges within the reach of SIM include imaging green fluorescent protein (GFP) expression in intact embryos, imaging antibody revealed protein expression, and fluorescent in situ hybridization to mRNA probes. We have already achieved some success imaging the clonal distribution of fluorescent dextrans within frog embryos. Improvements in optical sensitivity and whole mount labeling techniques should enable these advances in the near term. We are also currently working on developing organic dye labeling approaches capable of revealing the plasma membranes of cells throughout the embryo. In combination with the nuclear dyes that have proven successful in this study, these should enable clear visualization of all of the cells in intact vertebrate embryos. Biological problems that we expect SIM to address to in the near future include somitogenesis, gastrulation, and organ morphogenesis. In each case complex morphogenetic rearrangements are taking place

throughout large regions of the embryo, and a cellular level of detail is required to understand the process.

Experimental Procedures:

Sample Preparation

White leghorn chicken eggs were incubated at 37° C for two to three days until they reached the desired stage of development, typically 16-25 somites. They were then harvested into ice-cold Howard Ringer's Solution, and fixed overnight in fresh 4% PFA at 4°C. Following fixation the embryos were washed three times for 30 minutes each in PBS. Embryos of Xenopus laevis were obtained, cultured, and dejellied according to standard techniques [14]. Staging was done according to the Niewkoop and Faber normal tables of Xenopus development [15]. Embryos were cultured to the desired stage, fixed in Bouin Fixative (75% picric acid, 25% formaldehyde (37-40%), 5% glacial acetic acid) overnight, and rinsed exhaustively in (50% ethanol, 50% water with 50mM NH4OH). The frog embryos were then dehydrated to absolute ethanol, stored overnight in a –20°C freezer, changed to fresh ethanol, and rehydrated to PBS. Embryos from B6D2F1 hybrid mice were obtained from timed matings where noon of the day when the copulatory plug was found is designated as 0.5 dpc. Embryos were harvested into ice cold PBS and transferred into fresh 4% paraformaldehyde for fixation overnight at 4°C. Embryos were rinsed in PBS, dehydrated to 100% ethanol, and rehydrated to PBS.

Sample Labeling

Embryos were fixed in 4% PFA, rinsed in PBS, stained in either propidium iodide (50 micrograms per mL for 1 hour), DAPI (10 micrograms per mL for 1 hour), Syto 62 (1:50 dilution for 1 hour), or Topro3 (1:50 dilution for 1 hour) (all Molecular Probes, Eugene, Oregon). Samples labeled with Resolution Standard Stain (Resolution Sciences Corporation, Corte Madera, CA) were stained for 6 hours.   Dilutions were into PBS. Under all staining conditions, embryos were rinsed in PBS, then dehydrated to either methanol or ethanol.

Comparison to Confocal Microscopy

Chick embryos were fixed and stained in propidium iodide (50 micrograms per mL for 1 hour), then imaged in PBS on a Zeiss 410 confocal microscope, using a C-Apochromat 10x water immersion objective lens.   Image acquisition was 512x512 pixels, with the pinhole at 1 Airy unit, in-plane resolution at 1.7 microns, and 1.7 micron intervals between optical sections.   The embryos were then restained in propidium iodide and imaged by SIM with a 10x Plan Apochromat air objective lens, with 1.77 micron cubic isotropic voxels.   Both image stacks were imported into the LSM 510 imaging software, version 3.0 (Carl Zeiss, Inc, Thornwood, New Jersey) and all comparisons were made therein.

Sectioning and Imaging

To prepare a sample for SIM imaging, it needs to be labeled, fixed, dehydrated, infiltrated, and embedded.   We have imaged samples fixed in PFA (4%

paraformaldehyde in phosphate buffered saline (PBS), pH 7.4), formalin, Carnoy's Fixative, and Bouin Fixative [12]. Samples have been dehydrated to methanol, ethanol, or isopropanol. This flexibility in sample preparation enables customization to the specific needs of different tissue specimens, allowing for more optimal preservation of cellular detail and tissue integrity. Additionally, SIM is ideally suited to samples of varying density as it is able to section through dense and loose tissue with minimal chatter or unevenness.

Under all staining conditions, embryos were rinsed in PBS, then dehydrated to either methanol or ethanol. Following dehydration, embryonic tissues were equilibrated with a mixture of Resolution Standard Embedding Polymer and Resolution Standard Opacifier (Resolution Sciences Corporation, Corte Madera, CA) for 6 hours to allow for cellular infiltration. Opacifier is added to polymer to 82% of saturation to form 100% Stock Opacified Polymer (SOP), which may be stored in aliquots at -4 degrees Celsius for up to 3 months. Prior to embedding, the SOP is brought to room temperature, and then a working polymer is produced by adding to the 100% SOP sufficient additional fresh unopacified polymer to produce the final opacifier concentration appropriate to a given microscope objective. These concentrations have been empirically determined for a set of standard tissues; typical values for different objective lenses are 2x =10%, 4x=20%, 10x=30%, 20x=40%, 40x=50% opacity (Nikon Plan Apochromat series objective lenses). The embedding polymer was cured for 8 hours at 70° C.

The embedded tissue was mounted onto a vertically oriented translation stage assembly, which draws the sample over the edge of a diamond knife, removes the section with vacuum, then repositions the block face in its original location, in the field of view of a Nikon E600 fluorescence microscope with a Plan Apochromat 4x, 10x, or 20x objective lens. Images were collected to a Kodak Megaplus Model 4.2i charge coupled device (CCD) camera. Wavelength selection is accomplished with interference filters and dichroic beam splitters (Chroma Corporation, Brattleboro, VT). Individual images were reassembled into a three-dimensional volume that can be visualized and quantified on Resolution ResView 3.1 software. Alternatively, a series of two-dimensional images can be re-exported and computationally reconstructed into a three-dimensional volume that can be manipulated in other image processing programs. Because of the high inherent contrast between the sample and the block face, and the absence of a significant out-of-plane component in the image, there is no need for automated or manual deconvolution techniques to reconstruct accurate three-dimensional renderings from SIM datasets. The entire imaging process, from loading the block to finishing image collection, takes approximately three to six hours, depending on the number of sections that need to be cut.

Acknowledgments

1. Postlethwait SN: **Cinematography with Serial Sections**. *Turtox News* 1962:98-100.
2. Hegre ES, Brashear AD: **Block Surface Staining**. *Stain Technology* 1946, **21**:161-164.
3. Odgaard A, Andersen K, Melsen F, Gundersen HJG: **A direct method for fast three-dimensional serial reconstruction**. *Journal of Microscopy* 1990, **159**:335-342.
4. Weninger WJ, Mohun T: **Phenotyping transgenic embryos: a rapid 3-D screening method based on episcopic fluorescence image capturing**. *Nature Genetics* 2002, **30**:59-65.
5. Streicher J, Weninger WJ, Mueller GB: **External Marker-Based Automatic Conguencing: A New Method Of 3D Reconstructions From Serial Sections**. *The Anatomical Record* 1997, **248**:583-602.
6. Brune RM, Bard JBL, Dubreuil C, Guest E, Hill W, Kaufman M, Stark M, Davidson D, Baldock RA: **A Three-Dimensional Model of the Mouse at Embryonic Day 9**. *Developmental Biology* 1999, **216**:457-468.
7. Toga AW, Ambach KL, Quinn B, Shankar K, Schluender S: **Postmortem Anatomy**. In: *Brain Mapping, The Methods* Edited by Toga AW, Mazziotta JC, First ed. pp. 471. San Diego: Academic Press; 1996: 471.
8. Boppart SA, Brezinski ME, Bouma BE, Tearney GJ, Fujimoto JG: **Investigation of developing embryonic morphology using optical coherence tomography**. *Dev Biol* 1996, **177**:54-63.
9. Dhenain M, Ruffins SW, Jacobs RE: **Three-dimensional digital mouse atlas using high-resolution MRI**. *Dev Biol* 2001, **232**:458-470.
10. Sharpe J, Ahlgren U, Perry P, Hill B, Ross A, Hecksher-Sorensen J, Baldock R, Davidson D: **Optical projection tomography as a tool for 3D microscopy and gene expression studies**. *Science* 2002, **296**:541-545.
11. Pawley JB (ed.). *Handbook of Biological Confocal Microscopy*, Second Edition edn. New York: Plenum Press; 1995.
12. Schreibman MP, Presnell JK: *Humason's Animal Tissue Techniques*, 5th edn. Baltimore, MD: The Johns Hopkins University Press Ltd.; 1997.
13. Streicher J, Muller GB: **3D modelling of gene expression patterns**. *Trends Biotechnol* 2001, **19**:145-148.
14. Sive HL, Grainger RM, Harland RH: *Early Development of Xenopus Laevis: A Laboratory Manual*, First edn. Cold Spring Harbor: Cold Spring Harbor Laboratory Press; 2000.
15. Nieuwkoop PD, Faber J (eds.): *Normal Table of Xenopus laevis (Daudin)*, 2nd edn. New York: Garland Publishing, Inc.; 1994.

A Three Dimensional Analysis of Frog Gastrulation

Following investigations into the role of calcium signaling during gastrulation in the frog, *Xenopus laevis*, we became interested in a accurately the three dimensional structure of the *Xenopus* gastrula in normal and experimentally manipulated embryos. We developed a surface imaging microscopy (SIM) [1] to accomplish this goal. We have applied SIM to the study of *Xenopus* gastrulation and have recently competed a digital atlas of frog gastrulation, with every substage from blastula through neurula represented.

To take best advantage of these digital volumes, we developed a standard coordinate system for comparing embryos, then developed computational tools to define the surface of the embryos and extract curved surfaces and volumes according to this coordinate system. These computational tools enabled us to make detailed comparison of the same regions within different *Xenopus* embryos. We applied these techniques to visualize the internal events of gastrulation as a function of stage. We have also visualized the vegetal alignment zone, an arrangement of cells in the mesoderm predicted to close the blastopore, but never previously directly visualized in an intact embryo. We then imaged embryos, at two stages of development, that were overexpressing a mutant form of Disheveled in their dorsal mesoderm. These embryos had nearly normal archenteron lengths, but deficient mesodermal convergent extension, implying that the archenteron can elongate in the absence of normal mesodermal cell movements. We conclude by discussing plans to test this hypothesis, and to directly measure the extent of coupling of different morphogenetic processes during gastrulation.

Andrew Ewald, J. Michael Tyszka,

Scott E. Fraser, John Wallingford

Biological Imaging Center

California Institute of Technology

Introduction

My research into the control of cell movements in the *Xenopus* gastrula began by looking for molecular mechanisms for coordinating cell motility in the dorsal mesoderm. We discovered, characterized the tissue specificity of, and demonstrated the requirement for propagating intercellular waves of calcium in the dorsal mesoderm (Chapter 4). We concluded that calcium was required for the elongation of the dorsal mesoderm by examining the elongation of the embryo's developing anterior posterior axis (as revealed by in situ hybridization for a notochord specific molecular marker). The defect was profound and highly penetrant. I was unsatisfied with our ability to fully characterize the full extent of the phenotype though. *Xenopus* embryos are large and highly opaque, making optical analysis of whole embryos quite difficult. Traditional histological methods can be used to prepare thin sections of almost any part of the embryo, but it is very difficult to reconstruct three dimensional volumes accurately from isolated sections. I wanted to be able to interactively visualize whole frog embryos to determine the full nature of defects caused by different molecular disruptions. I wanted to understand what had gone wrong in response to a given perturbation and, just as important, what worked despite the perturbation.

In parallel experiments we were developing surface imaging microscopy as a tool for visualizing large embryo samples at high resolution (Chapter 4). Briefly, we have applied this technique to frog gastrulation, and have used to it visualize the

major events of gastrulation, and to evaluate the phenotype of disruptions in Disheveled signaling.

Results/Discussion

SIM Produces High Resolution Digital Frog Datasets

We have found that SIM is ideally suited to the study of early frog development. Since the magnification of the final images is selected prior to imaging, and the sample is destroyed during imaging, SIM works best with embryos that are of similar size, so that a similar level of detail can be observed in all conditions. We have previously tested SIM on chick, frog, and mouse embryos (Chapter 5). It produced high quality images of all three species, but the extensive growth that is characteristic of early mouse and chick development put practical limits on the developmental window that could be examined. Since early frog development occurs with very little net change in volume, we were able to select a single resolution and image embryos at all stages of gastrulation with equivalent contrast and resolution. We present a quick review of the technique behind SIM in Figure 6-1.

Comparison with Confocal Microscopy

The *Xenopus* embryos is highly opaque and scatters light very effectively. Consequently we have been unable to image more than a 20-30 microns into the surface of a living or fixed frog embryo. The use of Murray's Clearing Solution

minimizes these problems, and reduces scattering sufficiently to enable imaging of whole, intact frog embryos with a confocal microscope [2]. The quality of the individual sections is reasonable, but the resolution is highly anisotropic, making it very difficult to accurately visualize structures except within the original plane of optical section. Figure 6-2A demonstrates the quality of image data that can be achieved in whole embryos that have been cleared and imaged with a confocal microscope. As a contrast we present a typical quality SIM dataset of a late gastrula frog embryo in Figure 6-2B. The contrast and in-plane resolution are at least as good and the through plane resolution is much better. We are not aware of another technique which can image a sample of this size (1-1.2 mm) at this resolution (1.77 um^2).

The one technical feature that we are still working to develop in SIM, that is exceeded in confocal microscopy, is the visualization of specific fluorescent stains. We have used Resolution Standard Stain for all of the embryos in this chapter, and were not successful in imaging green fluorescent protein or labeled antibodies with SIM. This matter is discussed in Chapter 5.

Coordinate System

We have successfully imaged more frog embryos at every stage of frog gastrulation. To facilitate making comparisons between embryos at the same stage to assess the variability of events of gastrulation, or to compare normal embryos with experimentally perturbed embryos, we developed a standard

coordinate system for frog gastrulation. Since the frog gastrula is very nearly spherical, we decided to work in spherical coordinates. To define a spherical coordinate system, it is necessary to select a pole and the prime meridian. Once that is done all other points in the sphere can be uniquely identified. We chose to define the center of the blastopore as the South Pole, and a normal through that point to define the North Pole. We defined the prime meridian as the center of the dorsal lip of the blastopore. We spent some time trying to develop algorithms to automatically identify these landmarks, but it proved very challenging to computationally mimic the trained eye of a developmental biologist.   Instead we chose to develop algorithms (described Methods and in Appendix 2) to enable quick manual selection of these landmarks. Figure 6-3 shows screen captures of our blastopore and archenteron selection schemes.

Digital Atlas of Frog Gastrulation

We have successfully imaged approximately 40 frog embryos at different stages of development, covering Nieukoop and Faber stages 9-14 [3]. A selection of these embryos is presented in Figure 6-4. As can be seen clearly in Figure 6-4, the gastrula stage frog embryo is very nearly spherical.   The biological organization of the embryo at these stages is chiefly in radially concentric curved surfaces. We have taken advantage of these facts to digitally manipulate these datasets to visualize the major events of frog gastrulation. We computationally identify the sphere which best fits the surface of the embryo (see Appendix 2), then define a coordinate system for the embryo. Once this coordinate system is

selected we can extract any surface or volume from the embryo. Since the coordinate system enables us to compare similar regions in embryos of different stages or different experimental conditions, we can visualize internal events of gastrulation as a function of stage or perturbation.

To illustrate this process, we have selected four embryos from our digital atlas; they are presented in volume renderings in Figure 6-5. For our current purposes we are most interested in the polarity of cells and tissues in the dorsal marginal zone. Much recent work has focused on the molecular control of cell movements in this tissue (reviewed in [4-6]). We wanted to visualize three events in this tissue: tissue separation, bottle cell formation, and archenteron elongation. We have conducted a preliminary analysis and concluded that we have sufficient resolution and contrast to see these events.

Figure 6-6 depicts the two basic volumes that we have extracted from the embryos shown in Figure 6-5. To visualize the dorsal marginal zone we extracted surfaces from the center of the blastopore to the margin of the embryo, from a radius of 0.5 through 0.95 (with 1 being the surface of the best-fit sphere), and from a range of longitudes of +/- 60° from the center or the dorsal lip. We then mapped that volume to a rectangular block for ease of manipulations. We have also explored a variety of cartographic projections, but have yet to find one suitable for conveniently examining volumes. The second volume we extracted was a more superficial peel (radius 0.75-0.95), but ranging in latitude from the

South Pole (center of blastopore) to the North Pole, and ranging in longitude +/-
60° from the center of the dorsal lip of the blastopore.

Evaluation of Diagnostic Ability of Datasets

We have extracted these two volumes from the four embryos presented in Figure
6-5 and have just finished a preliminary evaluation of our computational tools. To
determine the utility of these datasets for analyzing the phenotypes
experimentally perturbed embryos, we developed techniques to visualize the key
diagnostic events of gastrulation. We present examples of several of these
below.

Involution and Tissue Separation

Figure 6-7 depicts two of the main events of gastrulation, involution and tissue
separation. One of the major functions of gastrulation is to establish the
developing gut, or archenteron. The archenteron forms when a group of cells at
the dorsal lip of the blastopore restricts their apical surfaces and forms the
indentation visible in Figure 6-7A. The gut then advances through the solid
tissue of the embryo (black line in 6-7B and 6-7C), and eventually forms a large
lumen (Figure 6-7D). Coincident with this process is the separation of different
adjacent tissues within the embryo [7, 8], which has been shown to be under the
control of Wnt signaling through Frizzled-7 [9]. We can clearly visualize the
interface between the separating tissues (black arrows in Figure 6-7) and can

visualize the spatial relationship between this interface and lengthening archenteron.

Vegetal Alignment Zone

Another key event of gastrulation is the closure of the blastopore. This is currently thought to be mechanically achieved through the development of bands of aligned cells in concentric hoops around the blastopore. Mediolateral alignment of cells in this region, consistent with this idea, was observed in the 1970s [10, 11], and bands of aligned cells were observed in explants of these tissues in the early 1990s [12]. Due to technical imaging challenges, these cell rearrangements have not been observed in intact embryos. We examined surfaces in gastrula embryos at the depths indicated in Figure 6-8. When examining the three dimensional volume, and surfaces extracted from that volume, we have found cell alignments consistent with the vegetal alignment zone (Figure 6-8 D-G). We are still testing methods to convincingly visualize this structure.

Mesendoderm Extension

The final structure that we chose to visualize is the leading edge of the mesendoderm. A semi-coherent population of mesoderm and endoderm starts near the floor of the blastocoel and migrates/extends over the surface of the blastocoel roof. We visualized this process in the long, thin embryo volumes and

depict this in Figure 6-9. This process was dynamically imaged in living embryos in a recent report [13], and our observations are consistent with theirs.

Experimental Disruption of Dishevelled Signaling

The process of convergent extension in the dorsal mesoderm of the frog embryo has been shown to be under the control of Wnt signaling through the planar cell polarity pathway [14, 15]. More recent studies have demonstrated a direct role for Dishevelled in the medio-lateral polarity of cells within the dorsal mesoderm [16], reviewed in [4, 5]. Since we demonstrated that our digital frog gastrulation atlas was capable of visualizing the major events of frog gastrulation, we decided to image embryos overexpressing a mutant form of Dishevelled, Xdd1 [17], in the dorsal mesoderm. We imaged control and injected embryos at the beginning (6-10) and end (Figure 6-11) of gastrulation.

The most striking thing about the early gastrula Xdd1 embryos is how normal they look. This time point (Stage 10.5) is prior to most of the major cell movements of gastrulation. Since the major cell movements up to this point involve the deep vegetal cells, which were untreated, this is not too surprising.

The late gastrula embryos have several obvious defects: the archenteron volumes are smaller, the blastocoel volume is larger, and the tissue between the archenteron and the surface of the embryo appears thicker. We were most struck by the fact that the archenteron elongation is fairly normal: the

archenterons are slightly (20%) shorter than control embryos. It is presently unclear how the volume of the archenteron increases and the blastocoel decreases, so we chose to focus on two of these differences: that the length of the archenteron is shorter, and the marginal zone is thicker. These two observations make two testable predictions: that radial intercalation within the dorsal marginal zone is dependent on Dishevelled function in the dorsal marginal zone, and that archenteron elongation is not.

Conclusions

We have applied surface imaging microscopy to the process of frog gastrulation and generated a digital atlas comprising all stages of gastrulation. We have developed a standard coordinate system for these embryos to facilitate comparisons, and have developed computational methods to extract deep surfaces from these datasets. We have just finished a preliminary analysis of the level of detail in this datasets and have concluded that we can observe bottle cell formation, tissue separation, archenteron elongation, blastopore closure, and mesendoderm extension. We also have suggestive evidence that we will be able to visualize the vegetal alignment zone in intact embryos. Finally we have imaged embryos with disruptions in Dishevelled function and have generated two novel testable predictions: that radial intercalation is and archenteron elongation is not dependent on Dishevelled function in the dorsal mesoderm. We have also developed techniques to test these hypotheses.

Future Directions

We will apply the computational methods described in this paper to the comparative analysis of the normal and Xdd1 embryos at both stages. In parallel, we plan to use simpler techniques to test the degree of coupling of archenteron elongation, dorsal mesodermal convergent extension, and blastopore closure in normal and Xdd1 embryos. We will measure the area of the blastopore normalized to the area of the embryo (Figure 6-12a), the length to width ratio of the notochord domain (Figure 6-12b), and then surgically bisect the embryos along the dorsal midline, and measure the length of the archenteron normalized to the diameter of the embryo. It is necessary to make all of the measurements relative to the size of the individual embryo, as early *Xenopus* embryos vary in size significantly. These measurements within normal embryos will give us a precise measure of the degree of coupling of these three processes during normal gastrulation. By also analyzing Xdd1 overexpressing embryos we can get a definite test of the our hypotheses that radial intercalation is affection and archenteron elongation is not.

Materials and Methods

Surface Imaging Microscopy

Frog embryos were prepared and imaged accordingly to protocols developed and reported in Chapter 5.

Best Fit Sphere and Shell Extraction

Appendix 2-14 details our approach to establishing a coordinate system for each dataset and extracting surfaces from those datasets. Figures 6-7 and 6-8 were generated with latitude –90-0, radius 0.5-0.95, longitude –60-60. Figure 6-9 was generated with latitude –90-90, radius 0.75-0.95, longitude –60-60.

Visualization

Volume renderings were done in ResView 3.2 (Figures 6-1, 6-4, 6-5, 6-6, 6-10, 6-11, 6-12). Extracted volumes were visualized in Amira (6-2, 6-3, 6-6, 6-7, 6-8).

1. Ewald AJ, McBride H, Reddington M, Fraser SE, Kerschmann R: **Surface imaging microscopy, an automated method for visualizing whole embryo samples in three dimensions at high resolution**. *Dev Dyn* 2002, **225**:369-375.
2. Sive HL, Grainger RM, Harland RH: *Early Development of Xenopus Laevis: A Laboratory Manual*, First edn. Cold Spring Harbor: Cold Spring Harbor Laboratory Press; 2000.
3. Nieuwkoop PD, Faber J (eds.): *Normal Table of Xenopus laevis (Daudin)*, 2nd edn. New York: Garland Publishing, Inc.; 1994.
4. Wallingford JB, Fraser SE, Harland RM: **Convergent extension: the molecular control of polarized cell movement during embryonic development**. *Dev Cell* 2002, **2**:695-706.
5. Keller R: **Shaping the vertebrate body plan by polarized embryonic cell movements**. *Science* 2002, **298**:1950-1954.
6. Keller R, Davidson L, Edlund A, Elul T, Ezin M, Shook D, Skoglund P: **Mechanisms of convergence and extension by cell intercalation**. *Philos Trans R Soc Lond B Biol Sci* 2000, **355**:897-922.
7. Ibrahim H, Winklbauer R: **Mechanisms of mesendoderm internalization in the Xenopus gastrula: lessons from the ventral side**. *Dev Biol* 2001, **240**:108-122.
8. Wacker S, Grimm K, Joos T, Winklbauer R: **Development and control of tissue separation at gastrulation in Xenopus**. *Dev Biol* 2000, **224**:428-439.
9. Winklbauer R, Medina A, Swain RK, Steinbeisser H: **Frizzled-7 signalling controls tissue separation during Xenopus gastrulation**. *Nature* 2001, **413**:856-860.
10. Keller RE: **Vital dye mapping of the gastrula and neurula of Xenopus laevis. II. Prospective areas and morphogenetic movements of the deep layer**. *Dev Biol* 1976, **51**:118-137.
11. Keller RE: **Vital dye mapping of the gastrula and neurula of Xenopus laevis. I. Prospective areas and morphogenetic movements of the superficial layer**. *Dev Biol* 1975, **42**:222-241.
12. Shih J, Keller R: **Patterns of cell motility in the organizer and dorsal mesoderm of Xenopus laevis**. *Development* 1992, **116**:915-930.
13. Davidson LA, Hoffstrom BG, Keller R, DeSimone DW: **Mesendoderm extension and mantle closure in Xenopus laevis gastrulation: combined roles for integrin alpha(5)beta(1), fibronectin, and tissue geometry**. *Dev Biol* 2002, **242**:109-129.
14. Sokol SY: **Analysis of Dishevelled signalling pathways during Xenopus development**. *Curr Biol* 1996, **6**:1456-1467.
15. Sokol SY, Klingensmith J, Perrimon N, Itoh K: **Dorsalizing and neuralizing properties of Xdsh, a maternally expressed Xenopus homolog of dishevelled**. *Development* 1995, **121**:3487.

16. Wallingford JB, Rowning BA, Vogeli KM, Rothbacher U, Fraser SE, Harland RM: **Dishevelled controls cell polarity during Xenopus gastrulation**. *Nature* 2000, **405**:81-85.

17. Rothbacher U, Laurent MN, Deardorff MA, Klein PS, Cho KW, Fraser SE: **Dishevelled phosphorylation, subcellular localization and multimerization regulate its role in early embryogenesis**. *Embo J* 2000, **19**:1010-1022.

Figure 6-1: Surface Imaging Microscopy: Surface imaging microscopy enables conversion of fixed frog embryos into high resolution digital datasets. Briefly, the frog embryo is fixed, labeled with Resolution Standard Staiin (Resolution Sciences Corporation, Corte Madera), dehydrated in ethanol, then embedded in Resolution Standard Embedding Polymer (Resolution Sciences Corporation, Corte Madera), and mounted onto the motorized translation stage (TS). This motorized stage brings the sample into the field of view of an objective lens, then draws the sample over a diamond knife to remove a thin section, then brings the freshly cut blockface of the sample back into the field of view of an objective lens. For more details see Chapter 5.

Figure 6-2: Comparison of Confocal and Surface Imaging Microscopy: Two different frog embryos were imaged with either confocal laser scanning microscopy (A) or surface imaging microscopy (B). Surface imaging microscopy provided higher contrast, more uniform imaging, and better through plane resolution. For more details see Chapter 5.

Figure 6-3: Frog Gastrulation Coordinate System: Two landmarks were selected to define a standard coordinate system for all frog gastrulae. Datasets were downsampled sixfold, and three orthogonal views through the dataset were presented to the user (A). The user then iteratively selected points until satisfied that the center of the blastopore had been identified. This point then defined the south pole of the embryo. To define the prime meridian, the program then

presented a range of sections perpendicular to the north pole–south pole axis, and presented these sections to the user. The user then identified the center of the dorsal lip of the blastopore. For more details see Appendix 2.

Figure 6-4: Digital Stage Series of Gastrulation: Four views are presented of each of six different datasets from frog gastrulae. In the first row is a volume rendering of each embryo taken from the perspective of a mid-saggital section. The second row provides a view of the outside surface of the vegetal hemisphere. The third row depicts a mid-saggital section through the dorsal midline of each embryo. Finally the bottom row shows a surface rendering of the surface of the two major cavities of the frog gastrulae: the blastocoel in purple and the archenteron in pink.

Figure 6-5: Subset of Gastrulation Series: Four embryos were selected from the digital frog gastrulation series for more detailed analysis. The same embryos are used in Figure 6-7, 6-8, 6-9 and are preserved in the same order.

Figure 6-6: Schematic of Digital Manipulations: Each of the embryo datasets from 6-5 were subjected to a three different manipulations to visualize three different morphogenetic processes. Two different volumes were extracted from the datasets. The first was a region from the south pole to the equator, with longitudinal extent ranging from +60° to –60° from the dorsal midline. When viewed from above this volume allowed us to examine the planar arrangement of

cells within epithelial sheets. When examined from edge on this same volume enabled us to view the bottle cells, the archenteron, and the interface between tissue layers. As a complementary volume we examined the entire dorsal length of the embryo, from north pole to south pole, at a longitudinal extent of +60° to –60° from the dorsal midline. When viewed from below this yielded a very useful perspective on the leading edge of the mesendoderm.

Figure 6-7: Archenteron Formation and Tissue Separation: Volumes were extracted from the series of embryos depicted in Figure 6-5 to visualize the development of tissue separation and the formation and elongation of the archenteron. Both A-D and E-H represent developmental series through the same embryos; A-D shows the 2D section at that point in the volume, whereas E-H shows the 3D volume. The tissue separation line known as Brachet's Cleft is clearly visible in each volume and its posterior limit is highlighted with a black arrow. It is worth noting that it has advanced nearly to the dorsal lip prior to involution. The arrangement of bottle cells is clearly visible in 6-7A as the dorsal lip of the blastopore first forms. The development of the archenteron progresses through sequential elongation of the archenteron (6-7B, 6-7C), followed by an inflation or expansion of the cavity (6-7D).

Figure 6-8: Vegetal Alignment Zone: The closure of the blastopore has been has been proposed to be dependent on circumferentially organized hoops of medio-laterally aligned cells, concentric with the blastopore (reviewed in [6]).

This arrangement of cells has been observed in explanted tissues [12], but not in whole embryos. To test whether we observe these cell arrangements, we selected a plane of section within the dorsal marginal zone just below Brachet's cleft (A-D) and examined the planar arrangement of cells within that layer (E-H). At early gastrula stages (E), the cells are predominantly round and display no obvious medio-lateral (left-right in panels E-H) polarity. As gastrulation proceeds more cells become polarized in the medio-lateral direction and this arrangement of cells spreads towards the anterior (top of panel) direction.

Figure 6-9: Mesendoderm Extension: The mesendoderm migrates/extends on the roof of the blastocoel at a similar time to other morphogenetic processes of gastrulation. We selected a volume along the entire dorsal length of the embryo, from north pole to south pole, at a longitudinal extent of +60° to –60° from the dorsal midline. When viewed from the perspective of the inside of the embryo looking out this volume clearly presents the leading edge of the mesendoderm (black arrows) moving along the roof of the blastocoel (faint areas). The roof of the blastocoel is thinner than surrounding tissues at these stages and so appears more transparent.

Figure 6-10: Xdd1 embryos at Stage 10.5: Embryos were injected with RNA encoding a mutant form of Dishevelled that disrupted Wnt signaling activity, Xdd1 [17]. Embryos were imaged with surface imaging microscopy at approximately

stage 10.5. No major differences were observed between control embryos and injected embryos.

Figure 6-11: Xdd1 embryos at Stage 12: Embryos were injected with RNA encoding a mutant form of Dishevelled that disrupted Wnt signaling activity, Xdd1 [17]. Embryos were imaged with surfac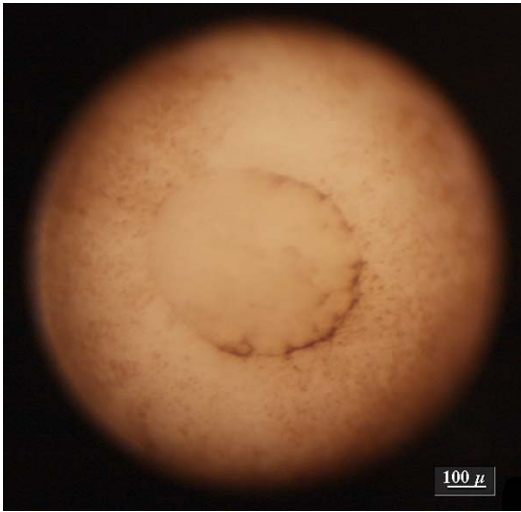e imaging microscopy at approximately stage 12. Several differences are apparent between control and treated embryos. In Xdd1 injected embryos the archenteron is shorter and has a smaller volume, while the blastocoel has a larger volume. The thickness of the dorsal marginal zone is also greater.
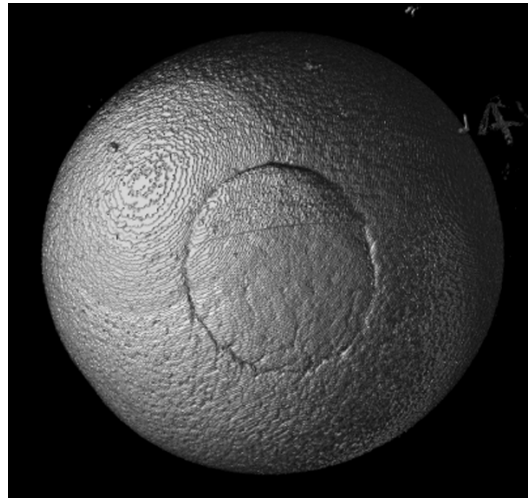
Figure 6-12: Morphometrics of Frog Gastrulation: We became interested in the coupling of different morphogenetic cell movements during gastrulation and devised a series of metrics to evaluate the degree of success of different processes in control and treated embryos. Embryos will first be photographed from the vegetal side (Panel A) to establish the degree of blastopore closure. Then the length to width ratio of the developing notochord will be calculated (Panel B). Finally the embryos will be bisected and the length of the archenteron will be normalized to the diameter of the embryo. Each of these measurements is converted to a unitless ratio to ease comparison between embryos of different sizes. Comparisons will be made between wildtype embryos to establish the normal degree of coupling of the different processes during gastrulation and

comparisons will be made between normal and experimental conditions to test which processes are obligately coupled.

Fixed Frog Embryo

Digital Frog Embryo
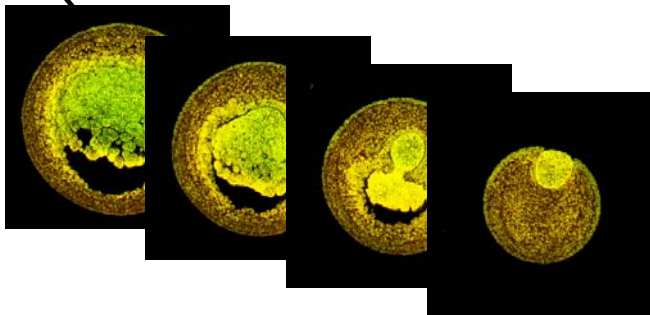
100 μ

A

Emission Filters

Dichroic Beam Splitter

Objective Lens

Sample

CCD

TS

CPU

Excitation Filters

Arc Lamp

Diamond knife
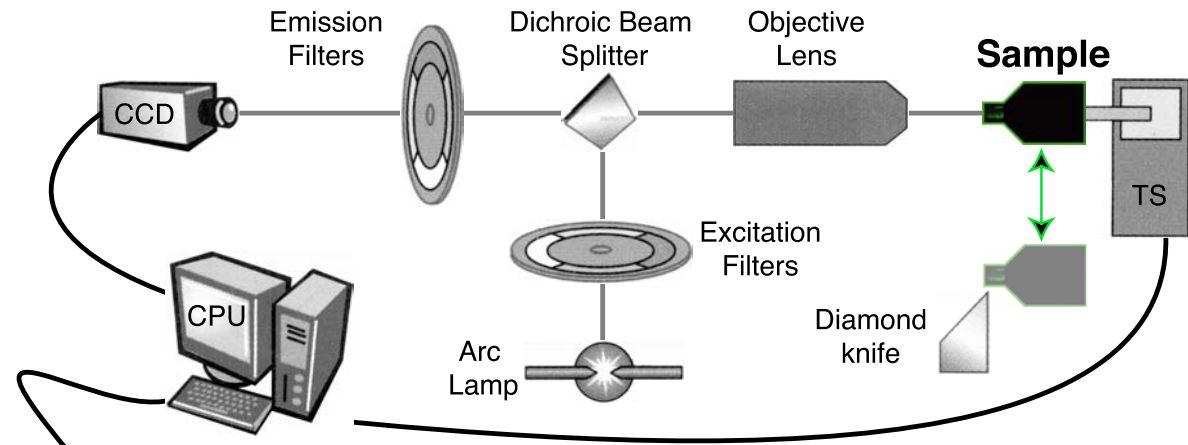
B **2D Raw Images**
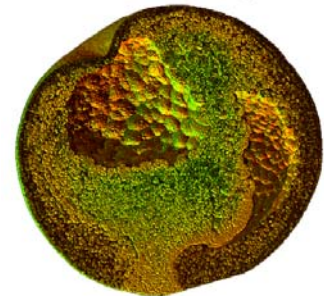
3D Reconstruction
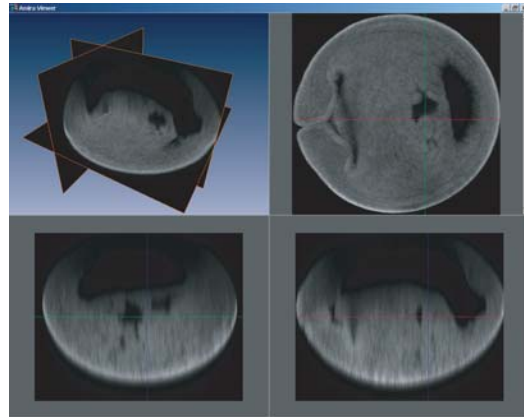
Confocal
Frog
Dataset

A
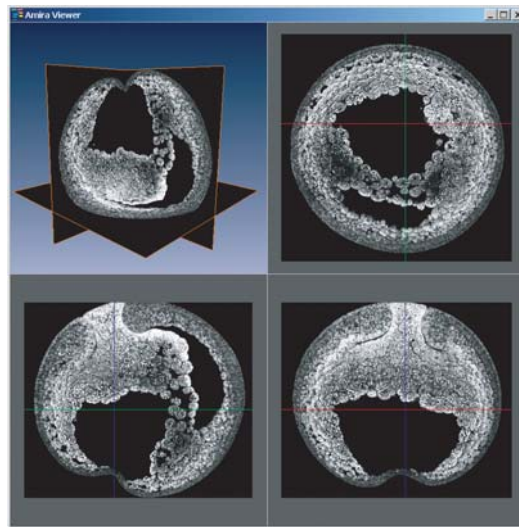
SIM
Frog
Dataset

B
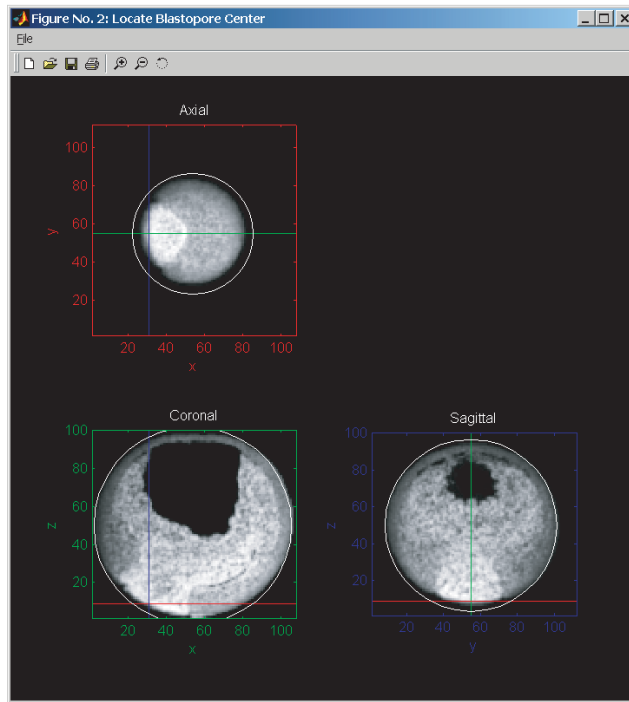
A
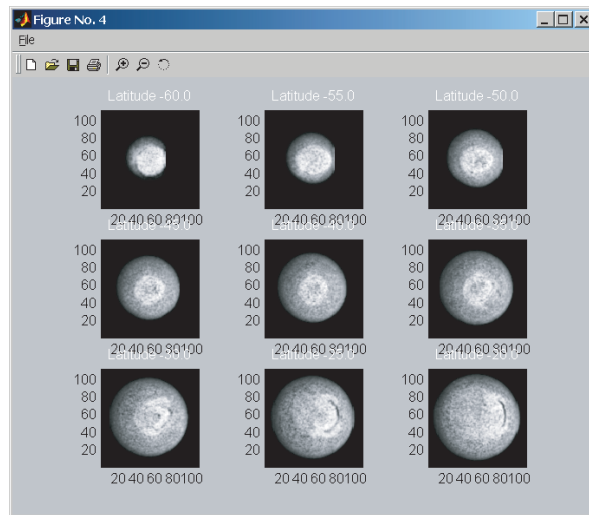
B

A Four Dimensional View of Normal Xenopus Gastrulation

6-24

A

B

C

D

Vegetal Alignment Zone

Archenteron

A

Mesendoderm Extension

B

A

B

C

D

D

E

F

G

A

B

C

D

D

E

F

G

A

B

C

D
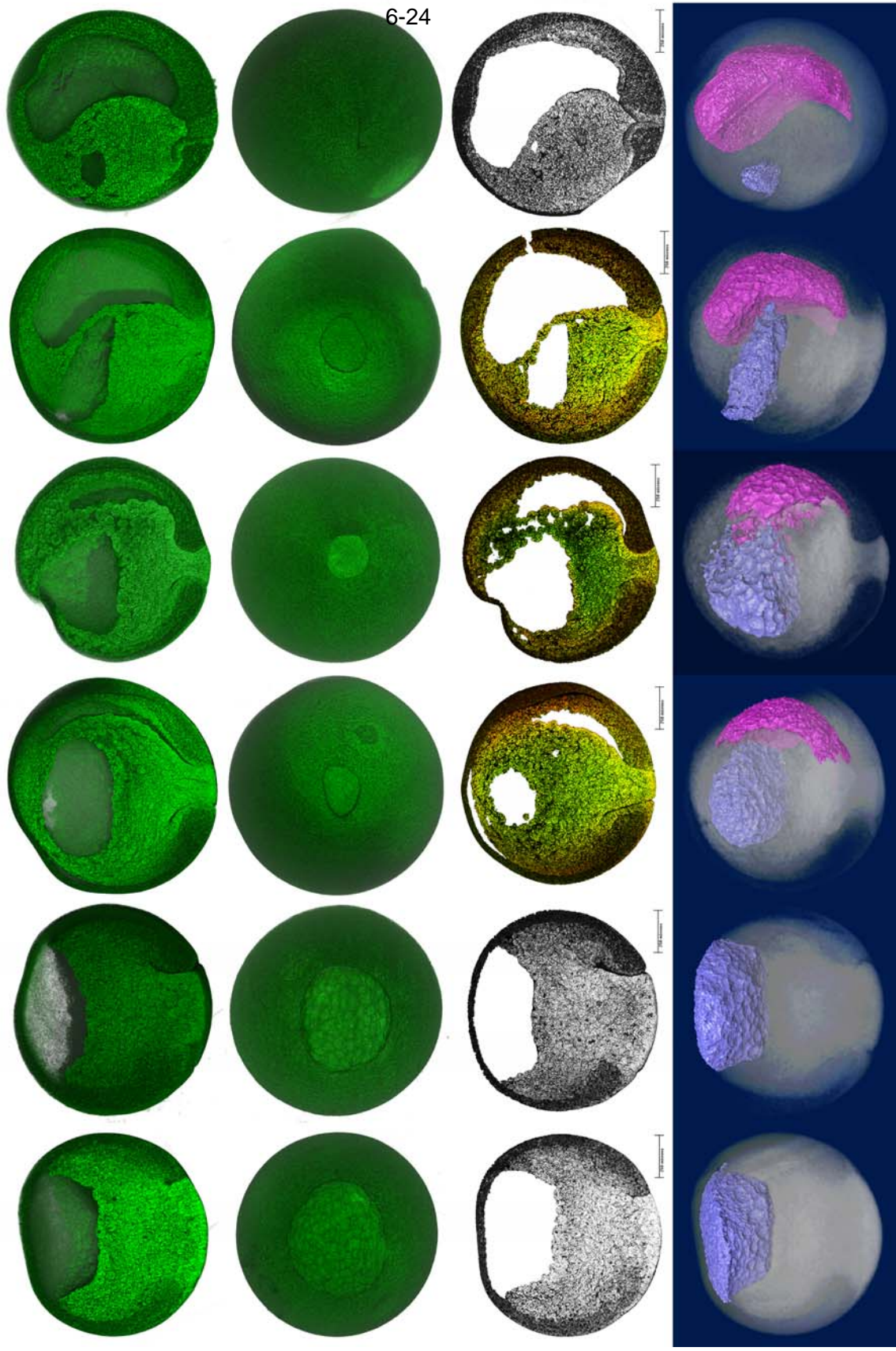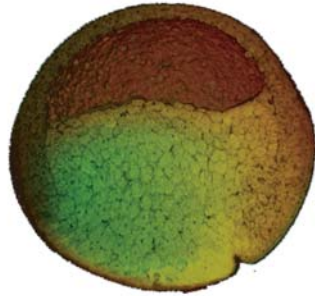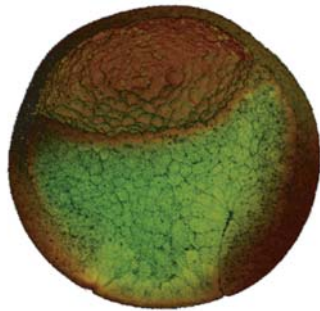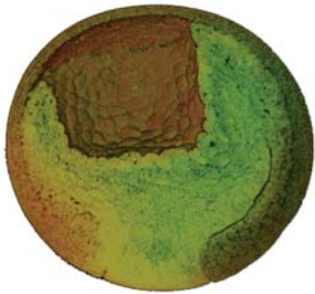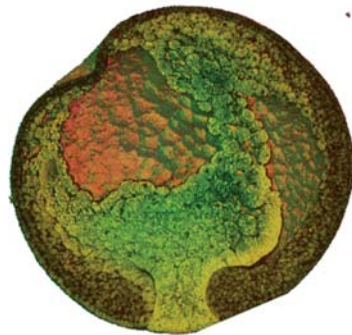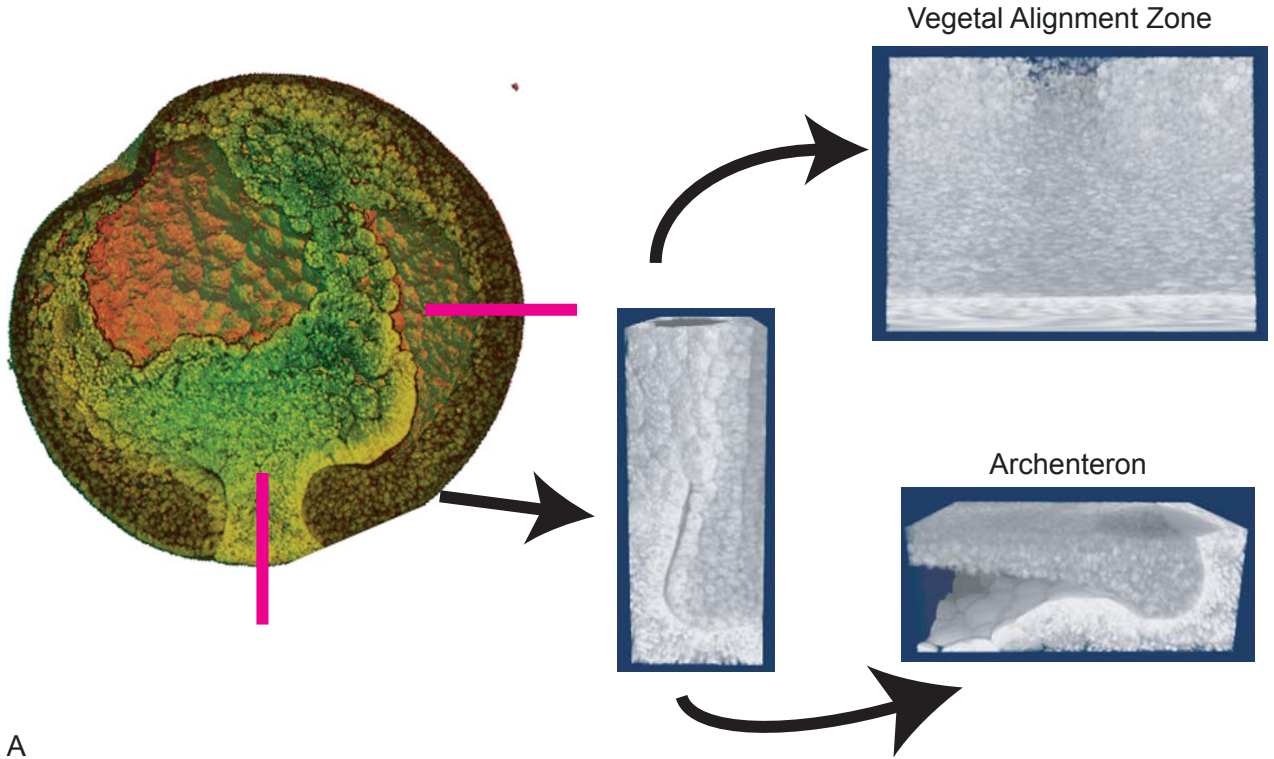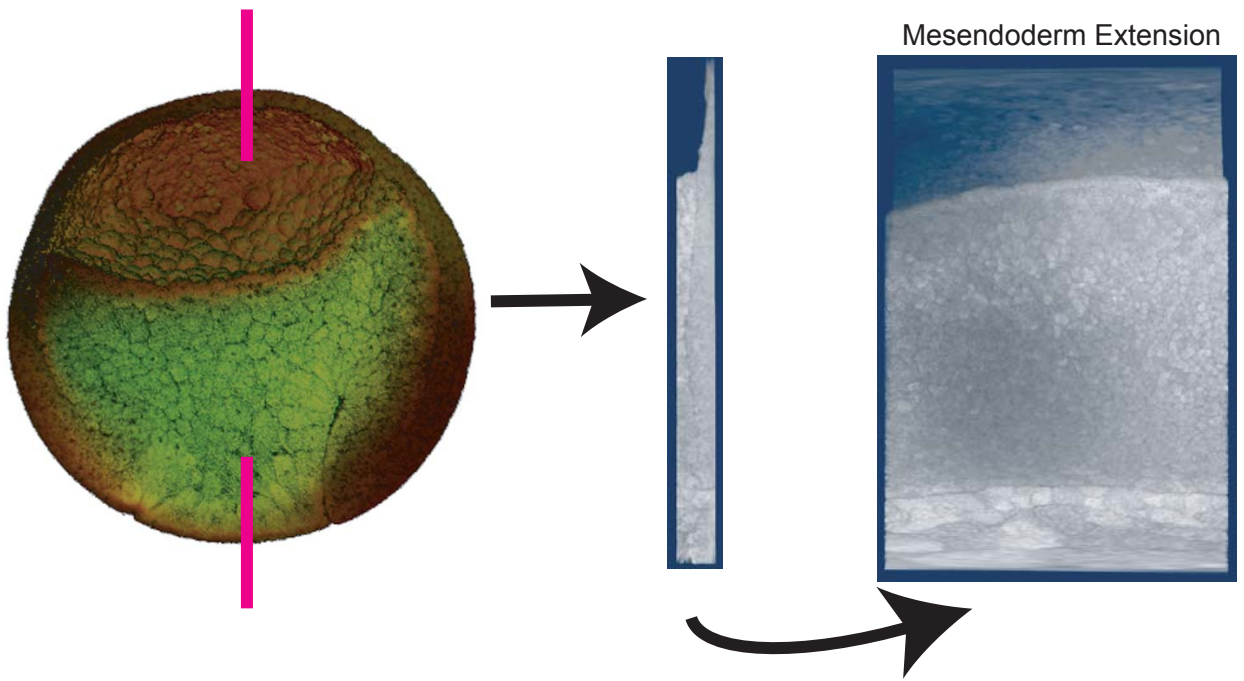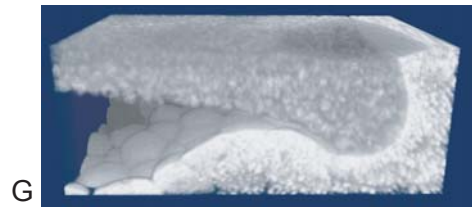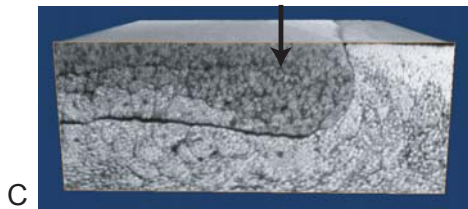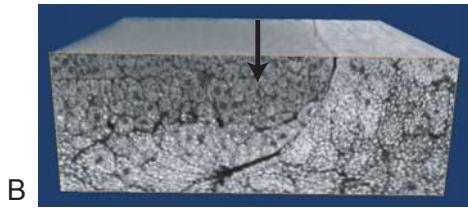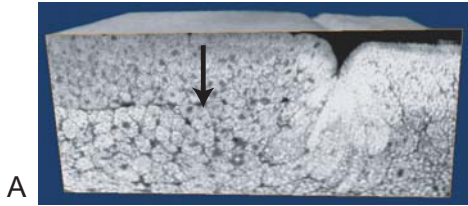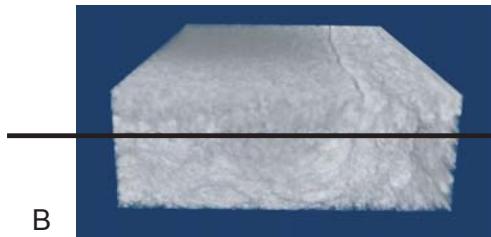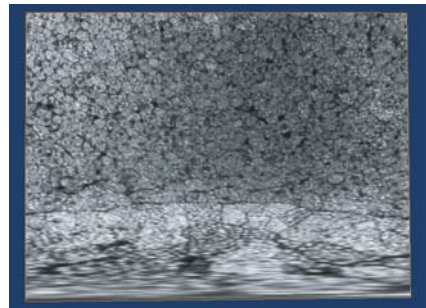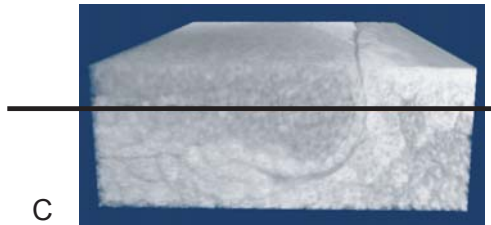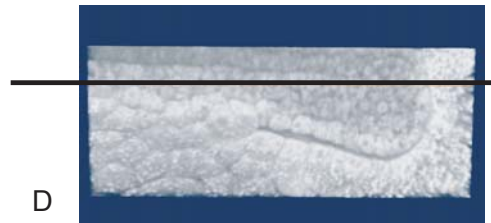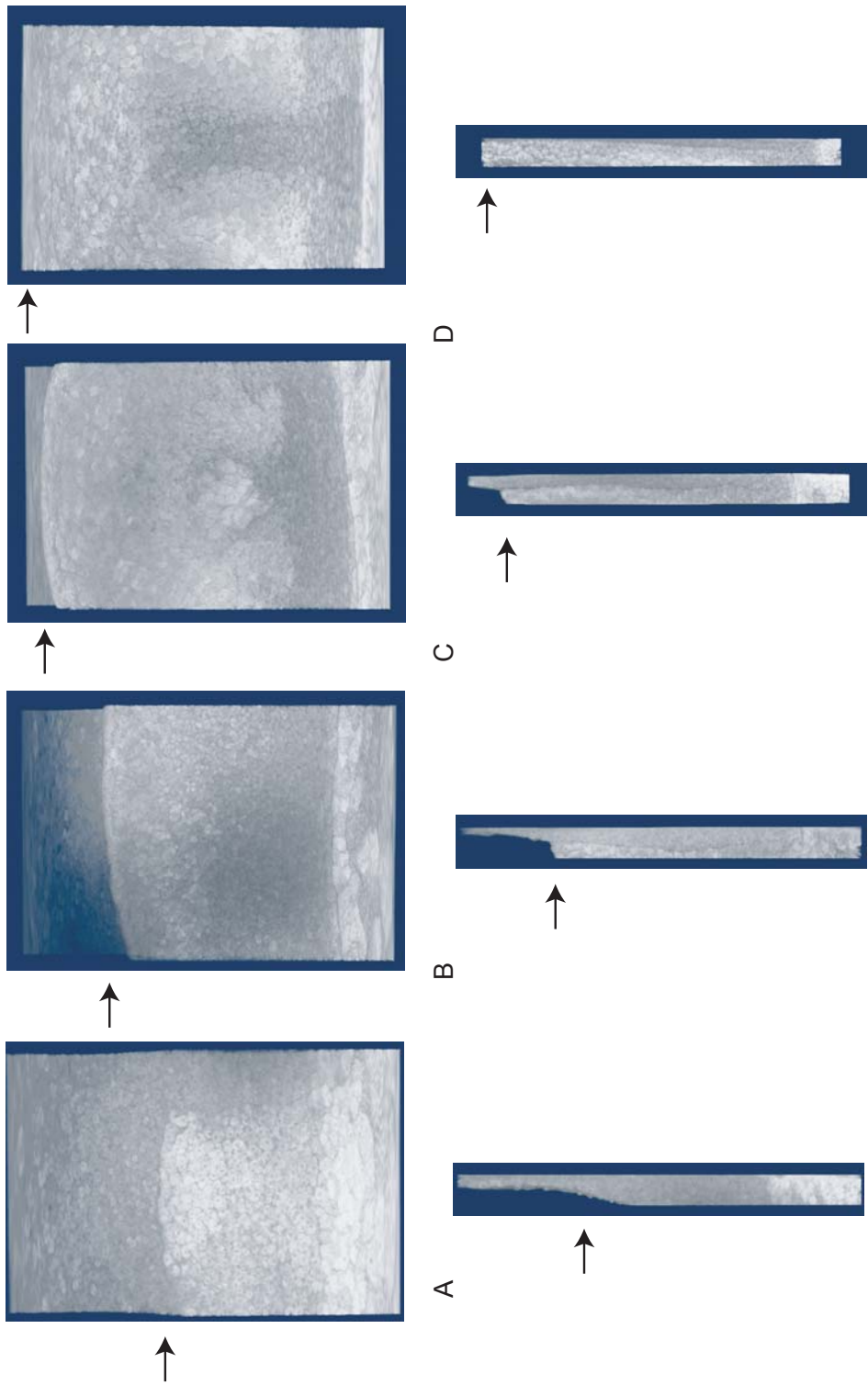
Control Stage 10.5 Frog Embryos   Xdd1 Injected Stage 10.5 Frog Embryos
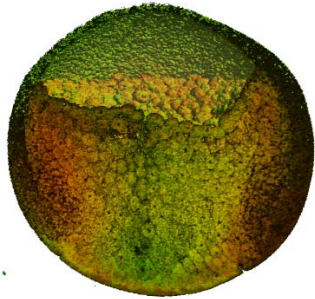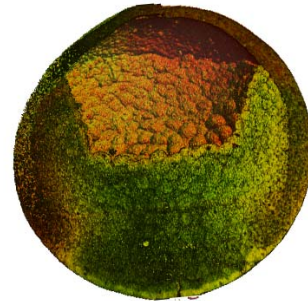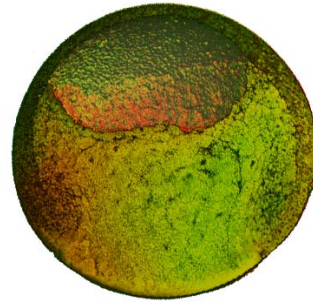
6-31

Control Stage 12 Frog Embryos

Xdd1 Injected Stage 12 Frog Embryos

Area of Embryo

Area of
Blastopore

100 μ

Length

Width

Diameter

Archenteron Length
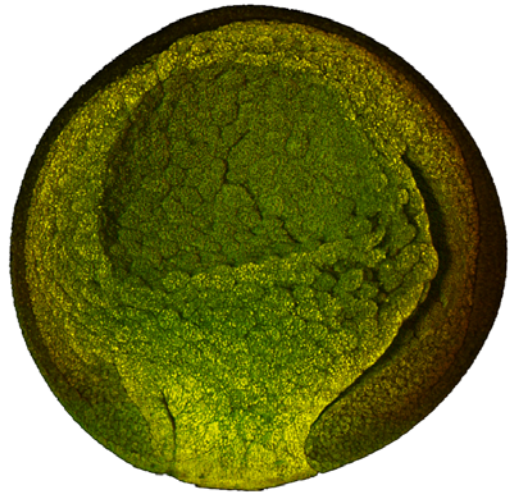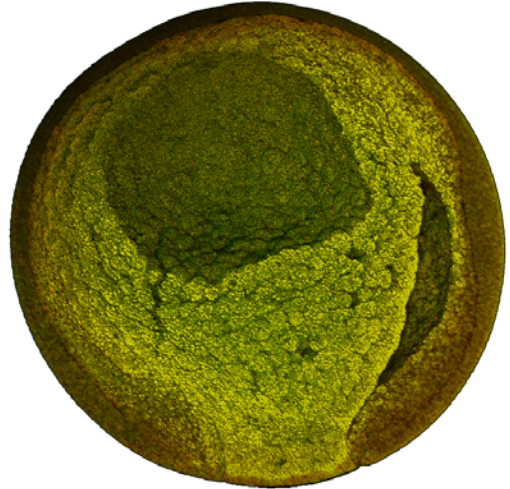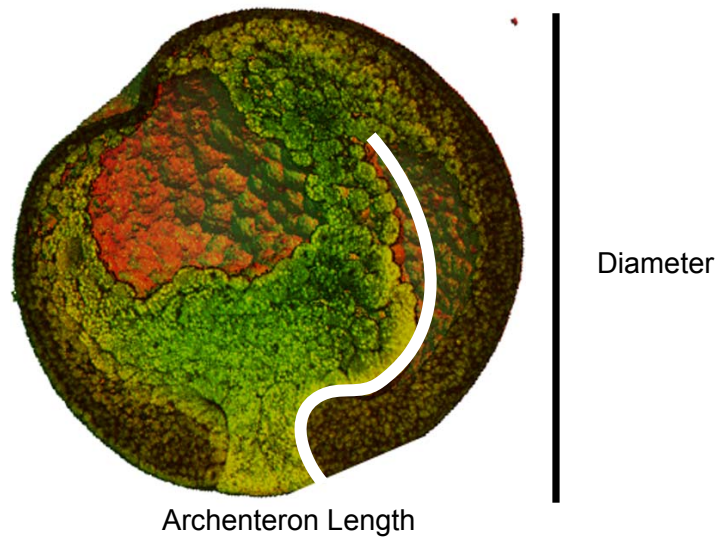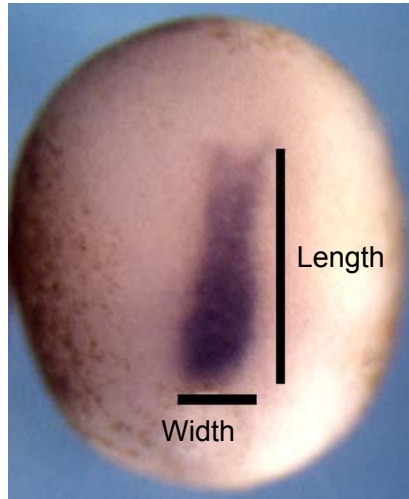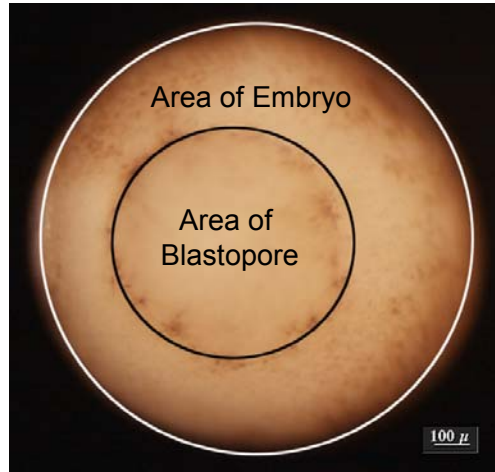
Mitofusins Mfn1 and Mfn2 Coordinately Regulate Mitochondrial Fusion and Are Essential for Embryonic Development

Hsiuchen Chen[1], Scott A. Detmer[1], Andrew J. Ewald[1,2],

Erik E. Griffin[1], Scott E. Fraser[1,2], and David C. Chan[1]

[1] Division of Biology
and [2] Biological Imaging Center,
Beckman Institute,
California Institute of Technology
MC114-96
Pasadena, CA 91125

Abstract

Mitochondrial morphology is determined by a dynamic equilibrium between organelle fusion and fission, but the significance of these processes in vertebrates is unknown. The mitofusins, Mfn1 and Mfn2, have been shown to affect mitochondrial morphology when overexpressed. We find that mice deficient in either Mfn1 or Mfn2 die in mid-gestation. However, whereas Mfn2 mutant embryos have a specific and severe disruption of the placental trophoblast giant cell layer, Mfn1-deficient giant cells are normal. Embryonic fibroblasts lacking Mfn1 or Mfn2 display distinct types of fragmented mitochondria, a phenotype we determine to be due to a severe reduction in mitochondrial fusion. Moreover, we find that Mfn1 and Mfn2 form homotypic and heterotypic complexes and show, by rescue of mutant cells, that the homotypic complexes are functional for fusion. We conclude that Mfn1 and Mfn2 have both redundant and distinct functions, and act in three separate molecular complexes to promote mitochondrial fusion. Strikingly, a subset of mitochondria in mutant cells lose membrane potential. Therefore, mitochondrial fusion is essential for embryonic development, and by enabling cooperation between mitochondria, has protective effects on the mitochondrial population.

Introduction

Mitochondria are remarkably dynamic organelles. Time-lapse microscopy of living cells reveals that mitochondria undergo constant migration and morphological changes (Bereiter-Hahn and Voth, 1994; Nunnari et al., 1997; Rizzuto et al., 1998). Even in cells with a seemingly "stable" network of mitochondrial tubules, there are frequent and continual cycles of mitochondrial fusion and fission, opposing processes that exist in equilibrium and serve to maintain the overall architecture of these organelles (Bereiter-Hahn and Voth, 1994; Nunnari et al., 1997).

In both yeast and flies, mitochondrial fusion is controlled by the nuclearly encoded mitochondrial transmembrane GTPase, *fuzzy onions* (Fzo). In *Drosophila*, Fzo is specifically and transiently expressed in spermatids. Disruption of Fzo prevents developmentally regulated mitochondrial fusion in post-meiotic spermatids and results in male sterility (Hales and Fuller, 1997). In budding yeast, deletion of *FZO1* disrupts the highly branched, tubular mitochondrial network typical of normal cells and results in numerous small, spherical mitochondria. *fzo1Δ* yeast form "petite" colonies that lack mitochondrial DNA (mtDNA) (Hermann et al., 1998; Rapaport et al., 1998). Furthermore, there is a disruption of mating-induced mitochondrial fusion (Hermann et al., 1998). Humans contain two Fzo homologs, termed mitofusin 1 (Mfn1) and mitofusin 2 (Mfn2), that can alter mitochondrial morphology when overexpressed in cell lines (Rojo et al., 2002; Santel and Fuller, 2001). Both mitofusins are broadly

expressed (Rojo et al., 2002), and therefore their functional redundancy is unclear.

Despite our increasing knowledge about the importance of mitochondrial fusion in lower eukaryotes, there is disagreement about its physiological role in vertebrates. Doubts have been raised about the frequency and importance of mitochondrial fusion in cultured mammalian cells (Enriquez et al., 2000). However, several observations suggest that this basic cellular process indeed plays a significant role in vertebrate cells. First, ultrastructural studies of mitochondria show that dramatic transitions occur during the development of certain tissues. For example, the mitochondria of rat cardiac muscle and diaphragm skeletal muscle appear as isolated ellipses or tubules in embryonic stages but then reorganize into reticular networks in the adult (Bakeeva et al., 1981; Bakeeva et al., 1978; Bakeeva et al., 1983). It is likely that these progressive morphological changes occur through mitochondrial fusion. Second, time-lapse fluorescence microscopy of cultured HeLa cells shows that the mitochondria are organized into extensive tubular networks that undergo frequent fusion and fission (Rizzuto et al., 1998). Third, experimentally induced cell hybrids demonstrate rapid mtDNA mixing (Hayashi et al., 1994) and complementation of mtDNA gene products (Nakada et al., 2001b; Ono et al., 2001). Finally, mitochondrial dynamics have been implicated in the regulation of apoptosis. Induction of cell death is sometimes associated with fragmentation of the mitochondrial network. This fragmentation requires Drp1, a dynamin-related protein involved in mitochondrial fission (Frank et al., 2001).

To assess the physiological role of mitochondrial fusion in vertebrates, we have generated knockout mice for Mfn1 and Mfn2. Our analysis reveals that Mfn1 and Mfn2 are each essential for embryonic development and mitochondrial fusion. These mitofusins can exist as both homotypic and heterotypic oligomers, and therefore can cooperate as well as act individually to promote mitochondrial fusion. In addition, our results suggest that mitochondrial fusion functions to allow cooperation between mitochondria, thereby protecting mitochondria from respiratory dysfunction.

Results

Identification of murine Fzo homologues

We identified two murine homologues of *fzo* from a mouse cDNA library. In accordance with the nomenclature for the human mitofusins (Santel and Fuller 2001), we designate these murine homologues as Mfn1 and Mfn2. Linkage analysis placed *Mfn1* at the proximal end of mouse chromosome 3 (~12-13 cM), in a region syntenic to human 3q26. *Mfn2* was localized to the distal end of mouse chromosome 4 (~70-80 cM), in a region syntenic to human 1p36.

As with the *fzo* genes from *D. melanogaster* (Hwa et al., 2002; Santel and Fuller, 2001), *H. sapiens* (Santel and Fuller, 2001), and *S. cerevisiae* (Hermann et al., 1998; Rapaport et al., 1998), each murine *Mfn* gene encodes a predicted transmembrane GTPase. The transmembrane segment is flanked by two regions containing hydrophobic heptad repeats, hallmarks of coiled-coil regions

(Lupas, 1996). Mfn1 and Mfn2 are 81% similar to each other, and are both 52% similar to *Drosophila* Fzo.

Generation of knockout mice deficient in Mfn1 and Mfn2

We constructed gene-replacement vectors for *Mfn1* and *Mfn2* using the neomycin resistance gene for positive selection and the diphtheria toxin subunit A gene for negative selection. In both cases, a stop codon was engineered at the very beginning of the GTPase domain, near the N-terminus (Fig. 1, A and E). In addition, the resulting genomic loci each contain a replacement of the G-1 and G-2 motifs of the GTPase domain with the neomycin expression cassette. These universal GTPase motifs are crucial for binding of the a and b phosphates of GTP and for Mg^{+2} coordination (Bourne et al., 1991; Sprang, 1997). Genetic analyses in *Drosophila* and *S. cerevisiae* (Hales and Fuller, 1997; Hermann et al., 1998), as well as our own studies (see later; Fig. 7C and 8C), demonstrate that an intact GTPase domain is essential for Fzo function. Therefore, the disrupted *Mfn1* and *Mfn2* alleles described here should be null alleles. Both Southern blot and PCR analysis confirmed germline transmission of the targeted alleles (Fig. 1, B, C, F and G). Importantly, Western blot analysis using affinity-purified antisera raised against Mfn1 or Mfn2 confirmed loss of the targeted protein in homozygous mutant lysates (Fig. 1, D and H).

Figure 1: Construction and verification of knockout mice

(A) Genomic targeting of *Mfn1*. The top bar indicates the wildtype *Mfn1* genomic locus, with exons aligned above. The dark gray segment contains coding sequences for the G-1 and G-2 motifs of the GTPase domain. A double crossover with the targeting construct (middle bar) results in a targeted allele (bottom bar) containing a premature stop codon (*) in exon 3 and a substitution of the G-1 and G-2 encoding genomic sequence with a neomycin resistance gene (light gray segment labeled Neo; flanking *loxP* sites indicated by triangles). PGK-DTA: diphtheria toxin subunit A driven by the PGK promoter; Xb: XbaI. (E) Genomic targeting of *Mfn2*. Drawn as in (A); RI: EcoRI. (B and F) Southern blot analyses of targeted ES clones and offspring. Genomic DNAs were digested with XbaI (B) for Mfn1 and EcoRI (F) for Mfn2 and analyzed with the probes indicated in (A and E). The wildtype and knockout bands are indicated, as are genotypes. (C and G) PCR genotyping. Three primers (labeled 1, 2, 3) were used simultaneously to amplify distinct fragments from the wildtype and mutant loci. The DNA samples are identical to those in (B and F), respectively. (D and H) Western analyses of wildtype and mutant lysates. Post-nuclear embryonic lysates were analyzed with affinity-purified antibodies directed against Mfn1 (D) and Mfn2 (H). b-actin was used as a loading control.

A

E

B

C

D

F

G
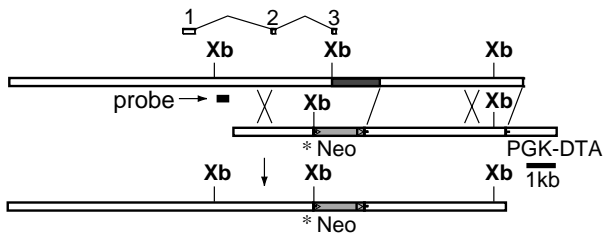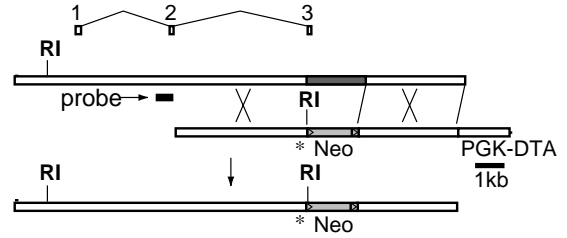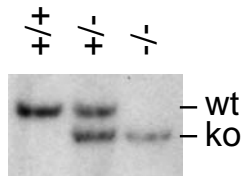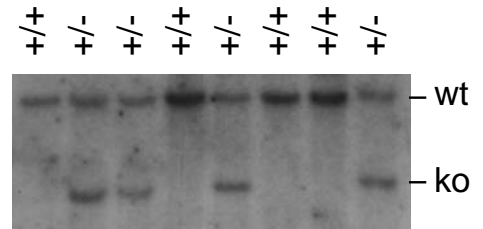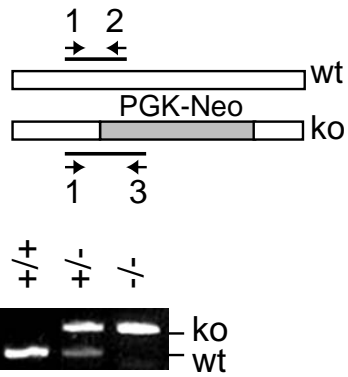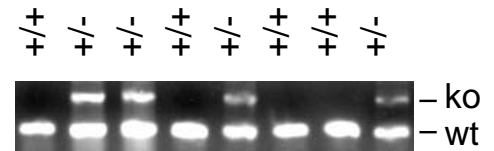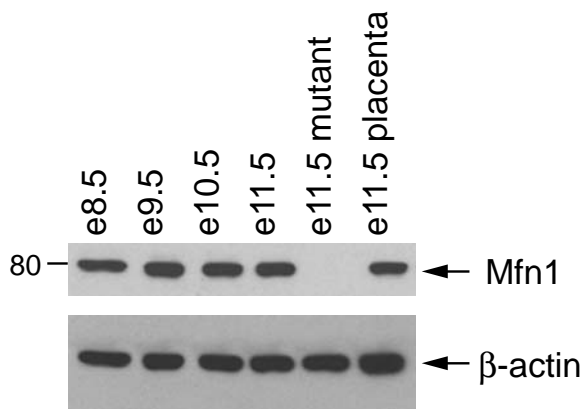
H
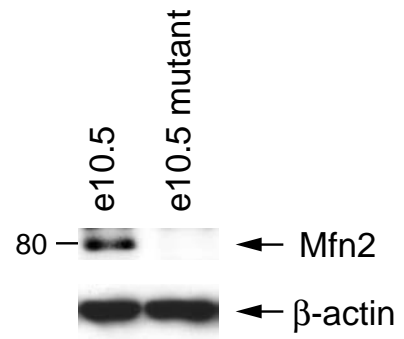
Embryonic lethality in homozygous mutant mice

Both the Mfn1 and Mfn2 knockouts demonstrate full viability and fertility in heterozygous animals, but result in embryonic lethality of homozygous mutants. For the Mfn1 knockout line, normal frequencies of live mutant embryos were obtained up to embryonic day 10.5 (e10.5; noon of the day a copulatory plug was detected is designated e0.5). However, by e11.5, 20% of the mutant embryos were resorbed, indicating inviability. At e12.5, most identifiable mutant embryos were resorbed (86%), and additional resorptions were so advanced that they could not be genotyped. Although resorptions were not evident until e11.5, by e8.5, all mutant embryos were significantly smaller and showed pronounced developmental delay. In addition, mutant embryos were often deformed.

In the Mfn2 knockout line, normal numbers of live homozygous mutant embryos were recovered up to e9.5. However, starting at e10.5, 29% of homozygous mutant embryos were in the process of resorption. By e11.5, 87% of homozygous mutant embryos were resorbed. The live homozygous mutant embryos at e9.5 and e10.5 were slightly smaller than their littermates, but were otherwise well-developed and showed no obvious malformations.

Preliminary studies indicate that double homozygous mutant embryos die earlier than either single mutant and show greater developmental delay (unpublished results). This observation suggests that Mfn1 and Mfn2 are both required, and may have a cooperative relationship, in a particular developmental event early in embryogenesis.

Placental defects in Mfn2 mutant mice

We examined placental development in detail because placental insufficiency is one of the most common causes of mid-gestation lethality (Copp, 1995). Hematoxylin-eosin stained histological sections of placentae from wildtype and heterozygous embryos showed the typical trilaminar structure composed of a proximal labyrinthine layer, a middle spongiotrophoblast layer, and a distal, circumferential giant cell layer (Fig. 2 E). Trophoblast giant cells are polyploid cells (derived from endoreplication, a process where DNA replication proceeds repeatedly without associated cytokinesis) that lie at the critical interface between fetal and maternal tissues and play important roles in hormone production, recruitment of blood vessels, and invasion of the conceptus into the uterine lining (Cross, 2000). Deficiencies in these cells lead to mid-gestation lethality (Hesse et al., 2000; Kraut et al., 1998; Riley et al., 1998; Scott et al., 2000). Strikingly, placentae from Mfn2 mutant embryos reproducibly show an impaired giant cell layer with two defects. The giant cells are deficient in quantity, and the few that are observed contain smaller nuclei, implying a reduction in the number of endoreplication cycles (Fig. 2 F). These observations were confirmed with DAPI staining, which highlights the giant cells because of their high DNA content (Fig. 2, A-D). No defects in placental development were detected in Mfn1 mutant embryos (unpublished data), despite expression of Mfn1 in the placenta (Fig. 1 D).

Using RNA *in situ* hybridization, we examined the expression of molecular markers specific for each of the three placental layers. With the giant cell marker

Figure 2: Defective giant cell layer of mutant placentae

(A-D) DAPI stained sections of placentae from e10.5 wildtype (A and C) and mutant (B and D) littermate embryos. The boxed areas of (A and B) are enlarged in (C and D). Arrows and arrowheads indicate trophoblast giant cells. Note that the giant cells in (D) are sparser and have smaller nuclei. (E and F) Hematoxylin-eosin stained sections from the placentae above. (G and H) PL-I (giant cell marker) RNA *in situ* analysis of placentae from e9.5 wildtype (G) and mutant (H) littermates.
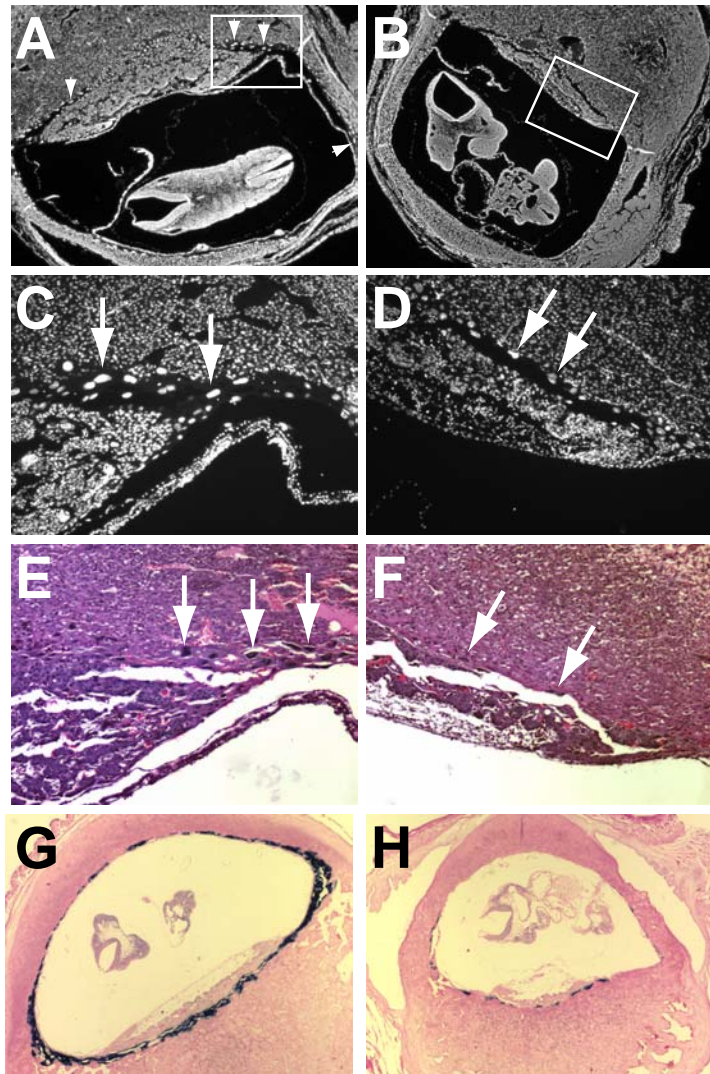
PL-I (Faria et al., 1991), wildtype placentae showed an intense full ring of giant cell staining, with multiple layers of giant cells packed in the region distal to the spongiotrophoblast layer (Fig. 2 G). In contrast, Mfn2 mutant placentae showed an incomplete ring of weakly staining giant cells (Fig. 2 H). Moreover, the giant cell layer was generally only one cell-layer thick. Similar results were seen in placentae from e8.5 through e10.5. These observations were confirmed with RNA *in situ* hybridizations (unpublished data) using the additional giant cell markers, proliferin (Lee et al., 1988) and Hand1 (Riley et al., 1998). Interestingly, our *in situ* hybridizations also revealed somewhat weaker staining with the ectoplacental cone and spongiotrophoblast marker 4311 (Lescisin et al., 1988), suggesting an additional but more subtle defect in this placental layer (unpublished data). No differences in staining between wildtype and Mfn2 mutant sections was observed using TEF5 (unpublished data), a marker for the labyrinthine layer (Jacquemin et al., 1998). Taken together, these findings suggest that the Mfn2 mutant embryos are dying in mid-gestation secondary to an inadequate placenta.

Both Mfn1- and Mfn2-deficient cells have aberrant mitochondrial morphology

To examine mitochondrial morphology in Mfn-deficient cells, we derived mouse embryonic fibroblasts (MEFs) from e10.5 embryos. The MEF cultures were infected with a retrovirus expressing mitochondrially targeted EYFP (enhanced yellow fluorescent protein). Wildtype MEFs showed a range of

mitochondrial morphologies. The major morphological class, which encompassed greater than 90% of wildtype cells, was characterized by a network of extended, wavy tubules distributed in a roughly radial manner throughout the cytoplasm. Such cells had no or only a few spherical mitochondria. The length of these mitochondrial tubules ranged from several microns to greater than 10 mm (Fig. 3, A and B; arrow). A much smaller morphological class, which encompassed only ~6% of wildtype cells, had mitochondria that were mostly spherical and were termed as "fragmented."

In contrast, Mfn1 mutant MEFs had dramatically fragmented mitochondria (Fig. 3, C and D). Greater than 95% of these cells contained only severely fragmented mitochondria, while only 1-2% of cells contained any significant tubules. Similarly, in 85% of Mfn2 mutant fibroblasts, the mitochondria appeared mostly as spheres or ovals (Fig. 3, E and F). Only a small minority of mutant cells (4.5%) contained significant tubules. Neither Mfn1 nor Mfn2 mutant cells ever displayed the networks of long, extended tubules that characterize the largest morphological class in wildtype cells. Thin-section electron microscopy revealed that, in spite of their aberrant dimensions, the spherical mitochondria in these mutant cells contained both cristae and the typical double membrane (unpublished data). These results are consistent with the hypothesis that Mfn1 and Mfn2 play major roles in mitochondrial fusion.

To determine whether mitochondrial defects underlie the placental insufficiency of Mfn2 mutant embryos, we derived trophoblast stem (TS) cell lines from wildtype and mutant blastocysts. With MitoTracker Red staining, the cells

Figure 3: Morphological defects in mitochondria of mutant cells

(A-F) Mitochondrial morphology in wildtype (A and B), Mfn1 mutant (C and D), and Mfn2 mutant (E and F) MEF cells. MEFs expressing mitochondrial EYFP (green) were counterstained with rhodamine-phalloidin (red). (B, D and F) Higher magnification images of the boxed areas in (A, C and E), respectively. Arrow indicates a tubule greater than 10 μm in length. (G and H) Mitochondrial morphology in live wildtype (G) and mutant (H) TS cells. The mitochondria were stained with MitoTracker Red, and the nuclei were stained with Syto16 (green). Several cells are tightly clustered.
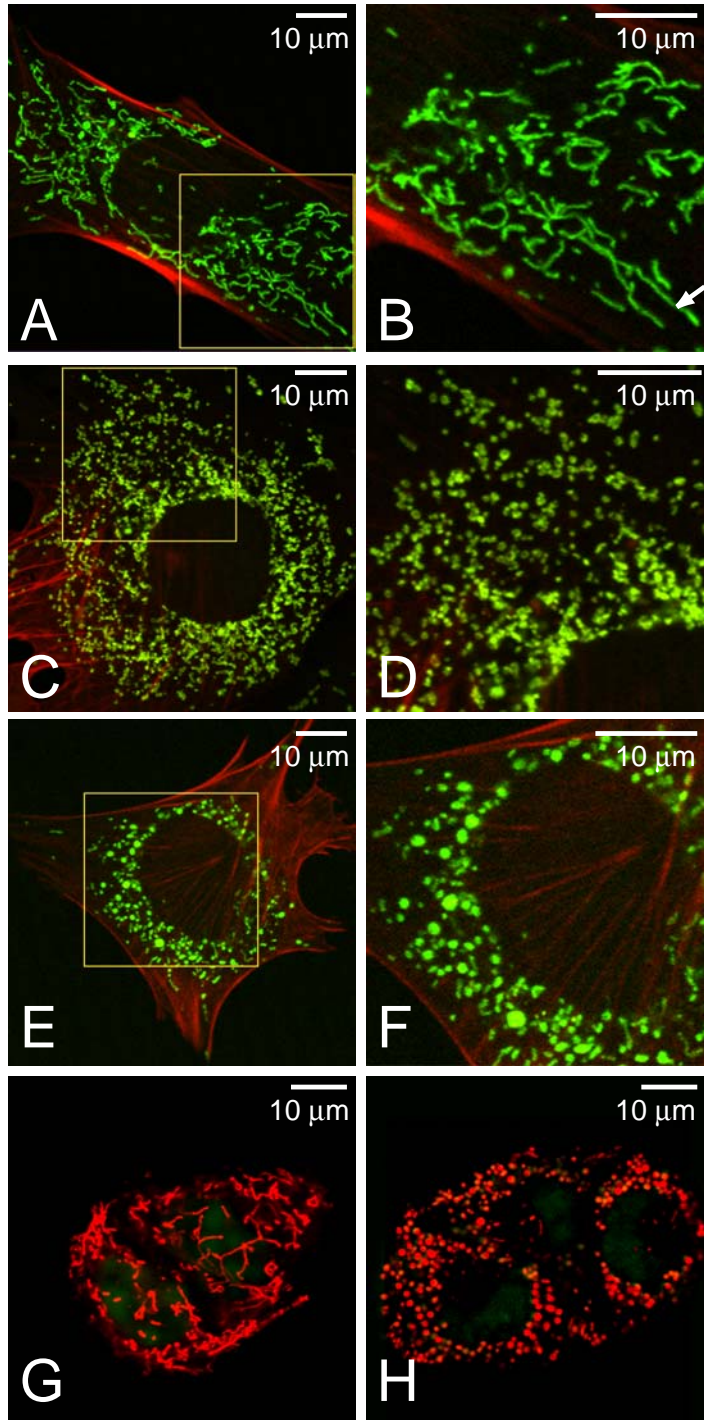
within wildtype TS colonies displayed a network of long mitochondrial tubules (Fig. 3 G). In contrast, Mfn2 mutant TS cells showed only spherical mitochondria (Fig. 3 H).

Although loss of either Mfn1 or Mfn2 results in fragmentation of mitochondrial tubules, the two mutations lead to characteristic mitochondrial morphologies that are readily distinguishable. Loss of Mfn1 leads to a greater degree of fragmentation, resulting in either very short mitochondrial tubules or very small spheres that are uniform in size, with diameters no larger than that of a normal tubule. In contrast, many Mfn2 mutant cells exhibit mitochondrial spheres of widely varying sizes. Interestingly, the diameters of some of the spherical mitochondria in both Mfn2 mutant MEF and TS cells are several times larger than the diameters of mitochondrial tubules in wildtype cells. Because a simple defect in mitochondrial fusion would be expected to result in shorter tubules and small spheres with the diameter of normal tubules, these observations suggest that, in addition to controlling mitochondrial fusion, Mfn2 is involved in maintaining tubular shape. Taken together, these results suggest that even though both Mfn1 and Mfn2 are expressed in fibroblasts, each protein is essential for mitochondrial fusion and may have some distinct functions.

Altered mitochondrial dynamics in Mfn-deficient cells

Because mitochondria are such dynamic organelles, we used time-lapse confocal microscopy to determine whether mutant MEFs display aberrations in mitochondrial dynamics. In wildtype cells, the mitochondria are highly motile, and

at least one apparent fusion or fission event was observed for most mitochondria during 20 minute recordings (Fig. 4 A; time lapse movie - supplementary materials A). In both Mfn1 and Mfn2 mutant cells, however, the ovoid or spherical mitochondria undergo fusion events much less frequently (time lapse movies - supplementary materials, B and C), although a few such events can be found (Fig. 4 C).

In addition to reduced fusion, our time-lapse movies revealed striking defects in the mobility of mitochondria in mutant cells. Most mitochondria in wildtype cells were tubular, directed radially, and move back and forth along their long axis on radial tracks (Fig. 4 A). This movement along defined tracks is consistent with reports that mitochondria can be anchored along microtubule or actin filaments, depending on the cell type (Morris and Hollenbeck, 1995; Nangaku et al., 1994; Tanaka et al., 1998b). The mitochondria of Mfn-deficient cells display a dramatic alteration in mobility; the spherical or ovoid mitochondria in mutant cells show random, "Brownian-like" movements (Fig. 4, B and C). This lack of directed movement is not due to disorganization of the cytoskeleton, because staining with an anti-tubulin monoclonal antibody or rhodamine-phalloidin revealed no defects (unpublished data and Fig. 3). Strikingly, in Mfn2 mutant cells with both spherical and short tubular mitochondria, the tubular mitochondria can still move longitudinally along radial tracks, whereas the spherical mitochondria do not. The two morphological classes are interchangeable, however, because tubules can project out of spheres and subsequently move away (Fig. 4 D), or conversely, tubules can merge with

Figure 4: Dynamics of mitochondria in wildtype and mutant cells

Still frames from time-lapse confocal microscopy. (A) In a wildtype cell, two pairs of mitochondria can be seen moving towards each other. These pairs contact end-to-end and fuse immediately. Note that mitochondria move along their long axes. (B) In a Mfn1 mutant cell, the mitochondria move in an undirected manner. (C) In a Mfn2 mutant cell, two ovoid mitochondria contact each other but do not fuse until much later. Note also the lack of directed movement in most mitochondria. (D) One spherical Mfn2-deficient mitochondrion protrudes a tubular extension that separates and then migrates away along its long axis. Images were processed in Adobe Photoshop with the emboss filter, and selected mitochondria were manually highlighted in blue.
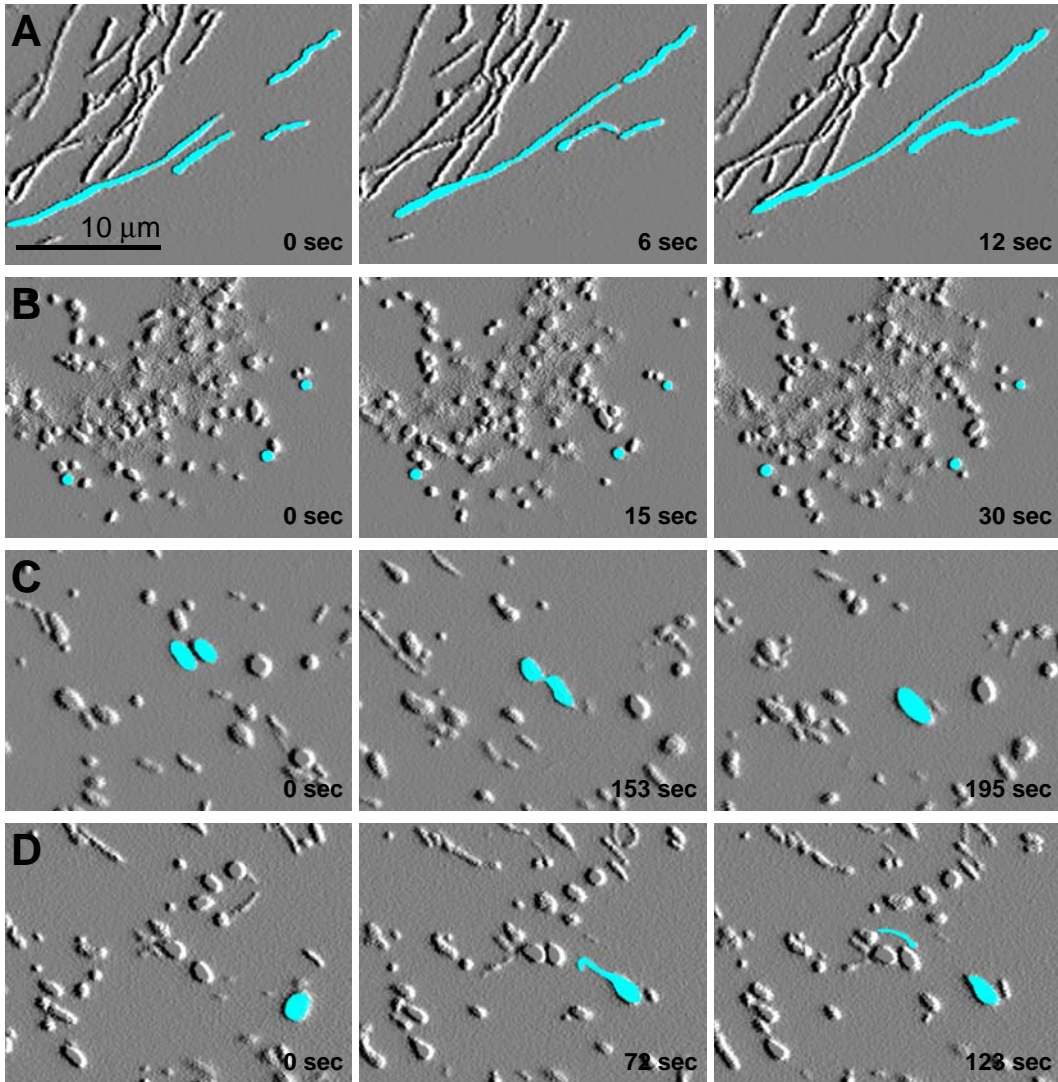
spheres and lose directed movement. These observations suggest that there is no intrinsic defect in mobilizing Mfn2-deficient mitochondria. Instead, the hampered mobility of spherical mitochondria is secondary to their altered morphology resulting from reduced fusion.

Decreased mitochondrial fusion rates in cells lacking Mfn1 or Mfn2

To definitively show that lack of fusion is the basis for the fragmented mitochondria in mutant cells, we measured mitochondrial fusion activity using a polyethylene glycol (PEG) cell fusion assay. A cell line expressing mitochondrially targeted dsRed was co-cultured with a cell line expressing mitochondrially targeted GFP, and PEG was transiently applied to fuse the cells. Cycloheximide was included to prevent synthesis of new fluorescent molecules in the fused cells. When wildtype cells were examined 7 hours after PEG treatment, all the fused cells (n=200) contained extensively fused mitochondria (Fig. 5 A), as demonstrated by co-localization of red and green fluorescent signals. In contrast, when Mfn1 mutant cells were examined 7 hours after PEG fusion, 57% (n=364) of the fused cells contained predominantly unfused mitochondria (Fig. 5, B and C), even when red and green mitochondria were dispersed throughout the fused cell. 35% of cells showed extensive mitochondrial fusion, and 8% showed partial fusion. Similarly, 69% (n=202) of fused Mfn2 mutant cells showed predominantly unfused mitochondria after 7 hours (Fig. 5, E and F); 1% showed extensive fusion, and 30% showed partial fusion. Mfn1 and Mfn2 mutant cells with unfused mitochondria were observed

Figure 5: Mitochondrial fusion assay

PEG fusion of cells containing mitochondrially targeted dsRed and GFP. (A) Wildtype cell showing extensive mitochondrial fusion. (B and E) Mfn1 (B) and Mfn2 (E) mutant cells displaying predominantly unfused mitochondria. (C and F) Magnified views of boxed portions in (B and E), respectively. (D) Sectoring effect in Mfn1 mutant cell.
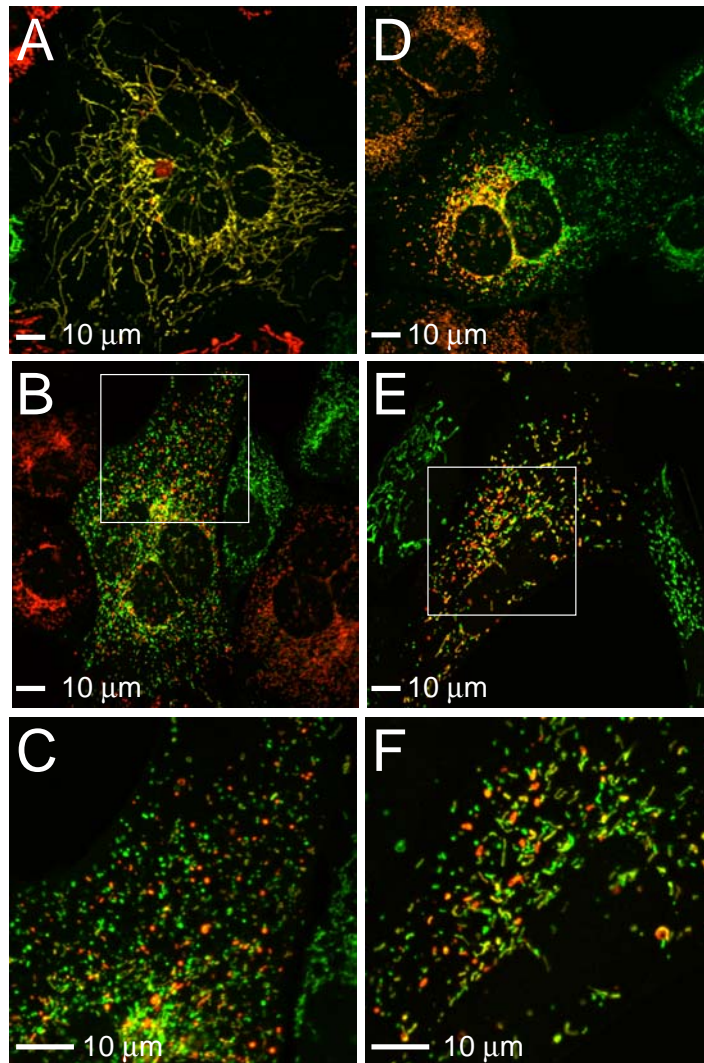
even 24 hours after PEG treatment (unpublished data). Thus, mutant cells have severely reduced levels of mitochondrial fusion. Interestingly, in 10% of fused Mfn1 mutant cells, the mitochondria did not readily spread throughout the cytoplasm, as shown by discrete sectors of red and green fluorescence (Fig. 5 D). Only 1% of fused Mfn2 mutant cells exhibited this sectoring effect. Therefore, it seems that the mobility of Mfn1-deficient mitochondria is impaired to a greater extent than that of Mfn2-deficient mitochondria, perhaps due to their more severely fragmented morphology.

Stochastic defects in mitochondrial membrane potential

We tested whether Mfn1 and Mfn2 mutant cells lose mtDNA, because there is complete loss of mtDNA in *fzo1Δ* yeast (Hermann et al., 1998; Rapaport et al., 1998). Southern blot and PCR analysis showed that both mutant cell lines contain normal levels of mtDNA (Fig. 6 A and unpublished data). In addition, the mitochondria in mutant cells expressed COX1, a mitochondrial protein encoded by mtDNA (Fig. 6, B and C). Therefore, unlike *fzo1Δ* yeast, Mfn-deficient cells clearly retain mtDNA, and this feature allows a critical assessment of the relationship between respiration and mitochondrial fusion. Like wildtype cells, both Mfn1 and Mfn2 mutant cultures showed high rates of endogenous and coupled respiration (unpublished data), indicating no gross defects in respiration and further confirming that mtDNA products are intact and functional.

Although the mutant cells are capable of respiration, we reasoned that functional defects may exist at the level of individual mitochondria. To test this

Figure 6: Stochastic loss of membrane potential in mitochondria of mutant cells

(A) mtDNA is detected by Southern blot analysis using a *COX1* probe. (B and C) COXI expression in Mfn1 (B) and Mfn2 (C) mutant cells. (D-F) Staining of mitochondria using dyes sensitive to membrane potential. Wildtype (D), Mfn1 mutant (E), and Mfn2 mutant (F) cells expressing mitochondrially targeted EYFP (green) were stained with the dye MitoTracker Red, whose sequestration into mitochondria is sensitive to membrane potential. In these merged images, note that in the mutant cells (E and F), a subset of mitochondria (arrows) stain poorly with MitoTracker Red and thus appear green.
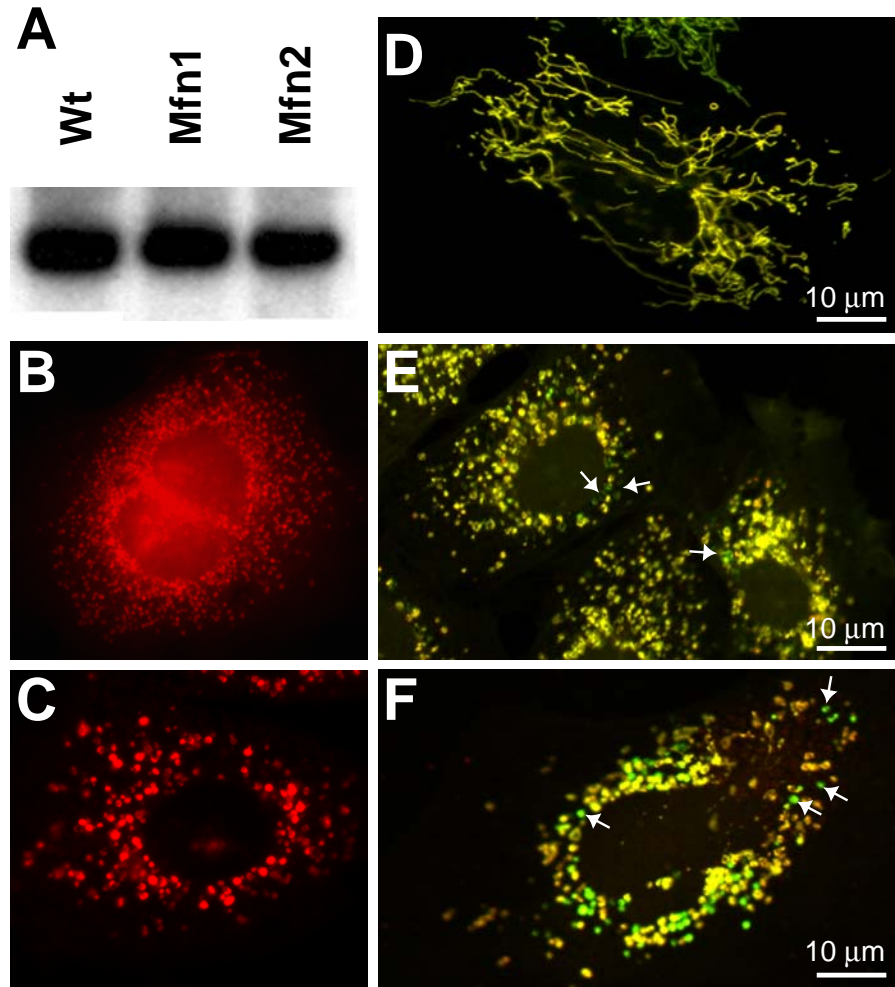
hypothesis, we used MitoTracker Red, a lipophilic cationic dye which is sensitive to the mitochondrial membrane potential, to stain MEFs expressing EYFP targeted to the mitochondrial matrix. In wildtype cells, EYFP-marked mitochondria were typically uniformly stained with MitoTracker Red, resulting in co-localization of the two fluorophores (Fig. 6 D). In 7% of wildtype cells, there existed isolated mitochondria that were labeled with EYFP but failed to sequester MitoTracker Red dye. Such mitochondria were invariably small and spherical, as opposed to the tubular mitochondria that predominate in these cells. In Mfn1 mutant cultures, almost every cell contained a subset of mitochondria that showed poor staining with MitoTracker Red (Fig. 6 E). Likewise, in Mfn2 mutant cultures, over one third of the cells showed some mitochondria that were marked by EYFP but not by MitoTracker Red (Fig. 6 F). It is likely that the compromised mitochondria detected by this assay initially contained membrane potential, because the matrix-targeted EYFP requires an intact membrane potential for import. Because of the high stability of EYFP, mitochondria that subsequently lose or reduce their membrane potential would still contain EYFP fluorescence. These results indicate that while bulk cultures display respiratory activity, the function of individual mitochondria is compromised in the absence of either Mfn1 or Mfn2.

Rescue of mitochondrial tubules by modulation of fusion or fission

To unequivocally demonstrate that the mitochondrial morphological defects observed in mutant cells are due to loss of Mfn, we tested whether these

defects could be rescued by restoration of Mfn function and whether such rescue depended on an intact GTPase domain. In uninfected Mfn1 mutant cultures or mutant cultures infected with an empty virus, greater than 95% of the cells showed highly fragmented mitochondria that lacked interconnections (Fig. 7, A and F). However, when Mfn1 mutant cultures were infected with a retrovirus expressing Mfn1-Myc, greater than 90% of the infected cells showed extensive mitochondrial networks consisting of long tubules (Fig. 7, B and F). Similarly, greater than 80% of Mfn2 mutant cells infected with a Mfn2-expressing retrovirus showed predominantly tubular mitochondria (Fig. 8, B and F). In contrast, constructs carrying mutations in the GTPase G-1 motif [Mfn1(K88T) and Mfn2(K109A)] had greatly reduced ability to restore tubular structure (Fig. 7, C and F; Fig. 8, C and F). These results show that both Mfn1 and Mfn2 promote mitochondrial fusion in a GTPase-dependent manner.

Although both Mfn1 and Mfn2 are clearly required for normal mitochondrial tubules in MEFs, we were able to rescue the morphological defects by overexpression of a single mitofusin. Overexpression of Mfn1 in Mfn2-deficient cells was sufficient for rescue of mitochondrial morphology (Fig. 8, D and F). In addition, overexpression of Mfn2 in Mfn1-deficient cells was sufficient to restore mitochondrial tubules (Fig. 7, D and F). These results show that although both Mfn1 and Mfn2 are required *in vivo* for normal mitochondrial morphology in MEFs, when overexpressed, each protein is capable of acting alone to promote mitochondrial fusion. Interestingly, these experiments also reveal differential activities of the two homologues. With Mfn2-deficient cells, both Mfn1-Myc and

Figure 7: Rescue of Mfn1-deficient cells

Mfn1 mutant cells (A) were infected with a retrovirus expressing Myc epitope-tagged versions of Mfn1 (B), Mfn1(K88T) (C), Mfn2 (D), or dominant-negative Drp1(K38A) (E). In the merged images, mitochondrial morphology is revealed by MitoTracker Red staining, and infected cells are identified by immunofluorescence with an anti-Myc antibody (green). In (E), the signals are largely non-overlapping because most of the Drp1 resides in a cytosolic pool. The results are summarized in (F), which depicts the percentage of infected cells belonging to each of four morphological classifications. Six hundred cells were scored for each infection.

A1-30

A   Uninfected

B   Mfn1

C   Mfn1(K88T)

D   Mfn2

E   Drp1(K38A)

F

- Tubular network
- >50% tubular
- >50% fragmented
- Completely fragmented

None   Mfn1   K88T   Mfn2   Drp1(K38A)

10 µm
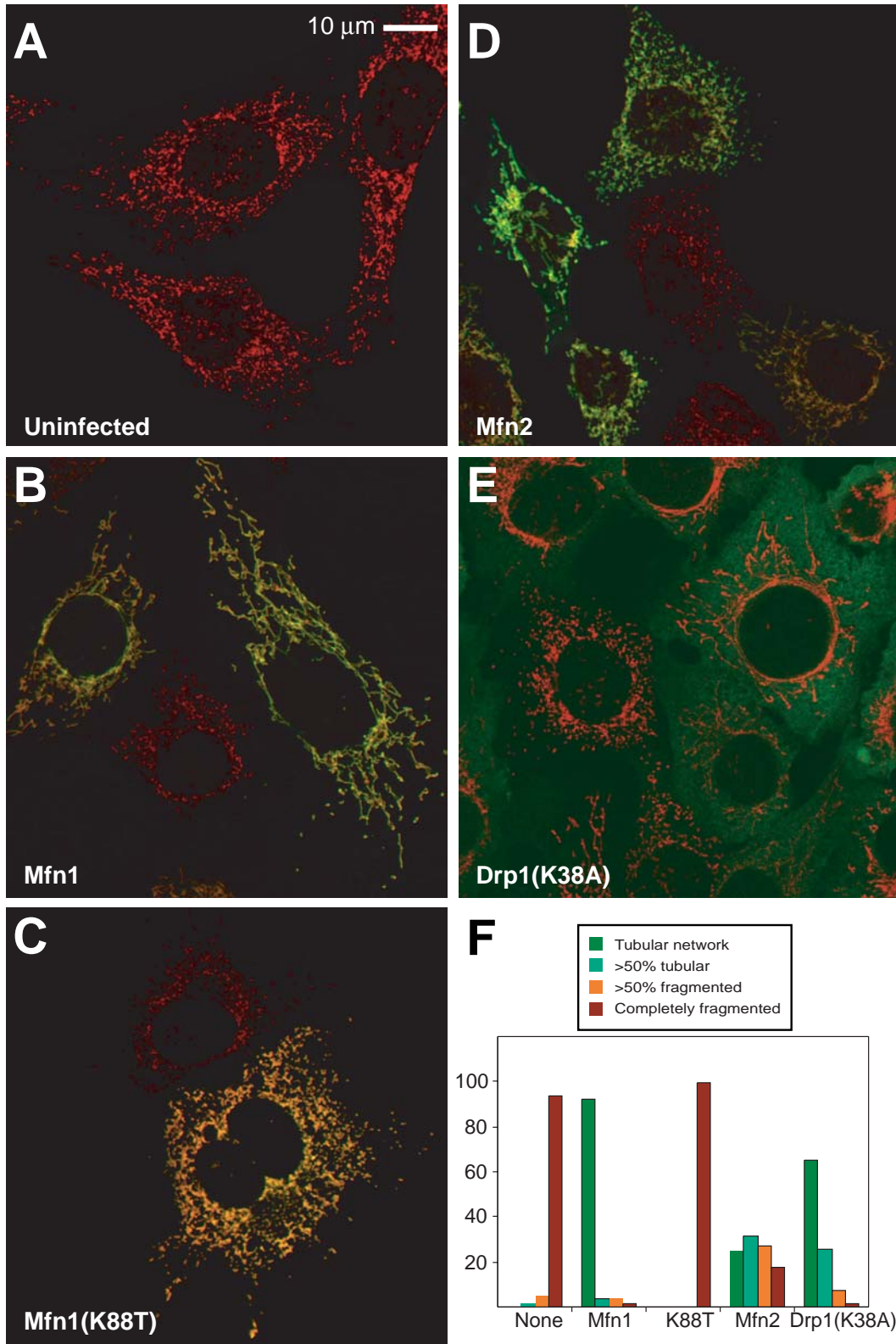
Mfn2-Myc were equally effective in restoring extensive mitochondrial networks, resulting in rescue in 75-80% of expressing cells (Fig. 8 F). In contrast, with Mfn1-deficient cells, 91% of Mfn1-Myc infected cells showed entirely tubular networks, but only 25% of Mfn2-Myc infected cells showed such a phenotype (Fig. 7 F).

Because the morphological defects in mutant cells were clearly reversible, we tested whether inhibition of mitochondrial fission could also restore tubular structure. Drp1, a dynamin-related protein, plays a key role in mediating mitochondrial fission. To inhibit fission, we constructed an allele of mouse Drp1 with the same mutation (K38A) as in a dominant-negative allele of human Drp1 (Smirnova et al., 2001). Infection of either Mfn1 or Mfn2 mutant cells with a retrovirus expressing Drp1(K38A) resulted in a striking restoration of mitochondrial tubules in 90% (Fig. 7, E and F) and 50% (Fig. 8, E and F) of the cells, respectively. Although the mitochondrial networks in these infected cells were tubular, they were imperfect compared to the networks obtained by rescue with Mfn1 or Mfn2. First, the thickness of the tubules promoted by Drp1(K38A) were less uniform, often showing regions of thinning attached to thicker knobs. Second, the mitochondrial networks were generally less dispersed, with an increase in density near the cell nucleus that often gave the appearance of circumferential rings. Nevertheless, these results indicate that a reduction in fusion caused by loss of Mfn1 or Mfn2 can be compensated, at least partially, by a reduction in fission.

Figure 8: Rescue of Mfn2-deficient cells

Mfn2 mutant cells (A) were infected with a retrovirus expressing Myc epitope-tagged versions of Mfn2 (B), Mfn2(K109A) (C), Mfn1 (D), or dominant-negative Drp1(K38A) (E). The cells were stained as in Figure 7. The results are summarized in (F). Two hundred cells were scored for each infection.

A1-33

A Uninfected
10 μm

B Mfn2

C Mfn2(K109A)

D Mfn1

E Drp1(K38A)

F
- Tubular network
- >50% tubular
- >50% fragmented
- Completely fragmented

None   Mfn2   K109A   Mfn1   Drp1(K38A)
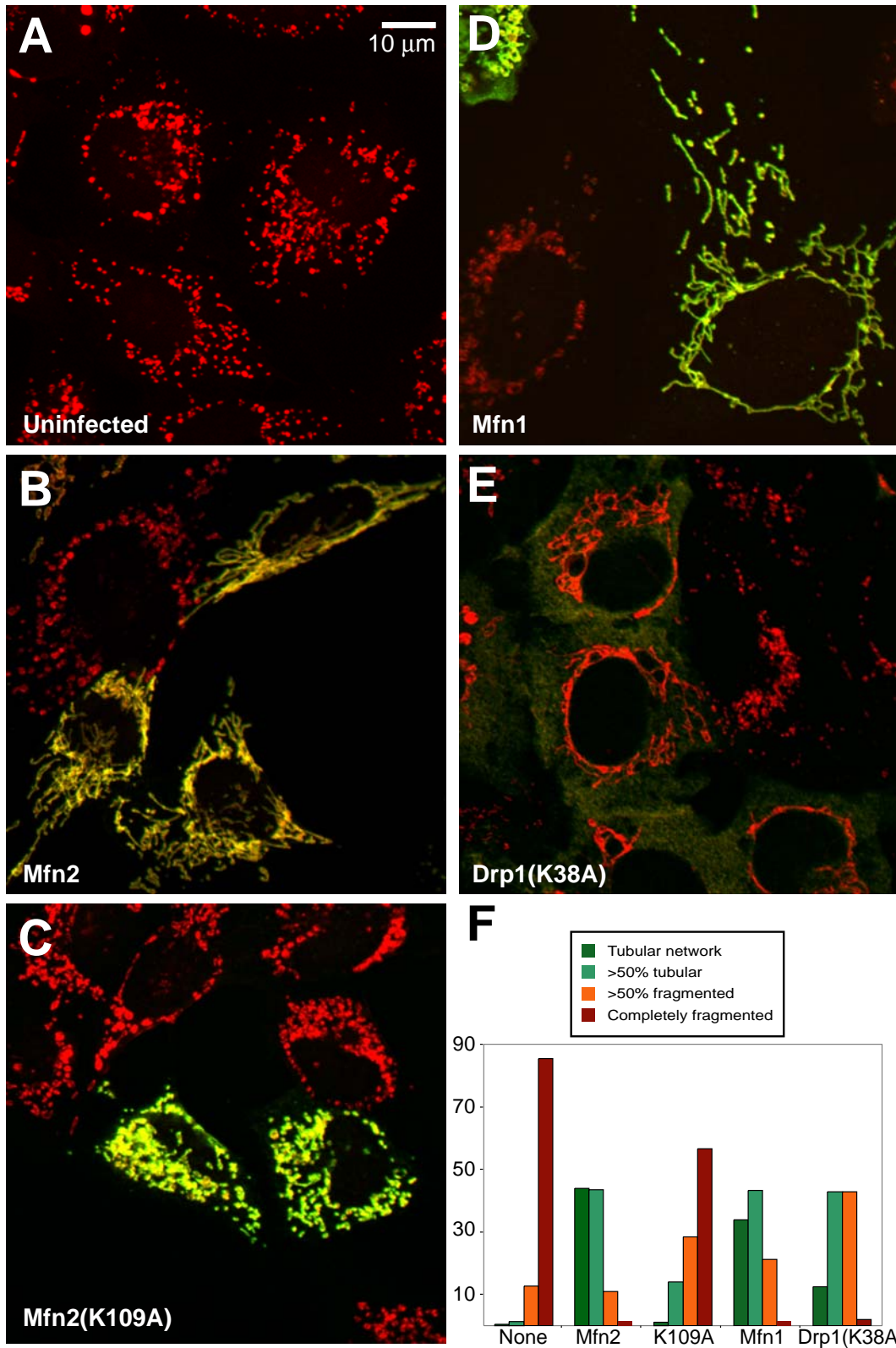
Mfn1 and Mfn2 form homotypic and heterotypic oligomers

Because both Mfn1 and Mfn2 are essential for normal mitochondrial morphology, it is possible that they act in concert to promote mitochondrial fusion. To explore this idea, we tested whether these two proteins form a complex when expressed in wildtype MEF cells (Fig. 9 A). Our results revealed three types of intermolecular interactions. First, both Mfn1 and Mfn2 can form homotypic complexes. Mfn1-HA is co-immunoprecipitated with Mfn1-Myc; analogously, Mfn2-HA is co-immunoprecipitated with Mfn2-Myc. Second, Mfn1 and Mfn2 form heterotypic complexes. Mfn2-HA is co-immunoprecipitated with Mfn1-Myc; conversely, Mfn1-HA is co-immunoprecipitated with Mfn2-Myc. All of these interactions are specific, because no HA tagged protein is found in the anti-Myc immunoprecipitate when the Myc-tagged protein is omitted (unpublished data) or when a control Drp1-Myc is used.

It is a formal possibility that the homotypic interactions detected might not be strictly homotypic due to the expression of endogenous Mfn1 and Mfn2 in the parental cells. To relieve these concerns, we also performed the immunoprecipitation assay in mutant MEFs (Fig. 9 B). We find that Mfn1-Mfn1 homotypic complexes are formed in Mfn2-deficient cells, thereby showing that this interaction is strictly homotypic. Likewise, we also detect Mfn2-Mfn2 homotypic complexes in Mfn1-deficient cells.

Figure 9: Immunoprecipitation of Mfn complexes

(A) Wildtype cells were infected with retroviruses expressing Myc- or HA-tagged Mfn1 (labeled 1), Mfn2 (labeled 2), or Drp1 (labeled D) as indicated on top. Anti-Myc immunoprecipitates (top) and total cell lysates (bottom) were analyzed by Western blotting against the HA epitope. The total cell lysate samples contain 1/6 cell equivalents compared to the immunoprecipitates. (B) Anti-Myc immunoprecipitates (top) and total cell lysates (bottom) from Mfn1 or Mfn2 mutant cells (indicated on top) were used in an analysis similar to (A).

A

1	2	1	2	1	2	HA
1	2	2	1	D	D	Myc

Mfn1-HA
Mfn2-HA

Mfn1-HA
Mfn2-HA

B

Mfn1 (-/-)   Mfn2 (-/-)

2	2	1	1	HA
2	-	1	-	Myc

Mfn1-HA
Mfn2-HA

Mfn1-HA
Mfn2-HA
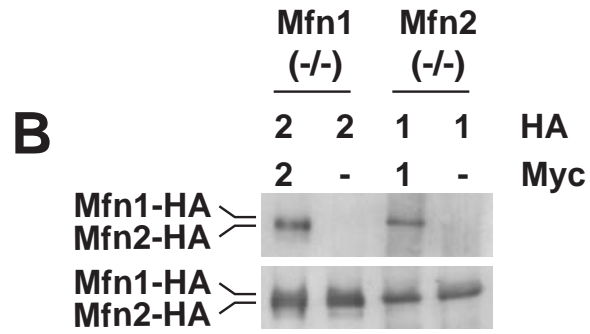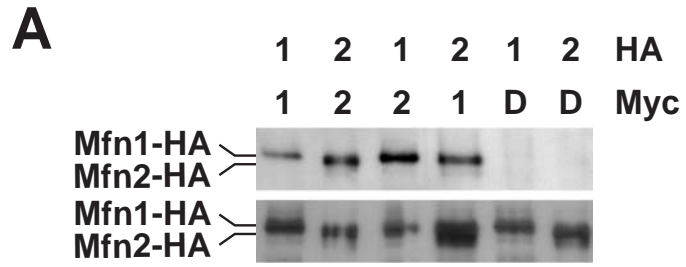
Discussion

An essential role for mitochondrial fusion in mouse development

Although mitochondrial dynamics involving fusion and fission has been previously demonstrated in vertebrates, the physiological importance of these processes has remained unclear. Our analysis of Mfn1 and Mfn2 mutant mice demonstrates an essential role for mitochondrial fusion in vertebrate development. Both lines of mice die in midgestation. For Mfn2-deficient mice, we observe a dramatic disruption in placental development, most obviously in the paucity of trophoblast giant cells. Trophoblast cell lines cultured from Mfn2 mutant blastocysts show fragmentation of mitochondrial tubules, consistent with a defect in mitochondrial fusion. These results show that, despite its broad expression pattern (unpublished data), Mfn2 is only required for selective developmental transitions.

Trophoblast giant cells are polyploid cells that arise from endoreplication, a process often associated with highly metabolically active cells (Edgar and Orr-Weaver, 2001). Because of their high metabolic rate, we speculate that, *in vivo*, trophoblast giant cells may be particularly vulnerable to perturbations in mitochondrial dynamics and presumably function. In fact, pre-eclampsia, the leading cause of fetal and maternal morbidity in the United States, is marked by shallow trophoblast invasion, often resulting in fetal growth retardation. Genetic and cellular evidence suggests that the underlying cause may be a mitochondrial defect (Talosi et al., 2000; Widschwendter et al., 1998).

We anticipate that there are other developmental processes in which the precise regulation of mitochondrial dynamics is essential. Thus, we have constructed conditional alleles of Mfn1 and Mfn2 that should facilitate the analysis of mitochondrial dynamics in adult tissues under both physiological and experimental conditions.

A model for the role of mitochondrial fusion in protecting mitochondrial function

It has been paradoxical why eukaryotes have invested in fusion and fission pathways in cells that have "stable" mitochondrial networks. Given that mitochondrial tubules can be maintained by reducing fusion and fission simultaneously (Bleazard et al., 1999; Fekkes et al., 2000; Mozdy et al., 2000; Sesaki and Jensen, 1999; Tieu and Nunnari, 2000), what is the advantage of maintaining mitochondria in a highly dynamic state?

Our analysis of Mfn-deficient cells suggests an answer to this question. Although bulk cultures of Mfn-deficient fibroblasts show normal levels of endogenous and coupled respiration by oxygen electrode measurements, when individual mitochondria are examined, we find that many cells contain a percentage of nonfunctional mitochondria, as evidenced by loss of membrane potential. In other cell culture systems, the use of dyes sensitive to mitochondrial membrane potential has revealed occasional and transient losses of membrane potential within small regions of a single mitochondrial tubule (Loew, 1999). We suggest that the dynamic nature of mitochondria protects these organelles by

ensuring that regional losses of membrane potential (Fig. 10A), caused perhaps by local depletion of metabolic substrates or mtDNA, are always transient. Mitochondrial fusion enables intermitochondrial cooperation by allowing exchange of both membrane and matrix contents, and therefore may help to restore local depletions and maintain mitochondrial function (Nakada et al., 2001a). Although there is no gross loss of mtDNA in mutant cells, we currently do not know if the individual, defective mitochondria have lost mtDNA.

Multiple molecular modes of mitofusin action

Given their broad and overlapping expression, it has been unclear why there are two separate mammalian mitofusins. Our results show that the two mitofusins form three distinct molecular complexes that are capable of promoting mitochondrial fusion - Mfn1 homotypic oligomers, Mfn2 homotypic oligomers, and Mfn1-Mfn2 heterotypic oligomers. We propose that the relative importance of each of these modes of mitofusin action can change depending on the cell type (Fig. 10B). In mouse fibroblasts, all three oligomeric complexes are likely to play important roles, because disruption of either Mfn1 or Mfn2 leads to severe mitochondrial fragmentation. Nevertheless, overexpression of Mfn1 homotypic oligomers or Mfn2 homotypic oligomers is sufficient to restore mitochondrial tubules, clearly demonstrating that the homotypic complexes are functional for fusion. In trophoblast giant cells, it appears that Mfn2 homotypic oligomers are

Figure 10: Models

(A) The protective role of mitochondrial fusion. At a low rate, individual mitochondria stochastically lose function. In wildtype cells, a defective mitochondrion (shaded) undergoes fusion with functional mitochondria and regains activity. In Mfn-deficient cells, such rescue occurs at a much reduced rate. (B) Three modes of mitofusin action. Mitofusins form homotypic and heterotypic complexes that lead to 3 activities (I, II, III) involving fusion. See text for details. Mfn1 mutant cells contain only activity III; Mfn2 mutant cells contain only activity I. Since disruption of either Mfn1 or Mfn2 fragments mitochondria and results in distinct phenotypes, MEFs appear to use all 3 activities (indicated by asterisks). In contrast, trophoblast giant cells predominantly use activity III, because they are affected in Mfn2 mutants and not Mfn1 mutants.
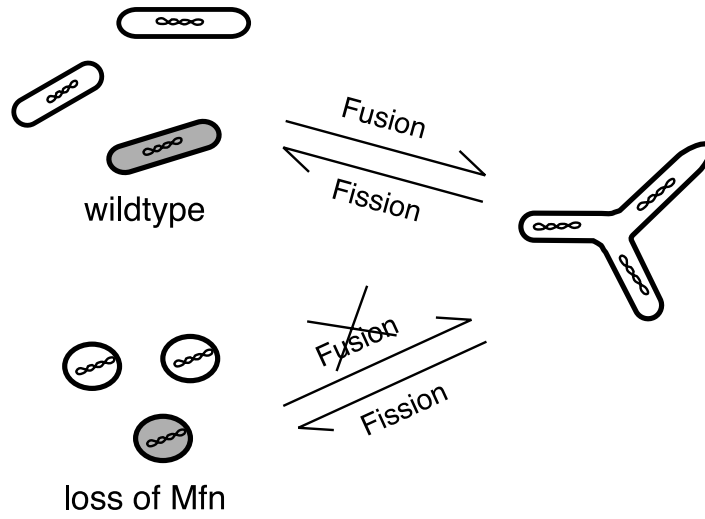
most important. As a result, this cell type is affected in Mfn2-deficient embryos but not Mfn1-deficient embryos.

It remains to be determined whether these three complexes function in the same or distinct types of mitochondrial fusion. It is also interesting to note that loss of Mfn2 leads to the formation of both large and small mitochondrial spheres. This phenotype is easily distinguished from loss of Mfn1. The larger mitochondrial fragments may be due to a higher residual fusion activity in Mfn2 mutant cells than in Mfn1 mutant cells. The loss of tubular shape may simply reflect the loss of cytoskeletal interactions, as noted in Fig. 4. Alternatively, it may be that Mfn2, and by extension, Mfn2 homotypic complexes, play a more direct role in maintaining mitochondrial tubular shape. Thus, although each of the Mfn complexes is involved in fusion, it is possible that they have distinct functions in addition to fusion.

In conclusion, in cells with continual cycles of fusion and fission, the mitochondrial population is essentially functionally homogeneous. At any given time point, however, individual mitochondria are functionally distinct entities (Collins et al., 2002). Therefore, without mitochondrial fusion, the stochastic differences between distinct mitochondria can accumulate to affect the well-being of the cell. The mammalian mitofusins, Mfn1 and Mfn2, function in three distinct molecular complexes to promote mitochondrial fusion, and thus protect mitochondrial function.

Materials and methods

Cloning of Mfn *cDNA and genomic constructs*

Homology searches using the *Drosophila* Fzo sequence (Hales and Fuller, 1997) identified a murine EST (IMAGE Consortium Clone ID 733269) that encodes a highly homologous polypeptide. This cDNA was used to screen a mouse kidney cDNA library, resulting in isolation of cDNAs for both *Mfn1* and *Mfn2*. These sequences are available from GenBank under accession no. AY174062 and AY123975.

Genomic clones of *Mfn1* and *Mfn2* were retrieved from a lambda 129/SvJ mouse genomic library (Stratagene). Genomic fragments were subcloned into the targeting vector pPGKneobpAlox2PGKDTA (a gift from F. Gertler and L. Jackson-Grusby) as the right arms. To insert the left arms, genomic fragments were amplified by PCR, which also introduced a stop codon just prior to the conserved GKS sequence in each GTPase domain. All constructs were verified by DNA sequence analysis. The sequences of all oligonucleotides used in this study are available from the authors.

To identify the chromosomal locations of *Mfn1* and *Mfn2*, the Jackson Laboratory (C57BL/6JEi x SPRET/Ei) F1 x SPRET/Ei backcross panel was used. Linkage analysis was performed by the Jackson Laboratory Mapping Resource.

Construction of knockout mice

Each gene-replacement vector was linearized with SacII, and electroporated into low-passage 129/SvEv embryonic stem cells using established procedures (Chester et al., 1998). Neomycin-resistant colonies were screened by Southern blot analysis. Two independently isolated clones for each targeted allele were injected into C57BL/6 blastocysts to generate chimeric mice. Excision of the neomycin cassette had no effect on phenotypes.

Confirmation of targeting event

For Southern blot analysis of targeted alleles, genomic DNAs were digested with XbaI (Mfn1 mutant line) or EcoRI (Mfn2 mutant line) and hybridized with a flanking genomic probe. PCR was used for routine genotyping of offspring. A forward genomic primer, a reverse genomic primer, and a reverse neomycin primer were used to detect both the targeted and wildtype alleles in a single reaction.

For Western blot analysis, chicken antisera was generated against Mfn1 (residues 348-579) or Mfn2 (residues 369-598) fused to an N-terminal histidine tag. IgY purified from chicken eggs was affinity-purified on a column coupled to a maltose-binding protein fusion protein containing either Mfn1 residues 348-579 or Mfn2 residues 369-598.

in situ *hybridization*

Individual implantation sites were fixed overnight at 4°C in 4% paraformaldehyde, dehydrated through an ethanol series, treated with xylenes, and embedded into paraffin blocks. For staining, 10 µm sections were cut in a transverse plane with respect to the placenta. Slides were processed for hematoxylin/eosin staining or *in situ* hybridization as previously described (Vortkamp et al., 1996). All riboprobe templates were derived from RT-PCR, using e11.5 placental RNA as template. No specific staining was detected using sense probes. For genotyping, embryonic tissue was scraped off unstained slides. DNA was recovered and genotyped by PCR.

Retroviral and plasmid constructs

To construct Mfn1 or Mfn2 with Myc epitope tags, a BamHI site was introduced immediately prior to the stop codon. The cDNA was subcloned into the vector pcDNA3.1(-)/Myc-His A (Invitrogen). Myc epitope tag cassettes, derived from pMMHb-3xMyc, were then inserted into the BamHI site to form pMfn-Myc. Mfn1(K88T) and Mfn2(K109A) were constructed by site-directed mutagenesis (Kunkel et al., 1991). To make the Mfn-HA constructs, *Mfn1* and *Mfn2* cDNAs were subcloned into a pcDNA3.1(-) vector containing a carboxyl terminal 3xHA tag. Murine *Drp1* was amplified from mouse placental RNA, and Drp1(K38A) was constructed by site-directed mutagenesis. The Drp1(K38A) insert was subcloned into a modified pcDNA3.1(-)/Myc-HisA vector containing 7 Myc epitope tags at the carboxyl terminus.

To generate retroviral expression constructs for each of the above, the epitope-tagged cDNAs were recloned into the retroviral vector pCLbW (gift of C. Lois). The retroviral expression vectors were co-transfected with the ecotropic retroviral packaging vector pCLEco (gift of C. Lois) into 293T cells. Retroviral stocks were harvested 48 hours after transfection and used to infect MEF cultures. Fragments encoding mitochondrially targeted GFP and dsRed (from plasmids HSZ and HSY, gift of H. Sesaki and R. Jensen) were subcloned into pCLbW to generate retroviral expression vectors.

MEF and TS cell lines

MEFs were derived from e10.5 embryos. Embryos were mechanically dispersed by repeated passage through a P1000 pipette tip and plated with MEF media [Dulbecco's Modified Eagle Medium, 10% fetal calf serum, 1x non-essential amino acids, 1 mM L-glutamine, penicillin/streptomycin (Life Technologies/Gibco BRL)].

For visualization of mitochondria, the MEFs were either stained with 150 nM MitoTracker Red CMXRos (Molecular Probes) or infected with a retrovirus expressing EYFP fused to the presequence from subunit VIII of human cytochrome c oxidase, which directs EYFP to the mitochondrial matrix (gift of R. Lansford; Okada et al. 1999). To facilitate immortalization, the MEFs were later infected with a retrovirus expressing SV40 large T antigen (gift of L. Jackson-Grusby; Jat et al. 1986). Neither retroviral infection nor immortalization affected mitochondrial morphology. To label actin filaments, cells were fixed in 4%

paraformaldehyde and stained with 2.5 units/ml rhodamine-phalloidin (Molecular Probes). The stained cells were post-fixed in 4% paraformaldehyde.

For time-lapse confocal microscopy, cells were plated at low density onto chambered glass coverslips. Cells with culture media were overlaid with light mineral oil and imaged in a 37°C chamber. EYFP-optimized filters and dichroics (q497lp, HQ500lp; Chroma) were used on a Zeiss 410 laser scanning confocal microscope.

TS cells from e3.5 blastocysts were derived using established protocols (Tanaka et al., 1998a). Live cells were stained with MitoTracker Red (150 nM) and Syto16 (100 nM; Molecular Probes).

PEG fusion

40,000 cells expressing mitochondrially targeted GFP were cultured overnight on 25 mm coverslips with 40,000 cells expressing mitochondrially targeted dsRed. The next morning, cells were fused for 60 seconds with 50% PEG 1500 (Roche). The cells were washed and grown for 7 hours or 24 hours in media containing 30 mg/ml cycloheximide before fixation.

Immunofluorescence

Cells grown on polylysine-coated coverslips were fixed with prewarmed (37°C) 3.7% formaldehyde and permeabilized in PBS/0.1% Triton-X-100. In some experiments, cells were incubated with 150 nM MitoTracker Red for 30 min. prior to fixation and then permeabilized with acetone at -20°C. Cells were blocked with 5% bovine calf serum, and incubated with primary antibody. For

Myc epitope-tagged proteins, the mouse monoclonal antibody 9E10 was used. For COX1, mouse monoclonal 1D6-E1-A8 (Molecular Probes) was used. For detection, Cy3- or Alexa Fluor 488-conjugated secondary antibodies (Jackson ImmunoResearch; Molecular Probes) were used. Cells were imaged with a Plan NeoFluar 63X objective on a Zeiss 410 laser scanning confocal microscope.

Analysis of mtDNA

Southern analysis of mtDNA was performed by linearizing with XhoI and probing with a radiolabeled PCR fragment containing the *COX1* gene.

Immunoprecipitation

Cell lines were infected with various combinations of retroviruses expressing Myc- and HA-tagged Mfn1, Mfn2, and Drp(K38A). Monolayers were resuspended in lysis buffer (150 mM NaCl, 50 mM Tris pH 8.0, 1% Triton, and a protease inhibitor cocktail) and immunoprecipitated with 9E10 antibody coupled to Protein A Sepharose beads. After washing, samples were immunoblotted with HA.11 (Covance).

Online Supplemental Materials

Mitochondrial dynamics in wildtype and mutant MEFs

Confocal time-lapse movies of EYFP-labeled mitochondria in wildtype (A), Mfn1 mutant (B) and Mfn2 mutant (C) MEFs. (A) and (C) are 20 minute recordings; (B) is a 10 minute recording. The microscopic field is 96 mm by 96 mm in (A), 68 mm by 68 mm in (B) and 75 mm by 75 mm in (C).

Acknowledgments

Abbreviations: Mfn, mitofusin; Fzo, fuzzy onions, mtDNA, mitochondrial DNA; Drp1, dynamin related protein 1; MEF, mouse embryonic fibroblast

References

1. Bakeeva, L.E., Y.S. Chentsov, and V.P. Skulachev. 1981. Ontogenesis of mitochondrial reticulum in rat diaphragm muscle. *Eur J Cell Biol*. 25:175-181.

2. Bakeeva, L.E., S. Chentsov Yu, and V.P. Skulachev. 1978. Mitochondrial framework (reticulum mitochondriale) in rat diaphragm muscle. *Biochim Biophys Acta*. 501:349-369.

3. Bakeeva, L.E., S. Chentsov Yu, and V.P. Skulachev. 1983. Intermitochondrial contacts in myocardiocytes. *J Mol Cell Cardiol*. 15:413-420.

4. Bereiter-Hahn, J., and M. Voth. 1994. Dynamics of mitochondria in living cells: shape changes, dislocations, fusion, and fission of mitochondria. *Microsc Res Tech*. 27:198-219.

5. Bleazard, W., J.M. McCaffery, E.J. King, S. Bale, A. Mozdy, Q. Tieu, J. Nunnari, and J.M. Shaw. 1999. The dynamin-related GTPase Dnm1 regulates mitochondrial fission in yeast. *Nat Cell Biol*. 1:298-304.

6. Bourne, H.R., D.A. Sanders, and F. McCormick. 1991. The GTPase superfamily: conserved structure and molecular mechanism. *Nature*. 349:117-127.

7. Chester, N., F. Kuo, C. Kozak, C.D. O'Hara, and P. Leder. 1998. Stage-specific apoptosis, developmental delay, and embryonic lethality in mice homozygous for a targeted disruption in the murine Bloom's syndrome gene. *Genes Dev*. 12:3382-3393.

8. Collins, T.J., M.J. Berridge, P. Lipp, and M.D. Bootman. 2002. Mitochondria are morphologically and functionally heterogeneous within cells. *Embo J*. 21:1616-1627.

9. Copp, A.J. 1995. Death before birth: clues from gene knockouts and mutations. *Trends Genet*. 11:87-93.

10. Cross, J.C. 2000. Genetic insights into trophoblast differentiation and placental morphogenesis. *Semin Cell Dev Biol*. 11:105-113.

11. Deng, C., A. Wynshaw-Boris, F. Zhou, A. Kuo, and P. Leder. 1996. Fibroblast growth factor receptor 3 is a negative regulator of bone growth. *Cell*. 84:911-921.

12. Edgar, B.A., and T.L. Orr-Weaver. 2001. Endoreplication cell cycles: more for less. *Cell*. 105:297-306.

13. Enriquez, J.A., J. Cabezas-Herrera, M.P. Bayona-Bafaluy, and G. Attardi. 2000. Very rare complementation between mitochondria carrying different mitochondrial DNA mutations points to intrinsic genetic autonomy of the organelles in cultured human cell. *J Biol Chem*. 275:11207-11215.

14. Faria, T.N., L. Ogren, F. Talamantes, D.I. Linzer, and M.J. Soares. 1991. Localization of placental lactogen-I in trophoblast giant cells of the mouse placenta. *Biol Reprod*. 44:327-331.

15. Fekkes, P., K.A. Shepard, and M.P. Yaffe. 2000. Gag3p, an outer membrane protein required for fission of mitochondrial tubules. *J Cell Biol*. 151:333-340.

16. Frank, S., B. Gaume, E.S. Bergmann-Leitner, W.W. Leitner, E.G. Robert, F. Catez, C.L. Smith, and R.J. Youle. 2001. The role of dynamin-related protein 1, a mediator of mitochondrial fission, in apoptosis. *Dev Cell*. 1:515-525.

17. Hales, K.G., and M.T. Fuller. 1997. Developmentally regulated mitochondrial fusion mediated by a conserved, novel, predicted GTPase. *Cell*. 90:121-129.

18. Hayashi, J., M. Takemitsu, Y. Goto, and I. Nonaka. 1994. Human mitochondria and mitochondrial genome function as a single dynamic cellular unit. *J Cell Biol*. 125:43-50.

19. Hermann, G.J., J.W. Thatcher, J.P. Mills, K.G. Hales, M.T. Fuller, J. Nunnari, and J.M. Shaw. 1998. Mitochondrial fusion in yeast requires the transmembrane GTPase Fzo1p. *J Cell Biol*. 143:359-373.

20. Hesse, M., T. Franz, Y. Tamai, M.M. Taketo, and T.M. Magin. 2000. Targeted deletion of keratins 18 and 19 leads to trophoblast fragility and early embryonic lethality. *Embo J*. 19:5060-5070.

21. Hwa, J.J., M.A. Hiller, M.T. Fuller, and A. Santel. 2002. Differential expression of the *Drosophila mitofusin* genes *fuzzy onions* (*fzo*) and *dmfn*. *Mechanisms of Development* 116: 213-216.

22. Jacquemin, P., V. Sapin, E. Alsat, D. Evain-Brion, P. Dolle, and I. Davidson. 1998. Differential expression of the TEF family of transcription factors in the murine placenta and during differentiation of primary human trophoblasts in vitro. *Dev Dyn*. 212:423-436.

23. Jat, P.S., C.L. Cepko, R.C. Mulligan, and P.A. Sharp. 1986. Recombinant retroviruses encoding simian virus 40 large T antigen and polyomavirus large and middle T antigens. *Mol Cell Biol*. 6:1204-1217.

24. Kraut, N., L. Snider, C.M. Chen, S.J. Tapscott, and M. Groudine. 1998. Requirement of the mouse I-mfa gene for placental development and skeletal patterning. *Embo J*. 17:6276-6288.

25. Kunkel, T.A., K. Bebenek, and J. McClary. 1991. Efficient site-directed mutagenesis using uracil-containing DNA. *Methods Enzymol*. 204:125-139.

26. Lee, S.J., F. Talamantes, E. Wilder, D.I. Linzer, and D. Nathans. 1988. Trophoblastic giant cells of the mouse placenta as the site of proliferin synthesis. *Endocrinology*. 122:1761-1768.

27. Lescisin, K.R., S. Varmuza, and J. Rossant. 1988. Isolation and characterization of a novel trophoblast-specific cDNA in the mouse. *Genes Dev*. 2:1639-1646.

28. Loew, L.M. 1999. Potentiometric membrane dyes and imaging membrane potential in single cells. *In* Fluorescent and luminescent probes for biological activity. W.T. Mason, editor. Academic Press, London. 210-221.

29. Lupas, A. 1996. Coiled coils: new structures and new functions. *Trends Biochem Sci*. 21:375-382.

30. Morris, R.L., and P.J. Hollenbeck. 1995. Axonal transport of mitochondria along microtubules and F-actin in living vertebrate neurons. *J Cell Biol*. 131:1315-1326.

31. Mozdy, A.D., J.M. McCaffery, and J.M. Shaw. 2000. Dnm1p GTPase-mediated mitochondrial fission is a multi-step process requiring the novel integral membrane component Fis1p. *J Cell Biol*. 151:367-380.

32. Nakada, K., K. Inoue, and J. Hayashi. 2001a. Interaction theory of mammalian mitochondria. *Biochem Biophys Res Commun*. 288:743-746.

33. Nakada, K., K. Inoue, T. Ono, K. Isobe, A. Ogura, Y.I. Goto, I. Nonaka, and J.I. Hayashi. 2001b. Inter-mitochondrial complementation: Mitochondria-specific system preventing mice from expression of disease phenotypes by mutant mtDNA. *Nat Med*. 7:934-940.

34. Nangaku, M., R. Sato-Yoshitake, Y. Okada, Y. Noda, R. Takemura, H. Yamazaki, and N. Hirokawa. 1994. KIF1B, a novel microtubule plus end-directed monomeric motor protein for transport of mitochondria. *Cell*. 79:1209-1220.

35. Nunnari, J., W.F. Marshall, A. Straight, A. Murray, J.W. Sedat, and P. Walter. 1997. Mitochondrial transmission during mating in Saccharomyces cerevisiae is determined by mitochondrial fusion and fission and the intramitochondrial segregation of mitochondrial DNA. *Mol Biol Cell*. 8:1233-1242.

36. Okada, A., R. Lansford, J.M. Weimann, S.E. Fraser, and S.K. McConnell. 1999. Imaging cells in the developing nervous system with retrovirus expressing modified green fluorescent protein. *Exp Neurol*. 156:394-406.

37. Ono, T., K. Isobe, K. Nakada, and J.I. Hayashi. 2001. Human cells are protected from mitochondrial dysfunction by complementation of DNA products in fused mitochondria. *Nat Genet*. 28:272-275.

38. Rapaport, D., M. Brunner, W. Neupert, and B. Westermann. 1998. Fzo1p is a mitochondrial outer membrane protein essential for the biogenesis of functional mitochondria in Saccharomyces cerevisiae. *J Biol Chem*. 273:20150-20155.

39. Riddle, R.D., R.L. Johnson, E. Laufer, and C. Tabin. 1993. Sonic hedgehog mediates the polarizing activity of the ZPA. *Cell*. 75:1401-1416.

40. Riley, P., L. Anson-Cartwright, and J.C. Cross. 1998. The Hand1 bHLH transcription factor is essential for placentation and cardiac morphogenesis. *Nat Genet*. 18:271-275.

41. Rizzuto, R., P. Pinton, W. Carrington, F.S. Fay, K.E. Fogarty, L.M. Lifshitz, R.A. Tuft, and T. Pozzan. 1998. Close contacts with the endoplasmic reticulum as determinants of mitochondrial Ca2+ responses. *Science*. 280:1763-1766.

42. Rojo, M., F. Legros, D. Chateau, and A. Lombes. 2002. Membrane topology and mitochondrial targeting of mitofusins, ubiquitous mammalian homologs of the transmembrane GTPase Fzo. *J Cell Sci*. 115:1663-1674.

43. Santel, A., and M.T. Fuller. 2001. Control of mitochondrial morphology by a human mitofusin. *J Cell Sci*. 114:867-874.

44. Scott, I.C., L. Anson-Cartwright, P. Riley, D. Reda, and J.C. Cross. 2000. The HAND1 basic helix-loop-helix transcription factor regulates

trophoblast differentiation via multiple mechanisms. *Mol Cell Biol*. 20:530-541.

45. Sesaki, H., and R.E. Jensen. 1999. Division versus fusion: Dnm1p and Fzo1p antagonistically regulate mitochondrial shape. *J Cell Biol*. 147:699-706.

46. Smirnova, E., L. Griparic, D.L. Shurland, and A.M. van Der Bliek. 2001. Dynamin-related protein drp1 is required for mitochondrial division in mammalian cells. *Mol Biol Cell*. 12:2245-2256.

47. Sprang, S.R. 1997. G protein mechanisms: insights from structural analysis. *Annu Rev Biochem*. 66:639-678.

48. Talosi, G., E. Endreffy, S. Turi, and I. Nemeth. 2000. Molecular and genetic aspects of preeclampsia: state of the art. *Mol Genet Metab*. 71:565-572.

49. Tanaka, S., T. Kunath, A.K. Hadjantonakis, A. Nagy, and J. Rossant. 1998a. Promotion of trophoblast stem cell proliferation by FGF4. *Science*. 282:2072-2075.

50. Tanaka, Y., Y. Kanai, Y. Okada, S. Nonaka, S. Takeda, A. Harada, and N. Hirokawa. 1998b. Targeted disruption of mouse conventional kinesin heavy chain, kif5B, results in abnormal perinuclear clustering of mitochondria. *Cell*. 93:1147-1158.

51. Tieu, Q., and J. Nunnari. 2000. Mdv1p is a WD repeat protein that interacts with the dynamin-related GTPase, Dnm1p, to trigger mitochondrial division. *J Cell Biol*. 151:353-366.

52. Vortkamp, A., K. Lee, B. Lanske, G.V. Segre, H.M. Kronenberg, and C.J. Tabin. 1996. Regulation of rate of cartilage differentiation by Indian hedgehog and PTH-related protein. *Science*. 273:613-622.

53. Widschwendter, M., H. Schrocksnadel, and M.G. Mortl. 1998. Pre-eclampsia: a disorder of placental mitochondria? *Mol Med Today*. 4:286-291.

Appendix 2: Detailed Protocols

Contents

Photolithographic Patterning of Proteins on Glass Coverslips

This protocols produces coverslips patterned over the majority of their surface area. There are still some batch to batch irregularities, but generally the quality is pretty good.

1. Acid Cleaning
   a. Set an 800 mL beaker in a bath of ice with a stirbar on a stirplate, in a fume hood. Wear a lab coat, goggles, and gloves and use the splash shield if available.
   b. Pour 75 mL of cold 30% hydrogen peroxide into the 800 mL beaker.
   c. While stirring, **<u>SLOWLY</u>** add 175 mL concentrated sulfuric acid to above solution.
   d. Mark coverslips to distinguish top from bottom, an etched L works fine
   e. Load coverslips in wafer basket
   f. Carefully remove stirbar from acid solution and add wafer basket.
   g. Allow to soak for 1 hr
2. Remove Wafer Basket from Acid Bath and Rinse
   a. 3 x 5 minutes water
   b. 1 x 5 minutes 95% ethanol
3. Silanize
   a. Mix 2% solution of APTES in 95% ethanol (8 mL APTES, 20 mL water, plus 372 mL 95% ethanol).
   b. Allow APTES solution to hydrolyze for 5 minutes.
   c. Put coverslips in Aptes for 10 minutes.
4. Remove Coverslips from Silane Solution and Rinse.
   a. 4 x 5 minutes 95% ethanol
5. Cure APTES layer by heating coverslips at ~100° C for 15 minutes.
6. Remove from oven and allow to cool.
7. Derivatize APTES Layer.
   a. Add 10 mg 4-benzoylbenzoic acid, succinimidyl ester to 1 mL DMSO
   b. Put blank coverslips on wafer trays.
   c. Place 90 uL drops of DMSO solution on each coverslip.
   d. Remove APTES coverslips from wafer basket and place on top of DMSO drop, L mark up, to form a coverslip sandwich.
   e. Leave overnight (~12 hours).
8. Transfer Coverslips to Wafer Basket.
9. Rinse 4 x 5 minutes 95% ethanol.
10. Rinse coverslips in PBS and store in the dark at 4° C until photopatterning.
11. Photopattern (in Michael Roukes' cleanroom on the mask aligner)
    a. Put 50 uL drop of protein solution (~1 mg/mL) on photo mask
    b. Place derivatized coverslip on drop, L mark up
    c. Expose to UV for 2-10 minutes, assuming a luminosity of 10 mW/cm^2.
    d. Transfer coverslips to PBS vial.

e. Repeat as necessary.
f. Rinse mask.

12. Rinse and Mount Slides
    a. Rinse 3 x 5 minutes PBS.
    b. Load coverslip in culture chamber.
    c. Apply 0.5-2 mL of fibronectin at 10ug/mL for 1 hour. Volume depends on size of coverslip and chamber.
    d. Rinse 2x PBS.
13. Coverslip is ready for cell culture.

Materials: Manufacturer

1. Conc. Sulfuric Acid   EM Sciences (VWR) SX1244-6
2. 30% Hydrogen Peroxide   EM Sciences (VWR) HX0635-2
3. 95% Ethanol   EM Sciences (VWR) EX0280-3
4. Aminopropyltriethoxysilane   Sigma   A-3648
5. 4-benzoylbenzoic acid, succinimidyl ester   Molecular Probes   B-1577
6. Dimethylsulfoxide   EM Sciences (VWR) MX1457-6
7. Wafer Basket: Fluoroware A14-018-0216
8. Wafer Basket Cover   Fluoware A14-028-0215
9. Wafer Basket Handle   Fluoware A029-0215 12"
10. Wafer Tray/Individual Coverslip Storage   Fluoware H22-15-0615
11. Wafer Tray Cover   Fluoware H22-151-0615

Alternate Photolithography Protocol

Example of a representative successful protocol for patterning coverslips, prior to optimization for simple organic solvents. All reagents are the same as previous patterning protocol. All organic solvents are reagent grade from EM Sciences. Coverslips generated with those protocol were not compatible with neural crest explant culture.

1) Soaked coverslips in Scavenger solution (210 mL HCl (36-38%) 90   mL H_2O_2 (30%)) for 2 hrs
   a) Rinse in flowing H20.
   b) Rinse 2 x 15 minutes ddH20 (800 mL)
   c) Rinse 1 x 15 minutes EtOH (400 mL)

2) Silanized coverslips overnight in 2% APTES/EtOH (total volume: 0.4L)

3) Washed coverslips
   a) 1 x 10 minutes   Toulene   500 mL
   b) 1 x 10 minutes   EtOH   500 mL
   c) 1 x 10 minutes   pH9.5 H20   800 mL
   d) 1 x 10 minutes   Toluene   500 mL
   e) 1 x 10 minutes   EtOH   500 mL
   f)   1 x 10 minutes   CH2Cl3   300 mL
   g) 1 x 10 minutes   Pentane   300 mL

4) Crosslinked coverslips overnight w/150 uL (10mg B1577 in 1 mL DMSO) at room temperature.

5) Rinsed all coverslips
   a) 1 x 10 minutes   CH2Cl3   300 mL
   b) 1 x 10 minutes   Toluene   500 mL
   c) 1 x 10 minutes   Pentane   500 mL

6) Exposed to UV for 30 minutes w/ 50 uL of 1 ug/uL protein solution.

7) Rinsed all coverslips
   a) 1 x 15 minutes   pH 9.0 Na Bicarb 0.1 M   300 mL
   b) 1 x 15 minutes   1 M NaCl   500 mL
   c) 1 x 15 minutes   ddH20   500 mL

Chlorosilane Patterning Protocol from Chris Chen, Johns Hopkins University

1) Acid wash coverslips as per general photolithography protocol (A2-2).
2) Rinse in ddH2O.
3) Bake at 90°C for 20 minutes.
4) Allow to cool.
5) Place in clean vacuum dessicator.
6) Add 1 drop of (tridecafluoro-1,1,2,2-tetrahydrooctyl)-1-trichlorosilane (United Chemical Technologies T-2492) to the bottom of the desiccator. The chlorosilane will irreversibly silanize any glass, so use disposable glass pipettes to transfer the solution. 1 drop will coat all of the glass inside a desiccator, so there is no need to carefully measure it.
7) Apply a static vacuum and wait 1 hour to overnight.
8) Apply a silicone mold to the glass.
9) Apply a light vacuum to the mold.
10) Suck a drop of 50:50 ethanol:water through the mold.
11) Suck a drop of 25:75 ethanol:water through the mold.
12) Suck 3 drops of water through the mold.
13) Suck a drop of protein (1-5 ug/mL) into the mold.
14) Wait 2-3 hours.
15) Suck 3-5 drops of water through the mold.
16) Submerge the mold in water, then remove it.

Quail Neural Crest Cultures – (Based on Protocol By Rusty Lansford)

1. Put quail eggs in shaking incubator big end up, 44-52 hours prior to culture.

Preparation: (Best done in laminar flow hood or other clean area)
2. Turn on blower/UV hours in advance.
3. Wipe down working area with 70% ethanol.
4. Wash hands carefully.
5. Wipe down everything entering hood with 70% ethanol.
6. Mix either Neural Crest Media or Defined Media.
7. Mix up dispase solution.
8. Add 1% Penn/Strep to sterile Howard Ringer's Solution.
9. Add fibronectin to substrate (glass or plastic) in 35 mm tissue culture dish, at 10-20 ug/mL.
10. Let substrate stand for 45 minutes to an hour at room temperature, then pipet off excess fibronectin solution, rinse once with PBS, and add culture media.

Tools to lay out in flow hood with dissecting scope:
>Scissors
>Serrated forceps
>Sharp tungsten needle probe
>Fine forceps
>3 mL syringe with 18 gauge needle
>1 mL syringe with 25 gauge needle (bent to moderate angle)
>1/10 India ink/Ringer's
>Petri dish with Ringer's

Start of Explant Procedure
11. Remove eggs from incubator and spray with 70% ethanol.
12. Allow eggs to stand at room temp for 30 minutes.
13. Prepare waste bag for eggs.
14. Fill ice bucket; put sterile 3 well glass dish on ice.
15. With 3 mL syringe remove 0.5-1 mL of albumin from each egg.
16. Open egg with scissors.
17. Inject small amount of ink under embryo (IF NEEDED).
18. Using serrated forceps and scissors, cut embryo out of egg.
19. Transfer embryo to dish filled with Ringer's solution.
20. Repeat for all 40 eggs.
21. Clean up embryos, using forceps to hold embryo and edge of tungsteen needle to cut out the trunk region.
22. Transfer trunk segments to cold 3 well glass dish with long sterile glass pipet, being careful not to allow trunks to enter body of pipet.

23. Remove most of the Ringer's solution.
24. Add dispase solution, mix trunk segments, remove dispase, and add fresh dispase solution.
25. Immediately put dish on ice; leave on ice for 15 minutes.
26. Add serum blocking solution to wells 2 and 3.
27. Pipet trunks gently up and down in dispase solution.
28. Watch trunk segments for signs of dissociation and change dispase regularly. Total time of pipetting trunk segments should be 5-15 minutes.
29. As neural tubes separate transfer them quickly to well #2, transferring minimal volume between wells.
30. Once all neural tubes are in well #2, transfer selectively to #3, checking to make sure that no notocords are still attached. Rinse in dispase again if needed.
31. Rinse neural tubes through 3 changes of serum blocking media, then 3 changes of appropriate serum free culture media.
32. Add neural tubes to culture dishes and return dishes to incubator.
33. Mechanically remove neural tubes 6-18 hours after start of incubation.

Standard Solutions

Dispase: 3 mg/mL Dispase II in 20 mM Hepes buffered DMEM, (made fresh)

Dissecting Solution: Howard Ringer's solution with 1% Penn/Strep
   a) Add 7.2 g NaCl, 0.23 g CaCl, 0.37 g KCl to 1/2 L ddH2O.
   b) Add 10.5 mL of dibasic sodium phosphate and 2.6 mL monobasic potassium acid phosphate to solution. (Stock dibasic is 0.946 g in 100 mL ddH2O and stock monobasic is 0.907 g in 100 mL ddH2O).
   c) Add 400 mL ddH2O.
   d) Adjust pH to 7.4 then fill to 1 L.

Serum Blocking Solution (neutralizes Dispase):
   i. 44 mL of DMEM
   ii. 5 mL Serum (usually fetal bovine serum; type not important)
   iii. 1 mL 1M Hepes
   iv. 0.5 mL Penn/Strep

Neural Crest Media: F12 Basal Media (contains L-glut), 1% Penn/ Strep, 1% N2 Supplement

Defined Media: DMEM High Glucose (contains L-glut), 1% Penn/Strep, 1% NEAA

Imaging Media: Neural Crest Media + 20 mM Hepes buffer.

Materials:	Manufacturer
1. Quail Eggs	AA Laboratories
2. India Ink (Fount India)	Koh-I-Noor 9150-1
3. DMEM, high glucose, plus L-glutamine	Irvine Scientific 9031
4. Hepes buffer solution, 1M	Irvine Scientific 9319
5. Penicillin-Streptomycin (Penn/Strep)	Irvine Scientific 9366
6. Fetal Bovine Serum	Irvine Scientific 3000
7. F-12 Nutrient Mixture (Ham)	Gibco/BRL 11765-054
8. Dispase II (neutral protease, grade II)	Boehringer Manheim 165 859
9. Human Fibronectin	BD Labware 4008B

Optical Tweezers Experimental Outline

Day 1

1) Set 40 quail eggs in plastic trays at 37°C, 44-52 hours prior to intended neural tube prep.

Day 2

1) Bead Derivatization: **(See protocol sheet A2-11)**
2) Silanize beads in aminopropyltriethoxysilane solution in ethanol.
   a. Rinse 3x in PBS
   b. Biotinylate in EZ-Link-Imino-Biotin
   c. Rinse 3x in PBS
   d. Streptavidinate beads.
   e. Rinse 3 times in PBS.
3) Protein Derivatization
   a. Incubate in protein mixture.
      i. negative control
      ii. biotin-Protein-G
   b. Rinse 3x in PBS
   c. Incubate half of negative control and Protein-G in ephrin-FC protein mixture.
   d. Rinse 3x in PBS

Day 3

1) Coverslip preparation (**See protocol sheet A2-13**)
   a. Acid wash
   b. Silanize
   c. Cure
   d. Coat in protein
2) Culture chamber assembly
   a. 40 mm coverslips in 6 well dishes
3) Neural tube prep **(See protocol sheet A2-6)**
   a. Surgically extract embryos from eggs.
   b. Surgically isolate trunk region of interest.
   c. Enzymatically isolate neural tube from trunk region.
   d. Treat with serum.
   e. Culture on coverslip chambers.

Day 4

1) Evaluate outgrowth
2) Mechanically remove neural tubes.
3) Assemble cell culture chamber with microenvironment on tweezers stage.
4) Experiment
    a. Film normal behavior (5-15 minutes)
    b. Stimulate cells with coated beads.
    c. Film reaction.

Materials: ## Manufacturer

1. Glass beads, 1.58 um diameter   Duke Scientific 8150
2. Aminopropyltriethoxysilane   Sigma   A-3648
3. EZ-Link NHS-Iminobiotin (Pierce)   Fisher Scientific 1117AJ
4. Streptavidin   Molecular Probes S-888
5. Protein G-Biotin Conjugate   Calbiochem 203198
6. Mouse ephrin-B1/FC chimera   R&D Systems 473-EB-200
7. 40 mm coverslips, 250/pk   BiopTechs 40-1313-0319
12. Conc. Sulfuric Acid   EM Sciences (VWR) SX1244-6
13. 30% Hydrogen Peroxide   EM Sciences (VWR) HX0635-2
14. 95% Ethanol   EM Sciences (VWR) EX0280-3
15. Aminopropyltriethoxysilane   Sigma   A-3648
16. Dimethylsulfoxide   EM Sciences (VWR) MX1457-6
17. Wafer Basket: Fluoroware A14-018-0216
18. Wafer Basket Cover   Fluoware A14-028-0215
19. Wafer Basket Handle   Fluoware A029-0215 12"
20. Wafer Tray/Individual Coverslip Storage   Fluoware H22-15-0615
21. Wafer Tray Cover   Fluoware H22-151-0615
22. Imaging Media: See A2-7.

Neutravidin Bead Coating Protocol (Based on Protocol by Kevin Thigpen)

1. Make up 2 batches of 2% aminopropyltriethoxysilane in dry ethanol (20 uL APTES in 1 mL EtOH), each in a 1.7 mL eppendorf.
2. Mix bead solution well, then transfer 100 uL of beads to each APTES/ethanol solution.
3. Silanize for 30 minutes at room temperature.
4. Centrifuge for 1 minute at 6 krpm.
5. Pipette away solution and discard.
6. Rinse 3x with PBS.
   a. Add 1 mL PBS to tube.
   b. Mix extensively.
   c. Centrifuge for 1 minute at 6 krpm.
   d. Pipette away solution.
7. Weigh out 6 mg of Pierce EZ Link NHS-LC-Biotin. Add 200 uL dry DMSO, then 800uL PBS.
8. Add 500 uL DMSO solution to each tube of beads.
9. Biotinylate for 10 minutes at 37° C.
10. Centrifuge for 1 minute at 6 krpm.
11. Pipette away solution and discard.
12. Rinse 3x with PBS.
    a. Add 1 mL PBS to tube.
    b. Mix extensively.
    c. Centrifuge for 1 minute at 6 krpm.
    d. Pipette away solution.
13. Add 200 ug streptavidin in 0.5 mL PBS to the tube.
14. Streptavidinate for 30 minutes at 37° C.
15. Centrifuge for 1 minute at 6 krpm.
16. Pipette away solution and discard.
17. Rinse 3x with PBS.
    a. Add 1 mL PBS to tube.
    b. Mix extensively.
    c. Centrifuge for 1 minute at 6 krpm.
    d. Pipette away solution.
18. Add 50 ug of Protein G in 0.5 mL PBS to tube.
19. Incubate for 30 minutes at 37° C.
20. Centrifuge for 1 minute at 6 krpm.
21. Pipette away solution and discard.
22. Rinse 3x with PBS.
    a. Add 1 mL PBS to tube.
    b. Mix extensively.
    c. Centrifuge for 1 minute at 6 krpm.
    d. Pipette away solution.
23. Add 200 uL of Imaging Media to Protein-G beads and store.

24. Add 20 ug of ephrin-B1 to 1 eppendorf of Protein-G beads.
25. Incubate for 30 minutes at 37°C.
26. Centrifuge for 1 minute at 6 krpm.
27. Pipette away solution and discard.
28. Rinse 3x with PBS.
    a. Add 1 mL PBS to tube.
    b. Mix extensively.
    c. Centrifuge for 1 minute at 6 krpm.
    d. Pipette away solution.
29. Add 200 uL of Imaging Media to ephrin-B1 beads and store.

Fibronectin Substrates for Optical Tweezers Experiments

1) Load 40 mm #1 glass coverslips (Bioptechs) into a Fluoware wafer basket.
2) Add 500 mL of 95% ethanol to a 1 L beaker, add wafer basket with coverslips to beaker and sonicate for 5 minutes.
3) Silanize coverslips in 2% aminopropyltriethoxysilane (APTES) solution (10 mL APTES, 25 mL water, 465 mL ethanol) for 15 minutes.
4) Rinse 3 x 500 mL 95% ethanol for 5 minutes each.
5) Cure at 65-80°C for 20 minutes to an hour.
6) Store under static vacuum until needed.
7) Before neural tube prep (A2-6), add a 400 uL drop of 20ug/mL human fibronectin to the bottom of a 60 mm petri dish. Place coverslip on top. Incubate at room temp for 1 hour.
8) Transfer coverslip to fresh 60 mm tissue culture dish, inverting the coverslip so that the fibronectin side faces up.
9) Add 5 mL of neural crest media (A2-7) and incubate at 37°C until needed.

Best-fit Sphere Analysis of *Xenopus Laevis* Embryos

All spherical coordinate analysis of the *Xenopus* volumetric data was implemented and executed in Matlab (The Mathworks Inc., Natick MA). Typically only one of the three 8-bit color channels was processed to reduce memory load. In order to estimate the best-fit sphere, the image volume was initially down-sampled by a factor of six in all dimensions and smoothed by a 0.65 sample radius Gaussian filter. The interior and exterior of the embryo were segmented by conversion to a binary image using a threshold determined by Otsu's Algorithm (1) prior to 2D hole filling using internal functions provided by Matlab. The isosurface mesh representing the external boundary of the embryo was generated from the segmented binary data again using internal Matlab functions. A least-squares best-fit sphere was calculated for the mesh vertices using a custom implementation of the algorithm suggested by David Eberly (2). The coordinates of the center and the radius parameterize the best-fit sphere, so the cartographic coordinates of the sphere surface require specification of a pole and prime meridian, both of which can be supplied by an experienced user. For this application, the "south pole" is defined as the center of the blastopore at the embryo surface and the prime meridian is the midline axis of symmetry of the archenteron. Once the blastopore center has been located, the down-sampled data is re-sampled along planes of constant latitude and redisplayed to allow the center of the archenteron to be specified. All further re-sampling can now be performed in the blastopore-archenteron spherical frame of reference. Shell

segments from within the high-resolution data were extracted by supplying ranges of radius, latitude and longitude to a custom rapid tri-linear interpolator implemented in C and interfaced to Matlab. The stacks of extracted shell segments are essentially three-dimensional (radius, latitude, longitude) image data which can be exported to other visualization applications or redisplayed using the Matlab Mapping Toolbox in various cartographic projections.

References

1.   Otsu N. Threshold Selection Method from Gray-Level Histograms. Ieee Transactions on Systems Man and Cybernetics 1979; 9:62-66.

2.   Eberly D. Least-squares Fitting of Data. http://www.magic-software.com/Documentation/LeastSquaresFitting.pdf.

Acknowledgements

Classic Stripe Assay (Protocol from Rusty Lansford)

Store silicone matrices are stored in 70% ethanol

Preparation: All done in tissue culture hood unless noted.

1. Take matrices out of 70% ethanol and allow to dry.

2. UV sterilize 35 mm tissue culture dishes for 2 hours.

3. Cut out 2.5 cm^2 of nitrocellulose filter. Dissolve in 10 mL methanol.

4. Add 100 uL of nitrocellulose solution to each dish, and rotate dish so that nitrocellulose coats uniformly.

5. Insert a small piece of PE-10 tubing into matrix fill channel.

6. Make up solutions (all solutions made up in PBS):

    a. Antibody Solution: 250 ug/mL goat anti-FC antibody, 100 ug/mL human fibronectin, 10 ug/mL BSA-Texas Red.

    b. Fibronectin Solution: 250 ug/mL human fibronectin.

    c. Ligand-FC Solution: 10 ug/mL ligand-FC

7. Filter sterilize all solutions through 0.2 micron filter.

8. Attach silicon matrices to culture dishes, making to sure to get a good seal.

9. Outline the extent of the matrix on the bottom of the dish with a Sharpie.

10. Take 1 mL of Antibody Solution in 1 mL plastic syringe, add fine gauge needle to syringe, and connect to tubing in matrix. Push 1/3 of solution through the matrix.

11. Wait 20 minutes.

12. Push 1/3 of solution through the matrix.

13. Wait 20 minutes.

14. Push 1/3 of solution through the matrix

15. Wait 20 minutes.

16. Push 1/2 mL PBS through matrix.

17. Remove matrix from dish and wash 3x with PBS.

18. Coat entire dish with Fibronectin Solution for 1 hour (typically 1.5 mL).

19. Remove PBS.

20. Add 1.5 mL Ligand-FC solution to dish.

21. Wait 2 hours.

22. Rinse 3x with PBS.

23. Add neural crest media.

24. Culture quail neural tubes as usual (See A2-6).

Materials: **Manufacturer**

1. Goat Anti-Human IgG   Jackson Immunoresearch, 109-005-098
2. Human Fibronectin   BD Labware, 4008B
3. BSA-Rhodamine   Sigma, A-2289
4. Silicon Matrices   Juergen Jung,
                               (MPI Entwicklungsbiologie)
5. PBS: Cell Culture Grade   Sigma, D8662
6. Nitrocellulose Paper   Schleicher & Schuell 20570

Movie	Cell	Logic	Protein	Beads	Cell Contact	Collapses	Polarity Changes	Score 0-2
A	1	No Stim	-	-	0	0	0	
	2	No Stim	-	-	0	2	1	
B	1	No Stim	-	-	3	1 (bleb)	0	
	2	No Stim	-	-	2	0	0	
	3	No Stim	-	-	3	0	0	
C	1	No Stim	-	-	0	0	0	
	2	No Stim	-	-	0	0	0	
D	1	No Stim	-	-	0	0	1	
E	1	No Stim	-	-	3	1	3	
	2	No Stim	-	-	4	0	2	
	3	No Stim	-	-	2	1	2	
	4	No Stim	-	-	4	0	0	
	5	No Stim	-	-	3	1	3	
F	1	No Stim	-	-	2	1	1	
	2	No Stim	-	-	2	0	0	
2	1	Leading Edge	ephrin-B1	1	1	0	1	1
3	1	Leading Edge	ephrin-B1	3	0	1	1	2
4	1	Seq Leading Edge	ephrin-B1	2 cluster	0	2	2	2
5	1	Tripod Leading Edge	ephrin-B1	1	0	1	1	1
6	1	Leading Edge	ephrin-B1	1	0	0	3	1
7	1	Leading Edge	Protein-G	1	1	1	0	0
	2	No Stim	Protein-G	-	1	1	0	0
8	1	Leading Edge	Protein-G	1	0	1	1	1
11	1	Multi-Stim	ephrin-B1	7	0	2	3	2
12	1	Leading Edge	ephrin-B1	4	0	1	1	2
	2	Multi-Stim	ephrin-B1	2	0	1	1	2

Movie	Cell	Logic	Protein	Beads	Cell Contact	Collapses	Polarity Changes	Score 0-2
13	1	No Stim	ephrin-B1	-	1	0	2	0
	2	Leading Edge	ephrin-B1	1	1	1	2	2
14	1	Leading Edge	ephrin-B1	2	1	2	3	2
	2	No Stim	ephrin-B1	-	1	2	2	0
15	1	Leading Edge	ephrin-B1	1*	0	1	1	1
16	1	Multi-Stim	Protein-G	3	0	3	4	2
17	1	Multi-Stim	Protein-G	4	0	0	1	0
18	1	Leading Edge	Protein-G	1*	0	0	0	0
19	1	Seq Leading Edge	Protein-G	1+cluster	0	0	1	0
20	1	Lateral Edge	ephrin-B1	1	0	1	1	1
21	1	Lateral Edge	ephrin-B1	1	1	0	0	0
	2	Lateral Edge	ephrin-B1	4	1	0	0	0
22	1	Lateral Edge	ephrin-B1	Cluster	0	1	1	2
23	1	Seq Leading Edge	ephrin-B1	2	1	2	2	2
	2	Lateral Edge	ephrin-B1	2	1	2	1	1
	3	Multi-Stim	ephrin-B1	4	1	1	4	1
24	1	Lateral, then Lead	ephrin-B1	4	0	2	2	1
25	1	Lateral Edge	ephrin-B1	2	0	1	1	1
26	1	Lateral Edge	Protein-G	3	0	1	2	1
27	1	Lateral Edge	Protein-G	1	0	1	1	1
28	1	Lateral Edge	Protein-G	6	0	1	2	2
29	1	Lateral Edge	Protein-G	2	0	0	0	0
30	1	Multi-Stim	ephrin-B1	11	0	0	0	0
31	1	Leading Edge	ephrin-B1	4	0	3	4	2
32	1	Leading Edge	ephrin-B1	cluster	0	2	3	2
33	1	Leading Edge	ephrin-B1	1 + cluster	0	1	1	2

Movie	Cell	Logic	Protein	Beads	Cell Contact	Collapses	Polarity Changes	Score 0-2
34	1	Leading Edge	ephrin-B1	1 cluster	1	2	1	2
35	1	Seq Stim	ephrin-B1	2 + cluster	1	0	2	2
	2	Leading Edge	ephrin-B1	1	1	0	1	0
36	1	Multi-Stim	ephrin-B1	4 + cluster	0	1	1	1
37	1	Multi-Stim	Protein-G	4	1	2	3	2
	2	No Stim	Protein-G	-	1	0	0	0
38	1	Leading Tripod	Protein-G	cluster	0	1	3	2
39	1	Leading Edge	Protein-G	5	1	2	2	2
	2	Multi-Stim	Protein-G	4	2	2	3	2
40	1	Leading Edge	Protein-G	4	0	1	1	2
41	1	Leading Edge	Protein-G	2	0	0	0	0
45	1	Leading Edge	ephrin-B1	1	0	1	1	1
46	1	Leading Edge	ephrin-B1	cluster	0	2	2	2
47	1	Leading Edge	ephrin-B1	2	0	0	1	1
48	1	Leading Edge	ephrin-B1	3	0	0	1	1
49	1	Leading Edge	ephrin-B1	1	0	1	2	1
	2	Leading Edge	ephrin-B1	1	0	2	2	2
50	1	Leading Edge	ephrin-B1	1	0	2	2	2
51	1	Leading Edge	ephrin-B1	1	0	0	0	0
52	1	Leading Edge	Protein-G	1	2	1	1	1
53	1	Leading Edge	Protein-G	1	0	1	2	1
54	1	Leading Edge	Protein-G	1 + cluster	0	1	2	2

A2-21

Movie	Cell	Logic	# of Beads	Protein	Collapses		Polarity		Score 0-2	
					Koos	Ewald	Koos	Ewald	Koos	Ewald
3	1	Leading Edge	3	**ephrin-B1**	0	1	1	1	1	2
4	1	Seq Leading Edge	2 cluster	**ephrin-B1**	2	2	2	2	2	2
5	1	Tripod Leading Edge	1	**ephrin-B1**	0	1	0	1	0	1
6	1	Leading Edge	1	**ephrin-B1**	0	0	0	3	0	1
8	1	Leading Edge	1	Protein-G	0	1	1	1	0	1
11	1	Multi-Stim	7	**ephrin-B1**	1	2	1	3	1	2
12	1	Leading Edge	4	**ephrin-B1**	1	1	1	1	1	2
	2	Multi-Stim	2	**ephrin-B1**	0	1	0	1	0	2
15	1	Leading Edge	1*	**ephrin-B1**	1	1	1	1	1	1
16	1	Multi-Stim	3	Protein-G	1	3	1	4	2	2
17	1	Multi-Stim	4	Protein-G	0	0	0	1	0	0
18	1	Leading Edge	1*	Protein-G	0	0	0	0	0	0
19	1	Seq Leading Edge	1+cluster	Protein-G	0	0	0	1	0	0
20	1	Lateral Edge	1	**ephrin-B1**	1	1	1	1	1	1
22	1	Lateral Edge	Cluster	**ephrin-B1**	1	1	1	1	2	2
24	1	Lateral, then Lead	4	**ephrin-B1**	0	2	0	2	0	1
25	1	Lateral Edge	2	**ephrin-B1**	1	1	0	1	0	1
26	1	Lateral Edge	3	Protein-G	0	1	1	2	0	1
27	1	Lateral Edge	1	Protein-G	0	1	0	1	0	1
28	1	Lateral Edge	6	Protein-G	1	1	1	2	0	2
29	1	Lateral Edge	2	Protein-G	0	0	0	0	0	0
30	1	Multi-Stim	11	**ephrin-B1**	0	0	0	0	0	0
31	1	Leading Edge	4	**ephrin-B1**	1	3	1	4	1	2
32	1	Leading Edge	cluster	**ephrin-B1**	2	2	2	3	2	2
33	1	Leading Edge	1 + cluster	**ephrin-B1**	0	1	0	1	1	2
36	1	Multi-Stim	4 + cluster	**ephrin-B1**	0	1	0	1	0	1
38	1	Leading Tripod	cluster	Protein-G	1	1	1	3	1	2
40	1	Leading Edge	4	Protein-G	1	1	1	1	2	2
41	1	Leading Edge	2	Protein-G	0	0	0	0	0	0
45	1	Leading Edge	1	**ephrin-B1**	1	1	1	1	1	1
46	1	Leading Edge	cluster	**ephrin-B1**	1	2	2	2	2	2
47	1	Leading Edge	2	**ephrin-B1**	0	0	0	1	0	1
48	1	Leading Edge	3	**ephrin-B1**	0	0	1	1	2	1
49	1	Leading Edge	1	**ephrin-B1**	1	1	1	2	1	1
	2	Leading Edge	1	**ephrin-B1**	1	2	1	2	2	2
50	1	Leading Edge	1	**ephrin-B1**	1	2	1	2	1	2
51	1	Leading Edge	1	**ephrin-B1**	0	0	0	0	0	0
53	1	Leading Edge	1	Protein-G	1	1	1	2	0	1
54	1	Leading Edge	1 + cluster	Protein-G	1	1	1	2	2	2